Title
The Role of Star-forming Galaxies in Cosmic Reionization

Author
Rehagen, Robin Eileen Mostardi

Publication Date
2015

Peer reviewed|Thesis/dissertation

University of California
Los Angeles

The Role of Star-forming Galaxies in Cosmic Reionization

A dissertation submitted in partial satisfaction
of the requirements for the degree
Doctor of Philosophy in Astronomy

by

Robin Eileen Mostardi Rehagen

2015

Abstract of the Dissertation

The Role of Star-forming Galaxies in Cosmic Reionization

by

Robin Eileen Mostardi Rehagen

Doctor of Philosophy in Astronomy

University of California, Los Angeles, 2015

Professor Alice Eve Shapley, Chair

One of the foremost goals in the study of cosmological reionization is understanding the nature of the sources of the ionizing photons. The search for leaking ionizing radiation from high-redshift star-forming galaxies has resulted in dozens of promising candidates, yet few confirmed detections. In this thesis, I present results from a survey for $z \sim 2.85$ ionizing Lyman-Continuum (LyC) emission in the HS1549+1933 field and place constraints on the amount of ionizing radiation escaping from star-forming galaxies. Using a custom narrow-band filter (NB3420) tuned to wavelengths just below the Lyman limit at $z \geq 2.82$, I probe the LyC spectral region of 49 Lyman break galaxies (LBGs) and 91 Lyα-emitters (LAEs) spectroscopically confirmed at $z \geq 2.82$. I also present high-resolution, $U_{336}V_{606}J_{125}H_{160}$ follow-up *HST* observations of 16 $z \sim 3$ candidate LyC emitters identified with the NB3420 filter. With these follow-up data, I obtain high spatial-resolution photometric redshifts of all subarcsecond components of the high-redshift galaxies in order to eliminate foreground contamination and identify robust candidates for leaking LyC emission. I find only one object with a robust LyC detection that is not due to foreground contamination. A comparison with representative samples of LBGs indicates that the most exceptional aspect of the stellar population fit to this object is its young age ($\lesssim$ 50Myr). I obtain a contamination-free estimate for the comoving specific ionizing emissivity at $z = 2.85$, indicating (with large uncertainties) that star-forming galaxies provide roughly the same contribution as QSOs to the ionizing background at this redshift. The results of my thesis work show that foreground contamina-

tion prevents ground-based LyC studies from obtaining a full understanding of LyC emission from $z \sim 3$ star-forming galaxies. Future progress in direct LyC searches is contingent upon the elimination foreground contaminants through high spatial-resolution observations, and upon acquisition of sufficiently deep LyC imaging to probe ionizing radiation in galaxies at the faint end of the luminosity function.

The dissertation of Robin Eileen Mostardi Rehagen is approved.

Marco CM Velli

Steven R Furlanetto

Alice Eve Shapley, Committee Chair

University of California, Los Angeles

2015

To my parents

Table of Contents

List of Figures

List of Tables

Acknowledgments

There are so many people who have supported me throughout my years in graduate school. Above all, I'd like to thank Alice Shapley for being such a caring advisor, for always being available for help whenever I needed it, and for her words of support and encouragement throughout the last six years. I also really appreciate the time she spent editing paper drafts with me; I know that during graduate school I have grown not only as a scientist, but as a writer too. I'd also like to thank Daniel Nestor for all his help with my first project, and the astronomy graduate students at UCLA, for creating such a fun and supportive community of students. I'd like to thank my husband Thomas, for teaching me how to relax, and for reading me thousands of pages of good literature in the pursuit of that goal. Finally, I'd like to thank my parents, for all their love and support throughout my life, for encouraging me to pursue my passions, and for teaching me to think like a scientist, even before I knew what science was.

Chapter 2 is a version of Mostardi et al. (2013), and is reproduced by permission of the AAS. Chapter 3 is a version of a paper that will soon be submitted for publication to the Astrophysical Journal, and will appear as Mostardi et al. (2015). I would like to thank my collaborators on these works: Alice Shapley, Dan Nestor, Charles Steidel, Ryan Trainor, Naveen Reddy, and Brian Siana.

This research was supported by NASA, through the Space Telescope Science Institute program GO-12959, and by the David and Lucile Packard Foundation.

Vita

2009 B.S. (Astrophysics), University of California, Berkeley

2011 M.S. (Astronomy), University of California, Los Angeles

Publications

Mostardi, R. E., Shapley, A. E., Steidel, C. C., Trainor, R. F., Reddy, N. A., & Siana, B. *A High-Resolution Hubble Space Telescope Study of Lyman-Continuum Leakers at* $z \sim 3$ (in prep)

Mostardi, R. E., Shapley, A. E., Nestor, D. B., Steidel, C. C., Reddy, N. A., & Trainor, R. F. *Narrowband Lyman Continuum Imaging of Galaxies at* $z \sim 2.85$, 2013, ApJ, 779, 65

Silverman, Foley, Filippenko, Ganeshalingam, Barth, Chornock, Griffith, Kong, Lee, Leonard, Matheson, Miller, Steele, Barris, Bloom, Cobb, Coil, Desroches, Gates, Ho, Jha, Kandrashoff, Li, Mandel, Modjaz, Moore, Mostardi, Papenkova, Sung, Perley, Poznanski, Reuter, Scala, Serduke, Shields, Swift, Tonry, Van Dyk, Wang, & Wong *BSNIP I. Observations, data reduction, and spectroscopic sample of 582 low-z Type Ia supernovae*, 2012, MNRAS, 425, 1789

CHAPTER 1

Introduction

Cosmology is the study of the evolution of the universe from the Big Bang until the present day. After the Big Bang, which occurred 13.8 billion years ago, the history of the universe has been characterized by several distinct epochs. The earliest of these is known as the inflationary epoch, a short period in which the universe underwent exponential expansion. The universe continued to expand after the inflationary epoch, although at a slower rate, and this expansion continues to the present day. The expansion caused the universe to cool, culminating in the creation of the first atoms (380,000 years after the Big Bang; $z \sim 1100$[1]; Bennett et al., 2003), which began a period of time known as the Dark Ages. Eventually, the first stars and galaxies began to form ($100 - 300$ million years after the Big Bang; $z \sim 15 - 30$; Loeb & Barkana, 2001), and the universe began to resemble the one we know today.

The formation of stars and galaxies had an important effect on the surrounding universe. The clouds and filaments of primordial gas from which galaxies formed, and which still link galaxies together in a cosmic web, are known as the intergalactic medium (IGM). Initially, just after the first stars and galaxies began to form, the IGM was composed of neutral atoms of hydrogen and helium gas. However, the extreme UV light emitted by the first stars eventually began to escape from galaxies into the IGM, stripping the neutral atoms in the IGM of their electrons and beginning a process known as reionization. Hydrogen

[1]Here, z refers to cosmological redshift, which can be thought of as a proxy to time. As light travels through the expanding universe from one point to another, its wavelength gets longer (redshifted) with the expansion of the universe itself. Thus, light that has been traveling for the longest time has the greatest redshift, and comes from the oldest sources. The present day corresponds to a redshift of $z = 0$. Redshift is directly linked to the relative size of the universe at any given time (also known as the scale factor, a), by the expression $a(t) = 1/(1 + z)$. It can also be easily calculated observationally from the expression $z = \lambda_{observed}/\lambda_{emitted} - 1$.

reionization is hypothesized to have occurred after the formation of the first stars, sometime between 300 million and one billion years after the Big Bang ($6 < z < 14$; Fan et al., 2006a). Once completed, reionization left the IGM full of ionized hydrogen gas, with a remaining fraction of neutral gas of only one in three thousand atoms at $z \sim 6$ ($f_{HI} = 10^{-3.5}$; Fan et al., 2006b), which has dropped to one in one hundred thousand atoms today ($f_{HI} = 10^{-5}$; Fan et al., 2006a). Any astronomer wishing to study the UV properties of extragalactic sources must observe these sources through the clouds of hydrogen gas in the IGM, and absorption of light from even the small fraction of neutral hydrogen left in the IGM becomes significant for galaxies at $z \gtrsim 1$. It is thus essential to understand how reionization progressed throughout time and how the ionization state of the IGM changes as a function of redshift. And to complete the story, we must understand the nature of the sources emitting the ionizing, far-UV light responsible for reionization.

1.1 Searches for the Sources Responsible for Reionization

There are several possible sources for the ionizing photons involved in reionization. Any photon with a wavelength less than 912Å (the Lyman limit) can ionize a hydrogen atom. Such wavelengths correspond to photon energies of 13.6 eV and higher: the ionization energy of hydrogen. These far-UV photons, also called Lyman continuum (LyC) photons, are only created by extremely hot sources. The two sources believed to contribute the most to reionization are quasars (accreting supermassive black holes at the centers of galaxies, also known as QSOs) and massive stars (Loeb & Barkana, 2001). Quasars peak in number density around $z \sim 2 - 3$ (Hopkins et al., 2007), and may produce a significant output of ionizing photons at lower redshifts. However, the low abundance of quasars at the higher redshifts at which reionization occurred indicates that another source must be responsible for the bulk of the ionizing photons early on. Thus, massive stars in the first galaxies represent the most likely source of the first ionizing photons. Theoretical models present the first generation of stars (metal-free Population III stars; Schaerer, 2002) as very massive, hot, short-lived entities that emit copious amount of ionizing radiation. After these massive stars die out

and enrich the surrounding gas with heavier atoms than hydrogen and helium, the following generations of stars develop with more standard stellar populations. Only the hottest and most massive of these subsequent generations of stars (namely, O and B stars) are capable of emitting significant ionizing radiation.

In order to test the theory of reionization as having progressed due to ionizing emission from hot stars, studies in the past 15 years have attempted to locate star-forming galaxies with leaking ionizing radiation and measure their ionizing properties. However, the process of identifying galaxies with leaking LyC emission has proven difficult. Even a small fraction of neutral hydrogen in the IGM between Earth and the galaxy of interest (one atom in ten thousand; Fan et al., 2006a) will result in complete absorption of any LyC photons escaping the galaxy. It is thus impossible to observe actual LyC photons during the epoch of reionization itself, as the hydrogen neutral fraction in the IGM is too high. We therefore must search for LyC-emitting galaxies at lower redshifts ($z \lesssim 4$), where the IGM is more transparent. Although the IGM is the most transparent to LyC photons in the local universe and at $z < 2$, searches for LyC emission from galaxies in this redshift range have yielded few detections (Grimes et al., 2007, 2009; Cowie et al., 2009; Bridge et al., 2010; Siana et al., 2007, 2010; Leitet et al., 2011, 2013; Borthakur et al., 2014). Studies at higher redshift ($z \sim 3 - 4$), however, have apparently been more successful, yielding dozens of candidate LyC-emitting galaxies (Steidel et al., 2001; Shapley et al., 2006; Iwata et al., 2009; Nestor et al., 2011, 2013; Siana et al., 2015; Vanzella et al., 2010a, 2012, 2015). Although none of these $z = 3 - 4$ LyC-emitting galaxies were directly involved in reionization, which occurred earlier ($6 < z < 14$), all LyC studies at $z \lesssim 4$ aim to both understand the general processes governing LyC photon escape from galaxies, and find ways to generalize the low-redshift results to the higher redshifts of cosmological reionization.

In this thesis, I present a detailed study of LyC emission in $z \sim 2.85$ star-forming galaxies in the HS1549+1933 field. The primary goal of this work is to locate and confirm individual high-redshift galaxies with leaking LyC emission. Definitive confirmation of leaking LyC-emitters is complicated by the issue of contamination from foreground galaxies, and to date only a handful of the high-redshift galaxies with putative LyC detections have, upon

further inspection, shown no evidence for foreground contamination (e.g., Vanzella et al., 2015; Nestor et al., 2013; Siana et al., 2015). A second important goal of this work is to analyze the multiwavelength properties of confirmed LyC leakers. We employ broadband photometry to help characterize the stellar populations of LyC leakers, UV spectroscopy to shed light on their ISM kinematics, and high-resolution *HST* imaging to enable us to study the morphologies of LyC leakers at different wavelengths. This data will inform our understanding of how ionizing photons escape from galaxies, and may provide us with ways to identify galaxies with leaking LyC emission during the higher redshifts of reionization, where direct observation of ionizing photons is impossible.

1.2 Identifying Star-forming Galaxies at High Redshift

In order to measure LyC emission from high-redshift galaxies, it is first necessary to locate large samples of star-forming galaxies at high redshift. The sample of galaxies presented in this thesis were identified via two different selection techniques for high-redshift galaxies: the Lyman break selection method and narrowband selection of Lyman alpha (Lyα) emission, which we discuss below.

Galaxies selected through the Lyman break technique are known as Lyman-break galaxies (LBGs). As a population, LBGs are star-forming galaxies with a large population of massive stars that provide a high rest-frame UV flux, with small to moderate amounts of dust extinction, and many of which are experiencing large-scale outflows due to their vigorous star-formation rates (Shapley et al., 2003). The Lyman break itself is a dip in the spectrum of a galaxy caused by the absorption of UV starlight in the LyC region of the spectrum. This absorption is due to neutral hydrogen atoms, both from the interstellar medium (ISM) of the galaxy itself and from the IGM between the galaxy and the observer. LBGs are selected based on their photometric colors from 3 broadband filters: two filters probing the slope of the rest-frame non-ionizing UV continuum, and a third filter probing flux in the LyC region in order to gauge the strength of the Lyman break. In one of the pioneering works that identified high-redshift galaxies using this method, Steidel et al. (1996) used the Hubble

Deep Field to identify 8 LBGs in the redshift range of $3 - 3.5$. The color criteria employed to select for LBGs were

$$\mathrm{F300W} - \mathrm{F450W} > 1.2 + (\mathrm{F450W} - \mathcal{R}),$$

which is equivalent to requiring that the break across the bluer passbands be greater than 3 times the break across the redder passbands, indicating the presence of a Lyman break in the spectrum. In the last 15 years, the number of galaxies identified by the Lyman break technique has grown from eight to thousands, and this technique has proven useful over a broad redshift range. By varying the central wavelengths of the filters used for the color selection and color criteria employed, galaxies have been found at a range of redshifts from $1.4 \leq z \leq 8$ (see, e.g., Adelberger et al., 2004; Steidel et al., 2003, 2004; Ouchi et al., 2004; Oesch et al., 2010). The sample of $z \sim 2.85$ UV-selected galaxy surveys discussed in this thesis were identified in the LBG surveys of Steidel et al. (2003, 2004, 2011).

A second method of locating high-redshift star-forming galaxies is through narrowband imaging of high-equivalent-width emission lines. This technique involves the creation of a narrowband filter designed to match the wavelength of a particular emission line at a given redshift. It has been used mainly to select galaxies based on their Lyman alpha emission line strength, and galaxies identified in this way are known as Lyα-Emitters (LAEs). In detail, the selection of LAEs requires both imaging in a narrowband filter centered on the Lyα emission line, as well as a broadband filter that probes the level of continuum emission around the Lyα line. LAEs are flagged as objects with red broadband minus narrowband colors, indicating a large ratio between the flux in the emission line and the flux density of the surrounding continuum. For example, in Steidel et al. (2000), LAEs were selected as objects with a color excess of $GV - NB = 0.7$. LAEs have been identified across a broad range of redshifts, from $z = 2.4$ to $z = 6.5$ (e.g., Cowie & Hu, 1998; Rhoads et al., 2000; Gronwall et al., 2007; Ouchi et al., 2008; Nilsson et al., 2010).

While both of these selection techniques provide astronomers with methods of locating star-forming galaxies, LBGs and LAEs sample different populations of star-forming galaxies.

LBGs have a typical number density of $1-2$ galaxies per square arcminute (Steidel et al., 1999, 2004), while Gronwall et al. (2007) have shown that, at magnitudes of $R < 25.5$, LAEs are roughly 3 times rarer than LBGs of similar magnitudes. As a population, LBGs have bright continuum magnitudes and a variety of emission line strengths, while LAEs have high-equivalent width Lyα emission and a variety of continuum magnitudes. The most massive LAEs are found to have stellar masses of $\sim 3 \times 10^9 M_\odot$ (Gawiser et al., 2007), while the typical LBG stellar mass is two orders of magnitude larger ($\sim 3 \times 10^{11} M_\odot$ Shapley et al., 2001; Adelberger et al., 2005). Because LAEs are selected by their emission line properties only, they often have intrinsically faint continuum magnitudes. It is therefore an ongoing challenge to model the stellar populations of LAEs and understand their relationship to LBGs and other populations of star-forming galaxies (see, e.g., Gawiser et al., 2007; Guaita et al., 2011).

1.3 Roadmap

In Chapter 2 of this thesis, I present deep LyC imaging of the HS1549 field, probing the ionizing properties of 49 LBGs and 91 LAEs spectroscopically confirmed at $z \sim 2.85$. I analyze the ionizing to non-ionizing UV flux-density ratios, Lyα equivalent widths, and rest-frame near-infrared colors of galaxies with putative LyC detections. I present simulations modeling the effects of foreground contaminants, and derive estimates of the average LyC escape fraction and comoving LyC emissivity at $z = 2.85$. This work has been published in the Astrophysical Journal (Mostardi et al., 2013).

In Chapter 3 of this thesis I present high-resolution, multiwavelength follow-up *HST* imaging of 16 candidate LyC emitters from Chapter 2. I obtain high spatial-resolution photometric redshifts for all subarcsecond components of each high-redshift galaxy in order to eliminate foreground contamination, resulting in a single robust detection of LyC emission in the LBG MD5. I examine the stellar population fit of this object with respect to those of typical star-forming galaxies, and conclude that the young age of its stellar population may be responsible for its observed LyC emission. I analyze the LyC emission properties of MD5,

and derive a revised value for the LyC emissivity at $z = 2.85$, based on the contaminant-free sample. This work will soon be submitted to the Astrophysical Journal, and will appear as Mostardi et al. (2015).

In Chapter 4, I provide some concluding thoughts on this project.

CHAPTER 2

Narrowband Lyman-Continuum Imaging of Galaxies at $z \sim 2.85$

2.1 Introduction

One of the foremost goals in the study of cosmological reionization is determining the sources of the ionizing photons. Quasars (QSOs), while able to maintain an ionized universe from $z \sim 0-2$ (Cowie et al., 2009), rapidly fall in number density at redshifts greater than $z \sim 2$ (Hopkins et al., 2007). Recent studies of the faint-end slope of the QSO luminosity function indicate that while the QSO contribution to the overall ionizing budget at $z \gtrsim 4$ may not be negligible, QSOs alone are still unable to sufficiently account for all of the ionizing radiation during the epoch of reionization (Fontanot et al., 2012; Glikman et al., 2011; Siana et al., 2008). It is generally assumed that star-forming galaxies fill in the remainder of the gap in the ionizing budget. Therefore, studying the ionizing Lyman-continuum (LyC) properties of high-redshift star-forming galaxies can provide vital information about the evolution of the intergalactic medium (IGM). Because the IGM at $z \gtrsim 6$ is opaque to LyC photons, we cannot directly observe the ionizing radiation at the redshifts corresponding to reionization. In order to directly measure the ionizing radiation escaping galaxies and study the galactic properties that give rise to significant LyC escape fractions, we must locate and study lower-redshift analogs to the star-forming galaxies that reionized the universe.

There have been several recent studies of LyC emission at both low and intermediate redshifts. To probe $0 < z < 2$, space-based far-UV observing facilities such as *HST*/STIS, *GALEX*, and *FUSE* have searched for LyC radiation from star-forming galaxies (Leitherer et al., 1995; Malkan et al., 2003; Siana et al., 2007, 2010; Grimes et al., 2007, 2009; Cowie

et al., 2009; Bridge et al., 2010) only to obtain null results (but see, e.g., Leitet et al., 2013). At $z \sim 3$, ground-based optical studies have shown that roughly 10% of star-forming galaxies have a moderately high escape fraction of ionizing radiation ($f_{esc} > 0.2$; Shapley et al., 2006; Iwata et al., 2009; Nestor et al., 2011, 2013). At even higher redshift ($z \sim 4$), Vanzella et al. (2012) find only one LyC-emitter out of 102 LBGs, although this small number of LyC detections might reasonably be attributed to the rapidly increasing IGM opacity rather than to processes internal to galaxies. Siana et al. (2010) investigate the conspicuous lack of LyC-emitting galaxies at low redshift, where LyC transmission through the IGM is high. Given the similar stellar populations for UV-luminous galaxies at $z \sim 1.3$ and $z \sim 3$, Siana et al. (2010) infer that LyC production does not change with redshift but the mechanism governing LyC escape must vary.

One key observational method used to measure LyC flux is deep imaging through a narrowband filter tuned to wavelengths just bluewards of the Lyman limit. Narrowband imaging provides a very effective way to simultaneously probe the LyC of large samples of galaxies at the same redshift. We have designed a narrowband imaging program to study the LyC properties of galaxies in the HS1549+1919 field. This field was observed as part of a larger survey of UV-selected star-forming galaxies at $z \sim 2-3$ (Steidel et al., 2003, 2004, 2011; Reddy et al., 2008) and contains a galaxy protocluster with a redshift-space overdensity of $\delta_{gal} \sim 5$ at $z = 2.85 \pm 0.03$ (Figure 2.1). The "spike" redshift coincides with that of a hyperluminous QSO (Trainor & Steidel, 2012). More than 350 UV-selected galaxies have been identified in the HS1549 field, ~ 160 of which have been spectroscopically confirmed at $1.5 \leq z \leq 3.5$. Additionally, narrowband imaging with a 4670Å filter tuned to the wavelength of Lyα at the redshift spike has revealed $\sim$300 potential Lyα Emitters (LAEs) and several Lyα "blobs" (Steidel et al., 2000, 2011). Such a large sample of star-forming galaxies at approximately the same redshift greatly facilitates the systematic narrowband imaging search for leaking LyC emission.

Our work in the HS1549 field parallels that of Nestor et al. (2011, 2013) and Iwata et al. (2009), who investigated another high-redshift protocluster (SSA22a; $z = 3.09$). Several questions emerged from these initial narrowband LyC studies, including the nature of galaxies

with large offsets (occasionally reaching several kpc) between the centroids of their non-ionizing UV-continuum and LyC emission. While significant offsets have been predicted in some simulations modeling the escape of ionizing photons (e.g., Gnedin et al., 2008), in practice it is difficult to determine whether the observed offsets provide information about the interstellar medium of a LyC-leaking galaxy, or are simply the result of a foreground contaminant (Vanzella et al., 2010b, 2012). Another key result presented in the SSA22a studies is the high apparent ratio of escaping ionizing to non-ionizing UV radiation measured for several LAEs. For some objects, this ratio exceeded unity (Nestor et al., 2011; Inoue et al., 2011). If such measurements are free of foreground contamination, they are at odds with standard models for the intrinsic spectral energy distribution of star-forming galaxies (Bruzual & Charlot, 2003). Consequently, as discussed by Vanzella et al. (2012), the most critical goal for LyC studies is to minimize the possibility that candidate LyC-leaking galaxies are contaminated by low-redshift interlopers. While previous $z \sim 3$ LyC studies have been plagued by small samples and lack of spectroscopic redshifts, in this work we present a sample of 131 spectroscopically confirmed galaxies (49 LBGs and 91 LAEs, 9 of which are constituents of both samples). While our seeing-limited, ground-based imaging makes it difficult to distinguish individual cases of foreground contamination, we have performed simulations to model the amount of expected contamination in our samples as a whole (as in Nestor et al., 2011, 2013).

In this work, we build upon previous high-redshift LyC studies by considering a large spectroscopic sample of galaxies in an independent field from the SSA22a observations. We present imaging for 12 new $z \sim 2.85$ galaxies with putative LyC detections and correct for foreground contamination and IGM absorption. For our LBG and LAE samples, we calculate the escape fraction of ionizing photons both in an absolute sense and relative to the escape fraction of non-ionizing UV photons. We also explore the differential multiwavelength properties of objects with and without leaking LyC radiation with regard to their Lyα equivalent widths, rest-frame near-infrared photometry, and stellar populations. The paper is organized as follows. In Section 2.2, we describe our observations, data reduction, and galaxy sample. In Section 2.3, we present the LyC and broadband photometric measurements and

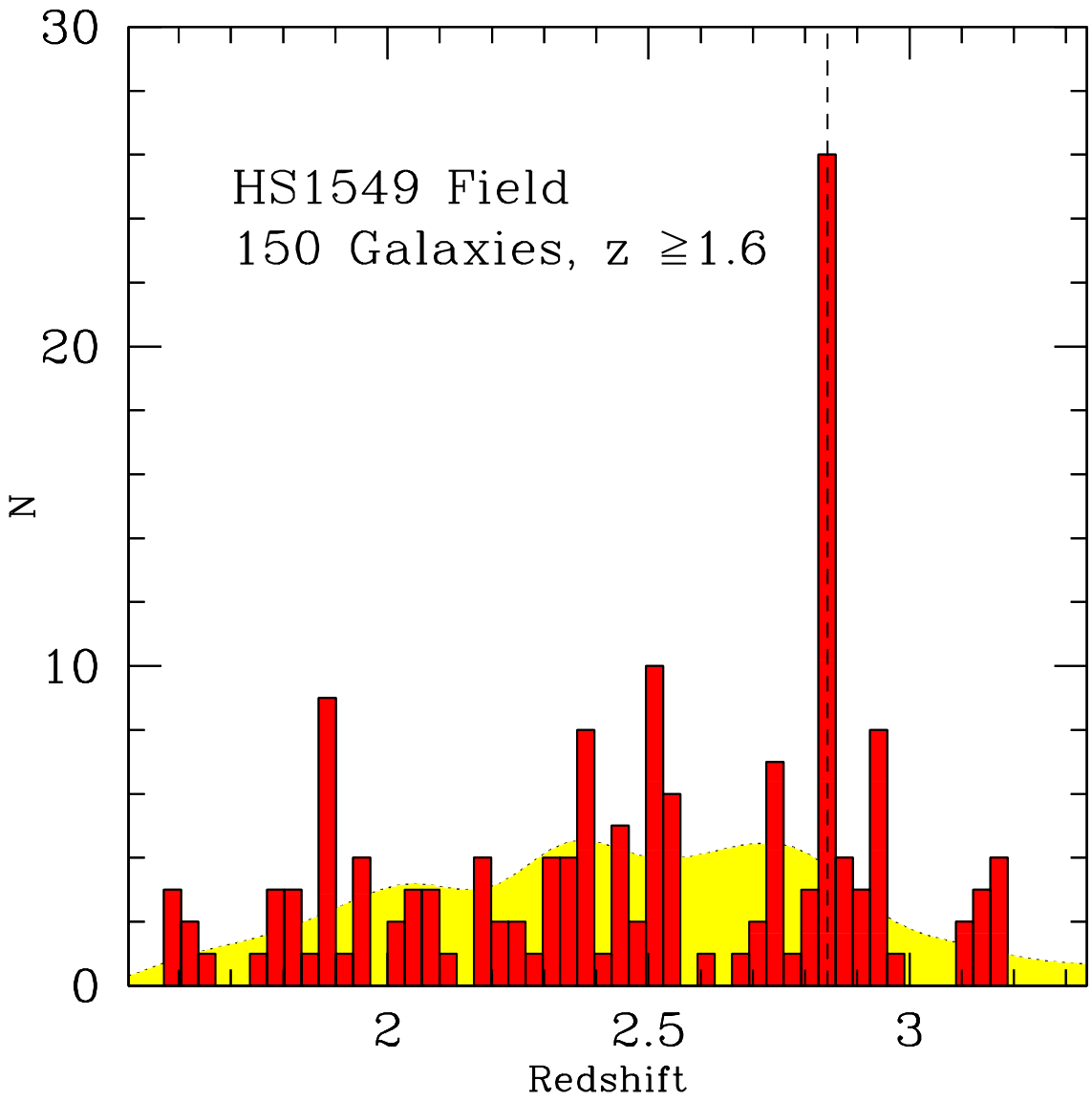

Figure 2.1 Redshift histogram of galaxies in the HS1549 field. The yellow curve represents the overall redshift selection function of the LBG survey (Steidel et al., 2003, 2004), normalized to the observed number of galaxies in HS1549. The overdensity of objects at $z = 2.85$ is indicated by the dashed line, representing the redshift of the HS1549 protocluster.

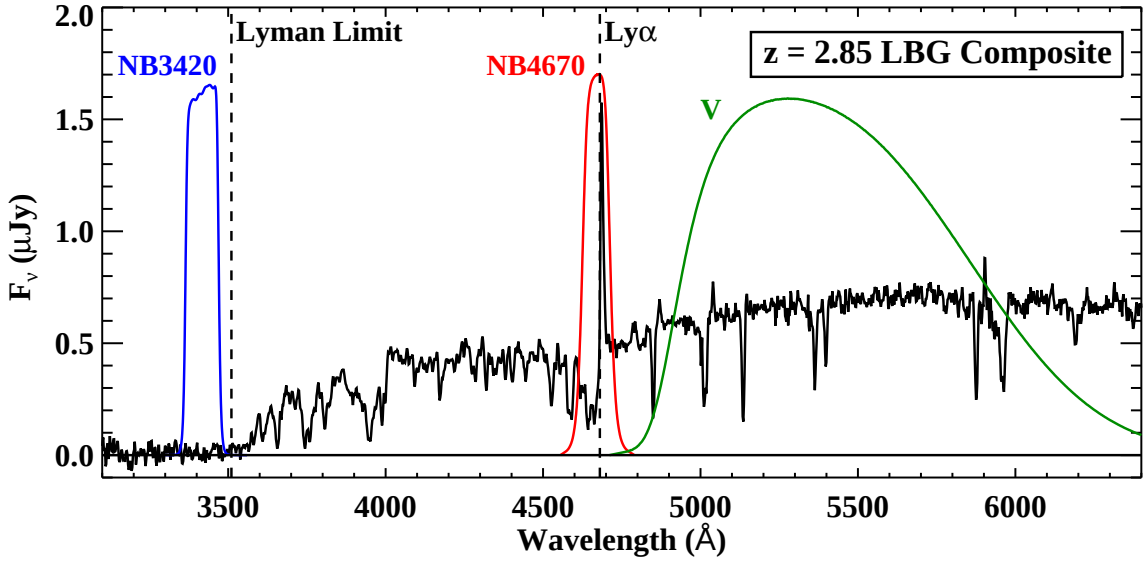

Figure 2.2 Narrowband filter transmission curves overlaid on a composite LBG spectrum (Shapley et al., 2006) redshifted to $z = 2.85$. The NB3420 filter (shown in blue) is located just bluewards of the Lyman limit at $z = 2.85$, and probes LyC emission for galaxies at $z \geq 2.82$. The V filter (shown in green) probes the non-ionizing UV continuum (rest-frame ~ 1400Å) of galaxies at $z \sim 2.85$. We note that the V image was taken with the d500 dichroic, which blocks light bluewards of 5000Å, slightly truncating the transmission curve shown in this figure. The NB4670 filter (shown in red) is centered on the Lyα emission line for objects at $z \sim 2.85$ and was used along with the V band to select the sample of LAEs. Dashed lines indicate the locations of the Lyman limit and Lyα feature at $z = 2.85$.

error analysis. Section 2.4 contains a discussion of the complexities involved in identifying foreground contaminants and our methods for correcting measured LyC magnitudes for both foreground contamination and IGM absorption. In Section 2.5, we discuss the colors of individual LyC-detected objects, the average properties of the LBG and LAE samples, and the implied LyC escape fraction and comoving emissivity. We present the multiwavelength properties of our targets in Section 2.6 and summarize our results in Section 2.7. Throughout the paper we employ the AB magnitude system and assume a cosmology with $\Omega_m = 0.3$, $\Omega_\Lambda = 0.7$, and $H_0 = 70$ km s^{-1} Mpc^{-1}. At $z = 2.85$, $1''$corresponds to 7.8 proper kpc.

2.2 Observations and Data Reduction

2.2.1 Photometric Observations

For observations of LyC emission, we used a custom narrowband filter manufactured by Barr Associates with central wavelength 3420Å and FWHM 105Å. This filter (hereafter referred to as NB3420) is designed to probe the LyC region blueward of 912Å for galaxies at $z \geq 2.82$ such that no contaminating flux ($\leq 0.4\%$) from the galaxy's non-ionizing UV continuum is transmitted. The filter lies well within one LyC mean free path for galaxies at $z = 2.85$, minimizing the effect of intervening Lyman Limit systems and allowing for a more direct probe of the LyC absorption properties internal to galaxies. At a redshift of 2.85, current estimates place the LyC mean free path at ~ 100 proper Mpc (Rudie et al., 2013; Faucher-Giguère et al., 2008; Songaila & Cowie, 2010) which corresponds to a rest-frame wavelength interval of $\sim 830 - 912$Å. At $z = 2.85$, the range of rest-frame wavelengths probed by the NB3420 filter is $872 - 904$Å. Figure 2.2 shows the wavelengths probed by the NB3420 filter with respect to a typical LBG spectrum at $z = 2.85$, along with the locations of the NB4670 and V filters relevant to the identification of LAEs and the photometry of the non-ionizing UV spectral region.

Our imaging was centered on the HS1549 field, at (α, δ) = (15:51:53.7, +19:10:42.3). Observations were taken through the NB3420 filter using the blue side of the Low Resolution

Imaging Spectrometer (LRIS, Oke et al., 1995; Steidel et al., 2004) on the Keck I telescope. During observing runs on 23 − 24 June 2009, 11 − 12 July 2010, and 9 August 2010, we acquired a total of 19.2 hours of data comprising thirty-seven 1800 second exposures, one 1500 second exposure, and one 900 second exposure. We dithered the telescope between exposures to minimize the effects of bad pixels and to cover the gap between the two LRIS-B CCDs. Because these two 2K × 4K detectors have slightly different quantum efficiencies below 4000Å, we obtained half of the exposures at a sky position angle of 0° and half at 180° in order to even out systematics between the two chips. Conditions were photometric during all observing runs, and the effective seeing FWHM in the final stacked NB3420 image is 0.″7 with a 1σ surface brightness limit of 29.4 mag/arcsec^2.[1]

Additional data in the HS1549 field includes broadband ground-based optical (U, G, V, $\mathcal{R}$) and near-IR (J, K) imaging, *Spitzer* IRAC and MIPS (24μm) photometry, along with HST/WFC3 $F160W$ and $F475W$ imaging and morphologies for a small portion of the field. At $z = 2.85$, the ground-based V and $\mathcal{R}$ images both probe the non-ionizing UV continuum in the vincinity of 1500Å and do not suffer from contamination by the Lyα emission line or Lyα forest line blanketing. Given the significant redshift spike in the HS1549 field, narrowband 4670Å imaging (NB4670; $\lambda_{eff} = 4667$Å, FWHM = 88Å) probing Lyα at $z = 2.85$ was also obtained. We used the combination of NB4670 and broadband V imaging to select LAEs near the redshift of the HS1549 protocluster (Steidel et al., 2011) and the NB4670$-V$ continuum subtracted image to examine the morphology of the Lyα emission. Replacing the $V-$band image with G also yields information about LAEs[2], so we experimented with selecting LAEs using NB4670$-G$ colors and examined the Lyα morphology in the NB4670$-G$ image as well. Table 2.1 gives a summary of the imaging in the HS1549 field most relevant to the LyC observations. Detailed photometry and error analysis are performed on the NB3420, V, and $\mathcal{R}$ images, as described in Section 2.3.

[1]The surface brightness limit quoted is a rough estimation made by evaluating sky counts in 1.″0 apertures placed randomly on blank areas of the image. We conduct a more detailed study of the NB3420 image properties and our photometric accuracy using Monte Carlo simulations, as described in Section 2.3.2

[2]While the G-band image is contaminated by emission from the Lyα feature, the $V-$band image is offset from Lyα in wavelength and thus may include a color term if the continuum is not flat in f_ν.

Table 2.1. Keck/LRIS Imaging Observations

Filter[a]	λ_{eff} (Å)	Seeing FWHM ($''$)	Exposure (s)
NB3420	3420	0.7	69000
NB4670	4670	0.7	18000
V	5506	1.0	10800
$\mathcal{R}$	6830	1.3	4800

[a]The NB3420 and NB4670 imaging were taken on LRIS-B, while the V and $\mathcal{R}$ imaging were taken on LRIS-R. Additionally, the $V-$band transmission is slightly affected by the use of the d500 dichroic.

2.2.2 NB3420 Imaging Reduction

We used standard IRAF image reduction procedures to reduce individual narrowband exposures and create the final NB3420 stacked image. For each exposure, we divided the image by a flatfield constructed from images of the twilight sky, subtracted the background, and masked out cosmic rays and satellite trails. In order to stack the 39 NB3420 frames, we registered >500 objects in the NB3420 frames with their counterparts in the astrometrically corrected $\mathcal{R}$-band image and resampled the pixels to the $\mathcal{R}$-band plate scale of $0\farcs2119$/pixel. Accurate image registration is necessary for creating a spatial map of the relative positions and morphology of escaping LyC and non-ionizing UV continuum radiation and identifying likely low-redshift contaminants.

In the process of combining the individual exposures, which ranged in airmass from 1.00 to 1.71, we scaled the flux in each frame such that each exposure was effectively observed at the minimum airmass. Narrowband images were calibrated onto the AB magnitude system using observations of spectrophotometric standard stars from the list of Massey et al. (1988). These AB magnitudes were also corrected for a Galactic extinction of $E(B-V) = 0.045$, based on IRAS 100μm cirrus emission maps from Schlegel et al. (1998) and the extinction

law from O'Donnell (1994). The final stacked image has an area of 35.5 arcmin^2.

2.2.3 Spectroscopic Observations, Data Reduction, and Analysis

Previous spectroscopy has already been performed in the HS1549 field, resulting in spectroscopic redshifts for a significant number of LBGs and LAEs (Section 2.2.4). In order to augment the existing spectroscopic sample and confirm the redshifts of potential LyC-leaking galaxies, we obtained additional spectra, favoring objects with NB3420 detections. Another of our original intentions was to acquire deep spectroscopy in the LyC region of galaxies with NB3420 detections, but we were limited by poor weather conditions.

We performed multi-object spectroscopy in May 2011 on the Keck 1 telescope, using the blue side of LRIS. We observed four slitmasks with exposure times of 16560, 9000, 8400, and 8100 seconds, respectively. For all masks, we used the 400 line mm^{-1} grism blazed at 3400Å, acheiving a spectral resolution of R = 800 for $1\farcs2$ slits. The "d500" dichroic beam splitter was used for the first mask (originally designed for deep LyC spectroscopy) and the "d560" dichroic was used for the three additional masks (designed to acquire redshifts). The conditions during the observing run were suboptimal, with intermittent clouds and a seeing FWHM of $0\farcs7 - 1\farcs0$ during clear spells.

When designing the slitmasks, we targeted both LBGs and LAEs with NB3420 detections. Slits were centered on the coordinates of the V (NB4670) centroid for LBGs (LAEs). While most LAEs were selected using the $V-$band image as the continuum band, a small fraction (20%) were selected using $G-$band (henceforth referred to as GNBs). Overall, we observed 46 objects on the four slitmasks, 29 of which had repeat observations.

Standard IRAF tasks were used to cut up the multi-object slitmask images into individual slitlets, flatfield the spectra using twilight sky flats, mask out cosmic rays, subtract the sky background, and average individual exposures to make stacked 2D spectra. These spectra were then extracted to one dimension, wavelength calibrated, and shifted into the vacuum frame. Details of these spectroscopic reduction procedures are discussed in Steidel et al. (2003). The centroid of the Lyα emission feature ($\lambda = 1215.67$) was used to estimate redshifts

for LAEs. Both Lyα emission and interstellar absorption lines (when detected) were used for LBGs, yielding separate emission and absorption redshifts when both types of features were detected. For objects with spectra taken on multiple masks, we averaged these spectra in order to determine redshifts in cases when doing so increased the S/N.

We successfully measured redshifts for 9 of the 12 LBG candidates, confirming three objects (MD5, M16, and D24) to be at $z > 2.82$ and identifying one as a star. We also measured redshifts for 11 out of 27 LAEs, thus providing us with five new LAE candidate LyC emitters. Of the remaining six LAE candidates for which we measured redshifts, two already had redshifts determined from previous spectroscopic studies of Steidel et al. (*lae*4680, *lae*7832; these objects were on the mask that was designed to directly detect LyC emission spectroscopically), one object had an NB3420 detection that was flagged as contamination after the spectroscopy was completed (*lae*3208), one object (*lae*6856) was at $z = 2.807$ (slightly too low redshift for NB3420 filter to probe uncontaminated LyC emission), and two objects (*lae*4152, $z = 2.447$; *lae*5165, $z = 1.873$) were at too low a redshift to be members of the HS1549 protocluster. Out of the seven GNBs, we acquired three redshifts (GNB2861, GNB4769, GNB5270), all of which placed the objects at $z \sim 2.85$, i.e., in the correct redshift range for our study. We note that in cases where no redshift could be measured, we did not draw conclusions about the quality of the object; the poor weather conditions, combined with the faintness of our targets, made it impossible to remove objects from our sample on the basis of a non-detection.

In summary, the analysis of the spectra allowed us to confirm $z \geq 2.82$ redshifts for 3 LBGs, 5 LAEs, and 3 GNBs with NB3420 detections. With these new redshifts, we were able to include the three additional LBGs in our LyC analysis. However, all five of the LAEs for which we confirmed redshifts have $m_{4670} > 26.0$. Because we do not have a complete and unbiased spectroscopic sample of LAEs with $m_{4670} > 26.0$ or GNBs (see Section 2.2.4), we did not include these objects in the LyC analysis. In the appendix, we present their postage stamp images and uncorrected NB3420 magnitudes in Figure 2.13 and Table 2.8, respectively.

2.2.4 Sample

Our initial sample consisted of 363 UV-selected galaxies and 289 narrowband-color selected LAEs. The UV-selected galaxies were identified using the $UG\mathcal{R}$ color selection criteria discussed in Steidel et al. (2003, 2004). Spectroscopic redshifts of 145 of these UV-selected galaxies were previously measured in this field (Reddy et al., 2008; Steidel et al., 2011) and our follow-up spectroscopy (described in Section 2.2.3) yielded an additional eight redshifts. For the purposes of studying LyC emission, we kept only galaxies that were spectroscopically confirmed to be at $z \geq 2.82$ with no AGN signatures in their spectra. This sample consists of 49 LBGs with $z_{spec} \geq 2.82$.[3] We note that while the spectroscopic studies of Reddy et al. (2008) and Steidel et al. (2011) were conducted without reference to the LyC properties of the LBGs, our follow-up spectroscopy was aimed at confirming redshifts of LBGs with NB3420 detections. While the addition of these objects may introduce a slight bias in the average non-ionizing to ionizing UV flux-density ratio for the full LBG sampe, it allows us to study the individual flux-density ratios of a larger number of LyC-emitting LBGs and perform a more useful differential analysis of the stellar populations of LBGs with and without LyC emission.

LAEs were selected via a broadband filter (V) and a narrowband filter (NB4670) designed to probe the Lyα emission line for galaxies in the range of $2.803 < z < 2.876$. In previous work (e.g., Steidel et al., 2000; Nestor et al., 2011), a broadband minus narrowband color excess of 0.7 magnitudes was used to identify LAEs, corresponding to an equivalent width threshold of 80 Å (corresponding to rest-frame 20 Å). Our HS1549 photometric LAE sample, however, is comprised of objects with $V-$ NB4670 > 0.6, a slightly lower threshold designed to increase the sample size by including LAEs with observed Lyα equivalent widths slightly less than 80 Å.[4] Spectroscopic follow-up of 116 of these narrowband excess objects confirmed

[3]We note that one of the 49 spectroscopically confirmed LBGs (D27) has an absorption redshift of 2.814 and a Lyα emission redshift of 2.816. Although it is at a lower redshift than our conservative cutoff of $z = 2.82$, less than 1% of the flux redwards of the Lyman limit is transmitted through the NB3420 filter at $z = 2.814$. Accordingly, we include it in the sample of spectroscopically confirmed LBGs.

[4]Three of the LAE candidates in the HS1549 field identified on the basis of an early generation of NB4670 and V-band photometry by Steidel et al. have been shown by subsequent deeper NB4670 data to have colors not quite red enough to satisfy $V-$NB4670 > 0.6. However, as these objects have already been confirmed spectroscopically to be at $z \sim 2.85$, we include them in the LAE sample regardless of $V-$NB4670 color.

99 to be LAEs at the redshift of the protocluster (Trainor et al., in prep). Of the 17 objects not confirmed to be at $z \sim 2.85$, two were found to be low-redshift galaxies (at $z = 1.983$ and $z = 2.7773$) and the other 15 did not yield spectroscopic redshifts. With the exclusion of Lyα blobs, galaxies with evidence for AGN emission in their spectra, and two LAEs that lie just below the redshift limit of the NB3420 filter ($z < 2.82$), the spectroscopically-confirmed LAE sample consists of 91 galaxies. The spectroscopic follow-up of LAEs was conducted independently of LyC observations; thus, the sample of LAEs with spectroscopic redshifts is unbiased with respect to LyC properties.

We also created an additional photometric LAE sample that includes 33 photometric candidates whose NB4670 magnitudes are in the same range as the LAEs with spectroscopy ($m_{4670} \leq 26$), and include photometry and postage-stamp images for these LAE photometric candidates in Appendix B. The lack of spectroscopic confirmation of these photometric LAE candidates creates a small likelihood of contamination due to lower-redshift galaxies. The first source of contamination arises from the fact that the NB4670 filter selects for Lyα emission at a range that extends down to $z \sim 2.80$, while the NB3420 filter only measures uncontaminated LyC emission for galaxies at $z \geq 2.82$. However, only 2 out of 99 LAEs confirmed by spectroscopy has $z_{spec} < 2.82$; these objects (at $z = 2.811$ and $z = 2.801$) lie in the tail of the redshift overdensity centered at $z = 2.85$. With the assumption that the redshift distribution of the LAEs without spectroscopy matches the distribution of those with spectroscopy, contamination from additional galaxies in the low-redshift tail should be negligible. The second potential source of contamination arises from [OII]-emitters at $z \sim 0.24 - 0.26$ whose emission lines fall within the NB4670 filter bandpass, but this type of contamination is also unlikely. Not only is the volume probed at $z \sim 2.80 - 2.88$ forty times larger than that probed at $z \sim 0.24 - 0.26$, but the photometrically measured equivalent widths of the LAE candidates, while typical for LAEs, would be considered exceptionally large if the objects were in fact low-redshift [OII]-emitters (see, e.g., Hogg et al., 1998). Additionally, as described in Section 2.3.4, the relative spatial positions of the NB3420, V, and NB4670-V emission point toward the LAE candidates being high-redshift objects. However, because of the increased likelihood of contaminated NB3420 detections within the

Table 2.2. Uncertainties in Simulated Photometry for $\mathcal{R}$, V, and NB3420

Magnitude Bin[a]	$\Delta\mathcal{R}$[b]	$\sigma_{\mathcal{R}}^{+}$[c]	$\sigma_{\mathcal{R}}^{-}$[c]	ΔV[b]	σ_{V}^{+}[c]	σ_{V}^{-}[c]	ΔNB[b]	$\sigma_{\rm NB}^{+}$[c]	$\sigma_{\rm NB}^{-}$[c]
22.5 − 23.0	0.00	0.03	0.03	0.00	0.02	0.02	0.00	0.02	0.02
23.0 − 23.5	0.00	0.05	0.05	0.00	0.03	0.03	0.00	0.03	0.03
23.5 − 24.0	0.00	0.08	0.07	0.00	0.05	0.05	0.00	0.05	0.04
24.0 − 24.5	0.00	0.12	0.11	0.00	0.07	0.06	0.00	0.07	0.07
24.5 − 25.0	0.00	0.17	0.15	0.00	0.10	0.09	0.00	0.11	0.10
25.0 − 25.5	0.00	0.25	0.21	0.00	0.14	0.13	0.00	0.17	0.14
25.5 − 26.0	0.01	0.34	0.26	0.00	0.22	0.18	0.01	0.25	0.20
26.0 − 26.5	0.06	0.45	0.31	0.01	0.32	0.25	0.03	0.34	0.26
26.5 − 27.0	0.17[d]	0.54	0.36	0.04	0.38	0.28	0.09	0.44	0.31
27.0 − 27.5	0.37[d]	0.71	0.43	0.13	0.51	0.34	0.24[d]	0.60	0.38
27.5 − 28.0	0.70[d]	1.22	0.56	0.25[d]	0.60	0.38	0.40[d]	0.79	0.45

[a]Recovered magnitude range of simulated galaxies. The statistics in this table are calculated for an object whose flux lies in the center of the bin; for example, this flux corresponds to a magnitude of 22.72 for the brightest bin.

[b]Average value of the difference between recovered and input magnitudes. In the fainter bins, significant departures from zero imply systematic biases in the photometry.

[c]The standard deviation in the difference between recovered and input magnitudes, used to calculate photometric uncertainties. Note that uncertainties in magnitudes are asymmetric because the standard deviation is calculated from the simulated flux distribution (Section 2.3.2).

[d]Magnitudes of objects with systematic biases greater than one third of the object's uncertainty are adjusted to reflect the systematic bias, as discussed in Section 2.3.2.

photometric LAE sample, we do not include these objects in the LAE analysis.

In summary, the samples of LBGs and LAEs with $z_{spec} \geq 2.82$ consist of 49 and 91 galaxies, respectively. There is some overlap in the final LBG and LAE samples: 9 LBGs are also LAEs. We exclude one of these overlap objects (MD12/*lae3540*) from our analysis of global LyC properties because of its complex morphology, but discuss its photometric properties in detail in Section 2.4.1. With the exclusion of MD12/*lae3540*, the final LBG and LAE samples consist of 48 and 90 galaxies, respectively.

2.3 Detecting LyC Emission

2.3.1 Photometric Measurements

Source identification and photometry were performed using SExtractor (Bertin & Arnouts, 1996). Objects were detected independently in all images to allow for different spatial distributions of light at different wavelengths. For $\mathcal{R}$-band and V-band images, we ran SExtractor in single-image mode using a Gaussian smoothing kernel with a FWHM of 2 pixels and a detection threshold of 1.0 standard deviation above the local smoothed background. For the NB3420 image, we ran SExtractor in dual-image mode with separate detection and measurement images, following the methodology of Nestor et al. (2011). For detection, we smoothed the NB3420 image by a Gaussian kernel with FWHM = 2.35 pixels and used a detection threshold of 2.25 standard deviations. For measurement, we used the unsmoothed NB3420 image. In the case of the NB3420 photometry, SExtractor parameters were chosen to reflect the higher signal to noise of the NB3420 image, to produce object number counts similar to those in Vanzella et al. (2010b), and to be complete in the faint magnitudes of interest for studying LyC emission. In all images, magnitudes were computed using "Kron-like" elliptical apertures (i.e., MAG_AUTO in SExtractor).

Because there has been some contention in this field concerning the most appropriate way to photometrically measure the flux-density ratio between ionizing (NB3420) and non-ionizing (V) UV emission (Vanzella et al., 2012; Nestor et al., 2011, 2013), we explain our methods here. Galaxies at $z \sim 3$ are known to exhibit clumpy morphologies (see e.g., Law et al., 2007). As LyC photons may not escape isotropically from all portions of the galaxy, it is possible that LyC emission will be observed emanating from only one clump of a given galaxy. With the seeing-limited resolution of our images, it is often impossible to distinguish individual star-forming clumps; thus LyC emission may appear to be offset from the centroid of the $V-$band emission. The idea of offset LyC emission is also supported by results from galaxy formation simulations. Simulations by Gnedin et al. (2008) claim that increased star-formation efficiencies in the more luminous LBGs result in higher scale heights of young stars relative to the HI in the disk. Therefore, minor interactions can disrupt the

HI sufficiently to reveal the young stars and allow significant emission of ionizing photons to escape the galaxy. With the proper orientation, this configuration can be recognized as LyC emission offset from the primary UV-continuum emission. Alternatively, Ricotti (2002) suggests that the formation of globular clusters may have reionized the universe, since luminous OB associations in the outer haloes may have escape fractions approaching unity. Globular clusters are still forming at $z \sim 3$ (Stetson et al., 1996), and would be observable in our data as LyC emission offset spatially from the primary galaxy. Because these models support the possibility that the spatial distribution of LyC emission may be offset from $V-$band emission or have different morphology (e.g., compact vs. diffuse), we must choose photometric methods that can account for such scenarios.

While Vanzella et al. (2012) suggest that flux-density ratios should be measured using both LyC and non-ionizing UV emission *only* from regions of escaping LyC emission, we argue here that the entire non-ionizing and ionizing UV flux should be measured. Measuring the flux-density ratio within an individual LyC-emitting region (defined by the isophote of the LyC emission) may provide useful information about the stellar populations of that region, but it does not provide information about the average LyC escape fraction among star-forming galaxies or the global LyC emissivity produced by these galaxies. The average escape fraction must be computed from the non-ionizing to ionizing flux-density ratio of an ensemble of $z \sim 3$ galaxies, including both galaxies without observed LyC emission and the non-LyC-emitting regions from galaxies with LyC emission. The calculation of the ionizing emissivity, moreover, relies entirely on the $z \sim 3$ UV luminosity function constructed by measuring non-ionizing UV light from *entire* galaxies, not from their constituent clumps. Alternatively, we find that a method in which LyC is measured solely within an isophote defined by the galaxy's non-ionizing UV also does not accomplish our photometric goals. As this "isophotoal" method does not allow for LyC emission to have a different spatial distribution from that of the non-ionizing UV, it will result in the systematic loss of LyC flux. A differential analysis of LAE magnitudes using this isophotal photometric method versus the "Kron-like" apertures to measure $V-$band and NB3420 magnitudes separately (i.e., the method presented here) corroborates the idea that LyC emission is systematically

missed in the isophotal method; the average LAE non-ionizing to ionizing flux-density ratio using the isophotal method is a factor of ~ 1.3 larger than the methods we use. While a factor of 1.3 is well within the 1σ uncertainty[5], it is an unnecessary loss of NB3420 flux. Therefore, we maintain that using the large "Kron-like" apertures to measure the full $V-$band and NB3420 magnitudes is the correct photometric method for the measurement of the global LyC escape fraction and emissivity.

2.3.2 Characterizing Photometric Uncertainties

We characterized both the statistical and systematic photometric uncertainties by running Monte Carlo simulations designed to reproduce our photometric measurement procedures. In the simulations, we added to each image fake galaxies of known magnitude and a range of radial profiles representative of the observed galaxies. In each iteration, one hundred fake galaxies were placed in random, empty positions chosen to avoid image edges and photometric blending with existing objects or previously placed fake galaxies. We ran SExtractor on each filter ($\mathcal{R}$, V, NB3420) using the same parameters as for the actual photometry. The process of adding fake galaxies was repeated until we recovered 50,000 in each simulation, enough to populate all magnitude bins of interest with a statistically significant number of objects. The bins of recovered magnitude are 0.5 magnitudes wide and span a range of $22.5 \leq m \leq 28$ in each band to encompass the magnitude range of the observed LBGs and LAEs.

Table 2.2 lists the systematic bias and photometric uncertainty associated with each magnitude bin, as derived from the results of the simulations. In each bin, the systematic bias is defined to be the average difference between input and recovered fluxes of fake galaxies, while the photometric uncertainty is defined to be the standard deviation of the distribution of differences between input and recovered fluxes. The uncertainty associated with an object of a given flux is a local quadratic interpolation between the uncertainties of neighboring bins. Because the errors in flux are Gaussian, all errors quoted in magnitudes are double-sided. Using the uncertainties estimated by our simulations, we define a 2σ photometric limit that

[5]The two photometric methods agree so well because the NB3420 detections in the LAE sample have very small offsets from the corresponding $V-$band detections.

corresponds to a magnitude limit of 27.33 in $\mathcal{R}$, 27.58 in V, and 27.30 in NB3420. In all filters, the simulations show that SExtractor misses a higher percentage of flux from fainter objects, resulting in a systematic offset in magnitude that is larger for fainter objects. In order to correct for this bias, we added the systematic offset determined from the simulation analysis to the flux of an object if the offset was greater than one third of the object's associated uncertainty. This threshold was chosen in order to avoid the unnecessary addition of noise into our measurements by adding systematic offsets much smaller than the 1σ error. In practice, this correction only affected a few of the fainter bins (see Table 2.2).

2.3.3 Object Matching

As we have two broadband filters (V and $\mathcal{R}$) that probe the non-ionizing rest-frame UV ($\sim$1500Å) for galaxies at $z = 2.85$, it is necessary to choose one to represent the non-ionizing UV flux. The spatial distributions of the V and $\mathcal{R}$ detections are well matched and their centroids agree within $0\farcs2$. The deeper $V-$band image has $1\farcs0$ seeing, while the $\mathcal{R}$ image has $1\farcs3$ seeing, larger photometric errors (see Table 2.2), and an elongated PSF. Although the $\mathcal{R}-$band image was originally used to identify LBGs, we adopt the $V-$band image for our non-ionizing UV photometry based on its superior quality and the fact that more LAEs are detected in V than in $\mathcal{R}$. We note that all but one of the LBGs with LyC detections is detected in V; M4 does not have a V detection because it falls off the edge of the V-band image. For this object, we calculate a V magnitude by linearly interpolating between its measured $\mathcal{R}$ magnitude and a G magnitude computed from its $G - \mathcal{R}$ color obtained from the parent LBG survey (Reddy et al., 2008; Steidel et al., 2004).

The coordinates of LBGs are defined by $V-$band centroids, while the coordinates of LAEs are defined by NB4670 centroids. In order to find non-ionizing rest-frame UV counterparts for LAEs, we compiled the positions and photometric measurements for any SExtractor detection in the $V-$band image within a 5 pixel ($1\farcs1 = 8.6$ kpc at $z = 2.85$) offset from the NB4670 coordinates of the target and successfully found counterparts for 77 out of 91 LAEs. Given that the largest galaxies reach sizes of ~ 10 kpc at $z \sim 2-3$ (Förster Schreiber et al.,

2009; Law et al., 2012a) and that we may be looking for LyC emission in the outskirts of these galaxies, we used a similar matching technique with a larger radius (9 pixel = 1.″9 = 14.8 kpc at $z = 2.85$) to find SExtractor detections in the NB3420 image near our LBGs and LAEs. This generous matching radius guarantees the inclusion of all NB3420 detections potentially associated with the galaxies in the sample. Our candidate with the largest offset between the galaxy centroid and the associated NB3420 detection (M16) has $\Delta_{Ly\alpha,LyC} = 1.''26 = 9.8$ kpc, but the majority of our NB3420 detections (especially around LAEs) are at much smaller offset (< 3 kpc).

In order to remove any obvious false matches corresponding to neighboring sources, we visually inspected each NB3420 source matched with a known LBG or LAE in the $\mathcal{R}$, V, and G images (probing rest-frame non-ionizing UV), and the $F160W$ image (probing rest-frame optical), if available. We also inspected LAEs with NB3420 matches in the continuum-subtracted NB4670$-V$ image, which probes the spatial distribution of Lyα emission. NB3420 matches were removed if they corresponded spatially to a visible counterpart in another image. We also removed matches where the LyC emission was further than 1.″9 away from the non-ionizing UV-continuum emission, which occasionally occurred because the LAE matching radius was centered around the Lyα emission, not the non-ionizing UV. Altogether, we retained matches to 4 LBGs and 7 LAEs, labeling the NB3420 detections corresponding to 4 LBGs and 16 LAEs as invalid.

2.3.4 Targets with NB3420 Detections

We report NB3420 detections in 4 out of 48 LBGs and 7 out of 90 LAEs. MD12/*lae3540* also has an NB3420 detection and is discussed in Section 2.4.1. Although they are not the focus of our study, we note that 2 of the 4 AGNs in the field at $z \geq 2.82$ have NB3420 detections. Tables 2.3 and 2.4 display photometric information for the NB3420-detected LBGs and LAEs. Postage-stamp images of targets with NB3420 detections are shown in Figures 2.3 and 2.4, indicating the NB3420 (LyC), NB4670$-V$ (Lyα), and V (non-ionizing UV continuum) morphologies.

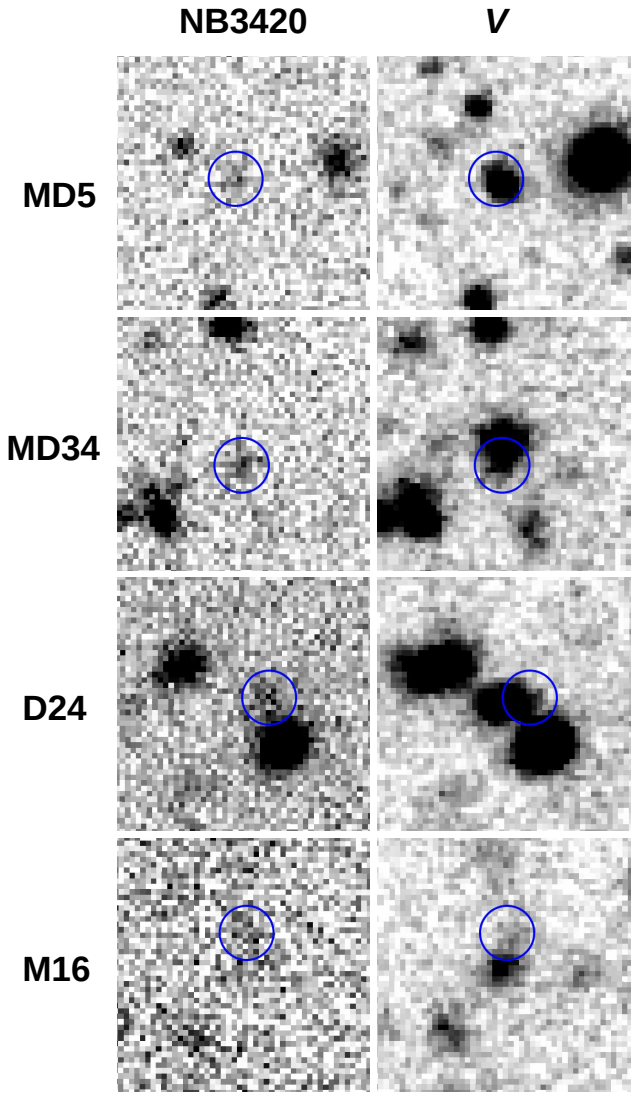

Figure 2.3 $10'' \times 10''$ postage stamp images of the 4 LBGs with NB3420 detections. Each object is displayed in two bands: NB3420 (indicating the LyC) and V (indicating the non-ionizing UV continuum). All postage stamps are centered on the V-band centroid and blue circles ($1''$radius) indicate the centroid of the NB3420 emission. All postage stamps follow the conventional orientation, with north up and east to the left.

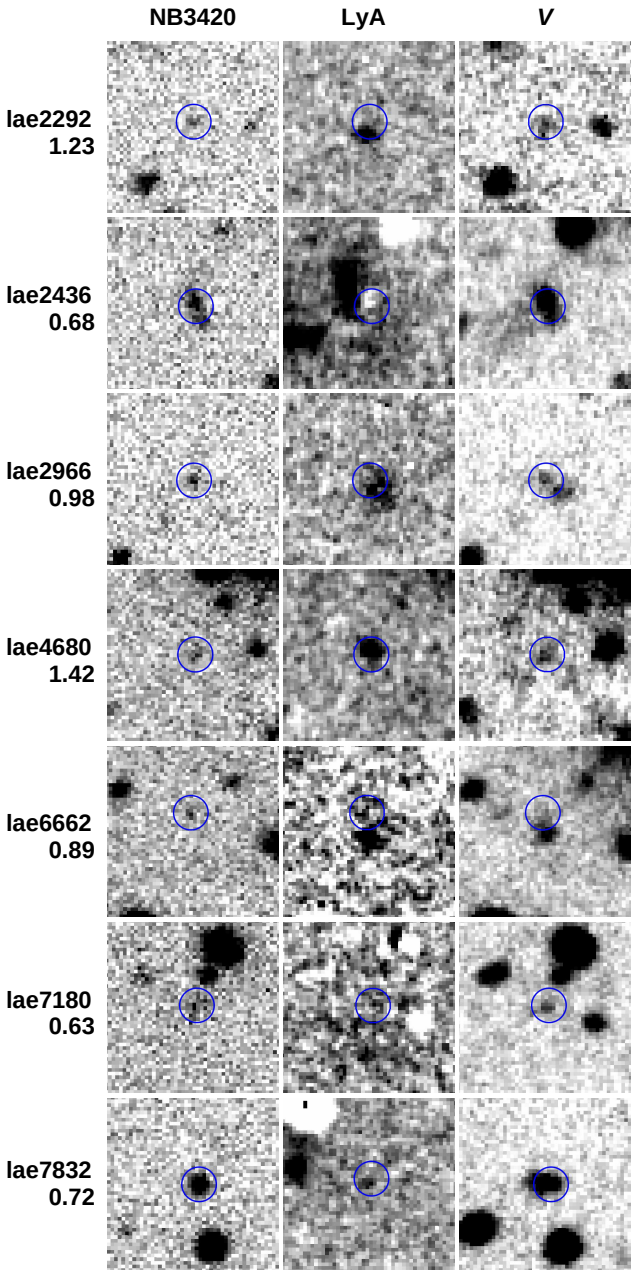

Figure 2.4 $10'' \times 10''$ postage stamp images of the 7 LAEs with NB3420 detections. Each object is displayed in three bands: NB3420 (indicating the LyC), NB4670$-V$ (indicating Lyα emission and labeled LyA), and V (indicating the non-ionizing UV continuum). The $V-$NB4670 color of each LAE is indicated below the object name. All postage stamps are centered on the V-band centroid and blue circles ($1''$radius) indicate the centroid of the NB3420 emission. All postage stamps follow the conventional orientation, with north up and east to the left. We note that LAEs with more diffuse Lyα emission may be difficult to distinguish in the NB4670$-V$ image, even though their $V-$NB4670 colors identify them as LAEs and their redshifts have been confirmed by spectroscopy; for such objects, we have increased the stretch of the NB4670$-V$ image to make the diffuse emission more easily visible.

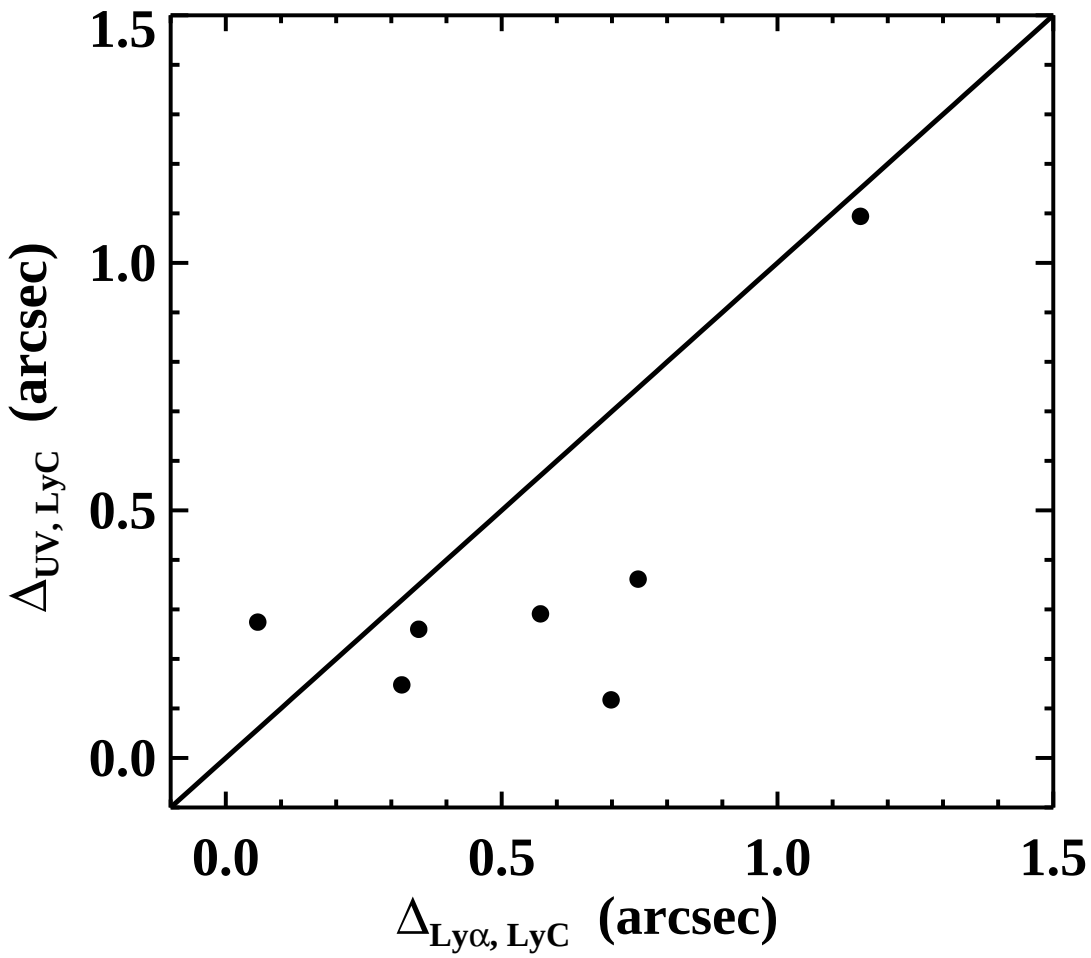

Figure 2.5 Comparison of the offsets between UV-continuum and LyC emission ($\Delta_{UV,\,LyC}$) and between Lyα and LyC emission ($\Delta_{Ly\alpha,\,LyC}$) for LAEs with NB3420 detections. On average, $\Delta_{UV,\,LyC} < \Delta_{Ly\alpha,\,LyC}$, reflecting the fact that Lyα photons are resonantly scattered; therefore, Lyα emission is unlikely to coincide exactly with the location of LyC emission. This observed trend supports the claim that the LAEs are not low-redshift [OII]-emitters (see Section 2.3.4).

Table 2.3. LBG Photometry

ID	RA (J2000)	Dec (J2000)	z_{em} [a]	z_{abs} [b]	V	NB3420	$\Delta_{UV,\,LyC}$ [c]	$\frac{F_{UV}}{F_{LyC}}_{obs}$ [d]
BX84	15:51:53.696	19:12:24.64	···	2.823	24.41	>27.30	···	>14.3
MD5	15:51:45.211	19:11:05.13	3.146	3.139	24.96	26.89	$0''.3$	5.9 ± 2.0
MD7	15:51:47.521	19:10:13.56	2.857	2.851	25.11	>27.30	···	>7.5
MD9	15:51:50.711	19:09:38.20	2.852	2.843	24.13	>27.30	···	>18.6
MD12[e]	15:51:51.882	19:10:41.16	2.856	2.849	24.56	26.74	$1''.0$	7.5 ± 2.5
MD34	15:52:06.315	19:12:48.60	···	2.849	24.23	26.56	$0''.8$	8.6 ± 2.7
C1	15:51:39.653	19:10:40.67	2.845	···	24.77	>27.30	···	>10.3
C2	15:51:40.960	19:13:12.77	3.100	···	23.76	>27.30	···	>26.1
C4	15:51:44.413	19:11:24.75	2.863	2.857	25.01	>27.30	···	>8.2
C5	15:51:44.627	19:10:59.73	3.173	···	25.14	>27.30	···	>7.3
C6	15:51:44.760	19:10:32.84	···	2.828	24.36	>27.30	···	>15.0
C7	15:51:45.247	19:12:13.21	···	2.841	24.53	>27.30	···	>12.8
C8	15:51:45.386	19:08:49.84	···	2.935	25.03	>27.30	···	>8.1
C9	15:51:46.707	19:11:52.39	2.925	2.919	23.67	>27.30	···	>28.2
C10	15:51:48.424	19:09:24.93	3.193	3.183	24.56	>27.30	···	>12.4
C12	15:51:49.360	19:09:52.55	···	2.835	24.93	>27.30	···	>8.8
C13	15:51:49.685	19:10:58.10	2.843	···	24.92	>27.30	···	>9.0
C14	15:51:50.616	19:09:18.46	···	2.841	24.87	>27.30	···	>9.4
C15	15:51:51.352	19:10:19.50	2.849	2.849	25.39	>27.30	···	>5.8
C17	15:51:55.283	19:12:19.48	2.941	2.934	24.92	>27.30	···	>9.0
C19	15:52:00.196	19:10:08.73	3.166	3.158	24.41	>27.30	···	>14.3
C20	15:52:00.402	19:08:40.75	3.115	···	25.09	>27.30	···	>7.6
C22	15:52:03.833	19:09:43.21	···	2.960	24.65	>27.30	···	>11.5
C24	15:52:05.618	19:13:11.73	2.834	2.826	25.24	>27.30	···	>6.7
C25	15:52:06.069	19:11:28.37	3.159	···	24.60	>27.30	···	>12.0
C27	15:52:07.041	19:12:19.29	2.931	2.922	24.32	>27.30	···	>15.5
D3	15:51:43.712	19:09:12.37	2.942	2.934	24.06	>27.30	···	>19.7
D4	15:51:43.976	19:11:39.67	2.863	2.856	24.43	>27.30	···	>14.1
D6	15:51:45.191	19:09:05.31	2.849	2.840	24.64	>27.30	···	>11.5
D7	15:51:46.246	19:09:50.11	2.943	2.932	24.51	>27.30	···	>13.0
D11	15:51:49.764	19:09:02.94	···	2.837	23.72	>27.30	···	>27.1
D13	15:51:51.724	19:10:15.89	2.852	2.842	24.39	>27.30	···	>14.5
D14	15:51:53.262	19:11:01.00	2.851	2.851	24.87	>27.30	···	>9.3
D16	15:51:54.848	19:11:31.18	3.139	3.130	24.00	>27.30	···	>20.8
D17	15:51:57.435	19:11:02.56	2.841	2.825	25.02	>27.30	···	>8.1

Table 2.3 (cont'd)

ID	RA (J2000)	Dec (J2000)	z_{em} [a]	z_{abs} [b]	V	NB3420	$\Delta_{UV,\,LyC}$ [c]	$\frac{F_{UV}}{F_{LyC}}_{obs}$ [d]
D18	15:51:59.695	19:09:39.25	2.850	···	24.60	>27.30	···	>12.1
D19	15:52:00.270	19:09:40.75	2.847	2.844	25.28	>27.30	···	>6.4
D20	15:52:00.484	19:10:27.55	···	2.825	24.11	>27.30	···	>18.8
D23	15:52:03.743	19:09:24.47	2.902	2.893	24.49	>27.30	···	>13.3
D24	15:52:05.278	19:09:45.17	2.951	2.942	24.24	27.01	$1\farcs1$	12.8 ± 4.0
D25	15:52:07.999	19:08:55.80	···	2.825	24.79	>27.30	···	>10.1
D27	15:52:08.314	19:09:48.82	2.816	2.814	23.95	>27.30	···	>21.8
M2	15:51:41.355	19:10:06.11	2.875	2.867	25.32	>27.30	···	>6.2
M5	15:51:41.970	19:08:22.21	2.936	2.931	25.00	>27.30	···	>8.3
M6	15:51:43.678	19:09:44.58	2.891	···	23.77	>27.30	···	>25.9
M16	15:51:53.636	19:09:29.49	2.955	2.953	25.28	26.56	$1\farcs3$	3.2 ± 1.4
M21	15:52:01.356	19:13:00.78	2.834	···	25.14	>27.30	···	>7.3
M22	15:52:02.705	19:09:40.06	3.159	3.149	24.77	>27.30	···	>10.3
M23	15:52:05.748	19:12:08.72	···	3.409	24.85	>27.30	···	>9.6

[a]Emission redshift of Lyα.

[b]Interstellar absorption redshift.

[c]Spatial offset between the centroids of V-band and NB3420 flux-densities.

[d]Observed ratio and uncertainty in the ratio of non-ionizing UV to LyC emission, inferred from the NB3420$-V$ color. This value has not been corrected for either contamination by foreground sources or IGM absorption.

[e]MD12 is not included in the LBG sample.

Table 2.4. LAE Photometry

ID	RA [a] (J2000)	Dec [a] (J2000)	z	NB4670	V	NB3420	$\Delta_{UV,\,LyC}$ [b]	$\Delta_{Ly\alpha,\,LyC}$ [c]	$\frac{F_{UV}}{F_{LyC}}_{obs}$ [d]
lae32	15:51:38.692	19:10:04.89	2.846	25.32	26.78	>27.30	···	···	>1.6
lae274	15:51:39.406	19:09:42.66	2.851	24.41	25.47	>27.30	···	···	>5.4
lae367	15:51:39.993	19:09:00.13	2.882	25.45	25.96	>27.30	···	···	>3.4
lae413	15:51:39.673	19:13:15.43	2.846	24.47	27.21	>27.30	···	···	>1.1
lae447	15:51:41.908	19:10:16.77	2.844	25.93	27.24	>27.30	···	···	>1.1
lae576	15:51:40.601	19:10:58.09	2.846	25.17	26.24	>27.30	···	···	>2.6
lae599	15:51:40.758	19:11:00.26	2.834	25.07	>27.58	>27.30	···	···	···
lae618	15:51:39.812	19:10:53.58	2.847	24.07	27.58	>27.30	···	···	>0.8
lae633	15:51:39.624	19:11:04.99	2.852	23.91	26.78	>27.30	···	···	>1.6
lae661	15:51:41.061	19:11:54.91	2.836	25.43	26.31	>27.30	···	···	>2.5
lae1012	15:51:42.495	19:10:34.26	2.839	24.21	25.69	>27.30	···	···	>4.4
lae1206	15:51:43.025	19:10:39.98	2.863	24.78	26.61	>27.30	···	···	>1.9
lae1261	15:51:43.596	19:11:57.22	2.851	25.70	26.99	>27.30	···	···	>1.3
lae1359	15:51:43.780	19:11:40.20	2.861	25.02	26.49	>27.30	···	···	>2.1
lae1375	15:51:43.969	19:11:02.19	2.864	25.83	27.20	>27.30	···	···	>1.1
lae1500[e]	15:51:43.955	19:11:39.63	2.863	23.93	24.43	>27.30	···	···	>14.1
lae1528	15:51:44.682	19:09:24.59	2.846	25.66	>27.58	>27.30	···	···	···
lae1540	15:51:44.490	19:11:47.22	2.845	24.90	26.88	>27.30	···	···	>1.5
lae1552	15:51:44.709	19:08:44.92	2.838	25.09	>27.58	>27.30	···	···	···
lae1599[f]	15:51:44.424	19:11:24.64	2.863	23.96	25.01	>27.30	···	···	>8.2
lae1610	15:51:44.873	19:11:02.12	2.840	24.77	26.54	>27.30	···	···	>2.0
lae1679	15:51:45.164	19:12:34.40	2.842	25.40	26.34	>27.30	···	···	>2.4
lae1751	15:51:45.449	19:11:11.71	2.840	25.50	27.12	>27.30	···	···	>1.2
lae1765	15:51:45.323	19:09:29.49	2.847	24.04	26.20	>27.30	···	···	>2.7
lae1774	15:51:53.129	19:10:57.03	2.852	23.20	25.04	>27.30	···	···	>8.0
lae1787	15:51:45.646	19:11:28.60	2.836	25.98	26.63	>27.30	···	···	>1.8
lae1803	15:51:45.697	19:11:53.03	2.852	25.55	>27.58	>27.30	···	···	···
lae1835	15:51:45.882	19:09:45.11	2.836	25.45	27.50	>27.30	···	···	>0.8
lae1843	15:51:45.676	19:09:58.21	2.847	25.81	27.18	>27.30	···	···	>1.1
lae2015	15:51:46.504	19:12:38.62	2.845	25.81	>27.58	>27.30	···	···	···
lae2063	15:51:45.966	19:08:22.13	2.849	24.49	25.91	>27.30	···	···	>3.6
lae2158	15:51:47.005	19:11:02.98	2.847	25.34	26.11	>27.30	···	···	>3.0
lae2174	15:51:47.001	19:08:22.06	2.885	25.89	26.69	>27.30	···	···	>1.8
lae2183	15:51:47.235	19:09:53.38	2.869	25.76	27.41	>27.30	···	···	>0.9
lae2292	15:51:47.635	19:10:00.50	2.851	25.86	27.19	27.11	$0''.3$	$0''.6$	0.9 ± 0.5

Table 2.4 (cont'd)

ID	RA [a] (J2000)	Dec [a] (J2000)	z	NB4670	V	NB3420	$\Delta_{UV,\,LyC}$ [b]	$\Delta_{Ly\alpha,\,LyC}$ [c]	$\frac{F_{UV}}{F_{LyC}}_{obs}$ [d]
lae2306[g]	15:51:47.509	19:10:13.34	2.857	24.60	25.11	>27.30	···	···	>7.5
lae2358	15:51:47.945	19:09:03.21	2.841	25.31	>27.58	>27.30	···	···	···
lae2436	15:52:03.231	19:12:52.43	2.832	23.44	24.11	25.21	0.″3	0.″3	2.7 ± 0.4
lae2489	15:51:48.187	19:08:30.15	2.845	25.24	27.05	>27.30	···	···	>1.3
lae2551	15:51:48.539	19:12:03.11	2.849	25.59	27.08	>27.30	···	···	>1.2
lae2561	15:51:48.346	19:13:13.88	2.828	24.71	26.13	>27.30	···	···	>2.9
lae2668	15:51:49.100	19:11:22.54	2.841	24.73	27.19	>27.30	···	···	>1.1
lae2747	15:51:49.311	19:08:44.33	2.842	24.77	26.84	>27.30	···	···	>1.5
lae2796	15:51:49.579	19:10:41.28	2.844	25.66	26.69	>27.30	···	···	>1.8
lae2854	15:51:49.793	19:12:47.89	2.836	25.84	>27.58	>27.30	···	···	···
lae2856	15:51:49.718	19:10:49.05	2.843	25.15	25.85	>27.30	···	···	>3.8
lae2949	15:51:49.870	19:10:53.62	2.840	25.14	27.45	>27.30	···	···	>0.9
lae2966	15:51:49.995	19:10:41.59	2.841	24.61	26.87	26.82	0.″1	0.″7	1.0 ± 0.4
lae2984[h]	15:51:49.695	19:10:57.98	2.843	23.83	24.92	>27.30	···	···	>9.0
lae3167	15:51:50.781	19:10:34.29	2.846	25.62	26.89	>27.30	···	···	>1.5
lae3208	15:51:50.908	19:11:16.18	2.844	25.28	27.32	>27.30	···	···	>1.0
lae3339[i]	15:51:51.354	19:10:19.71	2.849	24.69	25.39	>27.30	···	···	>5.8
lae3354	15:51:51.525	19:10:47.02	2.843	24.70	27.29	>27.30	···	···	>1.0
lae3540[j]	15:51:51.878	19:10:41.09	2.856	23.93	24.56	26.74	1.″0	0.″9	7.5 ± 2.5
lae3763	15:51:51.530	19:10:58.22	2.842	23.27	26.60	>27.30	···	···	>1.9
lae3798	15:51:53.127	19:10:34.46	2.852	25.47	27.01	>27.30	···	···	>1.3
lae3808	15:51:52.858	19:11:41.05	2.839	24.03	25.75	>27.30	···	···	>4.2
lae3866	15:51:52.742	19:11:39.09	2.839	23.32	25.42	>27.30	···	···	>5.7
lae3922	15:51:53.457	19:11:43.89	2.856	24.63	25.97	>27.30	···	···	>3.4
lae4147	15:51:54.158	19:11:05.14	2.841	24.70	27.12	>27.30	···	···	>1.2
lae4366	15:51:54.775	19:11:06.42	2.844	24.44	25.75	>27.30	···	···	>4.2
lae4680	15:51:56.206	19:09:56.72	2.848	25.24	27.07	27.05	0.″1	0.″3	1.0 ± 0.4
lae4684	15:51:56.167	19:11:56.65	2.849	25.50	26.15	>27.30	···	···	>2.9
lae4730	15:51:56.413	19:10:42.03	2.843	25.46	26.12	>27.30	···	···	>3.0
lae4796	15:51:56.367	19:11:06.15	2.868	24.68	26.30	>27.30	···	···	>2.5
lae4804	15:51:56.621	19:12:26.86	2.860	25.49	26.99	>27.30	···	···	>1.3
lae4882	15:51:56.873	19:13:06.72	2.835	25.23	27.35	>27.30	···	···	>1.0
lae4947	15:51:57.132	19:08:48.24	2.857	24.95	25.49	>27.30	···	···	>5.3
lae5132	15:52:01.057	19:09:47.89	2.849	24.76	27.18	>27.30	···	···	>1.1
lae5193	15:52:00.760	19:10:53.36	2.853	25.26	26.21	>27.30	···	···	>2.7

As indicated by studies of the SSA22a field (Nestor et al., 2013, 2011; Inoue et al., 2011; Iwata et al., 2009) and implied by the simulations of Gnedin et al. (2008) and Ricotti (2002) (see Section 2.3.1), the centroids of the UV-continuum and LyC emission may not always coincide. The NB3420 versus $V-$band offsets for the four LBGs with NB3420 detections span a large range: $0\farcs34$, $0\farcs85$, $1\farcs06$, and $1\farcs26$. The offsets for the 7 LAEs with NB3420 detections, however, are $\leq 0\farcs36 = 2.8$ kpc for all but one LAE (*lae6662*), which has an offset of $1\farcs09$. The smaller offsets of the NB3420 detections around LAEs strengthen the argument that these detections are truly associated with the LAEs in question, and also may indicate that LAEs are more compact galaxies than LBGs. For LAEs, we may also examine the offset between Lyα emission and LyC emission ($\Delta_{Ly\alpha,\,LyC}$) which is on average larger than both the offset between the UV-continuum and LyC ($\Delta_{UV,\,LyC}$) and the offset between UV-continuum and Lyα ($\Delta_{UV,Ly\alpha}$). While some spatial discrepancy between Lyα and LyC emission is to be expected due to the resonant scattering of Lyα photons, large offsets point to an increased probability of contamination and weaken the argument that the NB3420 detection is LyC emission associated with the high-redshift galaxy (Nestor et al., 2011, 2013; Vanzella et al., 2010b, 2012). However, while it is a good rule of thumb to assume that objects with $\Delta_{UV,\,LyC} \gtrsim 1''$ are likely contaminants, Nestor et al. (2013) demonstrated with high-resolution spectroscopy in the SSA22a field individual cases where putative LyC detections at large offset (for example, $\Delta_{UV,\,LyC} = 1\farcs0$) were found to be associated with the high-redshift galaxy, and detections at small offset (for example, $\Delta_{UV,\,LyC} = 0\farcs3$) were found to be contaminants.

The fact that $\Delta_{Ly\alpha,\,LyC}$ is often greater than $\Delta_{UV,\,LyC}$ provides additional evidence against significant contamination from low-redshift [OII]-emitters in the LAE sample, corroborating the conclusion drawn in Section 2.2.4. Figure 2.5 compares the offsets $\Delta_{Ly\alpha,\,LyC}$ and $\Delta_{UV,\,LyC}$ for LAEs, demonstrating the tendency for NB3420 detections to be more closely associated with V rather than NB4670 detections. If the LAEs were low-redshift [OII]-emitters rather than high-redshift LAEs, the NB3420 image would probe the rest-frame UV, the NB4670-V image would probe [OII] emission, and the V image would probe the rest-frame optical. In this case, both the NB3420 and NB4670-V images would probe active star formation,

Table 2.4 (cont'd)

ID	RA [a] (J2000)	Dec [a] (J2000)	z	NB4670	V	NB3420	$\Delta_{UV,\,LyC}$ [b]	$\Delta_{Ly\alpha,\,LyC}$ [c]	$\frac{F_{UV}}{F_{LyC}}_{obs}$ [d]
lae5322	15:52:00.102	19:10:17.14	2.832	23.53	25.44	>27.30	···	···	>5.5
lae5371[k]	15:52:00.265	19:09:40.41	2.848	24.54	25.28	>27.30	···	···	>6.4
lae5458[l]	15:51:59.696	19:09:39.30	2.849	24.04	24.60	>27.30	···	···	>12.1
lae5470	15:51:59.582	19:11:40.17	2.843	25.85	>27.58	>27.30	···	···	···
lae5713	15:51:58.999	19:09:20.60	2.857	25.57	>27.58	>27.30	···	···	···
lae5720	15:51:58.755	19:13:00.43	2.833	25.56	>27.58	>27.30	···	···	···
lae5740	15:51:59.315	19:10:35.10	2.831	24.96	25.90	>27.30	···	···	>3.6
lae5900	15:51:58.057	19:11:21.84	2.845	24.24	25.42	>27.30	···	···	>5.6
lae5995[m]	15:51:57.456	19:11:02.63	2.833	24.54	25.02	>27.30	···	···	>8.1
lae6193	15:52:07.992	19:11:23.26	2.836	25.79	26.10	>27.30	···	···	>3.0
lae6312	15:52:07.610	19:08:47.48	2.827	25.72	26.43	>27.30	···	···	>2.2
lae6662	15:52:06.357	19:10:42.74	2.833	25.16	25.94	27.23	$1\farcs1$	$1\farcs2$	3.3 ± 1.3
lae6774	15:52:06.090	19:11:36.81	2.845	25.80	>27.58	>27.30	···	···	···
lae6979	15:52:04.940	19:09:53.42	2.863	25.63	26.25	>27.30	···	···	>2.6
lae7180	15:52:04.662	19:11:42.19	2.930	25.86	26.38	25.85	$0\farcs3$	$0\farcs1$	0.6 ± 0.2
lae7542	15:52:03.575	19:12:50.73	2.841	24.28	25.48	>27.30	···	···	>5.4
lae7577	15:52:03.189	19:09:09.08	2.828	25.35	>27.58	>27.30	···	···	···
lae7803	15:52:02.304	19:09:03.58	2.865	25.97	26.89	>27.30	···	···	>1.4
lae7830	15:52:02.146	19:09:55.06	2.826	23.77	>27.58	>27.30	···	···	···
lae7832	15:52:02.201	19:10:48.59	2.829	24.23	24.83	25.11	$0\farcs4$	$0\farcs7$	1.3 ± 0.2
lae7893	15:52:01.861	19:12:49.92	2.858	25.32	>27.58	>27.30	···	···	···

[a]Coordinates of LAEs are based on NB4670 centroids.

[b]Spatial offset between the centroids of V and NB3420 emission.

[c]Spatial offset between the centroids of NB4760 and NB3420 emission.

[d]Observed ratio and uncertainty in the ratio of non-ionizing UV to LyC flux-densities, inferred from the NB3420$-V$ color. This value has not been corrected for either contamination by foreground sources or IGM absorption.

[e]D4

[f]C4

[g]D7

[h]C13

[i]C15

[j]MD12. This object is not included in either the LAE or LBG samples.

[k]D19

[l]D18

[m]D17

Table 2.5. Photometry in Stacked Images

Sample	N_{gal}	V[a]	NB3420[a]	NB3420$-V$	$\langle F_{UV}/F_{LyC}\rangle_{obs}$[b]
LBG, all	48	$24.59^{+0.09}_{-0.08}$	> 28.67	> 4.08	> 42.7
LBG, detect	4	$24.44^{+0.73}_{-0.43}$	$27.05^{+0.63}_{-0.39}$	$2.60^{+0.55}_{-1.16}$	11.0 ± 7.2
LBG, non-detect	44	$24.60^{+0.09}_{-0.08}$	> 28.62	> 4.03	> 40.8
LAE, all	90	$26.03^{+0.14}_{-0.13}$	> 29.01	> 2.98	> 15.6
LAE, detect	7	$25.49^{+0.40}_{-0.29}$	$25.97^{+0.35}_{-0.26}$	$0.48^{+0.38}_{-0.58}$	1.6 ± 0.6
LAE, non-detect	83	$26.09^{+0.15}_{-0.13}$	> 28.97	> 2.88	> 14.2
LAE, $24 < V < 25$	5	$24.67^{+0.09}_{-0.08}$	$26.51^{+2.01}_{-0.66}$	$1.84^{+0.67}_{-2.04}$	5.5 ± 4.6
LAE, $25 < V < 26$	21	$25.53^{+0.08}_{-0.07}$	> 28.22	> 2.69	> 11.9
LAE, $26 < V < 27$	30	$26.31^{+0.07}_{-0.06}$	> 28.41	> 2.10	> 6.9
LAE, $V > 27$	34	$27.31^{+0.18}_{-0.16}$	> 28.48	> 1.17	> 2.9

[a]Uncertainties listed are 1σ and include both photometric error and sample variance. All photometric lower limits are 3σ.

[b]Observed non-ionizing UV to LyC flux-density ratios and uncertainties, inferred from the NB3420$-V$ color of each stacked subsample. These values have not been corrected for either contamination by foreground sources or IGM absorption.

so a smaller offset would be expected between the centroids of the detections in these two images. However, larger values of $\Delta_{Ly\alpha,\,LyC}$ support the opposite interpretation; namely, the LAE candidates are truly high-redshift objects whose LyC and Lyα emission correlate more strongly with the non-ionizing UV-continuum than with each other. In Tables 2.3 and 2.4, we list the offsets $\Delta_{UV,\,LyC}$ and $\Delta_{Ly\alpha,\,LyC}$ for galaxies with NB3420 detections.

In addition to exploring the properties of individual objects leaking LyC radiation, we created stacked NB3420 and V images of subsamples of our targets to examine the average LyC emission properties and attempt a LyC measurement in the stacks of objects without NB3420 detections. These subsamples include LBGs, LAEs, and LAEs in bins of V magnitude. For each subsample, we also created two additional stacks comprising objects with and without NB3420 detections, respectively. Stacked images were made by averaging postage stamps of individual galaxies centered on the coordinates of either their V (LBGs) or NB4670 (LAEs) detections. Pixels contaminated by nearby objects were excluded from the stacks by creating a mask from the object detection isophotes in the SExtractor segmentation image. Stacked image photometry was performed using the IRAF PHOT routine using a $1\farcs9$ aperture, corresponding to the matching radius used to find detections. Although the postage stamps for individual galaxies were previously background subtracted as part of the data reduction process, we found that a second pass of background subtraction on the stacked image was necessary to remove remaining sky subtraction systematics. Bootstrap resampling was employed for each stack in order to include both sample variance and photometric error in the calculation of stack uncertainties. The results of the stacking analysis are presented in Table 2.5. None of the NB3420 stacks of individual LBGs and LAEs without LyC detections exhibited any significant flux; the NB3420 stack of LBG nondetections reached a 3σ limiting magnitude of 28.62 and the NB3420 stack of LAE nondetections reached a 3σ limiting magnitude of 28.97. These limits reflect only photometric errors. We note that for the NB3420 stacks of all LBGs and all LAEs, the addition of noise from a large number of galaxies undetected in NB3420 overpowered the signal from the few detected galaxies. As the resulting signal in the stack was detected at less than 3σ, we quote a lower limit in magnitude in Table 2.5.

2.4 Accounting for Contamination

In narrowband imaging studies of $z \sim 3$ LyC emission, it is critical to determine whether the detection in the narrowband filter is actually high-redshift LyC emission or contaminating radiation from a lower-redshift object. In this section, we analyze the morphology of several candidate LyC-emitters for which we have high-resolution *HST* imaging and discuss the complexities of identifying contaminants. Because we do not have high-resolution, multi-band imaging for all of our candidate LyC-emitters, we also discuss statistical corrections applied to our samples in order to account for foreground contamination by low-redshift galaxies (which artificially boosts the LyC signal) and LyC absorption by the IGM (which decreases the observed LyC emission).

2.4.1 Morphology of NB3420 Detections

In order to cull potential LyC detections from obvious neighbors, we have visually inspected each NB3420 detection in all available bands (as discussed in Section 2.3.3). This process of visual inspection, however, is limited by the depth and resolution of the data. Within our dataset, the *HST*/WFC3 imaging has the best resolution, followed by the ground-based optical data from Keck. The WFC3/UVIS *F475W* and WFC3/IR *F160W* images have PSF FWHMs of $0\farcs08$ and $0\farcs18$, respectively (Law et al., 2012b), while the seeing FWHMs of the Keck data are larger ($0\farcs7 - 1\farcs0$). Unfortunately, only 1 (2) of the targets in our samples with NB3420 matches fall within the small $2\farcm3 \times 2\farcm1$ ($2\farcm9 \times 2\farcm7$) field of view of the WFC3 IR (UVIS) imaging. Three additional objects with NB3420 detections (two in the photometric LAE sample and one LAE/LBG that we removed from both samples for its complicated morphology) also fall in the field of view of the WFC3 IR and UVIS images. Examining the morphologies of these objects across the ground-based and HST images highlights the difficulties associated with object matching.

Figure 2.6 shows four LAEs with HST imaging and NB3420 detections (the LAE photometric candidates *lae4070* and *lae2158*, along with spectroscopically confirmed LAEs *lae2966* and *lae4680*) displayed in five filters: NB3420 (LyC), NB4670$-V$ (Lyα), V (UV continuum),

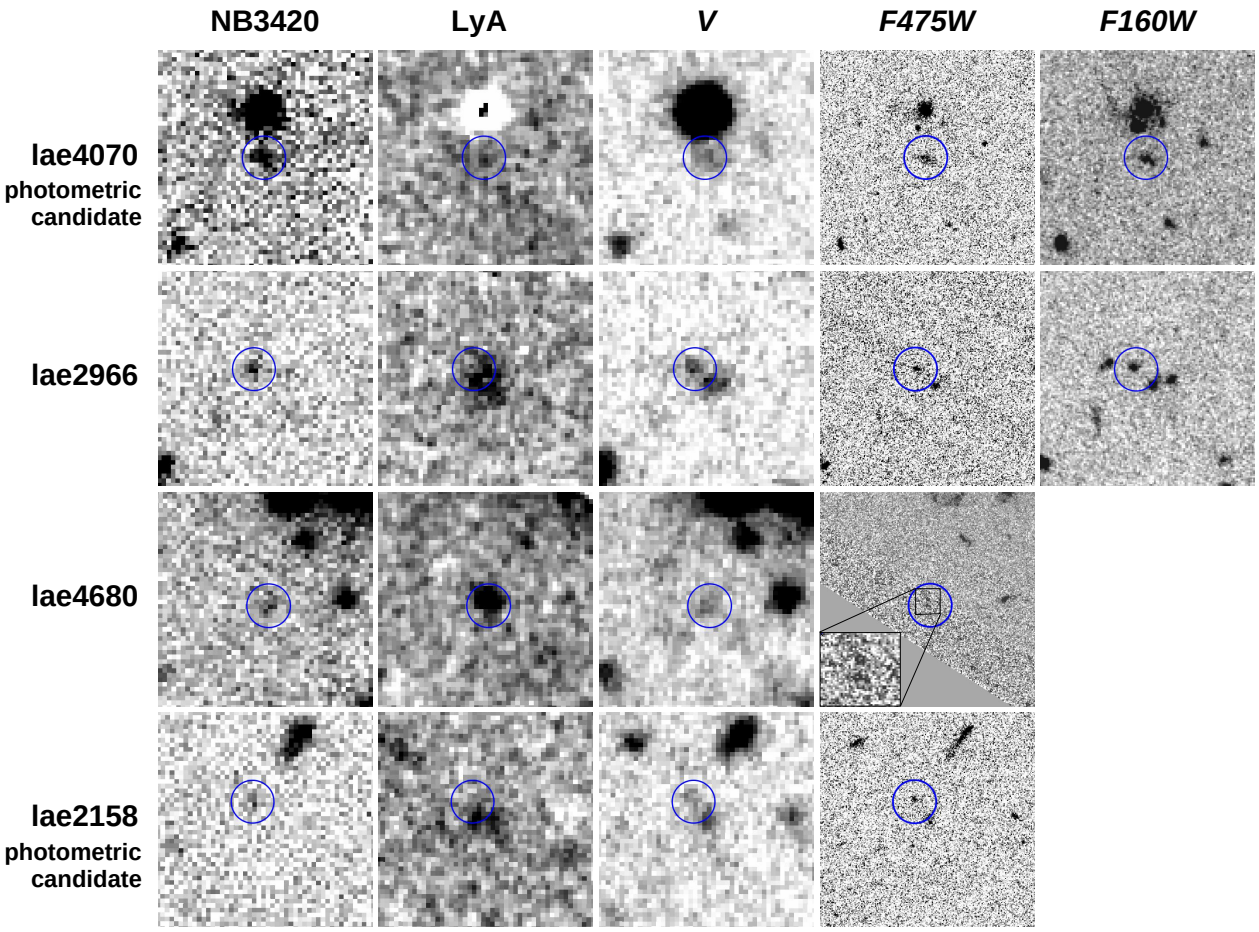

Figure 2.6 $10'' \times 10''$ postage stamp images of four LAEs with HST imaging and NB3420 detections (the LAE photometric candidates *lae4070* and *lae2158*, along with spectroscopically confirmed LAEs *lae2966* and *lae4680*). The postage stamps highlight the difficulties associated with interpreting the morphologies of these objects with ground-based resolution. Objects are displayed in up to 5 filters: NB3420 (indicating the LyC), NB4670$-V$ (indicating Lyα emission and labeled LyA), V (indicating the non-ionizing UV continuum), $F475W$ (rest-frame $\sim$1200Å), and $F160W$ (rest-frame $\sim$4000Å). All postage stamps are centered on the V-band centroid and blue circles ($1''$ radius) indicate the centroid of the NB3420 emission. All postage stamps follow the conventional orientation, with north up and east to the left.

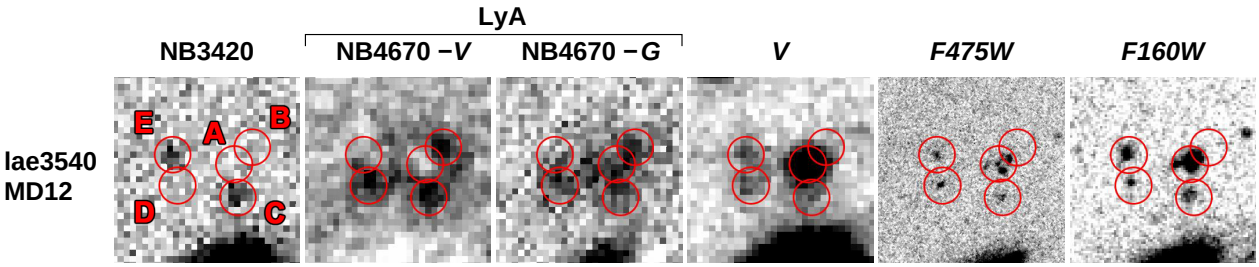

Figure 2.7 3.″2 × 3.″2 postage stamp images of the MD12/*lae3540*, an additional object with a potential LyC detection. Originally identified as both an LBG and LAE, MD12/*lae3540* was removed from both samples due to its complex morphology (see Section 2.4.1). The object is displayed in 6 filters: NB3420 (indicating the LyC), NB4670−V and NB4670−G (both indicating Lyα emission), V (indicating the non-ionizing UV continuum), $F475W$ (rest-frame ∼1200Å), and $F160W$ (rest-frame ∼4000Å). The clumpy morphology for MD12/*lae3540* is indicated by five red circles labeled A−E. Region A corresponds to the LBG and LAE centroids for MD12/*lae3540*, while regions B, C, and D correspond to areas of Lyα emission indicated by the NB4670−V image. Region C also corresponds to the location of the NB3420 emission. Region E likely indicates a lower-redshift galaxy along the line of sight. All postage stamps follow the conventional orientation, with north up and east to the left.

F475W (rest-frame 1240Å), and F160W (rest-frame 4000Å). *Lae4070* is an example of an object with a simple morphology. In all images, a single detection is visible, and the offsets between the centroids of the detection in each image are very small. Similarly, *lae4680* can be indentified with a single source in all images except $F475W$, where the object breaks into two clumps located 0.″3 apart. As this offset is very small, these clumps are likely part of the same system, although foreground contamination is still a possibility. For *lae4070* and *lae4680*, the only possibilities of contamination arise from either the small probability of [OII] emission being misidentified as Lyα emission or a lower-redshift foreground galaxy coincident with the LAE along the line of sight. We discussed the first possibility in Section 2.2.4 and concluded that it is small enough to ignore. The second possibility is quantified in Section 2.4.2 in the discussion of the contamination simulations. The analysis of the remaining two objects is more complex. In the case of *lae2966*, multiple clumps are visible in the V-band, $F475W$, and $F160W$ imaging, and the NB3420 emission is associated with only one clump. The spectroscopically-confirmed Lyα emission is extended and not distinctly associated with any single clump. Therefore, it is unclear whether the NB3420 detection is LyC emission from one clump of a $z \sim 2.85$ galaxy or a low-redshift interloper along the line of sight. In the case of *lae2158*, the HST imaging can be used to identify the NB3420 detec-

tion as contamination. While it is not possible to determine in the V-band image whether the UV-continuum light associated with the LAE belongs to multiple objects or whether it is merely extended, there are two distinct galaxies visible in the $F475W$ image. Since the northeastern galaxy is associated with the NB3420 detection while the southwestern galaxy is associated with the Lyα emission, we classify this system as a case of contamination.

We also highlight one object whose complex morphology led us to remove it from our analysis completely. This object (shown in Figure 2.7, with multiple clumps indicated) was originally identified in our catalogs as both an LBG (MD12) and an LAE (*lae3540*), with both the LBG and LAE centroids coincident with the bright $V-$band detection (indicated by region A). Analysis of the Lyα morphology in both the NB4670$-V$ and NB4670$-G$ images reveals extended emission in both Lyα images. Although both Lyα images show nearly identical morphology for all other LAEs with NB3420 detections, the extended Lyα emission around MD12 appears clumpy in the NB4670$-V$ image (associated with regions B, C, and D) and more diffuse in the NB4670$-G$ image. Also, while the Lyα emission appears to extend down to region C where the NB3420 detection is located ($1\farcs0$ to the south of the LBG centroid), this location is also coincident with detections in the $F475W$ and $F160W$ images that are not visibly connected to the LBG centroid in region A. Unfortunately, due to the slit position of 74°, the LRIS spectrum of this object only provides us with information about region A (where we observe double-peaked Lyα emission in the spectrum) and misses the region associated with the NB3420 detection. We note that region E likely indicates a lower-redshift interloper along the line of sight, as its position does not coincide with Lyα emission and it is located at the large offset of $2\farcs1$ from region A (the centroid of MD12).

The interpretation of the suite of imaging for MD12 is not straightforward, and it is impossible to fully understand the nature of these clumps with the current data. The clumps may comprise an extended, perhaps interacting, system, with all clumps at the same redshift. Alternatively, as region A has Lyα emission in its spectrum and regions B, C, and D are all associated with fairly compact Lyα emission in the NB4670$-V$ image, these four clumps may simply be several protocluster members along the line of sight located at slightly different redshifts; in this case, they should be treated as separate LAEs. A final possibility (supported

by the fact that the Lyα emission appears diffuse in the NB4670$-G$ image) is that the extended Lyα emission actually originates in the central part of the MD12 system and is being projected over a large area; in this case, the clump with the NB3420 emission in region C may be an interloper along the line of sight. Because of the ambiguity regarding the nature of MD12 as a either single, complex system or the superposition of multiple galaxies, we exclude both MD12 and *lae3540* from our LBG and LAE analysis. Nevertheless, this object represents another possible LyC-emitter.

Determining conclusively whether the NB3420 detections are contamination or true LyC emission requires imaging of each candidate galaxy with high enough resolution to discern the individual clumps and spectroscopy at high enough resolution that distinct spectra are obtained (and redshifts calculated) for each emitting region. This method has been recently implemented in the SSA22a field using HST/WFC3/$F336W$ to acquire high-resolution imaging below the Lyman limit for three $z \sim 3.1$ LBGs. Additionally, near-infrared spectroscopy of rest-frame optical [OIII] nebular emission was obtained using NIRSPEC on Keck II (Nestor et al., 2013; Siana et al., in prep). The seeing of $\sim 0\farcs5$ for these near-infrared observations enabled the spatial separation of clumps. One of three LBGs was confirmed to have escaping LyC radiation, and two others showed evidence of low-redshift contamination. Unfortunately, a similar study for the HS1549 field is not possible using ground-based or current space-based instrumentation. There is no appropriate imaging filter on HST that probes the region just below the Lyman limit at $z = 2.85$ without some contamination redwards of the limit. Furthermore, spectroscopy from the ground is unfeasible because the rest-frame optical features do not fall within windows of atmospheric transmission at $z = 2.85$. The next best option is to estimate photometric redshifts of each clump by acquiring high-resolution multi-band imaging. Such a technique has been successfully employed by Vanzella et al. (2012) for a sample of 19 LBGs with potential LyC emission at $3.4 \leq z \leq 4.5$ using multi-band HST imaging from the GOODS and CANDELS surveys.

2.4.2 Contamination from Foreground Galaxies

Although we currently do not have the high-resolution imaging or spectroscopic data required to prove the validity of each individual LyC detection, we can characterize the probability of foreground contamination statistically. With the assumption that all of our targets have been correctly identified as high-redshift galaxies, the NB3420 flux we measured can either be associated with LyC emission from the high-redshift galaxy itself or with contaminating radiation from a spatially coincident lower-redshift interloper. In order to statistically characterize the fraction of contaminated NB3420 detections in a given sample, we performed a simulation to calculate the expected number of uncontaminated LyC detections and the contamination-corrected average NB3420 magnitude for that sample. We summarize the simulation below, and further details are described in Section 5.1 of Nestor et al. (2013).

The contamination simulation was run separately for the LBGs and LAEs. Within the simulation, we considered as possible LyC detections all NB3420 SExtractor detections within $3\farcs5$ of our targets that fall within 1σ of the magnitude range of our reported LyC detections, corresponding to $26.19 \leq m_{3420} \leq 27.59$ for LBGs and $24.98 \leq m_{3420} \leq 27.70$ for LAEs. These SExtractor detections included both the detections considered to be candidates for LyC emission and detections previously identified by eye as belonging to interlopers visible in other wavelength bands. We computed the probability of each NB3420 detection being an interloper, which depends on both the global surface density of objects in the NB3420 image and the local surface density at the offset of the NB3420 detection from each LBG and LAE. In each iteration of the simulation, we used these probabilities to randomly determine whether or not each NB3420 detection was flagged as an interloper. Detections at large radial offset − where the local surface density approaches the global surface density − are more likely to be flagged as interlopers, as demonstrated in Figure 2.8. We removed the NB3420 magnitudes of objects flagged as interlopers before the average NB3420 magnitude was calculated, resulting in the contamination-corrected average NB3420 magnitude. The simulation was repeated 1000 times, and we recorded the average number of uncontaminated NB3420 detections and the average contamination-corrected NB3420

magnitude for both samples. Uncertainties in these average values were computed from the distribution of simulation results.

In Figure 2.8, we present histograms of the radial surface density of NB3420 detections around galaxies in the LBG and LAE samples, compared to the global surface density. The surface density of NB3420 detections is plotted using NB3420 offsets computed relative to $V-$band (non-ionizing UV continuum) for LBGs. For LAEs, offsets were computed relative to both $V-$band and NB4670 (a combination of Lyα and continuum emission in the vicinity of the Lyα wavelength). As discussed in Section 2.3.4, LyC emission is spatially more closely associated with the UV-continuum than with Lyα emission. Therefore, we adopt V-band coordinates to represent the LAE centroids, except in cases where the LAE is undetected in V and we must use NB4670 coordinates. Panels (b) and (c) of Figure 2.8, displaying $V-$band and NB4670 offsets, respectively, confirm that LyC emission is on average more closely associated with $V-$band emission than with NB4670, as the average offset in panel (b) is less than that in panel (c). All panels show an excess surface density at small offsets (although this excess is only statistically significant for the LAEs), suggesting that a large number of the NB3420 detections are physically associated with the LBG and LAE targets; the contamination simulation statistically quantifies this number. For the 4 LBGs detected in NB3420, the simulations predict on average 1.5 ± 1.0 uncontaminated detections. For the 7 NB3420-detected LAEs, the simulations predict 4.3 ± 1.3 uncontaminated detections. For both samples, the simulation yields the contamination-corrected average magnitude of the NB3420 detections. These values are used to compute the sample-averaged NB3420$-V$ colors and flux-density ratios presented in Table 2.6 and discussed in Section 2.5. We note that the removal of contaminants must increase the non-ionizing UV to LyC flux-density ratio for the ensembles containing the full sample of LBGs (or LAEs), as the total amount of LyC flux is decreased when a contaminant is removed while the total amount of non-ionizing UV flux stays the same. For ensembles that contain only objects with NB3420 detections, however, the flux-density ratio may not necessarily increase with the removal of the contaminants. In these cases, when an NB3420 detection is identified as a contaminant, both its LyC and non-ionizing UV emission are omitted from the sample when calculating

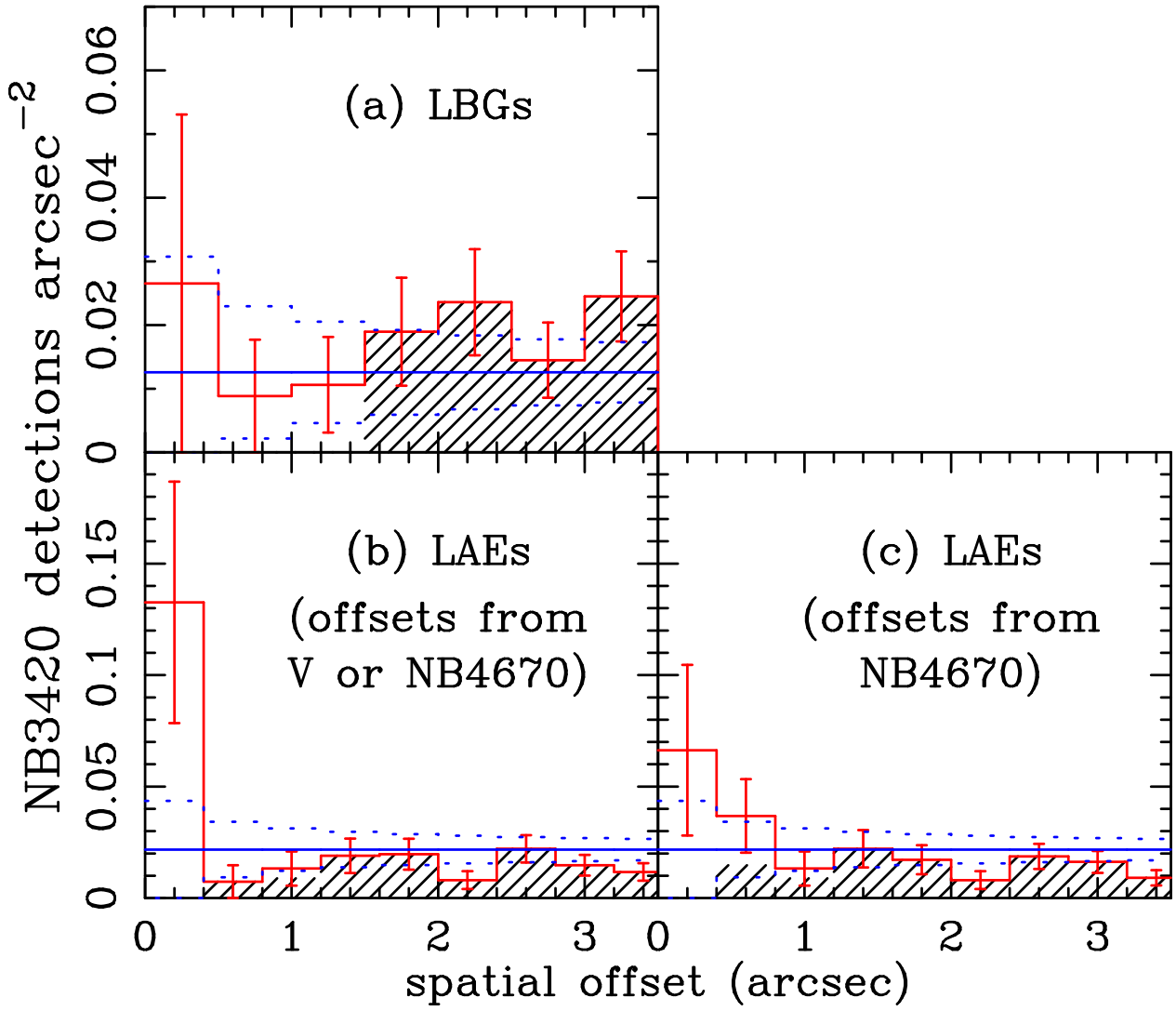

Figure 2.8 Radial surface density of NB3420 detections within 3.″5 of galaxies in our LBG and LAE samples (solid red histograms). The radial bin size for the LBG histogram is 0.″5, and the bin size for the LAE histograms is 0.″4. Red histogram error bars represent 1σ Poisson uncertainties in the number of NB3420 detections in each bin. The blue solid line represents the average surface density of NB3420 detections within the magnitude range ($\pm 1\sigma$) of the LAEs/LBGs, corresponding to the expected amount of contamination. Blue dotted lines indicate the 1σ uncertainties in the average surface density in each bin. Black hashed regions on the red histogram represent NB3420 detections that have been rejected by eye as contaminants and are not considered candidates for LyC emission. As described in Section 2.4.2, the surface density of NB3420 detections around LAEs is plotted using the NB3420 offsets calculated from LAE position defined by either a combination of NB4670 and $V-$band centroids (panel b) or NB4670 centroids only (panel c). In both cases, we observe a significant excess in surface density of NB3420 detections at small offset from LAEs, which indicates that many of the LAE NB3420 detections are likely uncontaminated LyC emission. We also note that panels (b) and (c) confirm that LyC emission is on average more closely associated with $V-$band emission than with NB4670, as the average offset in panel (b) is less than that in panel (c). As there are only 4 LBGs with NB3420 detections, the LBG excess over the average surface density at low spatial offset is much smaller.

the flux-density ratio as the object is no longer considered to have a true LyC detection.

2.4.3 Correction for IGM Absorption

In addition to correcting for contamination by low-redshift galaxies, we must also correct the NB3420 photometry for the absorption of LyC photons by neutral hydrogen in the IGM. In order to account for such attenuation, we ran a second set of simulations to determine the mean IGM correction factor and its associated uncertainty. We note that, as discussed in Nestor et al. (2011), our simulations do not take into account the possible environmental effects due to the presence of the $z \sim 2.85$ protocluster and the proximity to the hyperluminous QSO (Q1549), and it is not clear whether such effects would culminate in an increase or decrease of neutral hydrogen absorbers. We summarize the methods employed below, and further details are described in Nestor et al. (2011) and Nestor et al. (2013), the latter of which describes the current version of the methodology.

First, we constructed 500 model sightlines simulating the distribution of HI absorbers in the IGM. For each model sightline, absorbers were drawn randomly from their redshift and column density distributions (Rudie et al., 2013), spanning redshifts from $z = 1.7$ to the redshift of each object of interest. The model sightlines for the LAEs were created at the mean redshift of the LAEs ($z = 2.85$) since the narrow width of the NB4670 filter implies that the LAE targets lie within a small redshift range. Given that the LBGs span a wider range in redshift ($2.815 \leq z \leq 3.414$), we created a set of 500 model sightlines at the redshift of each LBG. We then calculated the mean transmission of each model sightline in the LyC region. For the purposes of these simulations, the LyC region consists of the fixed observed-frame bandpass of the NB3420 filter, taking into account the filter transmission profile. Figure 2.9 shows the probability distributions of the LyC transmission factor for model sightlines at $z = 2.85$ (representing typical LAE redshifts) and $z = 3.41$ (corresponding to our highest-redshift LBG with the most extreme case of attenuation).

The sample average transmission through the IGM ($\bar{t}_{sample}$) is equal to the mean transmission of the 500 $z = 2.85$ sightlines for the LAEs and the mean transmission of all model

sightlines for the LBGs at different redshifts. The uncertainty in $\bar{t}_{sample}$ is estimated by first assuming an exponential distribution of unattenuated LyC flux (the parameters of this exponential function are fit to our data via a maximum likelihood method, see Nestor et al., 2013) and then creating 1000 realizations of our sample by randomly choosing for each galaxy an unattenuated LyC flux from our exponential distribution and an attentuation factor from one of the simulated model sightlines at the redshift of the galaxy. We set the uncertainty in $\bar{t}_{sample}$ equal to the standard deviation of the 1000 simulated $\bar{t}_{sample}$ values. We find that $\bar{t}_{sample,LAE} = 0.44 \pm 0.03$ and $\bar{t}_{sample,LBG} = 0.35 \pm 0.04$. For both the LBG and LAE samples, we multiply the contamination-corrected non-ionizing to ionizing flux-density ratios by the transmission factor to obtain the IGM-and-contamination-corrected values presented in Table 2.6. Unlike the contamination correction discussed in Section 2.4.2, which decreases the average NB3420 flux, the IGM attenuation correction acts to increase it.

2.5 Results

In order to study the amount of ionizing radiation escaping star-forming galaxies at high redshift, we have imaged a large sample of $z \sim 2.85$ galaxies in a narrowband filter designed to probe LyC emission. As described in Section 2.3.4, we have detected 4 out of 48 LBGs and 7 out of 90 LAEs in our NB3420 filter. After application of the contamination and IGM corrections discussed in Sections 2.4.2 and 2.4.3, the average NB3420$-V$ properties of the galaxies in our sample provide information about the ratio of non-ionizing to ionizing UV flux density and, with some assumptions, the LyC escape fraction.

2.5.1 NB3420 minus V Colors and Flux-Density Ratios

In Figure 2.10, we plot NB3420$-V$ color versus V magnitude for LBGs and LAEs with NB3420 detections. The colors of the LBG and LAE stacks are also plotted. All of the data presented in Figure 2.10 represent observed values, uncorrected for foreground galaxy contamination and IGM absorption. Qualitatively, the color-magnitude diagram (CMD) for objects in the HS1549 field agrees with the CMD for objects in the SSA22a field (Nestor et al.,

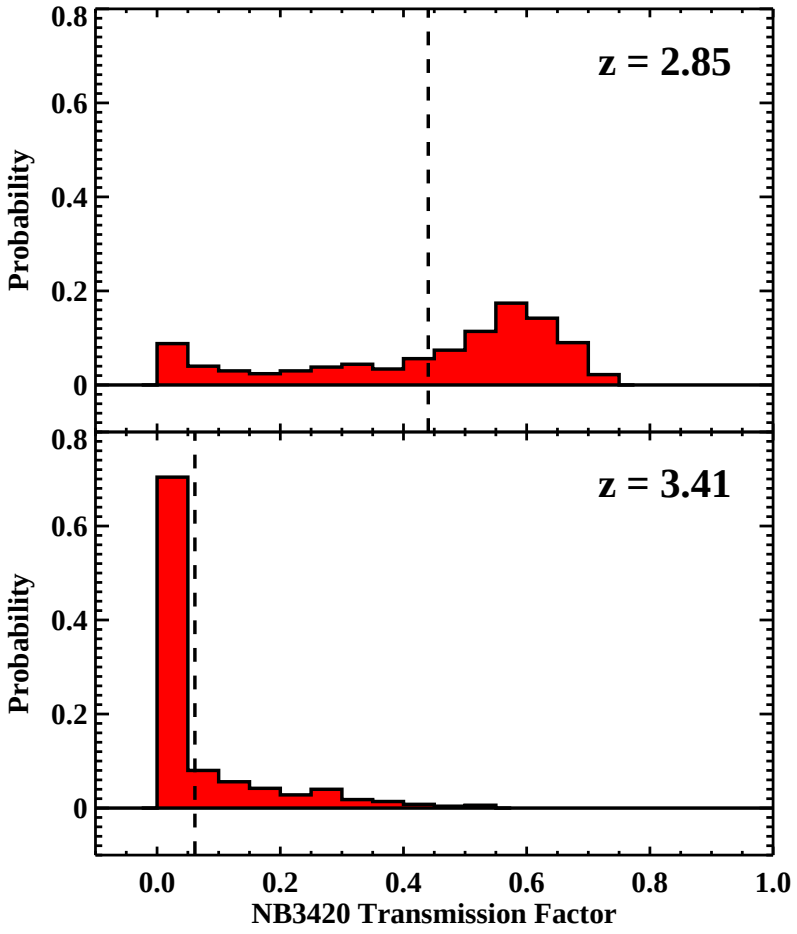

Figure 2.9 The probability distribution of the LyC transmission factor through the NB3420 filter for an object at $z = 2.85$ (top) and an object at $z = 3.41$ (bottom). The mean transmission at each redshift is indicated by the dashed lines. The top panel represents the vast majority of LBGs and LAEs that lie near the redshift spike at $z = 2.85$. The wide range of possible transmission values at $z = 2.85$ reflects the variation in IGM absorption at $z = 2.85$ and the slight peak around zero transmission corresponds to sightlines that encounter a Lyman limit system. The bottom panel corresponds to the redshift of M23, an LBG with a redshift far removed from the spike, and represents the most extreme case of attenuation. This large amount of attenuation is due to a combination of two effects. Not only is the sightline through the IGM longer for the photons coming from $z = 3.41$ (thus providing each photon with more time to encounter an absorber), but the $z = 3.41$ IGM has a higher fraction of neutral hydrogen − and thus more absorbers − than the $z = 2.85$ IGM.

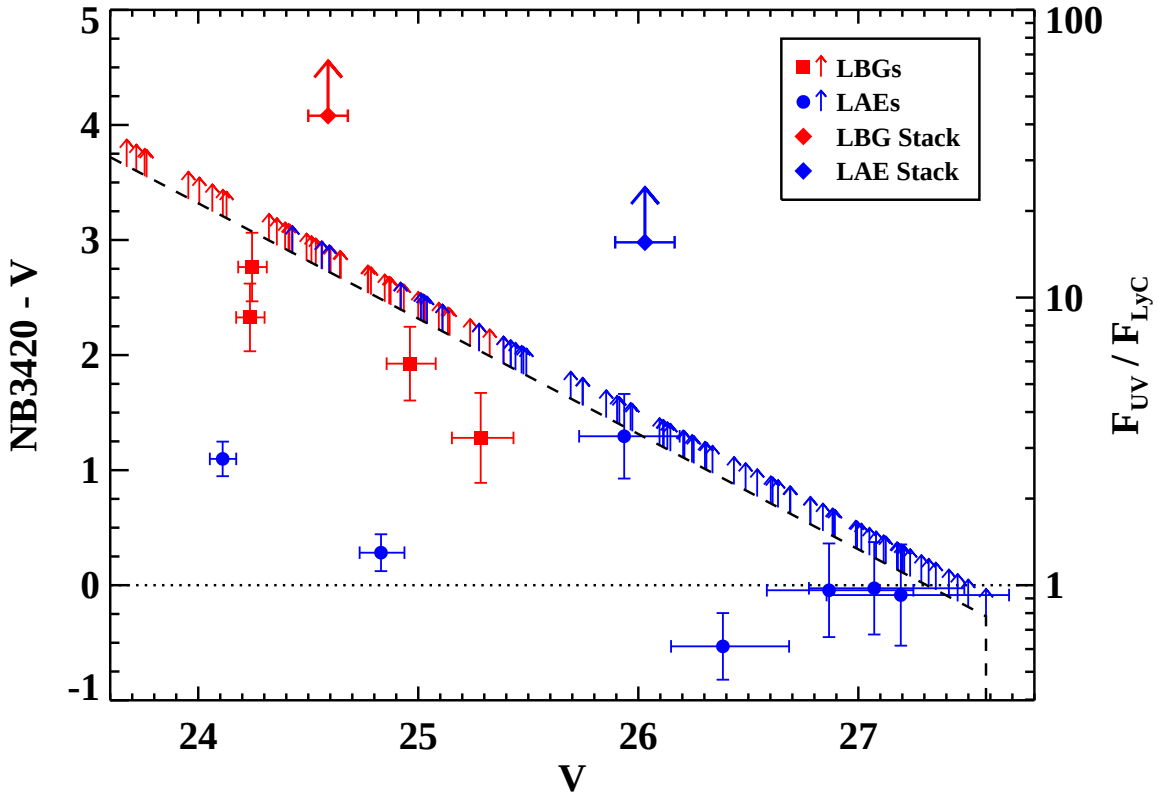

Figure 2.10 Color-magnitude diagram of observed NB3420$-V$ vs. V magnitude, with the equivalent values for F_{UV}/F_{LyC} indicated on the right-hand axis. LBGs are indicated by red squares and LAEs by blue circles. LBGs (LAEs) without NB3420 detections are plotted as 2σ lower limits, indicated by the red (blue) arrows. The typical $V-$band uncertainty associated with these lower limits is of similar size to the $V-$band uncertainty of data points, at a given V magnitude. The red (blue) diamond indicates the 3σ limit in NB3420-V color for the stack of all LBGs (LAEs). All data represent observed values, uncorrected for foreground galaxy contamination and IGM absorption. We note that an NB3420$-V$ color of zero ($F_{UV}/F_{LyC} = 1$), corresponds to a flat spectrum with no Lyman break. Such a blue spectrum cannot be reasonably explained by current stellar population synthesis models, and many of the LAEs on this plot lie uncomfortably close to or below this limit.

2011); both samples of galaxies exhibit narrowband minus continuum colors across a wide range of continuum magnitudes that are extremely blue with respect to expectations from standard stellar population models. For example, Bruzual & Charlot (2003) models with solar metallicity and a constant star-formation rate predict the intrinsic ratio of non-ionizing to ionizing radiation for LAEs to be roughly $3 - 6$, which corresponds to an NB3420$-V$ color of $1.2 - 2$. Out of the 7 LAEs with NB3420 detections, only one LAE (*lae6662*) has a color redder than 1.2. Even more surprising, especially given the small offsets ($\Delta_{UV,\,LyC} \leq 0\farcs36 =$ 2.8 kpc) of all LAEs except *lae6662*, 4 of the 6 remaining LAEs have NB3420$-V < 0$, implying a complete absence of a Lyman break (i.e., a flat spectrum). For typical LBG stellar populations (e.g., Shapley et al., 2001; Kornei et al., 2010), the intrinsic ratio is predicted to be >6 (corresponding to an NB3420$-V$ color >2); however, two out of the four NB3420-detected LBGs have NB3420$-V < 2$. Thus, the HS1549 field provides the first confirmation that the blue non-ionizing to ionizing UV colors observed in the SSA22a field are common among $z \sim 3$ galaxies, and not simply an unusual property of the SSA22a field itself. Tables 2.3 and 2.4 display the raw non-ionizing to ionizing flux-density ratios (F_{UV}/F_{LyC}) for individual LBGs and LAEs with NB3420 detections, and Table 2.5 shows the same values for the stacks.

The average corrected and uncorrected NB3420$-V$ colors and flux-density ratios for the samples of LBGs and LAEs are presented in Table 2.6. Because photometry of the stacks of LBGs and LAEs without NB3420 detections does not yield any NB3420 signal, we determine average NB3420 and V magnitudes by calculating the mean flux of all the galaxies in each sample and assuming zero flux for undetected objects. These average magnitudes agree with stacked photometry within the errors. As our V and NB3420 filters probe rest-frame wavelengths of 1430Å and 888Å, respectively, we can convert our observed NB3420$-V$ colors directly into non-ionizing to ionizing flux-density ratios (i.e., F_{UV}/F_{LyC}). We find uncorrected flux-density ratios of $(F_{UV}/F_{LyC})_{obs} = 92 \pm 49$ for LBGs and $(F_{UV}/F_{LyC})_{obs} = 11.2 \pm 5.4$ for LAEs. Considering only objects with NB3420 detections in each sample, we find $(F_{UV}/F_{LyC})_{obs} = 7.2 \pm 2.2$ for LBGs and $(F_{UV}/F_{LyC})_{obs} = 1.6 \pm 0.9$ for LAEs. In order to correct these colors and flux-density ratios for foreground contamination, we use adjusted

NB3420 and V magnitudes derived from the contamination simulation described in Section 2.4.2. Correcting for IGM attenuation, however, only affects NB3420 magnitudes because rest-frame $\sim$1500Å flux is not affected by HI absportion in the IGM. Thus, for the IGM correction we simply multiply the contamination-corrected flux-density ratio by the IGM transmission factor. With the application of these two corrections to the colors and flux-density ratios, we find $(F_{UV}/F_{LyC})_{corr} = 82 \pm 45$ for LBGs and $(F_{UV}/F_{LyC})_{corr} = 7.4 \pm 3.6$ for LAEs. For objects with NB3420 detections, we find corrected values of $(F_{UV}/F_{LyC})_{corr} = 2.2 \pm 1.6$ for LBGs and $(F_{UV}/F_{LyC})_{corr} = 0.7 \pm 0.5$ for LAEs.

Table 2.6. Average UV to LyC flux-density ratios.

Correction	LBGs		LAEs	
	$\langle \mathrm{NB3420} \rangle - \langle V \rangle$ [a]	$\langle F_{UV}/F_{LyC} \rangle$[b]	$\langle \mathrm{NB3420} \rangle - \langle V \rangle$[a]	$\langle F_{UV}/F_{LyC} \rangle$[b]
Full Ensembles				
none	$4.91^{+0.47}_{-0.84}$	92 ± 49	$2.62^{+0.43}_{-0.72}$	11.2 ± 5.4
contamination[c]	$5.93^{+0.47}_{-0.84}$	230 ± 130	$3.06^{+0.43}_{-0.72}$	16.8 ± 8.1
IGM + contamination[d]	$4.78^{+0.48}_{-0.88}$	82 ± 45	$2.17^{+0.43}_{-0.73}$	7.4 ± 3.6
Sources with NB3420 detections only				
none	$2.15^{+0.29}_{-0.39}$	7.2 ± 2.2	$0.54^{+0.46}_{-0.80}$	1.6 ± 0.9
contamination[c]	$2.18^{+0.49}_{-0.91}$	7.5 ± 4.2	$0.50^{+0.56}_{-1.22}$	1.6 ± 1.1
IGM + contamination[d]	$0.86^{+0.60}_{-1.44}$	2.2 ± 1.6	$-0.39^{+0.59}_{-1.36}$	0.7 ± 0.5

[a]Color determined from average NB3240 and V-band fluxes. Uncertainties include photometric and sample uncertainties.

[b]Ratio and uncertainty in non-ionizing UV and LyC flux-densities inferred from $\langle \mathrm{NB3420} \rangle - \langle V \rangle$ color.

[c]Color and flux-density ratio after statistically correcting sample for foreground contamination of NB3420 fluxes. For the ensembles containing all LBGs (or LAEs), the removal of contaminants must increase the non-ionizing UV to LyC flux-density ratio as the total amount of LyC flux is decreased. For ensembles that contain only objects with NB3420 detections, however, the flux-density ratio may not necessarily increase with the removal of the contaminants.

[d]Color and flux-density ratio after correcting sample for both foreground contamination and IGM absorption of NB3420 fluxes.

It has so far proven difficult to reconcile the observed low non-ionizing to ionizing flux-density ratios with intrinsic luminosity-density ratios predicted by current stellar-population synthesis models. Theoretical values of the intrinsic luminosity-density ratio featured in previous works range from $(L_{UV}/L_{LyC})_{intr} = 3 - 6$ (Steidel et al., 2001; Shapley et al., 2006; Siana et al., 2007). Many of the values in Table 2.6 − and especially those that consider only the NB3420-detected galaxies − do not fall within the theoretical range. We also note that if we were to consider the flux-density ratio in the region defined by the NB3420 isophote (thus only including $V-$band light in the vicinity of the NB3420 emission, which more closely emulates a single stellar population), there would be even more tension between the measurements and the models. Nestor et al. (2013) examined a wider range of theoretical $(L_{UV}/L_{LyC})_{intr}$ values using stellar population synthesis models from Bruzual & Charlot (2003) and the BPASS models from Eldridge & Stanway (2009), which include a more detailed treatment of massive stellar binaries (specifically, Wolf-Rayet stars) and nebular emission. The models were used to describe galaxies with an array of ages and metallicities, assuming a constant star-formation rate. The largest source of variation in $(L_{UV}/L_{LyC})_{intr}$ is due to the age of the galaxy, as $(L_{UV}/L_{LyC})_{intr}$ increases quickly as the stellar population evolves. The choice of model is also important, as the BPASS models predict ratios of $(L_{UV}/L_{LyC})_{intr}$ a factor of $\sim$1.5 lower than the Bruzual & Charlot (2003) models for a given age and metallicity. Changes in stellar metallicity cause smaller variations in $(L_{UV}/L_{LyC})_{intr}$ on the order of a few percent, but the magnitude of these changes increases with the age of the stellar population. It is important to note that, if the models are correct, the predicted value for $(L_{UV}/L_{LyC})_{intr}$ should serve as a lower limit to the observed non-ionizing to ionizing flux-density ratio of the galaxy. The observed flux-density ratio will likely be higher than this limit, as ionizing radiation may be absorbed by neutral hydrogen in both the interstellar medium (ISM) of the galaxy and the IGM. Thus, for any given galaxy, the observed value of F_{UV}/F_{LyC} should be greater than or equal to $(L_{UV}/L_{LyC})_{intr}$. We note that the two sets of stellar population synthesis models used in this analysis, as with all such models, are limited by the absence of direct observations in the LyC region of the O- and B-type stars that produce most of the ionizing radiation (Zastrow et al., 2013). Without

direct observations to verify that the models are accurate, the fact that our LyC observations disagree with the models may indicate that there is something systematically incorrect with the model spectra at ultraviolet wavelengths. Alternatively, the tension between the models and our observations may be due to the uncertainties involved in removing contaminants. Any low-redshift contaminants left in our sample (e.g., an [OII]-emitter or foreground galaxy) would also produce colors different from those predicted for models of $z \sim 2.85$ galaxies.

Here, we consider our inferred values of $(F_{UV}/F_{LyC})_{corr}$ with respect to the model predictions of $(L_{UV}/L_{LyC})_{intr}$. We first discuss the interpretation of $(F_{UV}/F_{LyC})_{corr}$ for samples of LBGs and LAEs with NB3420 detections because these are the samples for which LyC emission is actually measured. We consider the ensembles of NB3420-detected galaxies rather than individual galaxies because our statistical corrections for foreground contamination and IGM absorption do not apply to individual galaxies.

For the sample of LBGs with NB3420 detections, $(F_{UV}/F_{LyC})_{corr} = 2.2 \pm 1.6$. This value of 2.2 implies the unphysical ages of $\lesssim 10$ Myr using the Bruzual & Charlot (2003) and BPASS models. Adding the 1σ error to the LBG flux-density ratio implies $(F_{UV}/F_{LyC})_{corr} = 3.8$, which is consistent with a 100 Myr galaxy using the BPASS model. Typical LBGs are characterized by ages >100 Myr (Kornei et al., 2010; Shapley et al., 2005, 2001; although in Section 2.6.1 we show that this average age may be somewhat over-estimated, as it is based only on LBG samples with near- or mid-infrared detections) and not younger than ∼50 Myr (given the typical LBG dynamical timescale; Reddy et al., 2012). It is worth noting that using an average IGM correction for the NB3420-detections-only samples probably constitutes an overcorrection, as NB3420-detected galaxies are likely to have clearer sightlines through the IGM than the sample as a whole. Thus, the true value of $(F_{UV}/F_{LyC})_{corr}$ for LBGs is likely somewhere between 2.2 (corrected for contamination and IGM absorption) and 7.5 (corrected for contamination only). Values $\gtrsim 4.5$ are consistent with galaxy ages >100 Myr using BPASS models, and values $\gtrsim 6.1$ are consistent with the same limit in age using Bruzual & Charlot (2003) models.

As for the LAE sample, the value of $(F_{UV}/F_{LyC})_{corr} = 0.7 \pm 0.5$ is inconsistent with all models presented in Nestor et al. (2013). For models with metallicity $Z = 0.2\,Z_{\odot}$ and ages

of 1, 10, and 100 Myr, respectively, $(L_{UV}/L_{LyC})_{intr} = 1.33$, 2.10, and 3.16 for BPASS models and $(L_{UV}/L_{LyC})_{intr} = 1.98$, 3.59, and 6.17 for Bruzual & Charlot (2003) models. Only by considering values of the LAE flux-density ratio at $> 1\sigma$ from our measured value can we reconcile our flux-density ratio with those predicted by young BPASS models with ages of several Myr. Because the dynamical timescale argument (based on galaxy sizes and velocity dispersions) that limits LBG ages to >50 Myr may not apply to LAEs, it is possible that the extremely low non-ionizing to ionizing flux-density ratios we measure imply that LAEs are on average very young galaxies. Young ages for LAEs have been previously determined by SED fits of stacked photometry (e.g., Gawiser et al., 2007). We also note that, once again, the correction for IGM absorption may constitute an overcorrection, which would place the true value of $(F_{UV}/F_{LyC})_{corr}$ for LAEs between 0.7 (corrected for contamination and IGM absorption) and 1.6 (corrected for contamination only).

Until now, we have only discussed the interpretation of $(F_{UV}/F_{LyC})_{corr}$ for samples with NB3420 detections. We now consider the full samples of LBGs and LAEs, which include both objects with and without NB3420 detections. For the full sample of LBGs, $(F_{UV}/F_{LyC})_{corr} = 82 \pm 45$. This number is significantly higher than the lower limit required by stellar population synthesis models for typical LBGs with ages >100 Myr, namely $(L_{UV}/L_{LyC})_{intr} > 4.5$ for BPASS models and $(L_{UV}/L_{LyC})_{intr} > 6.1$ for Bruzual & Charlot (2003) models. This consistency with the models, however, arises not because all 48 LBGs have values of $F_{UV}/F_{LyC} \sim 82$, which would not conflict with models, but rather because 4 LBGs have low values of F_{UV}/F_{LyC} and the rest are undetected in LyC. For the full sample of LAEs, $(F_{UV}/F_{LyC})_{corr} = 7.4 \pm 3.6$. As with the LBGs, these values would not significantly conflict with models if they represented the typical LAE in the sample. However, the LAE sample is also comprised of some objects with very strong LyC emission and some objects with no observed emission. For both LBGs and LAEs, we must consider how values of $(F_{UV}/F_{LyC})_{corr}$ for individual galaxies compare with stellar population synthesis models, as the ensemble-averaged value does not take into account variation within the sample.

Table 2.7. Contributions to the Ionizing Background.

	LF[a]	F_{UV}/F_{LyC}[b]	Magnitude range[c]	ϵ_{LyC}[d]
(i)	LBG	82 ± 45	$M_{AB} \leq -19.7$	1.4 ± 0.8
(ii)	LAE	7.4 ± 3.6	$-19.7 < M_{AB} \leq -17.7$	3.2 ± 1.6
(iii)	LBG	7.4 ± 3.6	$-19.7 < M_{AB} \leq -17.7$	13.6 ± 6.7
(iv)	LBG	82 ± 45	$M_{AB} \leq -17.7$	2.6 ± 1.5
(v)	LAE	7.4 ± 3.6	$M_{AB} \leq -17.7$	6.8 ± 3.3
	Total (lum.-dep.)[e]	···	$M_{AB} \leq -17.7$	15.0 ± 6.7
	Total (LAE-dep.)[f]	···	$M_{AB} \leq -17.7$	8.8 ± 3.5

[a]Luminosity function parameters are the same as those described in Nestor et al. (2013).

[b]Sample average flux-density ratio corrected for foreground contamination and IGM absorption, from Table 2.6.

[c]Magnitude range over which the first moment of the luminosity function is determined. $M_{AB} = -19.7$ and -17.7 correspond to $0.34L_*$ and $0.06L_*$, respectively.

[d]Comoving specific emissivity of ionizing radiation in units of 10^{24} ergs s^{-1} Hz^{-1} Mpc^{-3}.

[e]Totals for the luminosity-dependent model, determined by summing rows (i) and (iii).

[f]Total for the LAE-dependent model, determined by summing 0.77× row (iv) and row (v).

2.5.2 The LyC Escape Fraction

Using the values of $(F_{UV}/F_{LyC})_{corr}$ for the full LBG and LAE samples presented in Table 2.6, we can determine the relative and absolute escape fractions for each sample. The relative escape fraction, a measure of how the observed flux-density ratio F_{UV}/F_{LyC} compares to the theoretical ratio, is defined to be

$$f_{esc,\,rel}^{LyC} = \frac{(L_{UV}/L_{LyC})_{intr}}{(F_{UV}/F_{LyC})_{corr}}, \tag{2.1}$$

where $(L_{UV}/L_{LyC})_{intr}$ is the intrinsic ratio of UV to LyC luminosity densities produced in star-forming regions. The absolute escape fraction includes an additional term for the escape fraction of non-ionizing UV photons (f_{esc}^{UV}) due to dust extinction:

$$f_{esc}^{LyC} = f_{esc,\,rel}^{LyC} \times f_{esc}^{UV}\,. \tag{2.2}$$

Thus,

$$f_{esc}^{LyC} = \left(\frac{F_{UV}}{F_{LyC}}\right)^{-1}_{corr} \left(\frac{L_{UV}}{L_{LyC}}\right)_{intr} \left(f_{esc}^{UV}\right) \tag{2.3}$$

Both unknowns f_{esc}^{UV} and $(L_{UV}/L_{LyC})_{intr}$ are uncertain and likely to vary from object to object. Following Nestor et al. (2013), we estimate these values based on the observed ages and $E(B-V)$ values of $z \sim 3$ LBGs and LAEs. For the escape fraction of non-ionizing UV photons, we adopt $f_{esc,LBG}^{UV} = 0.2$ and $f_{esc,LAE}^{UV} = 0.3$. For the intrinsic ratio of UV to LyC luminosity densities, we quote a range of values bracketed by the BPASS and Bruzual & Charlot (2003) models. For LBGs, we use 10^8 Myr, $Z = Z_\odot$ models to obtain $(L_{UV}/L_{LyC})_{intr,LBG} = 4.43 - 6.38$. For LAEs, which have been shown to be younger (Gawiser et al., 2007) and more metal-poor, we use 10^{6-7} Myr, $Z = 0.2Z_\odot$ models to obtain $(L_{UV}/L_{LyC})_{intr,LAE} = 1.33 - 3.59$. With these assumptions, we derive relative LyC escape fractions of $f_{esc,\,rel}^{LBG} = 5 - 8\%$ and $f_{esc,\,rel}^{LAE} = 18 - 49\%$, and absolute escape fractions of $f_{esc}^{LBG} = 1-2\%$ and $f_{esc}^{LAE} = 5-15\%$. As our measured values of F_{UV}/F_{LyC} have uncertainties of roughly fifty percent, the uncertainty in f_{esc} is at minimum fifty percent and likely higher due to uncertainties in our assumed values of f_{esc}^{UV} and $(L_{UV}/L_{LyC})_{intr}$.

Our values of f_{esc} are consistent with, though slightly lower than, those calculated by Nestor et al. (2013) for the SSA22a field using very similar methods: $f_{esc,LBG}^{LyC} = 5 - 7\%$, $f_{esc,LAE}^{LyC} = 10 - 30\%$. Using IGM-corrected values of F_{UV}/F_{LyC} from the literature and our assumptions for f_{esc}^{UV} and $(L_{UV}/L_{LyC})_{intr}$, we find additional values of f_{esc} in the literature that range from $19-27\%$ (Steidel et al., 2001; considering 29 averaged $z = 3.4$ LBG spectra), $24 - 35\%$ (Iwata et al., 2009; for $z \sim 3$ LBGs in the SSA22a field), and $4 - 6\%$ (Shapley et al., 2006), although the two LBGs in Shapley et al. (2006) with putative LyC emission were later shown to be a spurious detection (Nestor et al., 2011; Iwata et al., 2009) and a foreground contaminant (Nestor et al., 2013) such that f_{esc} calculated from this work would be consistent with zero. Using a slightly different method to make a direct measurement of f_{esc} for a sample of $3.4 < z < 4.5$ LBGs, Vanzella et al. (2010a) calculated $f_{esc} < 5 - 20\%$. Finally, by measuring HI opacity along 32 GRB sightlines in the redshift range $2.0 < z < 5.5$, Fynbo et al. (2009) determined $\langle f_{esc} \rangle = 0.02 \pm 0.02$ with a 95% confidence level upper limit of

$\langle f_{esc} \rangle \leq 0.07$. This wide range of values highlights how difficult it has proven to determine an accurate value for f_{esc}. These difficulties stem from many factors, including determination of redshifts, spatial resolution, foreground contamination, and the fact that only $\sim$10% of galaxies in the sample will be detected in the LyC. In our study, only 12 out of 131 spectroscopically-confirmed galaxies were observed to have NB3420 detections, and some of these are probably contaminated by foreground galaxies. Such a small sample size of NB3420 detections, while an improvement upon many previous studies of spectroscopically-confirmed galaxies, limits the precision of our f_{esc} measurements. Until there exist uncontaminated samples of LyC-emitting galaxies an order of magnitude larger, small sample sizes will be a constant source of uncertainty.

2.5.3 The LyC Emissivity of Star-forming Galaxies

We estimate the comoving specific emissivity of ionizing photons

$$\epsilon_{LyC} = \left(\frac{F_{UV}}{F_{LyC}} \right)^{-1}_{corr} \int_{L_{min}}^{L_{max}} L \, \Phi \, dL \tag{2.4}$$

following the assumptions of Nestor et al. (2013). In estimating ϵ_{LyC}, we assume that the UV luminosity functions of LBGs and LAEs do not change significantly from $z = 3.09$ to $z = 2.85$ and the only change in the value of $\int L \, \Phi \, dL$ is due to the integration bounds (i.e., L_{min} and L_{max}). Comparing our observed values for $(F_{UV}/F_{LyC})_{corr}$ to those of Nestor et al. (2013), we obtain $(F_{UV}/F_{LyC})^{HS1549}_{corr} = 4.6(F_{UV}/F_{LyC})^{SSA22a}_{corr}$ for LBGs and $(F_{UV}/F_{LyC})^{HS1549}_{corr} = 2.0(F_{UV}/F_{LyC})^{SSA22a}_{corr}$ for LAEs with spectroscopic redshifts. Nestor et al. (2013) suggest two different models for combining the LBG and LAE luminosity functions (see equations 4 and 5 in Nestor et al., 2013) to calculate the global ionizing emissivity. In the luminosity-dependent model, LAEs are assumed to represent galaxies with faint UV continuum magnitudes ($0.06L^* < L < 0.34L^*$, corresponding to $25.5 < V < 27.5$) and LBGs represent brighter galaxies ($L > 0.34L^*$). However, the fact that our data show no change in average LAE NB3420$-V$ color across a range in V magnitude (Figure 2.10) supports the idea that LAEs are a population of galaxies with properties distinct from those of LBGs, and

not simply faint LBG-analogs. This scenario is described by the LAE-dependent model, in which LAEs are assumed to comprise 23% of the LBG population (see Nestor et al., 2013), galaxies identified both as LBGs and LAEs are treated as LAEs, and the luminosity function is integrated over the full luminosity range ($0.06L^* < L < \infty$) for both LBGs and LAEs. Based on the values of $(F_{UV}/F_{LyC})_{corr}$ derived for the HS1549 field, $\epsilon_{LyC} = 15.0 \pm 6.7 \times 10^{24}$ ergs s^{-1} Hz^{-1} Mpc^{-3} for the luminosity-dependent model and $\epsilon_{LyC} = 8.8 \pm 3.5 \times 10^{24}$ ergs s^{-1} Hz^{-1} Mpc^{-3} for the LAE-dependent model. The uncertainties in ϵ_{LyC} reflect only uncertainties in $(F_{UV}/F_{LyC})_{corr}$, which dominate over uncertainties in the luminosity function. Our values of ϵ_{LyC} are roughly half of those calculated by Nestor et al. (2013) for star-forming galaxies in the SSA22a field: $\epsilon_{LyC}^{SSA22a} = 32.2^{+12.0}_{-11.4} \times 10^{24}$ ergs s^{-1} Hz^{-1} Mpc^{-3} for the luminosity-dependent model and $\epsilon_{LyC}^{SSA22a} = 16.8^{+6.9}_{-6.5} \times 10^{24}$ ergs s^{-1} Hz^{-1} Mpc^{-3} for the LAE-dependent model. In Table 2.7, we summarize the contributions to ϵ_{LyC} as determined from galaxies in the HS1549 field.

To place these values of ϵ_{LyC} for star-forming galaxies in context, we can compare to values of the total ionizing emissivity (ϵ_{LyC}^{tot}) derived from Lyα-forest studies, which represent an upper bound on the ionizing emissivity from star-forming galaxies. Using the formulation described in Nestor et al. (2011), we define ϵ_{LyC}^{tot} to be

$$\epsilon_{LyC}^{tot} = \frac{\Gamma_{\rm HI}\, h\, (3 - \alpha_s)}{\sigma_{\rm HI}\, \lambda_{\rm mfp}\, (1+z)^3} \tag{2.5}$$

where $\Gamma_{\rm HI}$ is the total hydrogen photoionization rate in the IGM at $z = 2.85$ (measured by Lyα-forest studies), h is Planck's constant, α_s is the power-law index of the UV spectral slope in the LyC region ($f_\nu \propto \nu^{\alpha_s}$; we adopt $\alpha_s = -3$), $\sigma_{\rm HI} = 6.3 \times 10^{-18}$ cm^2 is the atomic hydrogen photoionization cross section, and $\lambda_{\rm mfp} = 100$ Mpc is the ionizing photon mean free path through the IGM at $z = 2.85$ (Rudie et al., 2013; Faucher-Giguère et al., 2008; Songaila & Cowie, 2010). Using $\Gamma_{\rm HI} = 0.92 \times 10^{-12}$ s^{-1} inferred from Bolton & Haehnelt (2007), we derive the total ionizing photon emissivity at $z = 2.85$ to be $\epsilon_{LyC}^{tot} = 9.8 \pm 4.1 \times 10^{24}$ ergs s^{-1} Hz^{-1} Mpc^{-3}. Using $\Gamma_{\rm HI} = 0.53 \times 10^{-12}$ s^{-1} inferred from Faucher-Giguère et al. (2008), we derive $\epsilon_{LyC}^{tot} = 5.6 \pm 1.6 \times 10^{24}$ ergs s^{-1} Hz^{-1} Mpc^{-3}. Estimates of the contribution of QSOs

to the ionizing background at $z = 2.85$ are lower, and range from $\epsilon_{LyC}^{QSO} \sim 1.5 \times 10^{24}$ ergs s^{-1} Hz^{-1} Mpc (Cowie et al., 2009) to $\epsilon_{LyC}^{QSO} \sim 5.5 \times 10^{24}$ ergs s^{-1} Hz^{-1} Mpc (Hopkins et al., 2007). Within their errors, the values of ϵ_{LyC} that we report for star-forming galaxies in the HS1549 field are consistent with the inferred total ionizing emissivity from the Lyα-forest studies. This agreement between the total ionizing emissivity and the ionizing emissivity from star-forming galaxies leaves little room for the contribution to the emissivity from QSOs or from fainter star-forming galaxies not probed by our observations. Although the LyC emissivity we measure from star-forming galaxies may still be an overestimation, it is in better agreement with ϵ_{LyC}^{tot} determined from Lyα-forest studies than the higher values determined in past work (e.g., Nestor et al., 2013, 2011; Steidel et al., 2001). Even with the large uncertainties in ϵ_{LyC}^{tot}, ϵ_{LyC}^{QSO}, and ϵ_{LyC}^{gal}, our results may point to star-forming galaxies providing the dominant contribution of ionizing photons at $z = 2.85$.

2.6 Properties of LyC-Emitting Galaxies

The measurements of the ionizing to non-ionizing flux-density ratios of the galaxies in our samples point to a large spread in the amount of LyC emission escaping from galaxy to galaxy. While the majority of galaxies in our sample ($\sim$90%) appear to have no leaking LyC radiation, the remaining 10% exhibit very blue NB3420$-V$ colors, indicating a high escape fraction. Two possible scenarios may describe our data. One possibility is that galaxies with and without observed LyC emission have an intrinsically different physical property governing whether LyC radiation escapes from or is absorbed by the ISM. A second possibility is that LyC emission escapes from all star-forming galaxies, but only over a small solid angle where neutral hydrogren has been cleared away (e.g., by stellar winds or supernovae). In this section, we explore the differential properties of galaxies with and without observed LyC radiation, with the goal of distinguishing between these two scenarios. Specifically, we examine the rest-frame near-infrared properties of both LBGs and LAEs and the Lyα equivalent widths of the LAEs. The ultimate goal is to be able to identify galaxies associated with strong LyC emission by some other galactic property and search for analogs to such

galaxies at higher redshifts, in regimes where the IGM is opaque to LyC photons.

2.6.1 Rest-frame Near-Infrared Properties of LyC-emitting Galaxies

In addition to the optical and near-UV data in the HS1549 field, there exists imaging in several infrared bands. A small fraction of our objects lie in the footprint of the *HST*/WFC3 *F*160*W* image (rest-frame 4150Å) and the *Spitzer*/IRAC Channels 1 and 3 images (*Ch1*, 3.6 μm; *Ch3*, 5.8 μm; *Spitzer* program G03, PI: Steidel) corresponding respectively to rest-frame 0.9μm and 1.5μm. The entire field has been imaged by Palomar/WIRC in J and K (rest-frame 3250Å and 5700Å, respectively) and *Spitzer*/IRAC Channels 2 and 4 (*Ch2*, 4.5 μm; *Ch4*, 8 μm) corresponding respectively to rest-frame 1.2μm and 2.1μm. As the *Ch2* image is the deepest of these images, we focus our subsequent analysis on *Ch2*. In the deepest part of the mosiacs, the *Ch2* image has an exposure time of 18500 seconds and a 3σ limiting magnitude of 24.0 (AB). The typical *Ch2* IRAC PSF FWHM ($\sim$2.″5) is significantly larger than the seeing in the LRIS optical imaging. All of the LBG and LAE targets lie within the footprint of the *Ch2* image, and the majority lie within the deepest, central regions. We performed PSF-fitting photometry of the LBGs and LAEs in the *Ch2* image using procedures described in Reddy et al. (2006a). Results of the photometry indicate that 24 out of the 48 LBGs are detected in *Ch2* at the 3σ level, while there are *Ch2* detections for only 7 out of the 90 LAEs (2 of the 7 LAEs are also LBGs). The median limits in *Ch2* magnitude and $V-Ch2$ color for the nondetections are $Ch2>24.0$ and $V-Ch2<0.7$ for LBGs, and $Ch2>24.0$ and $V-Ch2<2.1$ for LAEs.

In order to understand the typical properties of LBG stellar populations in the HS1549 field, we obtained SED fits for each LBG with at least one infrared datapoint. While all 48 of the LBGs in our sample have U, G, and $\mathcal{R}$ photometry, only 33 of these also have detections in one or more infrared bands (J, K, $F160W$, and/or IRAC $Ch1-Ch4$). For these 33 objects, we derived SED fits based on the Bruzual & Charlot (2003) models using a Chabrier initial mass function (IMF). Following Reddy et al. (2012), we adopted constant star-formation rate models, the Calzetti et al. (2000) dust attenuation curve, and 50 Myr

lower limits in age (representing the typical LBG dynamical timescale). The ages of the galaxies range from 50 to 2200 Myr, with a median age of 202 Myr. Roughly one third of the sample was assigned the lowest allowed age value (50 Myr). The star-formation rates (SFRs) range from 5 to 214 $M_\odot$ yr^{-1}, with a median SFR of 43 $M_\odot$ yr^{-1}. The stellar masses range from $\log(M/M_\odot) = 9$ to $\log(M/M_\odot) = 11$ with a median of $\log(M/M_\odot) = 9.8$. Finally, the values of $E(B-V)$ range from 0 to 0.31, with a median value of 0.2. These values agree well with typical values of LBG properties quoted in the literature (e.g., Kornei et al., 2010). The 15 LBGs without IRAC photometry ($\sim$30% of our sample) for which SED fits could not be calculated are most likely undetected in IRAC bands because of their lower stellar mass and dust content. Thus, the inclusion of these objects would likely change the average distributions of SED fit parameters. A similar bias exists in the average LBG properties reported by Kornei et al. (2010); of the 321 $z \sim 3$ LBGs in their sample, roughly 25% of these LBGs did not have photometric detections redward of the Balmer break, and were therefore not modeled with SED fits. Out of the 33 LBGs in our sample that were modeled with SED fits, only one (MD34) has an NB3420 detection. The SED fit to MD34 produced the following values: age = 50 Myr (the minimum allowed), SFR = 137 $M_\odot$ yr^{-1}, $\log(M/M_\odot) = 9.8$, $E(B-V) = 0.28$. While it is not possible to draw conclusions about the global population of LBGs emitting LyC based on only one object, we note that MD34 has been assigned the lowest possible age allowed by our modeling and the second largest SFR of the 33 modeled galaxies.

Because only a fraction of the LBGs and LAEs have sufficient infrared photometry to obtain SED fits, we use $V-Ch2$ colors and limits to constrain the range of possible stellar populations of our full sample of galaxies. For galaxies at $z \sim 2.85$, the V and *Ch2* filters lie on either side of the Balmer Break and thus are a direct probe of the stellar mass-to-light ratio of the galaxy. Thus, we can convert $V-Ch2$ colors to stellar masses by assuming a range of values for $E(B-V)$ and using $V-$band imaging to estimate galaxy luminosty. We present a $V-Ch2$ vs. V color-magnitude diagram in Figure 2.11. Photometry for individual LBGs and LAEs is plotted for objects with and without NB3420 detections along with curves of constant stellar mass for various assumptions of $E(B-V)$. In the sample of LBGs, there

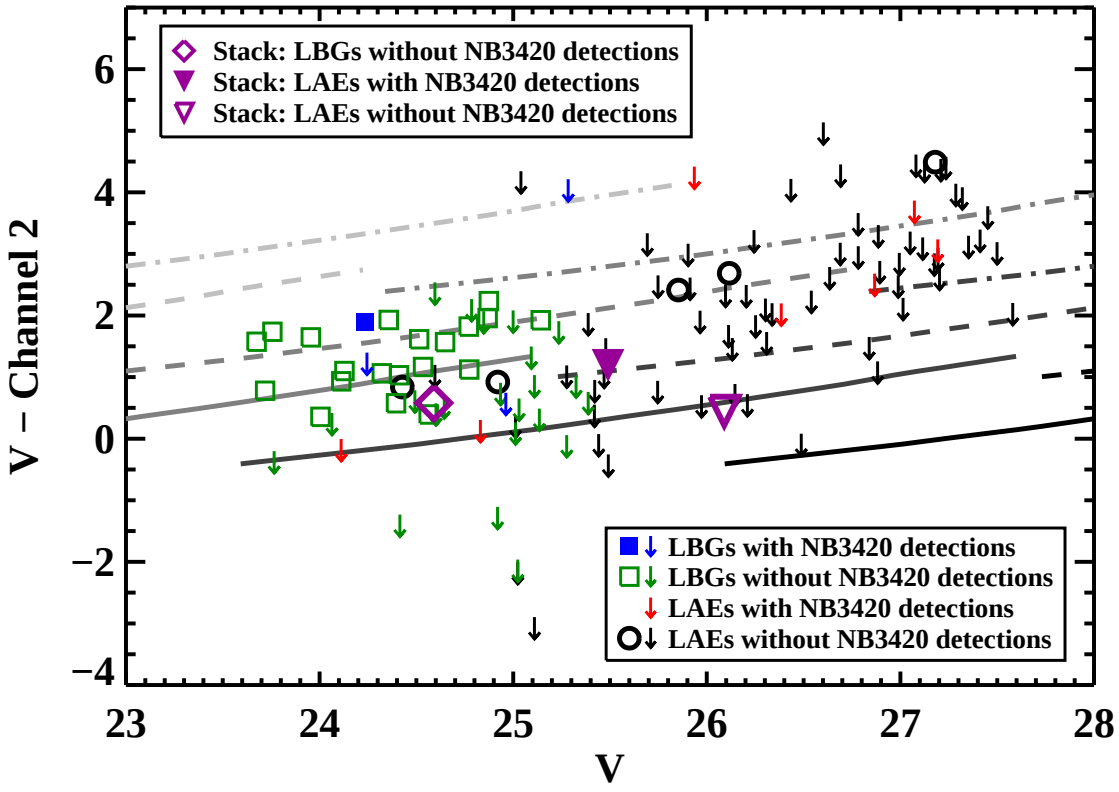

Figure 2.11 Color-magnitude diagram plotting $V-Ch2$ color against V magnitude for LBGs and LAEs with detections in V. Individual LBGs are plotted using filled blue squares for objects with NB3420 detections and open green squares for objects without NB3420 detections. LAEs without NB3420 detections are plotted with open black circles, and the two LAE detections brightest in V are also LBGs. Objects undetected in *Ch2* are plotted as 3σ upper limits in $V-Ch2$ color following the color scheme for the detected objects. All LAEs with NB3420 detections are undetected in *Ch2*; the upper limits on these objects are indicated by red arrows. The open purple diamond represents the color of the LBG stack of NB3420 non-detections. The filled (open) purple inverted triangle represents the upper limit in $V-Ch2$ color for the stack of LAEs with NB3420 detections (non-detections). Gray curves indicate lines of constant stellar mass, with $M_{stellar} = 10^8\,M_\odot$, $10^9\,M_\odot$, $10^{10}\,M_\odot$, and $10^{11}\,M_\odot$ shown in black, dark gray, medium gray, and light gray respectively. Values of $E(B-V)$ are indicated by solid, dashed, and dot-dashed lines, corresponding to $E(B-V)$= 0.0, 0.15, and 0.3, respectively. The curves of constant mass are produced by a Bruzual & Charlot (2003) SED fit to a $z = 2.85$ galaxy using a Chabrier IMF. The length of each curve corresponds to ages ranging from 50 Myr to 2300 Myr (the age of the universe at $z = 2.85$).

is only one galaxy (MD34) with both a *Ch2* detection and an NB3420 detection; MD34 does not differ significantly from the other *Ch2*-detected LBGs in its $V-Ch2$ vs. V properties. In the sample of LAEs, there only five objects with both *Ch2* and V detections, none of which have NB3420 detections. While we cannot make any strong statements comparing the $V-Ch2$ properties of LAEs with and without NB3420 detections, we can note that the limits of LAEs with NB3420 detections do not distinguish them from LAEs without NB3420 detections. Deeper *Ch2* data is necessary to make any stronger inferences. The preliminary results from this analysis seem to show no strong differences between the stellar populations of galaxies with and without NB3420 detections, implying that the detection of LyC emission from a small portion of galaxies stems from the effect of varying observer perspective with respect to the geometry of the ISM of each galaxy, rather than intrinsic physical differences between galaxies. According to such a scenario, galaxies are described by a constant escape fraction that appears to vary between objects based on the perspective of the observer. Another important feature of Figure 2.11 is that the curves of constant stellar mass indicate that the $V-Ch2$ limits of nearly all the LAEs are consistent with $M_{stellar} < 10^{10}$ $M_{\odot}$ galaxies with $E(B-V) \lesssim 0.3$. A notable outlier is *lae1843*, the LAE with $V-Ch2 > 4$. *Lae1843* is not located near an obvious contaminant in any of our images, but there is still the possibility of a very red foreground galaxy not visible in the shorter-wavelength images or a foreground galaxy in those images that cannot be distinguished from *lae1843* at the current spatial resolution.

Because the *Ch2* data are not deep enough to characterize the individual rest-frame near-infrared properties of all of our target galaxies, we also performed photometry on stacked images of galaxies with and without LyC detections for the LBG and LAE samples. The stacks were created using methods similar to those described in Appendix D of Reddy et al. (2012), with the requirement that objects included in the stack not be blended with a nearby neighbor in the *Ch2* image. $V-Ch2$ colors of the LBG and LAE stacks are plotted in Figure 2.11. We use stellar population synthesis models to estimate masses from the stacked photometry; while this method is not necessarily equivalent to reporting the average properties of individual SED fits, it provides rough insights into the relative properties of

different subsamples in the absence of SED fits for every object in our sample.

Unfortunately, it is not possible to draw definitive conclusions from the LBG stacks. While the stack of LBGs without NB3420 detections yields a *Ch2* magnitude of 24.01 ± 0.10 and $V-$ *Ch2* $= 0.58$, we were unable to make a useful stack for the LBGs with NB3420 detections because two of the four objects are blended with bright neighbors in the *Ch2* image. Of the two LBGs with NB3420 detections and unblended *Ch2* photometry, MD34 has a magnitude of 22.34 ± 0.12 and MD5 has a 3σ lower limit of >24.22. While the *Ch2* photometry of MD34 and MD5 is consistent with that of the LBGs undetected in NB3420, the small sample size precludes us from making any comparisons between objects with and without LyC detections. We can also compare the LBG properties determined by $V-$*Ch2* color to those determined by the SED fits. The $V-$*Ch2* color of the stack of LBGs without NB3420 detections implies $\log(\mathrm{M}/\mathrm{M}_{\odot}) = 9.60$ (9.10), assuming $E(B-V) = 0.0$ (0.1). Higher values of $E(B-V)$ imply younger galactic ages, and assumptions of $E(B-V) > 0.1$ do not result in meaningful fits to the stacked color because they imply ages <50 Myr. The assumption of $E(B-V) = 0.1$ requires an age of ~ 60 Myr, significantly younger than the median age derived for the sample of LBGs with SED fits (202 Myr). However, LBGs have been shown to have typical reddening values of $E(B-V) \sim 0.17$ (Kornei et al., 2010), and assuming such a value further decreases the average age implied by the stacked photometry. This apparent discrepancy (i.e., the fact that the median age implied by the stacks is lower than that implied by the SED fits) arises because the stacks include all LBGs regardless of whether or not they are detected in *Ch2*, while the SED fits only include the older or more massive LBGs with IRAC photometry redwards of the Balmer break. We can further demonstrate this discrepancy by contrasting the $V-$ *Ch2* color of the stack of all LBGs without LyC detections ($V-$ *Ch2* $= 0.58$) with the average $V-$ *Ch2* color of the objects in that stack that have *Ch2* detections ($V-$ *Ch2* $= 1.33$). Because the stack includes all LBGs regardless of whether or not they have infrared data, the $V-$ *Ch2* color of the stack is much bluer than the $V-$ *Ch2* color of the subset of objects within the stack that have *Ch2* detections.

In the case of the stacks of LAEs with and without NB3420 detections, neither stack

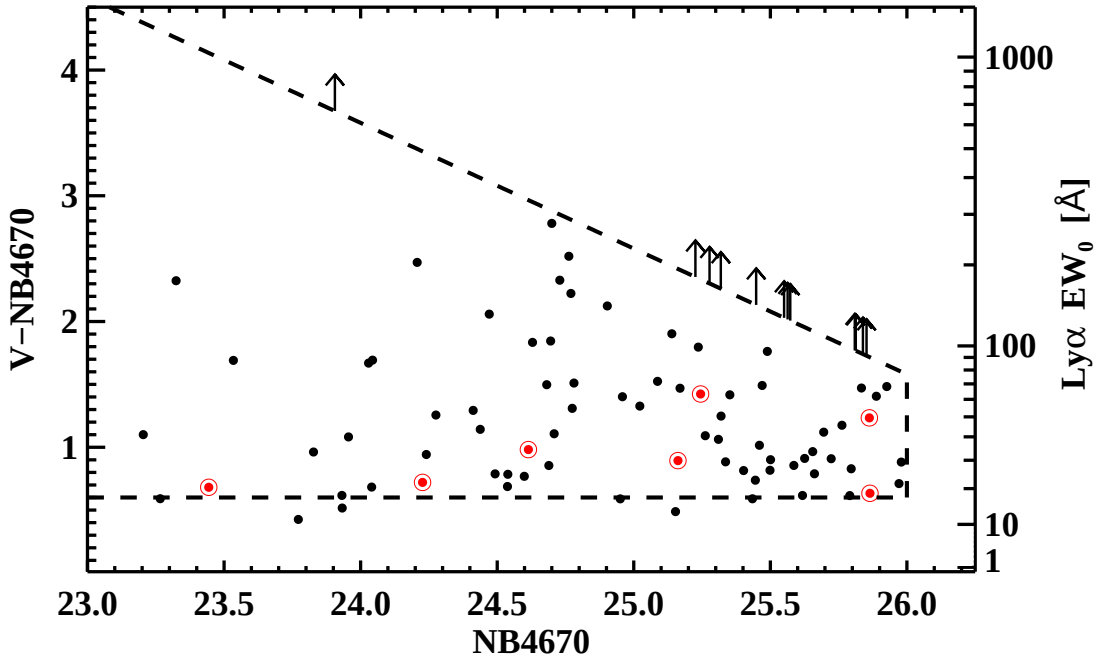

Figure 2.12 Color-magnitude diagram plotting $V-$NB4670 vs. NB4670 for LAEs. The rest-frame Lyα equivalent width corresponding to a given $V-$NB4670 color is indicated on the right-hand axis. Galaxies without NB3420 detections are shown in black and galaxies with NB3420 detections are shown as red with a circle around each point. Lower limits correspond to objects undetected in V and follow the same color scheme as the detections. The dashed diagonal line indicates the observational limit on $V-$NB4670 color, which is determined by our $V-$band magnitude limit of 27.58. The vertical dashed line indicates the cutoff of $m_{4670} < 26.0$ applied in order to ensure the robustness of our sample (see Section 2.2.4). The horizontal dashed line corresponds to the color cut of $V - \mathrm{NB4670} > 0.6$ used for LAE selection. A few LAEs fall below this line because they were selected as LAEs on the basis of earlier, shallower photometry, and were already spectroscopically confirmed to lie at $z = 2.85$.

was detected in *Ch2*; the stacks reached 3σ limiting magnitudes of >24.30 and >25.64, respectively, corresponding to $V-Ch2 < 1.19$ and $V-Ch2 < 0.45$. While these limits on LAE $V-Ch2$ color do not give any constraints on the differential properties between LAEs with and without NB3420 detections, they do indicate that LAEs are preferentially low-mass galaxies with small values of $E(B-V)$. Converting the limits on LAE $V-Ch2$ color into limits on stellar mass results in $\log(M/M_{\odot}) < 9.72$ (9.38) for LAEs with NB3420 detections and $\log(M/M_{\odot}) < 8.87$ (8.35) for LAEs without NB3420 detections, assuming $E(B-V) = 0.0$ (0.1). The $E(B-V) = 0.1$ fit to the deeper LAE stack (LAEs without NB3420 detections) corresponds to an age slightly less than 50 Myr. While such a young age is unphysical for LBGs based on dynamical timescale arguments, LAEs may be more compact systems where such young ages are feasible; such young ages have been determined for LAEs in previous work (Gawiser et al., 2007).

In summary, the analysis of the infrared data does not yield firm results differentiating between the two proposed models of LyC escape presented at the beginning of this section: that objects with and without LyC detections are either intrinsically different, or intrinsically similar with anisotropic emission of LyC radiation. Although the individual galaxies and stacks plotted in Figure 2.11 do not indicate strong differences in the $V-Ch2$ properties of galaxies with and without LyC emission, the fact that only one galaxy (MD34) with an NB3420 detection is actually detected in *Ch2* severely limits our interpretation of the *Ch2* data. At the same time, we find that MD34 (the only object with a LyC detection modeled by an SED fit) has been assigned the lowest possible age allowed by our modeling and the second largest SFR of the 33 modeled LBGs. A larger sample of LBGs with both LyC detections and IRAC photometry is needed to test whether or not LBGs with LyC detections are preferentially young. In terms of the overall sample properties, the $V-Ch2$ color of our LBG stacks (which include all LBGs in the sample) indicate an age for LBGs that is younger than the median age of LBGs modeled with SED fits, suggesting a possible bias in previous LBG stellar population studies (e.g., Shapley et al., 2001; Kornei et al., 2010) limited to objects with near- or mid-infrared detections. Finally, the $V-Ch2$ colors and limits we observe for the LAEs in our sample indicate that they are preferentially low-mass

galaxies with small values of $E(B-V)$, consistent with previous results in $z \sim 3$ LAE stellar population studies. The two obstacles hindering our understanding of the rest-frame near-infrared properties of the galaxies in our sample are the low *Ch2* detection rate of both LBGs and LAEs and the lack of spatial resolution, resulting in the blending of several galaxies with bright nearby neighbors. Deeper and higher resolution data enabling robust SED fits for all galaxies in our sample would constitute a much more powerful tool to distinguish between the proposed models of LyC escape.

2.6.2 The relationship between LyC emission and Lyα emission

In addition to exploring the differential rest-frame UV − near-infrared colors of galaxies with and without LyC emission, we studied their relative Lyα properties. Figure 2.12 shows the $V-$NB4670 vs. NB4670 color-magnitude diagram for LAEs with and without NB3420 detections (shown in red and black, respectively), indicating the rest-frame Lyα equivalent width (EW) on the right-hand axis. Although the LAEs with NB3420 detections have lower measured values of Lyα EW on average than LAEs without NB3420 detections, they span a range in NB4670 magnitude equivalent to that of the full LAE sample. In order to account for the fact that for several LAEs the measured EWs are only lower limits, we used the package ASURV ("*A*stronomy *SURV*ival *A*nalysis") Rev 1.2 (Isobe & Feigelson, 1990; Lavalley et al., 1992) to calculate the Lyα EW mean and standard error of LAEs with and without NB3420 detections using survival analysis. This analysis shows that the mean Lyα EW for objects with NB3420 detections is 34.0 ± 5.9 Å and the mean Lyα EW for objects without NB3420 detections is 80.1 ± 8.3 Å. These results confirm that galaxies with NB3420 detections tend to have lower Lyα EWs, on average, than galaxies without NB3420 detections, a correlation that has been previously reported in the SSA22a field by Nestor et al. (2011).

In testing the connection between Lyα and LyC emission, we must also consider changes in LyC emission when Lyα EW is the independent variable. To determine if $(F_{UV}/F_{LyC})_{corr}$ is positively correlated with Lyα EW, we calculated $(F_{UV}/F_{LyC})_{corr}$, the non-ionizing to ionizing flux-density ratio corrected for contamination and IGM absorption, for LAEs in two

bins of Lyα EW separated by the mean LAE Lyα EW (46 Å). For LAEs with smaller and larger EWs, respectively, we find $(F_{UV}/F_{LyC})_{corr}^{\mathrm{EW}\leq 46\mathring{\mathrm{A}}} = 4.9 \pm 2.6$ and $(F_{UV}/F_{LyC})_{corr}^{\mathrm{EW}>46\mathring{\mathrm{A}}} = 33 \pm 23$; LAEs with lower EWs have smaller values of $(F_{UV}/F_{LyC})_{corr}$ (indicating stronger LyC emission) and LAEs with larger EWs have larger values of $(F_{UV}/F_{LyC})_{corr}$. These two values are consistent with the results of the survival analysis: LAEs with LyC detections are characterized by a smaller average Lyα EW than those without LyC detections.

One explanation of the observed anticorrelation between Lyα EW and LyC emission strength consists of the fact that Lyα photons are simply reprocessed LyC photons. As a LyC photon propagates through the ISM of a galaxy, one possibility is that the photon escapes without being absorbed by a neutral hydrogen atom, and LyC emission is observed from the galaxy. A second possibility is that the photon encounters a neutral hydrogen atom and is absorbed, ionizing the atom. When the free electron recombines with the hydrogen ion, the emission cascade spectrum will often culminate in the release of a Lyα photon. Thus, for a fixed production rate of LyC photons, galaxies with larger Lyα EWs should tend to exhibit less LyC emission.

The fact that the stellar populations of galaxies with and without LyC detections do not appear to differ significantly (see Section 2.6.1) suggests that detecting LyC in a given galaxy depends on the orientation of the galaxy with respect to the observer. If the hypothesis that LyC detectability depends on observer orientation is correct, then the anticorrelation between observed LyC and Lyα emission implies that Lyα EW must also depend on orientation, and in such a way to support the anticorrelation. Results from several recent galaxy simulations (of both isolated galaxies and those set in cosmological context) suggest that the observed Lyα EW is strongly dependent on the orientation of the observer (Verhamme et al., 2012; Barnes et al., 2011; Yajima et al., 2012). Specifically, these simulations predict orientation effects for disk galaxies: a disk galaxy, when viewed face-on, will have a much greater observed Lyα EW than the same galaxy viewed edge-on. This orientation effect stems from the fact that Lyα photons are resonantly scattered; for a Lyα photon, the direction of final escape from the galaxy is nearly independent of its original trajectory. As trajectories perpendicular to the plane of the galaxy present the paths of least opacity, more Lyα photons will escape

perpendicular to the galactic plane. It is still unclear how the spatial redistribution of Lyα photons relates to that of LyC photons, and how these distributions are affected by the clumpy morphologies of high-redshift galaxies. If, for example, Lyα and LyC photons are both more likely to escape along lines of sight with lower hydrogen column densities, a positive correlation between observed Lyα and LyC emission might be expected − contrary to the anticorrelation observed in the LAE populations of the HS1549 and SSA22a fields. In any case, it would be extremely useful for simulations to examine the effect that galaxy orientation produces on the relationship between observed Lyα and LyC emission. It would also be useful for such simulations to consider morphologies that more closely represent those of high-redshift galaxies (i.e., clumpy and irregular morphologies; Law et al., 2007). If orientation effects *cannot* explain the observed trend that smaller observed Lyα EWs in LAEs coincide with more LyC emission, then the difference in Lyα EWs must indicate some intrinsic difference between galaxies exhibiting strong or weak LyC emission that can be traced by Lyα emission. Along these lines, we note that the mean rest-frame Lyα EW for LAEs without NB3420 detections (80 Å) is close to that expected by the "Case B" assumption for 100% absorption of LyC photons in a dust-free environment ($\sim$100 Å; Steidel et al., 2011). In the presence of dust, the resonant scattering of Lyα photons would tend to decrease the expected "Case B" Lyα EW. If Lyα orientation effects do not correlate with LyC in the manner described above, then the larger Lyα EWs in our sample of LAEs without NB3420 detections indicates a higher rate of LyC absorption within the ISM of these objects.

Also relevant for understanding the connection between Lyα and LyC emission, we find a lower average non-ionizing to ionizing UV flux-density ratio among LAEs (which have a median Lyα EW of 46 Å) than among LBGs (which have a much lower median Lyα EW of 5 Å). Considering LAEs in the same magnitude range as LBGs ($V < 25.4$), we derive $(F_{UV}/F_{LyC})_{corr}^{LAE,V<25.4} = 4.1 \pm 2.7$ which is significantly lower than the value for LBGs, $(F_{UV}/F_{LyC})_{corr}^{LBG} = 82 \pm 45$. The relative values of $(F_{UV}/F_{LyC})_{corr}$ for LAEs and LBGs apparently suggest a *positive* correlation between Lyα EW and LyC emission, in the opposite sense of the trend traced by the LyC vs. Lyα emission properties of LAEs. However, LBGs have been shown to differ from LAEs in several galactic properties, including dust content

and gas/dust covering fraction. As dust destroys UV photons, and Lyα photons travel particularly long path lengths before they escape their galaxy due to resonant scattering, Lyα photons suffer greater dust attenuation than other UV photons. Thus, while the amount of dust in a galaxy will not affect the creation of Lyα photons from LyC photons, it will affect the observed Lyα EW. Observational studies have confirmed that LBGs with larger Lyα EWs have smaller values of $E(B-V)$ (e.g., Atek et al., 2009; Shapley et al., 2003) and simulations have reproduced the same result (e.g., Yajima et al., 2012; Dayal et al., 2009). Also, LBGs with larger Lyα EWs have weaker interstellar absorption lines, indicating lower gas covering fraction (Shapley et al., 2003). Thus, it is possible that the low median Lyα EW observed in LBGs compared to LAEs is due to increased dust attenuation (LBGs have median values of $E(B-V)$ that are typically higher than those of LAEs; Gronwall et al., 2007; Blanc et al., 2011) and larger gas covering fraction. In summary, the observed strengths of Lyα and LyC emission may be anti-correlated (as seen in the LAE sample) except in the cases of higher interstellar extinction where Lyα photons are systematically destroyed (as in the case of the LBGs).

2.7 Summary

We have presented an analysis of the $z \sim 3$ LyC properties of the HS1549 field. Multiple LyC studies of star-forming galaxies have been conducted in the SSA22a field (e.g., Inoue et al., 2005; Shapley et al., 2006; Iwata et al., 2009; Nestor et al., 2011, 2013) and HS1549 therefore provides an important independent set of $z \sim 3$ LyC measurements. The HS1549 field contains a galaxy protocluster at $z = 2.85$, and our narrowband (NB3420) imaging has targeted the LyC spectral region of 131 spectroscopically confirmed galaxies at $z \geq 2.82$ (49 LBGs and 91 LAEs, 9 of which are constituents of both samples). We have detected 12 galaxies in NB3420 and implemented simulations to correct the average NB3420 magnitudes of subsamples of these galaxies for both foreground galaxy contamination and absorption from neutral hydrogren in the IGM. In addition to more than 19 hours of imaging in the NB3420 filter, we have analyzed ancillary narrowband Lyα imaging and broadband imaging

in the rest-frame non-ionizing UV, optical, and near-infrared in order to determine non-ionizing to ionizing UV flux-density ratios and place limits on other galactic properties. Our main conclusions are as follows:

1. We find 4 LBGs and 7 LAEs with NB3420 detections, along with one additional object (MD12/*lae3540*) that we have removed from both samples. The NB3420 detections of the LBGs range in magnitude from $26.56 \leq m_{3420} \leq 27.01$ and those of the LAEs range from $25.11 \leq m_{3420} \leq 27.23$. Our contamination simulations predict that 1.5 ± 1.0 LBG NB3420 detections and 4.3 ± 1.3 LAE NB3420 detections are uncontaminated by foreground galaxies.

2. The ratio of non-ionizing to ionizing UV radiation of the LBGs and LAEs is traced by the observed NB3420$-V$ color. The colors of our targets vary widely, with NB3420-detected galaxies at a given V magnitude having NB3420 magnitudes up to a factor of ten brighter than the NB3420 limits of undetected galaxies; i.e., a small percentage of galaxies are detected strongly in NB3420 and the rest remain undetected. These results confirm those presented in Nestor et al. (2011) for galaxies in the SSA22a field, and lend further support to the hypothesis that LyC radiation escapes galaxies through cleared holes in the ISM and can only be viewed by the observer with fortuitous orientation. The large variation in individual galaxy NB3420 properties makes it necessary to consider properties of the full ensemble of LBGs and LAEs in order to determine the average LyC properties of $z \sim 3$ galaxies.

3. One of the principal difficulties in performing accurate LyC photometry is the presence of low-redshift foreground galaxies that introduce contaminating light into the NB3420 filter. At the spatial resolution of *HST*, galaxies at $z \sim 3$ tend to exhibit clumpy morphology. Separating a $z \sim 3$ clump from a foreground contaminant is impossible unless the individual redshifts of each clump are known. While simulations of the amount of foreground contamination can help correct the observed non-ionizing to ionizing UV flux-density ratios, it is very difficult to study the properties of LyC-emitting galaxies when the simulations predict that roughly half of the NB3420-detected sample may

be contaminated. To obtain spectroscopic or photometric redshifts at the high spatial resolution necessary to distinguish each clump requires imaging from a high-resolution, space-based observing facility such as *HST* coupled with deep, high-resolution spectroscopy from the ground.

4. Reconciling the low observed non-ionizing to ionizing UV flux-density ratios (F_{UV}/F_{LyC}) with intrinsic values predicted by stellar population synthesis models has been a challenge in all $z \sim 3$ LyC studies. As in the SSA22a field, the observed flux-density ratios of many of the LBGs and LAEs with putative LyC detections are too low to be reasonably explained by current models. There are possible ways of solving the problem; for example, one could make the assumption of no IGM absorption along the line of sight for galaxies with observed LyC detections. However, this condition is unlikely to hold for all galaxies with putative LyC detections. As of now, the discrepancy between the LyC observations and models remains unresolved.

5. Using estimates of the UV escape fraction from observational studies of $z \sim 3$ galaxies and a range of estimated values for the theoretical ratio of intrinsic UV to LyC luminosities given by the Bruzual & Charlot (2003) and BPASS (Eldridge & Stanway, 2009) models, we derive relative LyC escape fractions of $f_{esc,\,rel}^{LBG} = 5 - 8\%$ and $f_{esc,\,rel}^{LAE} = 18{-}49\%$, and absolute escape fractions of $f_{esc}^{LBG} = 1{-}2\%$ and $f_{esc}^{LAE} = 5{-}15\%$. The uncertainties on the escape fractions we calculate are on the order of 50%. We also determine a comoving specific ionizing emissivity of LyC photons (ϵ_{LyC}) in the range of $8.8 - 15.0 \times 10^{24}$ ergs s^{-1} Hz^{-1} Mpc^{-3}. This range of emissivity values was determined by using two different models to combine the LBG and LAE samples (as discussed in Section 2.5.3); the luminosity-dependent model yields $\epsilon_{LyC} = 15.0 \pm 6.7 \times 10^{24}$ ergs s^{-1} Hz^{-1} Mpc^{-3} and the LAE-dependent model yields $\epsilon_{LyC} = 8.8 \pm 3.5 \times 10^{24}$ ergs s^{-1} Hz^{-1} Mpc^{-3}. These values of ϵ_{LyC} for star-forming galaxies are consistent with the total ionizing emissivity inferred from the Lyα-forest studies of Bolton & Haehnelt (2007) and Faucher-Giguère et al. (2008). The rough agreement between the total ionizing emissivity and the ionizing emissivity from star-forming galaxies leaves little

room for the contribution to the emissivity from QSOs or from fainter star-forming galaxies not probed by our observations. While the LyC emissivity we measure from star-forming galaxies may still be an overestimation, it is in better agreement with the total LyC emissivity determined from Lyα-forest studies than the higher values determined in past work.

6. Examining the rest-frame near-infrared properties of galaxies in our sample based on IRAC *Ch2* imaging, we find no significant difference in the *Ch2* or $V-Ch2$ properties of objects with and without NB3420 detections. This agreement indicates that objects with and without LyC detections are drawn from a populations of star-forming galaxies with similar distributions of stellar mass, age, $E(B-V)$, and star-formation rate. We caution, however, that our interpretation is limited by the fact that only one galaxy (MD34) with an NB3420 detection is detected in *Ch2*. While the $V-Ch2$ vs. V properties of this object do not distinguish it from LBGs without NB3420 detections, in the SED modeling, it has been assigned the lowest possible age allowed and the second largest SFR of the 33 modeled LBGs. A much larger sample of LBGs with both LyC detections and IRAC photometry is needed to test whether LBGs with LyC detections are preferentially young, or whether LBGs with and without LyC detections come from similar populations.

7. While we do not find significant differences in the stellar populations of objects with and without LyC detection, we do find that LAEs with LyC detections have smaller Lyα equivalent widths on average than those without. A comparison of $(F_{UV}/F_{LyC})_{corr}$ for LAEs in two bins of equivalent width yields $(F_{UV}/F_{LyC})_{corr}^{\mathrm{EW}\leq 46\mathrm{\AA}} = 4.9 \pm 2.6$ and $(F_{UV}/F_{LyC})_{corr}^{\mathrm{EW}>46\mathrm{\AA}} = 33 \pm 23$. These results imply an inverse relationship between the amount of Lyα and LyC emission observed from LAEs. One possibility is that this relationship stems from the fact that Lyα photons are reprocessed LyC photons, so an overall increase in Lyα photons must correlate with a decrease in LyC photons. The details of LyC and Lyα radiative transfer through the ISM of clumpy, high-redshift galaxies, however, are still unclear, as are the effects of varying the observer's orienta-

tion while observing Lyα and LyC emission. We also note that despite this apparent anti-correlation between the strength of Lyα and LyC emission, LBGs (which have lower median Lyα equivalent widths than LAEs) display much weaker LyC emission than LAEs in the same magnitude range. This trend may be explained by the higher dust content in LBGs systematically destroying both LyC photons and resonantly-scattered Lyα photons.

Future progress in this field is contingent upon amassing a large and well-defined sample of LyC-emitting star-forming galaxies and eradicating the possibility that LyC measurements are contaminated by foreground interlopers. A detailed, multi-wavelength analysis of such a sample would reveal definitively whether LyC-emitting objects possess specific properties that facilitate LyC escape or whether LyC emission escapes from all galaxies through randomly-oriented paths cleared through the ISM. With the goals of removing contamination and obtaining multiwavelength photometry, we are currently pursuing follow-up observations of our NB3420-detected galaxies in the HS1549 field with *HST*/WFC3.

We thank Kevin Hainline for his helpful discussions regarding our photometric simulations, Katherine Kornei for advice on the spectroscopic data reduction, and the anonymous referee for constructive suggestions. R.E.M., A.E.S., and D.B.N. acknowledge support from the David and Lucile Packard Foundation. C.C.S. acknowledges additional support from NSF grant AST-0908805 and GO-11638.01 from the Space Telescope Science Institute. We wish to extend special thanks to those of Hawaiian ancestry on whose sacred mountain we are privileged to be guests. Without their generous hospitality, most of the observations presented herein would not have been possible.

2.8 APPENDIX A: GNBs and Faint LAEs

Here we present photometry (Table 2.8) and postage stamp images (Figure 2.13) for eight additional Lyα-emitting galaxies with NB3420 detections for which we have obtained spectroscopic redshifts (see Section 2.2.3). This sample comprises three GNBs and five faint

Table 2.8. Photometry for GNBs and LAEs with $m_{4670} > 26.0$

ID	RA [a] (J2000)	Dec [a] (J2000)	z	NB4670	V	NB3420	$\Delta_{UV,\,LyC}$ [b]	$\Delta_{Ly\alpha,\,LyC}$ [c]	$\frac{F_{UV}}{F_{LyC}}_{obs}$ [d]
GNB2861	15:51:53.603	19:11:36.53	2.844	26.80	26.08	26.86	0.28	0.33	2.1 ± 1.0
GNB4769	15:51:59.873	19:08:42.73	2.849	25.30	26.54	27.33	0.34	0.52	2.1 ± 0.9
GNB5270	15:51:57.364	19:09:53.38	2.847	24.84	25.14	26.43	0.40	0.30	3.3 ± 1.0
lae1670	15:51:45.121	19:10:15.34	2.846	26.18	27.27	26.45	0.25	0.65	0.5 ± 0.1
lae3506	15:51:52.242	19:11:41.01	2.841	26.71	27.58	27.09	0.11	0.08	0.6 ± 0.3
lae3828	15:51:53.228	19:13:08.50	2.892	26.64	26.85	26.27	0.28	0.33	0.6 ± 0.3
lae5404	15:52:00.008	19:08:54.42	2.816	26.60	27.16	26.53	0.21	0.15	0.6 ± 0.3
lae7890	15:52:01.943	19:12:42.47	2.850	26.02	26.13	25.91	0.23	0.17	0.8 ± 0.3

[a]GNB and LAE coordinates are based on NB4670 centroids.

[b]Spatial offset between the centroids of V and NB3420 emission.

[c]Spatial offset between the centroids of NB4760 and NB3420 emission.

[d]Observed ratio and uncertainty in the ratio of non-ionizing UV to LyC flux-densities, inferred from the NB3420$-V$ color. This value has not been corrected for either contamination by foreground sources or IGM absorption.

LAEs ($m_{4670} > 26$). As we do not have a complete and unbiased sample of these objects, we do not include them in the main LAE sample.

2.9 APPENDIX B: Photometric LAE Sample

Here we present photometry of 33 LAE photometric candidates without spectroscopically confirmed redshifts (see Section 2.2.4). Ten of these LAEs have NB3420 detections. Table 2.9 contains photometric information for all 33 LAE photometric candidates, and Figure 2.14 displays postage stamp images for the ten candidates with NB3420 detections. While some of these NB3420 detections may be true LyC detections, the high rate of NB3420 detections in this sample may be due to the increased probability of contamination for objects without spectroscopic redshifts. For this reason, we do not include these objects in the LAE analysis.

Table 2.9. Photometry for LAE Photometric Candidates

ID	RA [a] (J2000)	Dec [a] (J2000)	NB4670	V	NB3420	$\Delta_{UV,\,LyC}$ [b]	$\Delta_{Ly\alpha,\,LyC}$ [c]	$\frac{F_{UV}}{F_{LyC}}_{obs}$ [d]
lae759	15:51:41.039	19:09:57.61	25.54	26.79	>27.30	···	···	>1.6
lae803	15:51:41.598	19:10:19.54	25.68	27.02	>27.30	···	···	>1.3
lae1043	15:51:42.623	19:13:00.70	26.00	27.07	>27.30	···	···	>1.2
lae1058	15:51:42.791	19:11:07.95	26.00	27.14	>27.30	···	···	>1.2
lae1080	15:51:42.918	19:12:33.53	25.92	26.37	26.03	0″.3	0″.4	0.7 ± 0.2
lae1569	15:51:44.416	19:08:43.92	25.16	25.84	25.51	0″.3	0″.4	0.7 ± 0.2
lae1840	15:51:45.875	19:11:55.76	25.98	27.19	>27.30	···	···	>1.1
lae1883	15:51:45.893	19:12:23.30	25.49	26.28	>27.30	···	···	>2.6
lae2278	15:51:47.324	19:12:01.54	25.77	>27.58	>27.30	···	···	···
lae2369	15:51:47.863	19:11:24.63	25.93	>27.58	>27.30	···	···	···
lae2431	15:51:48.048	19:09:04.50	25.97	>27.58	>27.30	···	···	···
lae2482	15:51:48.129	19:09:48.31	25.29	>27.58	>27.30	···	···	···
lae2664	15:51:49.090	19:11:00.51	25.52	>27.58	>27.30	···	···	···
lae2666	15:51:49.161	19:13:17.59	25.80	26.89	>27.30	···	···	>1.4
lae3038	15:51:50.091	19:09:02.19	25.74	26.25	26.44	0″.7	0″.2	1.2 ± 0.4
lae3348	15:51:51.561	19:11:20.54	25.90	26.98	>27.30	···	···	>1.3
lae3365	15:51:51.691	19:11:20.50	25.90	26.78	>27.30	···	···	>1.6
lae3616	15:51:52.218	19:08:21.79	25.10	26.96	27.17	1″.9	1″.4	1.2 ± 0.6
lae4070	15:51:54.054	19:10:26.76	25.93	27.47	25.88	0″.2	0″.1	0.2 ± 0.1
lae4079	15:51:54.023	19:10:05.98	25.19	25.71	>27.30	···	···	>4.3
lae4468	15:51:55.367	19:12:57.55	25.82	26.46	25.97	0″.6	0″.4	0.6 ± 0.2
lae5157	15:52:01.016	19:08:50.34	26.00	>27.58	>27.30	···	···	···
lae5200	15:52:01.083	19:11:25.97	25.83	27.19	26.70	0″.2	0″.1	0.6 ± 0.3
lae5252	15:52:00.519	19:08:31.67	26.00	26.38	25.72	0″.0	0″.1	0.5 ± 0.2
lae5446	15:51:58.774	19:12:46.40	25.43	26.01	>27.30	···	···	>3.3
lae5661	15:51:59.092	19:12:39.74	25.89	26.31	>27.30	···	···	>2.5
lae5665	15:51:57.738	19:12:27.59	23.96	25.31	24.78	0″.0	0″.7	0.6 ± 0.1
lae6041	15:51:57.864	19:11:14.43	25.56	25.58	>27.30	···	···	>4.9
lae6436	15:52:07.285	19:11:54.07	25.50	26.30	>27.30	···	···	>2.5
lae6510	15:52:06.976	19:12:03.51	25.80	25.94	25.41	0″.1	0″.1	0.6 ± 0.2
lae7110	15:52:02.523	19:12:07.71	25.98	26.96	>27.30	···	···	>1.4
lae7247	15:52:04.452	19:10:48.30	25.96	26.83	>27.30	···	···	>1.5
lae7642	15:52:03.478	19:12:58.32	25.26	26.20	>27.30	···	···	>2.7

[a]Coordinates for LAEs are based on NB4670 centroids.

[b]Spatial offset between the centroids of V and NB3420 emission.

[c]Spatial offset between the centroids of NB4760 and NB3420 emission.

[d]Observed ratio and uncertainty in the ratio of non-ionizing UV to LyC flux-densities, inferred from the NB3420$-V$ color. This value has not been corrected for either contamination by foreground sources or IGM absorption.

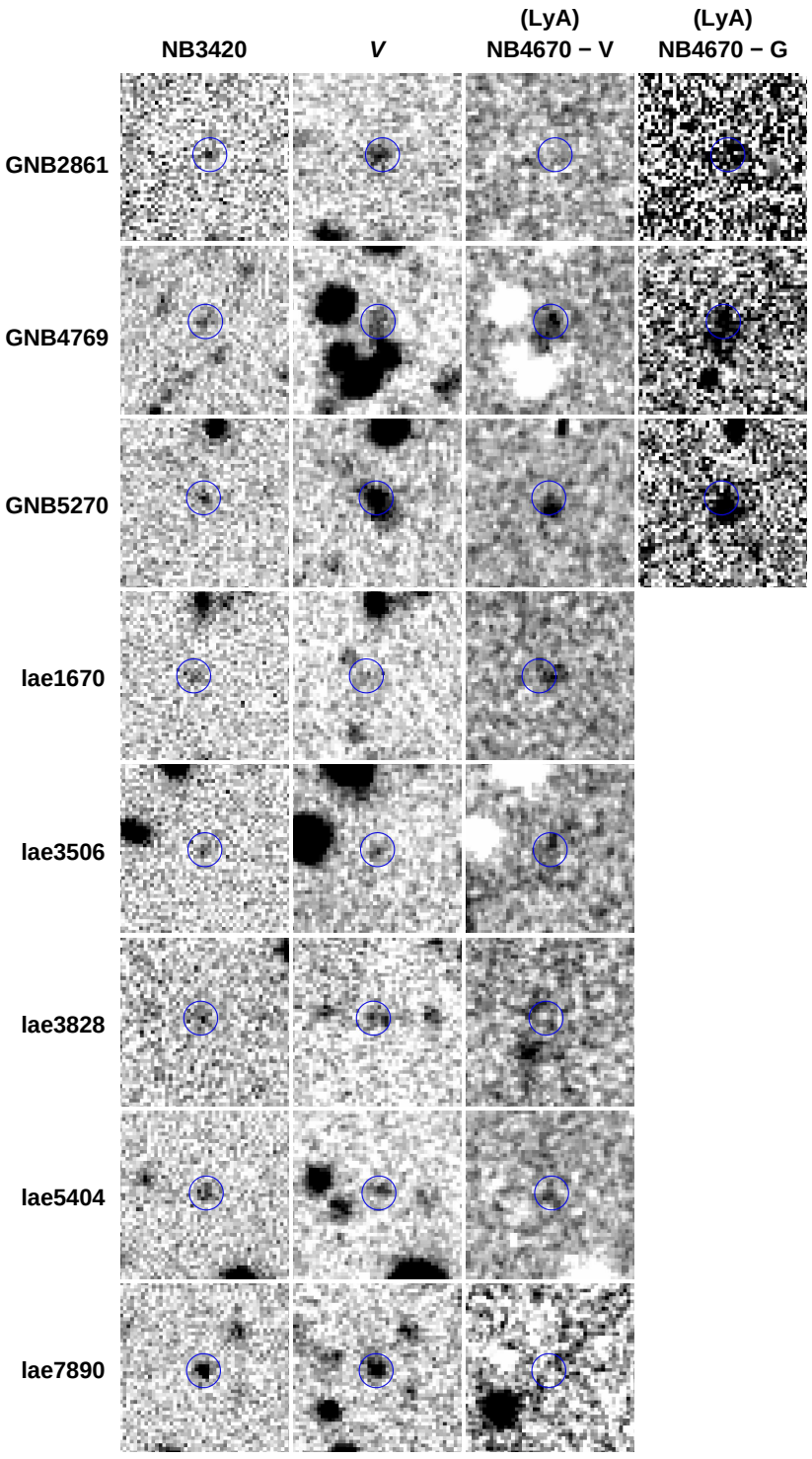

Figure 2.13 $10'' \times 10''$ postage stamp images of the three GNBs and five faint LAEs with NB3420 detections. Objects are displayed in the following bands: NB3420 (indicating the LyC), V (indicating the non-ionizing UV continuum), NB4670$-V$ (indicating Lyα emission), and NB4670$-G$ (also indicating Lyα emission; GNBs only). All postage stamps are centered on the NB4670 centroid and blue circles ($1''$radius) indicate the centroid of the NB3420 emission. All postage stamps follow the conventional orientation, with north up and east to the left.

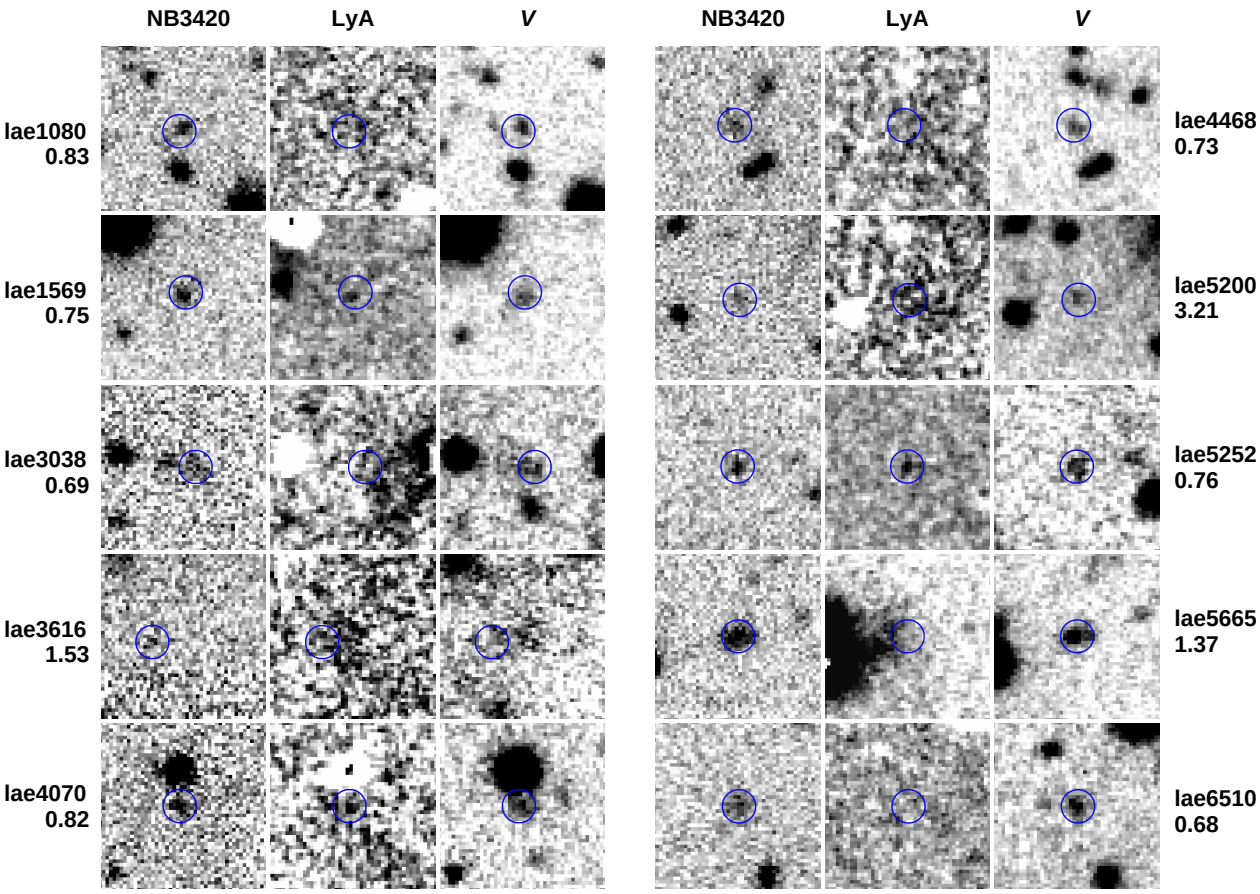

Figure 2.14 $10'' \times 10''$ postage stamp images of the 10 LAE photometric candidates with NB3420 detections. Objects are displayed in the following bands: NB3420 (indicating the LyC), NB4670$-V$ (indicating Lyα emission), and V (indicating the non-ionizing UV continuum). The $V-$NB4670 color of each LAE is indicated below the object name. All postage stamps are centered on the V centroid and blue circles ($1''$ radius) indicate the centroid of the NB3420 emission. All postage stamps follow the conventional orientation, with north up and east to the left. We note that LAEs with more diffuse Lyα emission may be difficult to distinguish in the NB4670$-V$ image, even though their $V-$NB4670 colors identify them as LAEs; for such objects, we have increased the stretch of the NB4670$-V$ image to make the diffuse emission more easily visible.

CHAPTER 3

A High-Resolution Hubble Space Telescope Study of Lyman Continuum Leakers at $z \sim 3$

3.1 Introduction

The sources responsible for cosmic reionization are still not well understood. Evidence that quasars (QSOs) cannot be solely responsible for reionization (Fontanot et al., 2012; Glikman et al., 2011; Siana et al., 2008) has prompted many searches for ionizing Lyman continuum (LyC) emission from star-forming galaxies. While the IGM at $z \gtrsim 6$ is opaque to LyC photons and prevents direct observations of LyC-emitting galaxies during the epoch of reionization, many studies have attempted to detect lower-redshift analogs to galaxies responsible for reionization. Although IGM transmission is highest in the local universe, studies at $z < 2$ (e.g., Grimes et al., 2007, 2009; Cowie et al., 2009; Bridge et al., 2010; Siana et al., 2007, 2010) have yielded very few detections of LyC emission, with only three objects identified to date (Leitet et al., 2011, 2013; Borthakur et al., 2014). At redshift $z \sim 3-4$, the search for LyC-emitting galaxies has appeared to be more fruitful. However, even though the examination of hundreds of galaxies (in works such as Steidel et al., 2001; Shapley et al., 2006; Iwata et al., 2009; Nestor et al., 2013; Mostardi et al., 2013; Siana et al., 2015; Vanzella et al., 2010a, 2012, 2015) has yielded many promising LyC-emitting candidates, there exist only two robust detections (Vanzella et al., 2012, 2015).

Amassing large samples of LyC detections in high-redshift star-forming galaxies has been difficult for several reasons. First, large parent samples of high-redshift galaxies must be identified and confirmed spectroscopically, requiring extensive galaxy surveys (often ground-based) and time-consuming spectroscopic follow-up. Second, it is necessary to probe flux

in the LyC spectral region for these galaxies, either with deep spectroscopy, also very time-intensive, or through narrowband imaging in a filter just blueward of the Lyman limit, in which it is difficult to match a single narrowband filter to the LyC region for many galaxies at once. Even after potential high-redshift LyC-emitting candidates are identified, there remains the possibility that apparent LyC emission is actually due to a lower-redshift interloper along the line of sight, which cannot be distinguished in ground-based, seeing-limited data.

One method that has proven successful at identifying potential LyC-emitting galaxies is narrowband LyC imaging of galaxy protoclusters. Large ground-based surveys of UV-selected star-forming galaxies at $z \sim 2-3$ (Steidel et al., 2003, 2004, 2011; Reddy et al., 2008) have identified and spectroscopically confirmed thousands of high-redshift star-forming galaxies. These surveys have also located galaxy protoclusters, areas on the sky with large overdensities of galaxies at similar redshift. A very effective way to simultaneously probe the LyC of large samples of galaxies at the same redshift is to perform deep imaging through a narrowband filter tuned to the LyC spectral region at the protocluster redshift (e.g., Iwata et al., 2009; Nestor et al., 2011, 2013; Mostardi et al., 2013).

Initially, these protocluster studies were entirely based upon ground-based data with seeing FWHMs of $0\farcs7-1\farcs0$, and thus suffered from the possibility of foreground contamination. Vanzella et al. (2010b) demonstrated that statistical simulations modeling the distribution of foreground galaxies result in high rates of foreground contamination for high-redshift objects in ground-based studies. While simulations can account for contamination statistically in LyC-emitting samples (as in Nestor et al., 2011; Mostardi et al., 2013), contaminants cannot be eradicated on an individual basis. As two of the main goals of LyC studies are to determine the mechanism of LyC photon escape from the interstellar medium (ISM), and to identify additional features of LyC-emitting galaxies that may enable their identification through other means, it is crucial to identify robust, individual candidates for LyC emission where foreground contamination has been ruled out.

Eliminating contaminants is a complex process. High-resolution imaging shows that the majority of high-redshift galaxies are not morphologically simple, but are composed of mul-

tiple compact clumps and/or diffuse emission (e.g., Law et al., 2007). Contamination can only be firmly ruled out if the redshifts of individual galaxy clumps are measured, and if the clump associated with LyC emission is confirmed to be at the redshift of the target galaxy. In order to address the issue of contamination in the narrowband LyC survey of the $z = 3.1$ SSA22a protocluster Nestor et al. (2011, 2013), Siana et al. (2015) obtained near-IR spectroscopy with Keck/NIRSPEC to measure the spectroscopic redshifts of the sub-arcsecond components of 5 LyC candidates. These authors found two foreground contaminants, one galaxy with a misidentified redshift, and two galaxies that could not be definitively confirmed as LyC-emitters. For galaxies at slightly higher redshifts ($z \sim 3.7$), Vanzella et al. (2012) used photometric redshifts obtained through the high-resolution imaging in the CANDELS survey (Grogin et al., 2011; Koekemoer et al., 2011) to analyze the sub-arcsecond clumps of 19 candidate LyC-emitters, finding 18 contaminants and one bona-fide LyC emitter. These two studies have shown that both methods − high-resolution spectroscopy and photometric redshifts − are effective ways to locate foreground contaminants.

In Mostardi et al. (2013) (hereafter M13), we performed a narrowband LyC imaging survey of a galaxy protocluster in the HS1549+1919 field (Steidel et al., 2011). In this work, we present follow-up observations with *HST* for the sample of candidate LyC emitters in M13 with the goal of using photometric redshifts to eliminate contaminants from the LyC emitter sample. The HS1549 protocluster has a redshift-space overdensity of $\delta_{gal} \sim 5$ at $z = 2.85 \pm 0.03$, and this "spike" redshift coincides with that of a hyperluminous QSO (Trainor & Steidel, 2012). More than 350 UV-selected galaxies have been identified in the HS1549 field, ~ 160 of which have been spectroscopically confirmed at $1.5 \leq z \leq 3.5$. Additionally, narrowband imaging with a 4670Å filter tuned to the wavelength of Lyα at the redshift spike has revealed $\sim$300 potential Lyα Emitters (LAEs) and several Lyα "blobs" (Steidel et al., 2000, 2011). In M13, we used a narrowband filter (NB3420) tuned to wavelengths just below the Lyman limit at $z \geq 2.82$, thus observing the LyC spectral region for hundreds of Lyman break galaxies (LBGs) and LAEs at $z \geq 2.82$, including 49 LBGs and 91 LAEs with spectroscopic confirmation. We identified putative LyC emitters in the NB3420 imaging, and also performed a stacking analysis of objects undetected in the NB3420 filter (measuring no

signal). Although we found an NB3420 detection rate of $\sim 9\%$ in both the LBG and LAE samples, simulations indicated that 40-75% of the individual NB3420 detections may have resulted from foreground contamination, highlighting the need for further work to disentangle true LyC emitters from low-redshift contaminants.

Our aims in the current work are two-fold. Our primary goal is to address the question of foreground contamination in the M13 LyC-emitter sample. Ideally, as in Siana et al. (2015), we would obtain spatially-resolved spectroscopy in the vicinity of each putative LyC detection, with resolution of $\leq 0\farcs5$, in order to measure the redshifts of all components. However, ground-based optical spectroscopy probing the rest-frame UV provides insufficient spatial resolution, and ground-based near-IR spectroscopy of rest-frame optical nebular emission lines (with or without the assistance of adaptive optics) is not feasible because at $z \sim 2.85$ the strongest nebular emission lines (Hα, [OIII]λ5007, Hβ, and [OII]λ3727) are lost either in the thermal background or gaps in atmospheric transmission. Therefore, we have identified high-resolution, multi-band *HST* imaging as the best method for estimating spatially resolved photometric redshifts for the individual galaxy subcomponents associated with apparent LyC emission. Our second goal is to analyze the properties of galaxies we have verified to be true sources of LyC emission (such as their morphologies, stellar populations, and the ratio of their ionizing to non-ionizing flux densities) with respect to properties of star-forming galaxies without LyC detections. Such an analysis will help determine whether galaxies with high escape fractions of ionizing photons come from a physically different population than those without detectable leaking ionizing radiation, and may provide insight into star formation and the structure of the ISM in high-redshift galaxies.

In addition to presenting high-resolution, multiwavelength follow-up *HST* observations of high-redshift LyC-emitting candidates at $z \sim 2.85$ from M13, we discuss the implications for continuing searches for ionizing radiation in star-forming galaxies. The paper is organized as follows. Section 3.2 describes our methodology, while the galaxy sample and *HST* observations are presented in Section 3.3. In Section 3.4 we describe the techniques used to reduce the *HST* imaging data and perform photometry on the sub-arcsecond components of each galaxy. Section 3.5 contains a discussion of our methods of fitting photometric redshifts to

Table 3.1. Description of Samples

Sample[a]	N_{tot}[b]	$N_{\rm NB3420}$ $[N_{UVJH}]$[c]	$N^{\rm no}_{\rm NB3420}$ $[N_{UVJH}]$[d]
LBGs (with z_{spec})	49	5 [4]	44 [12]
LAEs (with z_{spec})	82[e]	7 [6]	75 [18]
LAEs (without z_{spec})	33	10 [4]	23 [7]
Faint LAEs (with z_{spec})	—	8 [2]	—
GNBs (with z_{spec})	—	3 [0]	—

[a]The samples described in M13.

[b]The total number of galaxies in the M13 sample.

[c]The number of galaxies with NB3420 detections. In brackets, we indicate the number of these galaxies for which we have obtained $U_{336}V_{606}J_{125}H_{160}$ imaging.

[d]The number of galaxies without NB3420 detections. In brackets, we indicate the number of these galaxies for which we have obtained $U_{336}V_{606}J_{125}H_{160}$ imaging.

[e]The number of LAEs that are not part of the LBG sample, i.e., 91 LAEs minus the 9 overlap objects (which are listed here as part of the LBG sample).

the data, as well as an analysis of each candidate LyC emitter and any sources of foreground contamination. In Section 3.6 we analyze the properties of our best candidate for true LyC emission (MD5) with respect to the larger population of star-forming galaxies. In Section 3.7, we consider the broader implications of these results, and the prospects for future direct searches for LyC radiation at high redshift. We summarize our results in Section 3.8. Throughout the paper we employ the AB magnitude system and assume a cosmology with $\Omega_m = 0.3$, $\Omega_\Lambda = 0.7$, and $H_0 = 70$ km s^{-1} Mpc^{-1}. At $z = 2.85$, $1''$corresponds to 7.8 proper kpc.

3.2 Methodology

To evaluate the amount of foreground contamination in M13 using photometric redshifts, we selected four *HST* filters (WFC3/UVIS U_{336}, ACS/WFC V_{606}, and WFC3/IR J_{125} and

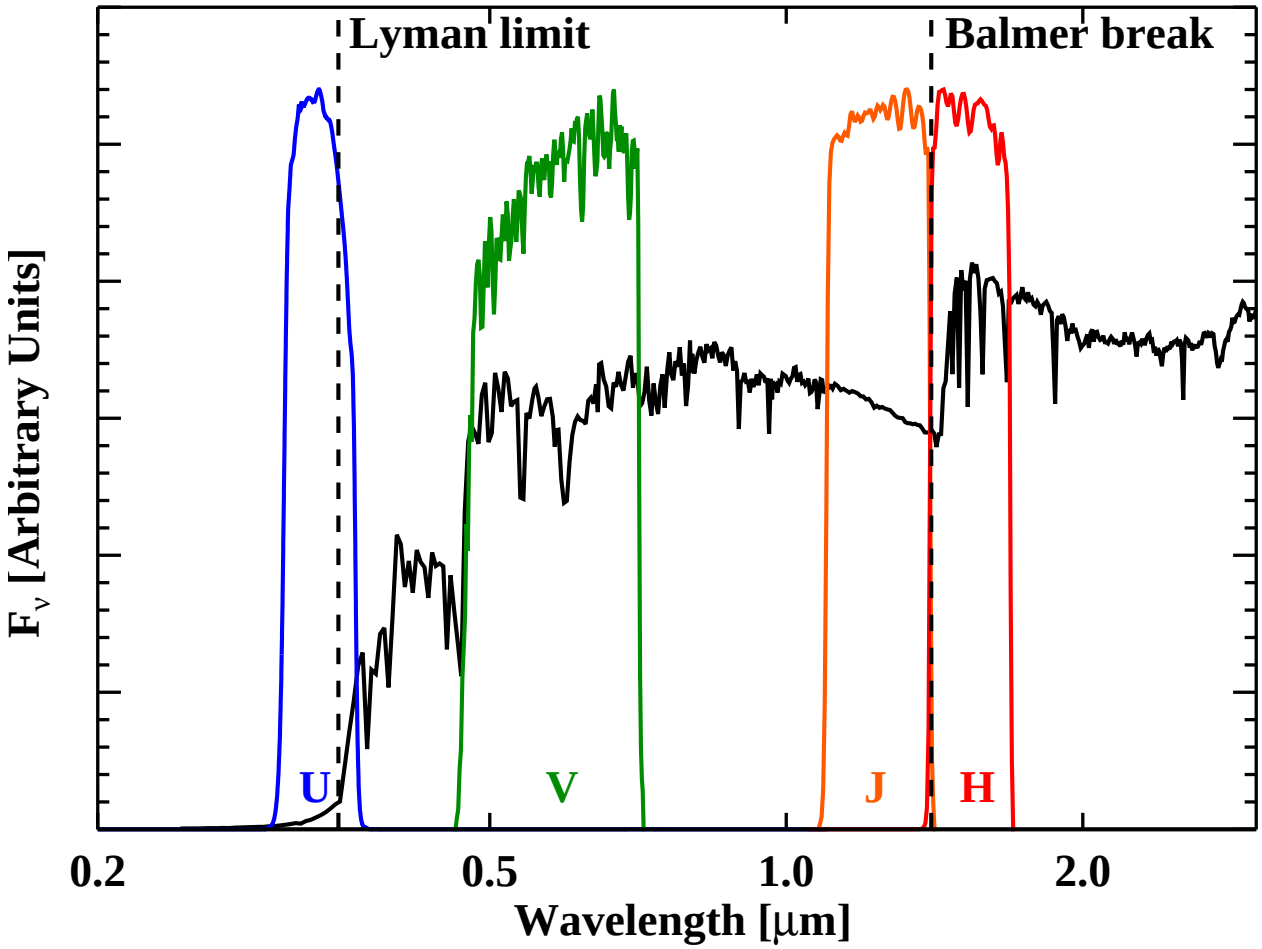

Figure 3.1 U_{336}, V_{606}, J_{125}, and H_{160} filters superimposed over a model $z = 2.85$ galaxy spectrum. The model spectrum is a solar-metallicity 100 Myr constant star-formation rate model from Bruzual & Charlot (2003), reddened to $E(B-V) = 0.15$ with the Calzetti et al. (2000) attenuation curve. The U_{336} filter probes the LyC spectral region, but with some contamination ($\sim 20\%$) redwards of the Lyman limit. The V_{606} filter probes the rest-frame non-ionizing UV continuum, and the J_{125} and H_{160} filters probe flux on either side of the Balmer break. With both the Lyman and Balmer breaks sensitively probed at $z = 2.85$, we can determine photometric redshifts for individual sub-arcsecond components of galaxies within our LAE and LBG samples. These photometric redshifts enable us to determine whether the NB3420 detections associated with these galaxies are true LyC emission, or contamination from foreground galaxies.

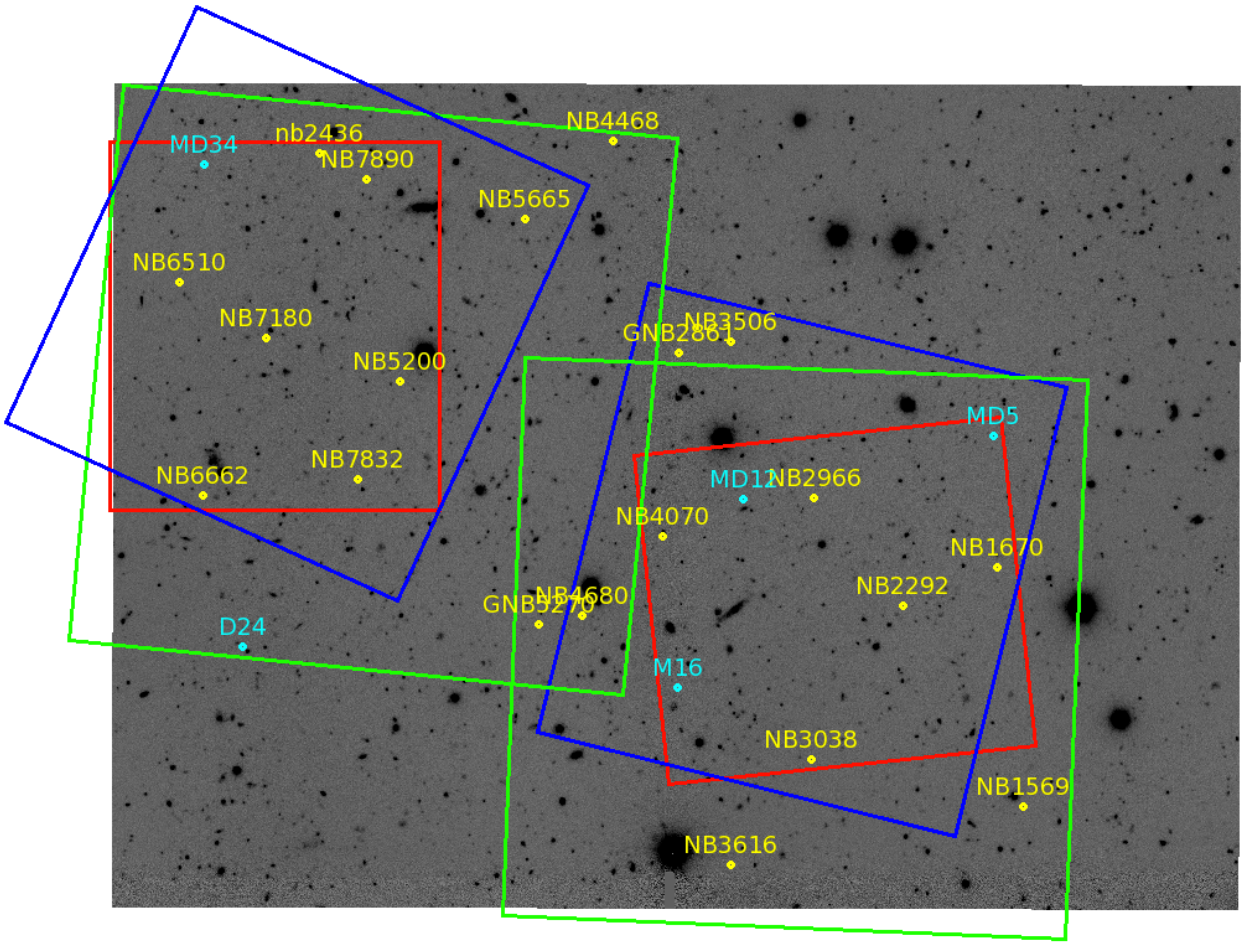

Figure 3.2 Footprints of HST pointings superimposed on the $5' \times 7'$ LRIS NB3420 (LyC) image. Blue squares indicate the footprint of U_{336}, green squares indicate the footprint of V_{606}, and red squares indicate the footprints of J_{125} and H_{160}. Cyan and yellow circles indicate the positions of LBGs and LAEs with NB3420 detections that lie within the footprints of the *HST* images.

H_{160}) designed to probe the strengths of the Lyman and Balmer breaks at $z \sim 2.85$. Figure 3.1 shows the locations of the U_{336}, V_{606}, J_{125}, and H_{160} filters superimposed over a model Bruzual & Charlot (2003) galaxy spectrum redshifted to $z = 2.85$. The choice of J_{125} and H_{160} filters is particularly powerful for this test, due to the observed wavelength of the Balmer break at $z = 2.85$ ($\lambda_{obs,BB} = 1.4\mu$m). This wavelength corresponds exactly to the red cut-off of J_{125} and the blue cut-off of H_{160}. Therefore, the $J_{125} - H_{160}$ color is very sensitive to the presence of the Balmer break, and provides information about the age of the stellar population. Additionally, the $V_{606} - J_{125}$ color probes the rest-frame UV slope at $z \sim 2.85$, providing information about the stellar populations and dust extinction. At $z < 2$, where most of the contaminants found by Vanzella et al. (2012) are located, the J_{125} filter falls entirely on the red side of the Balmer break, and therefore, extremely flat $J_{125} - H_{160}$ colors are expected, with the Balmer break falling instead between V_{606} and J_{125}. At the other end of the spectrum, the U_{336} filter does not lie entirely bluewards of the Lyman limit at $z = 2.85$ (only 80% of its wavelength range falls below the Lyman limit) and thus does not exclusively probe the LyC spectral region. However, given that the Lyman break passes through this filter at redshifts $z = 2.40 - 2.95$, the $U_{336} - V_{606}$ color should be sensitive to the magnitude of the Lyman break at $z = 2.85$, and to its absence at significantly lower redshift. With both Lyman and Balmer breaks sensitively probed at $z = 2.85$ using $U_{336}V_{606}J_{125}H_{160}$ photometry, we can distinguish between true sources of LyC emission, and those NB3420 detections attributable to non-ionizing radiation at lower redshift.

Several complications may arise from the method of estimating the photometric redshifts using only these four filters. First, galaxies with leaking LyC emission may have intrinsically high ratios of escaping ionizing to non-ionizing radiation, and may not exhibit as strong a Lyman break as expected from normal $z = 2.85$ galaxies. We keep this caveat in mind during our subsequent analysis, with the understanding that the $U_{336} - V_{606}$ color may not be accurately represented by the models. Second, young galaxies ($\lesssim$ 20 Myr) may not have a significant Balmer break. The combination of these two scenarios may result in a young, high-redshift, LyC emitter with a relatively featureless spectrum, making it difficult to distinguish such galaxies from low-redshift contaminants. In our photometric redshift

analysis, we highlight cases of galaxies with ambiguous SED shapes and the possible stellar populations these SEDs may indicate.

3.3 Sample and Observations

The HS1549 galaxy sample discussed in M13 consists of 49 LBGs and 91 LAEs, all spectroscopically confirmed at $z \geq 2.82$. There are 9 objects part of both the LAE and LBG samples; for simplicity in displaying our data, we group these objects with the LBGs.[1] The redshift limit of $z \geq 2.82$ ensures that the NB3420 filter is sensitive only to LyC emission, with no contamination from flux redward of the Lyman limit. Out of these galaxies, 5 LBGs and 7 LAEs have NB3420 detections within $1\farcs9$ of the non-ionizing UV centroid of the galaxy, indicating potential LyC emission if there is no lower-redshift galaxy contaminant along the line of sight.

In M13 we also present an additional sample of 33 photometric LAE candidates (no spectroscopic confirmation) in the HS1549 field whose magnitudes in the narrowband filter used to select LAEs (NB4670) are in the same range as those of the spectroscopically-confirmed LAEs[2]. While these objects are not included in the analysis of M13 because the lack of spectroscopic redshifts increases the possibility of contamination, 10 of them are reported to have NB3420 detections.

Finally, in M13 we present 8 spectroscopically confirmed LAEs with NB3420 detections that are either fainter than the magnitude limit of the main LAE sample ($m_{4670} > 26$; 5 objects) or were selected by their $G-$NB4670 color rather than $V-$NB4670 (3 objects). We did not include these objects in the analysis of M13 because we had not assembled a complete and unbiased spectroscopic sample of LAEs with $m_{4670} > 26$ or LAEs selected by their $G-$NB4670 color.

In the follow-up observations presented in this work, we considered all objects with

[1] One of the objects in both the LAE and LBG samples is the putative LyC-emitter MD12/*lae3540*, which is discussed in detail in M13. In this work, we refer to this object simply as MD12.

[2] All LAEs within the spectroscopic LAE sample of M13 had $m_{4670} \leq 26$. Thus, the photometric LAE sample of M13 was defined to be any additional LAEs with $m_{4670} \leq 26$ that did not have spectroscopic confirmation.

NB3420 detections presented in M13 and chose *HST* pointings oriented to maximize the number of these potential LyC-emitting targets on the image footprints. As the fields of view attained by the various *HST* instruments employed for these observations (ACS/WFC: 3.′5×3.′5; WFC3/UVIS: 2.′9×2.′7; WFC3/IR: 2.′3×2.′1) are much smaller than the Keck/LRIS field of view (5′×7′), we were unable to acquire imaging for all of the potential LyC-emitters. However, with two separate *HST* pointings in each of the 4 filters (see Figure 3.2), we obtained $U_{336}V_{606}J_{125}H_{160}$ photometry for all but two of the spectroscopically confirmed galaxies in the main sample: 4/5 LBGs and 6/7 LAEs. We also obtained $U_{336}V_{606}J_{125}H_{160}$ photometry for 4/10 photometric LAE candidates, and 2/6 of spectroscopically confirmed LAEs with $m_{4670} > 26$, totaling 16 galaxies with NB3420 detections covered in all four filters. Eight additional objects with NB3420 detections are covered by at least one *HST* filter (usually V_{606}, which has the largest field of view), and may be examined morphologically, although it is not possible to obtain photometric redshifts for galaxies without imaging in all four filters. These objects are presented in the Appendix. In addition to the 16 galaxies with NB3420 detections, we acquired $U_{336}V_{606}J_{125}H_{160}$ imaging for 30 spectroscopically confirmed galaxies at $z \geq 2.82$ without NB3420 detections (12 LBGs and 18 LAEs), which allows us to calibrate our photometric redshift fitting methods on galaxies without LyC detections and facilitates the differential analysis of the stellar populations of galaxies with and without LyC detections. Finally, 50 additional spectroscopically confirmed galaxies at $z \geq 2.82$ without NB3420 detections (30 LBGs and 20 LAEs) were partially covered by our suite of *HST* imaging. Table 3.1 summarizes the *HST* coverage of the samples.

In total, we obtained 5 orbits for each of the WFC3/UVIS U_{336} and ACS/WFC V_{606} pointings and 3 orbits for each of the WFC3/IR J_{125} and H_{160} pointings as part of *HST* Program ID 12959 (PI: A. Shapley) between 2012 December and 2013 August. Table 3.2 lists details of the observations. Individual exposures were half-orbit (∼1400 seconds) for U_{336} and quarter-orbit (∼600 seconds) for V_{606}, J_{125}, and H_{160}, and total exposure times per pointing were 14 ks (U_{336}), 12 ks (V_{606}), and 8 ks (J_{125} & H_{160}). We used a combination of the WFC3/UVIS DITHER-BOX and DITHER-LINE patterns for U_{336}, the ACS/WFC DITHER-BOX pattern for V_{606}, and the WFC3/IR DITHER-LINE pattern for J_{125} and

Table 3.2. *HST* Imaging Observations

Filter	λ_{eff} (Å)	PSF FWHM (″)	Depth[a] (mag)	Exposure (s)	Pixel Scale[b] (″/pixel)	`Pixfrac`[b]
U_{336}	3355	0.081	29.20	14176	0.025	0.7
V_{606}	5921	0.092	30.22	11848	0.03	0.7
J_{125}	12486	0.178	28.93	7835	0.075	0.7
H_{160}	15369	0.186	28.63	7835	0.075	0.7

[a]The 3σ limiting depth obtained in a circular aperture with a diameter of 1.5 times the PSF FWHM.

[b]The *AstroDrizzle* parameters for pixel scale (`pixscale`) and `pixfrac` listed here represent the parameters used to attain optimal resolution.

H_{160}. In order to mitigate charge transfer efficiency (CTE) losses in our WFC3/UVIS U_{F336} exposures, we used the "post-flash" capability with FLASH=8 (Biretta & Baggett, 2013). The final 3σ surface-brightness sensitivities and PSF FWHMs of the U_{336}, V_{606}, J_{125}, and H_{160} images are, respectively, 24.53, 25.71, 25.79, and 25.56 AB arcsec^{-2} and 0.″081, 0.″092, 0.″178, and 0.″186. The 3σ depths obtained in circular apertures with a diameter of 1.5 times the PSF FWHM are, respectively, 29.20, 30.22, 28.93, and 28.63 magnitudes.

3.4 Data Reduction and Photometry

Data reduction was performed on calibrated, flat-fielded, and CTE-corrected (in the case of WFC3/UVIS and ACS/WFC) images with *DrizzlePac* (Fruchter, 2010; Koekemoer et al., 2003). The task *TweakReg* was used to align all exposures within each visit, and the *AstroDrizzle* pipeline was used to perform sky subtraction, mask cosmic rays and bad pixels, and combine the exposures in the final, drizzled image. Final images were drizzled onto two scales: one optimized for the highest resolution in each filter (for analysis of galaxy morphologies), and one where the pixel scale was consistent across all filters (for matched-aperture photometric analysis). For the images drizzled to optimum resolution, the *AstroDrizzle* parameters `pixscale` and `pixfrac` are indicated in Table 3.2. For the images

used in photometric analysis, all filters were drizzled to a pixel scale of 0.03 ″/pixel, using a pixfrac value of 0.7 for U_{336} and 0.8 for V_{606}, J_{125}, and H_{160}. The `pixfrac` values were chosen in order to achieve the optimum balance between the signal-to-noise ratio and visibility of low-surface-brightness features. Final drizzled images were registered to each other using the tasks *TweakReg* and *TweakBack*, achieving alignment between the V_{606}, J_{125}, and H_{160} filters with an rms of $0\farcs003 - 0\farcs006$, and between V_{606} and U_{336} with an rms of $0\farcs01$. The *HST* images were also aligned to the world coordinate system of the Keck/LRIS $V-$band image from M13 (the image to which all other Keck/LRIS images were registered) in order to map where the ground-based NB3420 (LyC) detections fell relative to emission in the *HST* images. After registration with *TweakReg*, residual astrometric distortions between the LRIS and *HST* images were corrected to a precision of $0\farcs09$ (less than half the size of an LRIS pixel) using the IRAF task CCMAP. Figures 3.3 − 3.5 display postage stamp images of the 16 galaxies with NB3420 detections and $U_{336}V_{606}J_{125}H_{160}$ imaging.

For objects where imaging in all four filters ($U_{336}V_{606}J_{125}H_{160}$) was available, the widest PSF was that of H_{160} ($0\farcs186$). Accordingly, in order to perform matched-aperture photometry, we smoothed the higher-resolution *HST* images to match the PSF of the H_{160} image. When infrared data were unavailable because of the smaller field of view of the WFC3/IR instrument, the widest PSF was that of V_{606} ($0\farcs092$) and we smoothed the U_{336} data to match this PSF. In order to perform the PSF-matching, we first created an empirical PSF from 10−30 (depending on the filter) bright, isolated, and unsaturated stars using the IDL routine `psf_extract` from *StarFinder* (Diolaiti et al., 2000). These empirical PSFs were then input into the IRAF routine PSFMATCH, which outputs the convolution kernel and the PSF-matched image. The curves of growth of the stellar profiles in the H_{160} and V_{606} images agree with those of the PSF-matched images to $\leq$2% for the majority of the stellar profile, and agree within $\leq$10% at small radii ($\leq$3 pixels).

For objects with $U_{336}V_{606}J_{125}H_{160}$ coverage, matched-aperture photometry was performed with *SExtractor* (Bertin & Arnouts, 1996) in dual-image mode, using the PSF-matched V_{606} image to detect sources and define isophotes, and applying these isophotes (which can be examined using the SExtractor segmentation image) to the U_{336}, J_{125}, and H_{160} images.

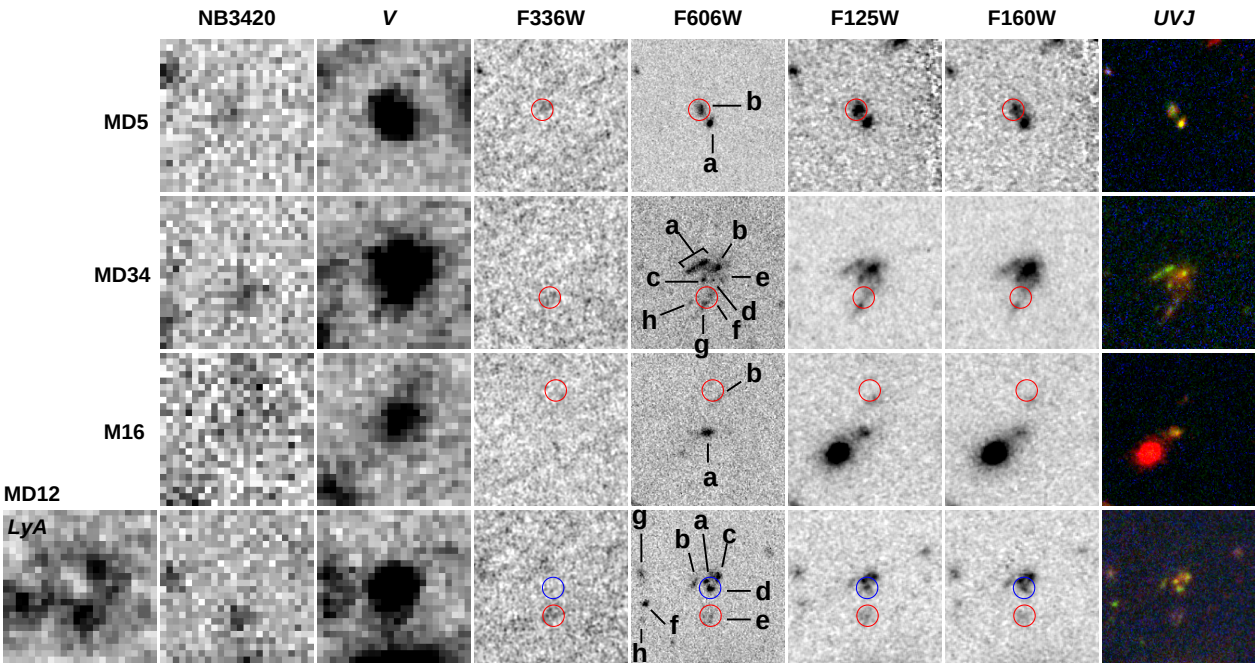

Figure 3.3 $5'' \times 5''$ postage stamp images of spectroscopically-confirmed LBGs with NB3420 detections and imaging in all four *HST* filters. From left to right, objects are displayed in the LRIS NB4670$-V$ continuum-subtracted image (indicating Lyα emission; MD12 only), LRIS NB3420 (LyC emission), LRIS V (non-ionizing UV continuum), *HST* U_{336} (a combination of LyC and non-ionizing UV), *HST* V_{606} (non-ionizing UV continuum), *HST* J_{125} (optical, bluewards of the Balmer break), and *HST* H_{160} (optical, redwards of the Balmer break). The final column shows a color-composite image of *HST* U_{336} (blue), V_{606} (green), and J_{125} (red). Red circles ($1\farcs0$ diameter) indicate the centroid of the NB3420 emission, and blue circles indicate the centroid of the Lyα emission for MD12. Photometry was performed individually on sub-arcsecond components associated with each LBG, and all components are labeled in the V_{606} image. Postage stamps follow the conventional orientation, with north up and east to the left.

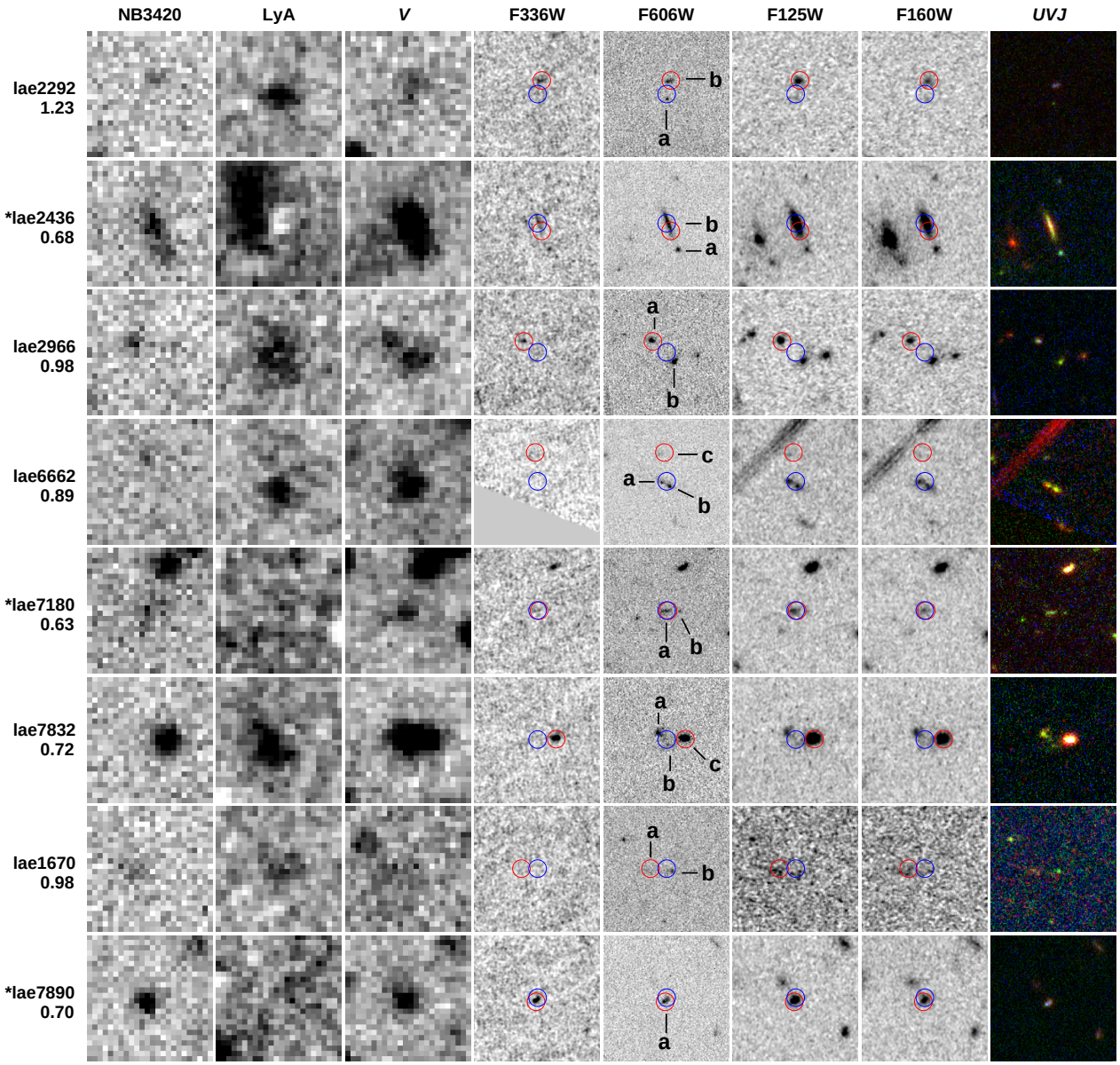

Figure 3.4 $5'' \times 5''$ postage stamp images of spectroscopically-confirmed LAEs with NB3420 detections and imaging in all four *HST* filters. From left to right, objects are displayed in LRIS NB3420 (LyC emission), LRIS NB4670$-V$ (indicating Lyα emission), LRIS V (non-ionizing UV continuum), *HST* U_{336} (a combination of LyC and non-ionizing UV), *HST* V_{606} (non-ionizing UV continuum), *HST* J_{125} (optical, bluewards of the Balmer break), and *HST* H_{160} (optical, redwards of the Balmer break). The final column shows a color-composite image of *HST* U_{336} (blue), V_{606} (green), and J_{125} (red). Red (blue) circles ($1\farcs0$ diameter) indicate the centroid of the NB3420 emission (Lyα emission). Photometry was performed individually on sub-arcsecond components associated with each LAE, and all components are labeled in the V_{606} image. Postage stamps follow the conventional orientation, with north up and east to the left. The $V-$NB4670 color of each LAE is indicated below the object name, and objects marked by an asterisk (*) were found to have misidentified spectroscopic redshifts (see Section 3.5.3).

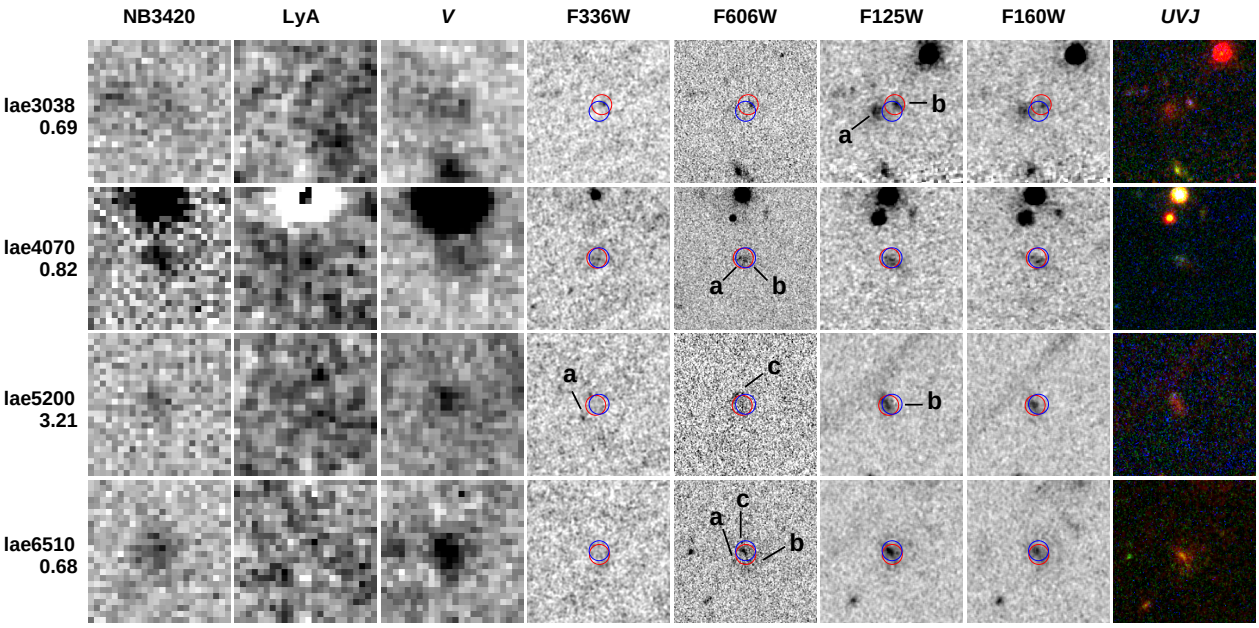

Figure 3.5 $5'' \times 5''$ postage stamp images of LAE photometric candidates (no spectroscopic confirmation) with NB3420 detections and imaging in all four *HST* filters. Objects are displayed and labeled as in Figure 3.4.

Because the V_{606} image was already smoothed to the H_{160} PSF, no filtering was used, and the *SExtractor* detection threshold was set to 4.0σ. When photometry was extracted for galaxies without J_{125} and H_{160} imaging, the unsmoothed V_{606} image was filtered with a Gaussian kernel of σ=4 pixels before source extraction. As most of the galaxies in our $z \sim 2.85$ sample have clumpy morphologies, *SExtractor* was run with maximum deblending (DEBLEND_MINCONT = 0.0) in order to separate clumps within the galaxies for individual analysis. All galaxy clumps defined by *SExtractor* were examined visually in the segmentation image to guarantee that the subregions visible by eye were properly identified. For some galaxies, the detection threshold parameter was slightly modified ($\pm 1\sigma$) to achieve the best isophote. There were also instances in which substructure was not visible in the V_{606} image; in these cases, the relevant isophotes were defined in the U_{336} or J_{125} images where the substructure was visible. The background subtraction algorithm in SExtractor was set to LOCAL, which defines a square sky annulus around the object in question. However, in cases where multiple adjacent galaxy clumps were deblended, the annulus defined by *SExtractor* was often contaminated by nearby sources to the extent that the resulting background estimation was biased. In such cases, we created our own uncontaminated sky

annulus around the object and estimated the background using the sigma-clipped mode, the procedure employed by *SExtractor*.

In order to estimate photometric uncertainties for objects in the PSF-matched images, we followed the methods of Förster Schreiber et al. (2006) and computed photometric errors as a function of isophotal aperture size. First, we identified 1000 blank regions that avoided objects and image edges in each of the PSF-matched U_{336}, V_{606}, J_{125}, and H_{160} images used for isophotal photometry. We then performed photometry on these blank regions with circular apertures of various sizes corresponding to the isophotal areas of our LBGs and LAEs. We defined the photometric uncertainty for a given object with isophotal area, A, as the standard deviation of the number of counts in the 1000 blank apertures of area A. The relationship between aperture size and background rms in our images is qualitatively similar to that found in Förster Schreiber et al. (2006). From this analysis, we estimated 3σ limiting magnitudes in apertures with a diameter of 1.5 times the PSF FWHM for each of the unsmoothed U_{336}, V_{606}, J_{125}, and H_{160} images, and list them in Table 3.2. Photometric data for individual objects are listed in Table 3.3.

Table 3.3. LBG and LAE Photometry.

ID[a]	R.A.[b]	Dec.[b]	U_{336}[c]	V_{606}[c]	J_{125}[c]	H_{160}[c]	z_{spec}[d]	z_{phot} PÉGASE	z_{phot} BPASS	SED Type[e]
lae1670a	15:51:45.176	19:10:15.261	> 28.69	$29.39^{+0.28}_{-0.22}$	$28.24^{+0.20}_{-0.17}$	> 28.64	—	1.19	1.67	c
lae1670b	15:51:45.110	19:10:15.225	> 28.11	$28.25^{+0.16}_{-0.14}$	> 28.53	> 28.18	2.846	2.28	1.82	r
lae2292a	15:51:47.633	19:10:00.319	> 29.01	$29.14^{+0.16}_{-0.14}$	$28.97^{+0.32}_{-0.25}$	$28.65^{+0.33}_{-0.25}$	2.851	1.61	1.44	r
lae2292b	15:51:47.626	19:10:01.034	$27.31^{+0.20}_{-0.17}$	$27.73^{+0.10}_{-0.09}$	$26.71^{+0.07}_{-0.07}$	$26.76^{+0.11}_{-0.10}$	—	1.15	1.17	c
lae2436a	15:52:03.209	19:12:51.261	$27.33^{+0.32}_{-0.25}$	$26.98^{+0.08}_{-0.07}$	$26.92^{+0.10}_{-0.09}$	$26.32^{+0.08}_{-0.07}$	2.04[f]	2.29	2.33	c
lae2436b	15:52:03.239	19:12:52.296	$26.13^{+0.29}_{-0.23}$	$25.16^{+0.04}_{-0.04}$	$24.46^{+0.03}_{-0.02}$	$24.33^{+0.03}_{-0.03}$	0.44[f]	0.42	1.65	c
lae2966a	15:51:50.037	19:10:42.064	> 27.54	$26.82^{+0.07}_{-0.07}$	$26.23^{+0.07}_{-0.07}$	$26.20^{+0.10}_{-0.09}$	—	1.09	1.42	c
lae2966b	15:51:49.975	19:10:41.263	> 27.14	$26.29^{+0.06}_{-0.06}$	$26.11^{+0.09}_{-0.08}$	$25.74^{+0.09}_{-0.08}$	2.841	3.03	2.90	r
lae3038a	15:51:50.131	19:09:02.336	> 27.47	$28.02^{+0.25}_{-0.20}$	$26.17^{+0.07}_{-0.07}$	$26.08^{+0.09}_{-0.08}$	—	1.18	3.10	a
lae3038b	15:51:50.077	19:09:02.483	$27.93^{+0.36}_{-0.27}$	$28.20^{+0.15}_{-0.13}$	$27.03^{+0.09}_{-0.09}$	$27.08^{+0.14}_{-0.12}$	—	1.20	1.21	c
lae4070a	15:51:54.072	19:10:26.789	$28.24^{+0.31}_{-0.24}$	$28.48^{+0.13}_{-0.11}$	$28.30^{+0.23}_{-0.19}$	$27.75^{+0.19}_{-0.16}$	—	1.25	1.21	a
lae4070b	15:51:54.061	19:10:26.731	$27.38^{+0.28}_{-0.22}$	$27.51^{+0.11}_{-0.10}$	$26.85^{+0.10}_{-0.09}$	$26.81^{+0.14}_{-0.12}$	—	1.24	1.23	c
lae5200a	15:52:01.125	19:11:25.487	$28.87^{+0.30}_{-0.23}$	$30.29^{+0.43}_{-0.31}$	> 29.74	> 29.34	—	1.10	0.99	c
lae5200b	15:52:01.097	19:11:25.994	> 27.73	$27.90^{+0.17}_{-0.15}$	$26.69^{+0.07}_{-0.07}$	$26.50^{+0.09}_{-0.08}$	—	1.23	1.51	a
lae5200c	15:52:01.111	19:11:26.206	> 27.84	$27.93^{+0.16}_{-0.14}$	$27.05^{+0.09}_{-0.09}$	$27.43^{+0.19}_{-0.16}$	—	1.11	1.52	c
lae6510a	15:52:07.004	19:12:02.999	> 28.68	$29.25^{+0.26}_{-0.21}$	$29.26^{+0.43}_{-0.31}$	> 28.90	—	2.03	1.71	c
lae6510b	15:52:06.976	19:12:02.822	> 27.71	$27.95^{+0.18}_{-0.16}$	$27.61^{+0.18}_{-0.15}$	$27.58^{+0.25}_{-0.21}$	—	1.31	1.35	c
lae6510c	15:52:06.981	19:12:03.350	> 26.81	$26.59^{+0.12}_{-0.11}$	$25.73^{+0.06}_{-0.06}$	$25.58^{+0.08}_{-0.08}$	—	1.24	1.38	a
lae6662a	15:52:06.369	19:10:42.590	> 27.82	$27.31^{+0.09}_{-0.08}$	$27.01^{+0.09}_{-0.08}$	$26.64^{+0.09}_{-0.08}$	2.833	2.82	2.28	r

Table 3.3 (cont'd)

ID[a]	R.A.[b]	Dec.[b]	U_{336}[c]	V_{606}[c]	J_{125}[c]	H_{160}[c]	z_{spec}[d]	z_{phot} PÉGASE	z_{phot} BPASS	SED Type[e]
lae6662b	15:52:06.350	19:10:42.450	> 27.49	$26.73^{+0.07}_{-0.07}$	$26.68^{+0.09}_{-0.08}$	$26.22^{+0.08}_{-0.08}$	2.833	2.85	2.80	r
lae6662c	15:52:06.376	19:10:43.706	> 28.55	$28.84^{+0.19}_{-0.16}$	$28.63^{+0.24}_{-0.20}$	$28.60^{+0.35}_{-0.26}$	—	1.26	1.33	c
lae7180a	15:52:04.669	19:11:42.083	> 27.62	$27.29^{+0.11}_{-0.10}$	$26.72^{+0.08}_{-0.08}$	$26.67^{+0.11}_{-0.10}$	—	1.07	1.54	a
lae7180b	15:52:04.631	19:11:42.088	> 28.66	$29.19^{+0.24}_{-0.20}$	$28.88^{+0.29}_{-0.23}$	> 28.89	—	1.75	1.74	—
lae7832a	15:52:02.222	19:10:48.807	> 26.88	$26.08^{+0.07}_{-0.07}$	$26.08^{+0.08}_{-0.08}$	$25.62^{+0.08}_{-0.07}$	2.829	2.77	2.70	r
lae7832b	15:52:02.199	19:10:48.379	> 27.91	$27.65^{+0.11}_{-0.10}$	$27.68^{+0.16}_{-0.14}$	$27.37^{+0.17}_{-0.15}$	2.829	2.68	1.86	r
lae7832c	15:52:02.155	19:10:48.614	$25.57^{+0.13}_{-0.11}$	$25.16^{+0.03}_{-0.03}$	$24.48^{+0.02}_{-0.02}$	$24.51^{+0.03}_{-0.03}$	—	0.72	1.72	c
lae7890a	15:52:01.957	19:12:42.255	$26.61^{+0.19}_{-0.16}$	$26.52^{+0.06}_{-0.06}$	$25.73^{+0.04}_{-0.04}$	$25.86^{+0.06}_{-0.06}$	—	0.95	1.38	c
M16a	15:51:53.648	19:09:29.392	> 27.05	$26.15^{+0.06}_{-0.06}$	$25.32^{+0.04}_{-0.04}$	$25.19^{+0.06}_{-0.05}$	2.954	3.92	2.50	r
M16b	15:51:53.619	19:09:30.486	> 27.89	$28.45^{+0.25}_{-0.20}$	$27.26^{+0.14}_{-0.13}$	$27.21^{+0.19}_{-0.16}$	—	1.25	1.36	c
MD5a	15:51:45.206	19:11:04.887	> 27.21	$25.87^{+0.04}_{-0.04}$	$25.68^{+0.06}_{-0.05}$	$25.32^{+0.06}_{-0.05}$	3.143	3.04	2.88	r
MD5b	15:51:45.226	19:11:05.300	> 27.05[g]	$25.85^{+0.05}_{-0.04}$	$25.57^{+0.06}_{-0.05}$	$25.53^{+0.08}_{-0.07}$	3.143	3.50	1.94	a
MD12a	15:51:51.887	19:10:41.313	> 28.70	$27.38^{+0.04}_{-0.04}$	$26.92^{+0.05}_{-0.05}$	$26.51^{+0.05}_{-0.05}$	2.852	3.17	2.88	r
MD12b	15:51:51.915	19:10:41.281	> 27.20	$26.67^{+0.09}_{-0.08}$	$26.59^{+0.13}_{-0.12}$	$26.10^{+0.12}_{-0.11}$	2.852	2.83	2.56	r
MD12c	15:51:51.866	19:10:41.457	> 27.15	$25.95^{+0.05}_{-0.04}$	$25.64^{+0.06}_{-0.05}$	$25.21^{+0.05}_{-0.05}$	2.852	3.17	2.91	r
MD12d	15:51:51.879	19:10:41.091	> 27.56	$26.41^{+0.05}_{-0.05}$	$26.31^{+0.07}_{-0.07}$	$25.97^{+0.08}_{-0.07}$	2.852	3.00	2.94	r
MD12e	15:51:51.880	19:10:40.126	$27.29^{+0.30}_{-0.23}$	$27.26^{+0.10}_{-0.09}$	$26.62^{+0.09}_{-0.09}$	$26.57^{+0.12}_{-0.11}$	—	1.25	1.25	c
MD12f	15:51:52.028	19:10:40.582	> 27.81	$27.10^{+0.07}_{-0.07}$	$27.35^{+0.17}_{-0.14}$	$27.25^{+0.21}_{-0.18}$	2.852	2.93	2.74	r
MD12g	15:51:52.036	19:10:41.535	$27.26^{+0.35}_{-0.26}$	$27.03^{+0.09}_{-0.09}$	$26.50^{+0.10}_{-0.09}$	$26.15^{+0.10}_{-0.09}$	—	1.35	1.26	c

Table 3.3 (cont'd)

ID[a]	R.A.[b]	Dec.[b]	U_{336}[c]	V_{606}[c]	J_{125}[c]	H_{160}[c]	z_{spec}[d]	z_{phot} PÉGASE	z_{phot} BPASS	SED Type[e]
MD12h	15:51:52.035	19:10:40.060	> 28.86	$29.11^{+0.18}_{-0.15}$	> 29.14	> 28.79	—	1.95	1.60	—
MD34a	15:52:06.336	19:12:48.673	> 26.70	$25.49^{+0.05}_{-0.05}$	$25.21^{+0.04}_{-0.04}$	$24.67^{+0.04}_{-0.04}$	2.852	3.15	2.87	r
MD34b	15:52:06.307	19:12:48.550	> 26.83	$25.67^{+0.05}_{-0.05}$	$24.84^{+0.03}_{-0.03}$	$24.15^{+0.02}_{-0.02}$	2.852	3.37	2.66	r
MD34c	15:52:06.334	19:12:48.205	> 27.60	$26.93^{+0.08}_{-0.07}$	$26.15^{+0.05}_{-0.05}$	$25.67^{+0.04}_{-0.04}$	2.852	3.20	2.65	r
MD34d	15:52:06.314	19:12:48.195	> 29.54	$28.97^{+0.08}_{-0.08}$	$28.06^{+0.06}_{-0.06}$	$27.46^{+0.05}_{-0.05}$	2.852	2.71	2.63	r
MD34e	15:52:06.295	19:12:48.191	> 29.34	$28.94^{+0.10}_{-0.09}$	$27.98^{+0.07}_{-0.06}$	$27.38^{+0.06}_{-0.05}$	2.852	2.76	2.65	r
MD34f	15:52:06.318	19:12:47.708	> 27.27	$26.92^{+0.10}_{-0.09}$	$25.88^{+0.05}_{-0.05}$	$25.45^{+0.05}_{-0.05}$	2.852	2.12	2.60	r
MD34g	15:52:06.333	19:12:47.380	> 27.50	$27.25^{+0.11}_{-0.10}$	$26.27^{+0.06}_{-0.06}$	$26.23^{+0.08}_{-0.08}$	—	1.21	1.33	c
MD34h	15:52:06.365	19:12:47.446	> 29.43	$29.90^{+0.23}_{-0.19}$	$29.54^{+0.29}_{-0.23}$	$29.32^{+0.36}_{-0.27}$	2.852	1.73	1.59	a

[a]Objects are listed by their IDs from M13. The final letter of the object name indicates the sub-arcsecond component of the galaxy, according to the labels in Figures 3.3, 3.4, and 3.5.

[b]Object centroids calculated from V_{606}.

[c]Isophotal magnitudes and photometric errors as a function of aperture size (see Section 3.4). Limits are 3σ.

[d]Spectroscopic redshifts listed were obtained via ground-based spectroscopy, and thus in general it is not possible to distinguish between individual sub-arcsecond components of galaxies within the spectrum. We list spectroscopic redshifts only when the SED fit indicates that the object is not a foreground contaminant. Spectroscopic redshifts are not listed for the following types of objects: LAEs without spectroscopic follow-up, contaminants identified via photometric redshifts, and objects where $U_{336}V_{606}J_{125}H_{160}$ photometric data were insufficient to determine a photometric redshift.

[e]This column indicates whether the SED of the object implies a real $z \sim 2.85$ galaxy (r) or a foreground contaminant (c). The letter (a) indicates an ambiguous SED shape, defined in Section 3.5.1.

[f]The original Lyα redshift associated with *lae2436* from M13 was $z = 2.832$. Subsequent reanalysis of the available spectra near this object indicates that the $z = 2.832$ emission was associated with a nearby Lyα blob (see Section 3.5.3.1).

[g]Although MD5b is formally undetected in U_{336} at 3σ, emission at the location of MD5b is visible by eye in the U_{336} imaging. This emission corresponds to a 2.25σ detection in U_{336} ($m_{336} = 27.37^{+0.64}_{-0.40}$), which is consistent within errors of the detection in NB3420 ($m_{NB3420} = 26.89^{+0.43}_{-0.31}$).

3.5 Estimation of Photometric Redshifts

One important challenge in isolating LyC emission from high-redshift galaxies is that the majority of these systems have complex morphologies. In our sample of $z \sim 2.85$ LBGs and LAEs, roughly 80% of the objects have complex morphology in the $U_{336}V_{606}J_{125}H_{160}$ imaging, whether it be due to diffuse emission or multiple sources of nucleated emission. This fraction of objects with complex morphology is similar to that found in Law et al. (2007) for a sample of 66 $z \sim 3$ LBGs with rest-frame UV *HST* imaging ($\sim 85\%$), and demonstrates that for most high-redshift galaxies, high-resolution images reveal significant substructure. For the NB3420-detected galaxies, the NB3420 flux may be due to LyC emission from the high-redshift galaxy, or contamination from a lower redshift contaminant. Therefore, we must obtain photometric redshifts for individual subcomponents in order to identify possible contaminants.

In this section, we begin by discussing the expected SED shapes of $z \sim 2.85$ galaxies and low-redshift contaminants, and present the range of properties exhibited by galaxies in our sample. Next, we explain our procedures for fitting photometric redshifts with EAZY (Brammer et al., 2008), using the U_{336}, V_{606}, J_{125}, and H_{160} photometry acquired with *HST*. Finally, we consider each NB3420-detected galaxy individually, discussing the photometric redshifts of each clump and the implications for the source of the galaxy's NB3420 detection.

3.5.1 Empirical Analysis of SEDs

In order to describe the SED shapes of "typical" $z \sim 2.85$ star-forming galaxies, we first present SEDs from the sample of LBGs and LAEs without LyC detections. This sample is described in more detail in Section 3.5.2. Figure 3.6 shows $U_{336}V_{606}J_{125}H_{160}$ photometry for several galaxies in the sample that span the range of typical SED shapes. As expected, the Lyman break is present in the SEDs of all galaxies without LyC detections. Furthermore, every object in the LyC non-detection sample is undetected in U_{336}, which is consistent with the NB3420 non-detections in M13. The presence of the Lyman break is one of the most important features for distinguishing low- and high-redshift galaxies in the sample of

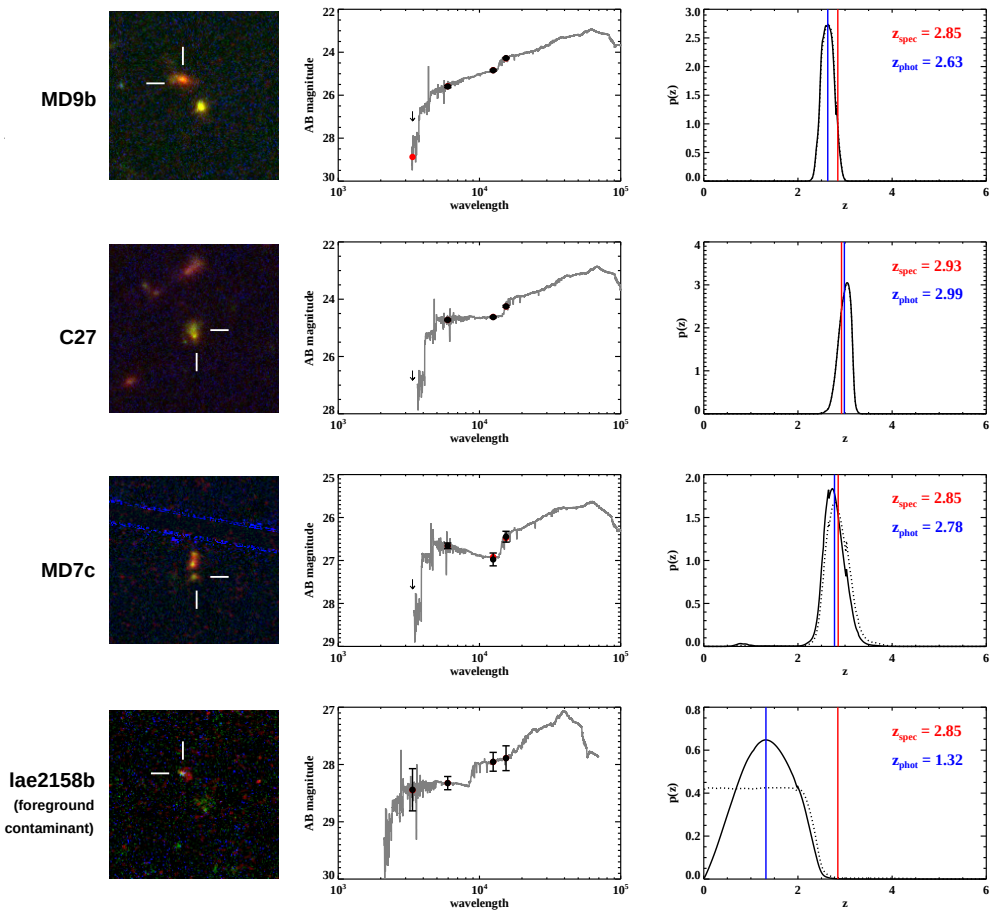

Figure 3.6 Representative SED shapes found within our $z \sim 2.85$ galaxy sample. The first three rows display $z \sim 2.85$ galaxies without NB3420 detections. From top to bottom, the objects shown are typical examples of SED shapes for objects with a red rest-frame UV slope ($V_{606} - J_{125} > 0.1$), a flat rest-frame UV slope ($-0.1 \leq V_{606} - J_{125} \leq 0.1$), a blue rest-frame UV slope ($V_{606} - J_{125} < -0.1$). The final row shows a typical example of the SED shape of a foreground contaminant. The left-most panel displays *HST* $U_{336}V_{606}J_{125}$ composite color images and indicates which sub-arcsecond component is being plotted in subsequent columns. The middle column shows the $U_{336}V_{606}J_{125}H_{160}$ photometry for that component (black circles with 1σ error bars; downward-pointing arrows for 3σ limits), the best-fit SED using the SMC-reddened BPASS models in EAZY (gray line), and the expected location of the photometric points based on the best-fit model (red circles). The right-most panel shows the redshift probability distribution, with the solid black curve indicating the probability distribution after a magnitude-based prior has been applied (see discussion of priors in Brammer et al., 2008) and the dotted black curve indicating the probability distribution before applying the prior. Blue vertical lines indicate the best-fit photometric redshift (z_{phot}) and red lines indicate the observed spectroscopic redshift (z_{spec}). The top three objects demonstrate relatively narrow probability distributions that, while they do not have extremely high redshift precision, do encompass the true spectroscopic redshift. In general, the precision of the redshift probability distributions decrease with increasing photometric errors. The final object shows a clear example of a foreground contaminant with the photometric colors described in Section 3.5.1; accordingly, the EAZY redshift probability distribution does not align with the spectroscopic redshift. For the case of *lae2158*, the actual LAE is visible in the image to the lower right of the foreground contaminant.

galaxies without LyC detections. It must be kept in mind, however that the strength of the Lyman break may not be an effective way to identify the redshifts of LyC-emitting galaxies (see, e.g., Cooke et al., 2014). While the galaxies in the LyC non-detection sample all exhibit a non-detection in U_{336}, there was a large range of $V_{606} - J_{125}$ colors in both the LAE and LBG samples, indicating the corresponding range in rest-frame UV slopes among the galaxies in our sample (see the upper panel of Figure 3.7). In the LBG sample, the $V_{606} - J_{125}$ color ranged from $-0.32 \leq V_{606} - J_{125} \leq 1.03$ (median $V_{606} - J_{125} = 0.24$), with most galaxies displaying red rest-frame UV slopes. In contrast, the LAE sample had $-0.66 \leq V_{606} - J_{125} \leq 1.7$ (median $V_{606} - J_{125} = -0.02$), with most galaxies displaying blue rest-frame UV slopes. While on average the LAEs had bluer UV slopes than the LBGs, the LAE sample also contained the galaxy with the reddest $V_{606} - J_{125}$ color (*lae1843*, $z_{spec} = 2.847$, which contains clumps with $V_{606} - J_{125} = 0.95$ and $V_{606} - J_{125} = 1.7$). The $J_{125} - H_{160}$ colors of galaxies ranged from $0.20 \leq J_{125} - H_{160} \leq 1.19$ (mean $J_{125} - H_{160} = 0.53$), and did not differ significantly between the LBG and LAE samples (see the lower panel of Figure 3.7).

Additionally, there were a few objects in the LyC non-detection sample that demonstrated the typical SED shapes of low-redshift contaminants (see the bottom panel of Figure 3.6). We found that the main features that help identify a low-redshift interloper are the presence of flat $U_{336} - V_{606}$ and $J_{125} - H_{160}$ colors, especially when accompanied by a large break between V_{606} and J_{125}. For contaminants, the break between V_{606} and J_{125} corresponds to a Balmer break or 4000Å break between $0.5 \leq z \leq 2.2$, and has typical values of $0.3 \leq V_{606} - J_{125} \leq 1.2$. The only complication, however, is that young, dusty galaxies may also present nearly flat $J_{125} - H_{160}$ colors with red $V_{606} - J_{125}$ colors. If $U_{336} - V_{606}$ is flat (i.e., no Lyman break), then galaxies with flat $J_{125} - H_{160}$ colors and red $V_{606} - J_{125}$ colors can easily be identified as low-redshift contaminants. However, if $U_{336} - V_{606} > 0$, we must disentangle the degeneracy between contaminants and young, dusty galaxies. In our analysis, we label galaxies with such SEDs "ambiguous cases", an example of which is shown in Figure 3.9. As the redshifts of galaxies with ambiguous SED shapes are uncertain, we do not include them in our analysis of $z \sim 2.85$ galaxies without LyC detections. We also stress again that employing the $U_{336} - V_{606}$

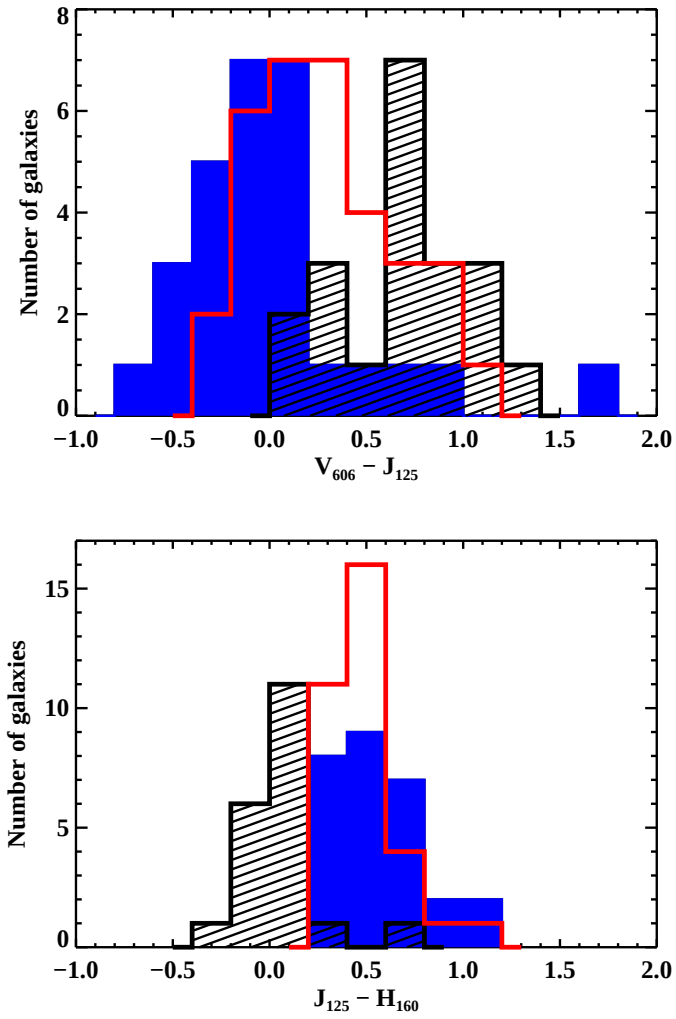

Figure 3.7 Histograms of $V_{606} - J_{125}$ and $J_{125} - H_{160}$ color for objects with $U_{336}V_{606}J_{125}H_{160}$ photometry that do not have ambiguous SED shapes. LBGs are plotted in red, LAEs are plotted in blue, and contaminants are plotted in black. The top panel shows the wide range of $V_{606} - J_{125}$ colors present in both the LAE and LBG samples, although on average LAEs have a bluer rest-frame UV slope than LBGs. The bottom panel demonstrates how important $J_{125} - H_{160}$ color is in distinguishing typical $z \sim 2.85$ galaxies from contaminants, although there are some exceptions (e.g., objects with ambiguous SEDs; see open circles in Figure 3.8).

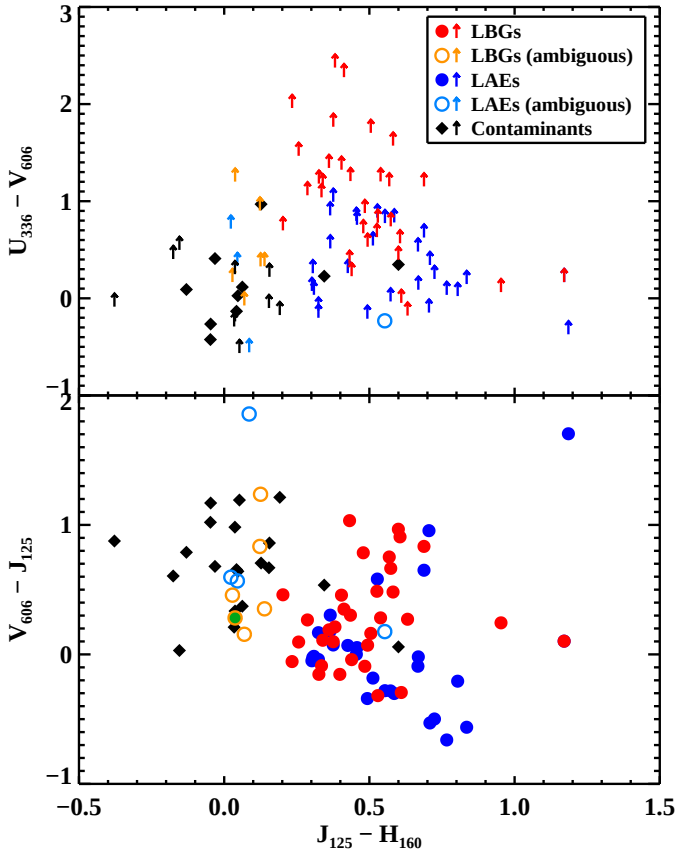

Figure 3.8 $U_{336} - V_{606}$ vs. $J_{125} - H_{160}$ and $V_{606} - J_{125}$ vs. $J_{125} - H_{160}$ color-color plots of all objects with $U_{336}V_{606}J_{125}H_{160}$ photometry. LBGs with typical SED shapes are indicated by solid red circles, and LBGs with ambiguous SED shapes are indicated by open orange circles. LAEs with typical SED shapes are indicated by solid blue circles, and LAEs with ambiguous SED shapes are indicated by open light-blue circles. Foreground contaminants are indicated by black diamonds. Lower limits for all objects are indicated by upward-pointing arrows following the same color scheme. In the lower panel, the best candidate for true LyC emission (MD5b) is indicated by an orange open circle filled with green.

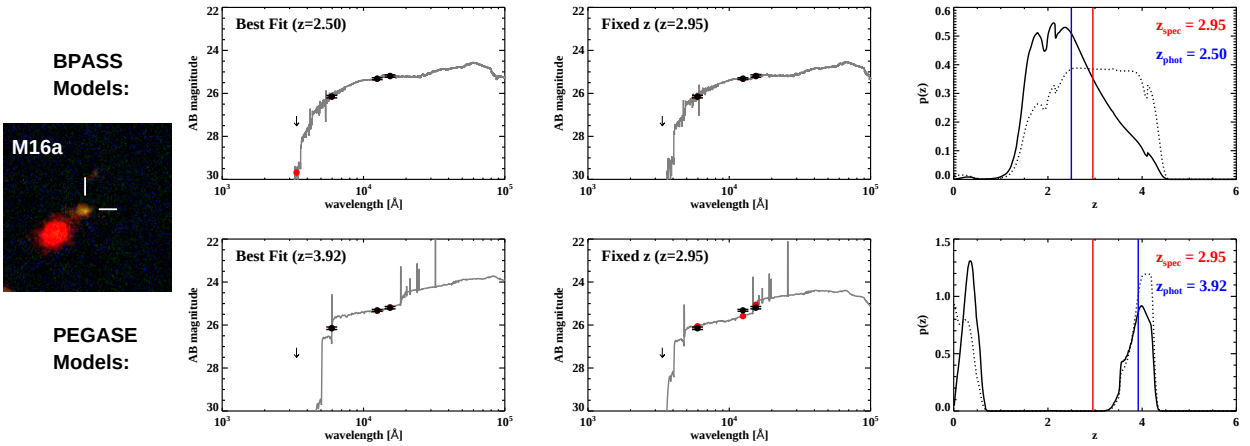

Figure 3.9 M16a demonstrates the typical shape of an "ambiguous" SED, one that can be fit with a wide range of redshifts that encompass both the spectroscopic redshift and lower redshifts typical of foreground contaminants. Results from EAZY are plotted in the three right hand panels, and both the SMC-reddened BPASS models (top row) and the PÉGASE models that include nebular emission (bottom row) are shown to demonstrate the differences between models. In the left-most panel, the redshift is allowed to float during SED fitting, while in the middle panel the redshift is fixed to the spectroscopic redshift. The right-most panel shows the redshift probability distribution. Colors and symbols are as in Figure 3.6. The plot showing the PÉGASE fit at fixed redshift demonstrates the limitations of the PÉGASE models in terms of plotting young galaxies with dust attenuation; even with the redshift known, the PÉGASE templates could not provide a satisfactory fit. Analysis of both the BPASS and PÉGASE redshift probability distributions shows that for an SED of this shape, there is no way to narrow down the redshift to better than $0 < z < 4.5$.

color to distinguish a contaminant from a $z \sim 2.85$ galaxy may be problematic when applied to galaxies with potential LyC emission, as the magnitude of the Lyman break for LyC galaxies is not well understood (M13; Nestor et al., 2013; Steidel et al., 2014). We keep this caveat in mind in Section 3.5.3 when discussing our targets with NB3420 detections. Figure 3.8 demonstrates the relationships between $U_{336} - V_{606}$, $V_{606} - J_{125}$, and $J_{125} - H_{160}$ colors for galaxies at $z \sim 2.85$, galaxies with ambiguous SED shapes, and foreground contaminants. In the $V_{606} - J_{125}$, and $J_{125} - H_{160}$ plot, $z \sim 2.85$ galaxies generally occupy a different region of color-color space from that of foreground contaminants, with the ambiguous cases (differentiated from contaminants by having $U_{336} - V_{606} > 0$) straddling both distributions.

3.5.2 Modeling SEDs with EAZY

While the empirical SED shapes suggest qualitative divisions between low- and high-redshift galaxies, we can also obtain more systematic estimates of the redshifts of our targets. We used the photometric redshift code EAZY (Brammer et al., 2008) to fit the U_{336}, V_{606}, J_{125}, and H_{160} photometry acquired with HST and estimate the redshifts of each sub-arcsecond component in the vicinity of our LAE and LBG targets. In order to choose the best input parameters for EAZY and learn how to interpret the output EAZY produces, we first ran the code on a test sample of $z \sim 2.85$ LBGs and LAEs in our HST images with known spectroscopic redshifts, unambiguous SED shapes, and no NB3420 detections. Later, we supplemented this sample with $z \sim 2.85$ components of galaxies from the NB3420-detected sample for which there was no LyC detection (i.e., galaxies for which the NB3420 detection was proven to be associated with foreground contamination from another clump). This test sample of galaxies should have a low rate of contamination by foreground interlopers, and thus help us evaluate whether or not EAZY can accurately identify galaxies known to be at $z \sim 2.85$ with the photometry provided. Additionally, we were able to analyze galaxies in this sample that exhibited complex morphologies and evaluate the SED fits for each galaxy clump separately. In this way, we developed a procedure for differentiating between clumps that belonged to the spectroscopically confirmed LBG or LAE and those that were lower redshift interlopers. As the galaxies in the test sample do not have NB3420 detections, we were able to make such a distinction without the complication of possible LyC emission, which might be associated with "non-standard" SEDs. Finally, we note that we did not include any components where the SED shape was ambiguous (see definition in Section 3.5.1) because it was not clear from the SED shape if that component was at high or low redshift.

We varied several input parameters to EAZY in order to determine their optimal values. First, we experimented with fitting our data using different stellar population synthesis models. EAZY defaults to PÉGASE models (Fioc & Rocca-Volmerange, 1997), which span a range of star-formation histories, metallicities, ages, and reddenings using the Calzetti

et al. (2000) attenuation curve. EAZY also includes a set of model templates from Blanton & Roweis (2007) (BR07), which are based on Bruzual & Charlot (2003) models. Both the PÉGASE and BR07 models provided good, qualitatively similar fits to most of our LBGs and LAEs, but failed to accurately represent galaxies with blue UV slopes ($V_{606} - J_{125} < -0.1$) and galaxies with SEDs younger than ∼50 Myr (see Figure 3.9). Therefore, we experimented with additional stellar population models that might provide a better fit to the bluest and youngest galaxies in our sample. These included BPASS models, which have a more accurate treatment of Wolf-Rayet stars and massive stellar binaries (Eldridge & Stanway, 2009), and Starburst99 (SB99) models with updated treatment of stellar rotation (Leitherer et al., 2014). Additional impetus for considering bluer templates is their increased emission in the LyC spectral region, which may provide a method of more accurately modeling galaxies with LyC detections. In addition to experimenting with the choice of stellar population models, we also used two different extinction curves to redden the BPASS and SB99 models, for which only constant star-formation (CSF) histories are available. The Calzetti et al. (2000) attenuation curve has been traditionally used to model extinction in high-redshift star-forming galaxies, but recent work (e.g., Siana et al., 2009; Reddy et al., 2006b, 2010, 2012) has shown that an SMC extinction curve may be more appropriate for galaxies with ages younger than 100 Myr. Therefore, we made two sets of CSF templates with each of the BPASS and SB99 models, one template set reddened exclusively with the Calzetti et al. (2000) attenuation curve, and another reddened with the Calzetti et al. (2000) attenuation curve for templates with older galactic ages and the SMC extinction curve from Gordon et al. (2003) for templates with ages less than 100 Myr.

Based on the analysis of objects without LyC detections, we verified that, for the majority of galaxies, EAZY estimates the correct redshift of the galaxy within roughly ±0.5 of the spectroscopic redshift. Thus, we can successfully use photometric redshifts to determine if most galaxy clumps are at $z \sim 2.85$ or are low-redshift contaminants, keeping in mind that we have fairly coarse redshift precision. As EAZY provides several estimators for the

photometric redshift (e.g., z_p[3], z_{m2}[4], z_{peak}[5]), we investigated each of them while varying the input parameters to the program and determined that z_{peak} provided the best estimate of the spectroscopic redshift. All photometric redshifts we quote use the z_{peak} estimator. Of the range of input parameters tested on the sample of objects without LyC detections, we determined that the PÉGASE models provide the best overall fits to the SEDs. These models had both the smallest systematic offset and lowest standard deviation of all the variations of input parameters we tried, yielding $(z_{phot} - z_{spec})/(1 + z_{spec}) = -0.03 \pm 0.07$. We note that while the PÉGASE models work best for the sample as a whole, the BPASS models provide the best fits to galaxies with blue rest-frame UV slopes ($V_{606} - J_{125} < -0.1$). Also, as the EAZY PÉGASE models only include 5 templates, they did not accurately fit galaxies with younger SEDs. Better fits were achieved for young galaxies by implementing a fine grid of young BPASS templates, specifically by including SMC-reddened models with ages of 1 Myr, 5 Myr, 10 Myr, 30 Myr, and 50 Myr. Throughout our analysis of the galaxies with potential LyC detections (Section 3.5.3), we employ both the PÉGASE models and the SMC-reddened BPASS models with additional young galaxy templates in order to fully examine the likely photometric redshifts for each galaxy. All figures in this paper displaying output from EAZY show fits using the SMC-reddened BPASS models, unless otherwise indicated.

3.5.3 Results of Photometric Redshift Fits for Potential LyC Emitters

In total, we have observations in all four $U_{336}V_{606}J_{125}H_{160}$ filters for 16 galaxies with potential LyC detections. These 16 galaxies include 4 LBGs and 8 LAEs with spectroscopic confirmation, as well as 4 LAE photometric candidates. In this section, we discuss the results of our analysis of these potential LyC emitters. We describe the sources of contamination for 11 targets with obvious contaminants, present 4 galaxies with ambiguous SEDs that may or may not be at high redshift, and argue for MD5 as a true LyC emitter. We also note 3 objects for which the *HST* imaging revealed that the spectroscopic redshift was incorrectly

[3]Redshift where the likelihood is maximized after applying the magnitude-based prior.

[4]Redshift marginalized over the posterior probability distribution.

[5]Hybrid between z_p and z_{m2} to address the pathological case where there are two widely-separated peaks in the probability distribution that have similar integrated probabilities.

assigned in M13.

3.5.3.1 Foreground Contaminants in the LyC Sample

Seven objects with Keck/LRIS spectroscopic redshifts (2 LBGs: MD12, M16; 5 LAEs: *lae1670*, *lae2292*, *lae2966*, *lae6662*, and *lae7832*) and one object in the photometric LAE sample (*lae3038*) had contaminants that stood out plainly with the combination of high-resolution *HST* imaging and SED fitting. Each of these objects was resolved into several clumps in the *HST* imaging. In all cases, at least one of the clumps had an SED fit corresponding to the redshift of the Keck/LRIS spectrum (or consistent with the spike redshift $z = 2.85$, in the case of *lae3038*), while the clump associated with the LyC emission had the unambiguous SED of a $0.5 \leq z \leq 2.2$ contaminant (flat $U_{336} - V_{606}$ and $J_{125} - H_{160}$, red $V_{606} - J_{125}$; similar to the example contaminant shown in the bottom panel of Figure 3.6). For these eight objects, the NB3420 emission had a fairly large offset from the original galaxy coordinates; the offsets between the NB3420 detection and Lyα emission ranged from $0\farcs57$ to $1\farcs15$ with a median value of $0\farcs65$ (5.0 kpc at $z = 2.85$), and offsets between the NB3420 emission and the LRIS $V-$band emission ranged from $0\farcs12$ to $1\farcs26$ with a median value of $0\farcs72$ (5.7 kpc at $z = 2.85$). The morphology of these objects in the *HST* images supports the evidence from the SED fits that these objects are not physically associated; the clumps are distinct, with no evidence for diffuse emission between them that might indicate interactions between galaxies at the same redshift.

A third LBG in our sample, MD34, has an NB3420 detection coincident with two clumps in the *HST* imaging, only one of which is from a foreground contaminant. Figure 3.3 shows the eight distinct components associated with MD34 (MD34a though MD34h). Components MD34a through MD34f all have SED shapes that place them at the spectroscopic redshift of MD34 ($z = 2.85$), and MD34g and MD34h have SED shapes indicative of foreground contaminants. The NB3420 emission for MD34 is coincident with two clumps in the *HST* imaging: MD34f ($z = 2.85$) and MD34g ($z < 2.5$), separated on the sky by $0\farcs31$. Both MD34f and MD34g exhibit emission in the U_{336} filter, although both detections are less

than 3σ. It is unclear whether the NB3420 emission associated with MD34 is due solely to non-ionizing UV radiation from the foreground contaminant MD34g, or also in part to LyC emission from the $z = 2.85$ component MD34f. As the high-resolution U_{336} image does not exclusively probe the LyC spectral region at $z = 2.85$, and the foreground contaminant MD34g is too close to MD34f to distinguish in the seeing-limited NB3420 image, we cannot confirm MD34 as having a robust LyC detection. Because the interpretation of this case is ambiguous, we do not include MD34 in the final sample of LyC emitters.

For an additional object, *lae2436*, the presence of an extended Lyα blob (Steidel et al., 2000, 2011) near the position of the LAE made the original analysis of the LRIS imaging and spectra difficult. The deep, high-resolution *HST* imaging helped us clarify the interpretation of this object and determine that the NB3420 detection is associated with a foreground contaminant. Figure 3.10 shows the complex morphology of *lae2436* in both the LRIS $V-$band and the continuum-subtracted Lyα images. The Lyα blob extends over more than $5''$, and in the LRIS $V-$band image two bright galaxies (X and Y) appear to be in the vicinity of the Lyα blob, with diffuse emission between them. As shown in Figure 3.10, both Galaxy X and Galaxy Y exhibit Lyα emission in the LRIS spectrum (L3 and L1, respectively) and were identified as LAEs in M13. Galaxy X was originally identified as the LAE *lae2436* ($z = 2.832$), and this galaxy is clearly detected in the NB3420 image. There are no other NB3420 detections nearby. Finally, there is a Lyα emission line (L2) in the LRIS spectrum coincident with the diffuse emission between Galaxies X and Y in the LRIS $V-$band image. This diffuse emission was originally attributed to the presence of the Lyα blob and thought to be associated with Galaxy X, as L2 and L3 have nearly identical wavelengths.

In the *HST* imaging, much additional substructure is revealed in the vicinity of the Lyα blob. First, it becomes clear that the diffuse emission in the LRIS $V-$band image is due to several unresolved, faint galaxies in close proximity. One of these galaxies (Z) is roughly coincident with the L2 Lyα emission line in the LRIS spectrum, and the SED fit to this galaxy using *HST* photometry places it near $z = 2.832$, the redshift of the emission line.[6]

[6]We note that Galaxy Z has a unique and extremely red SED, with $V_{606} - J_{125} = 2.08$ and $J_{125} - H_{160} = 1.18$. This galaxy is a sub-millimeter source that will be further described in Steidel et al., in prep.

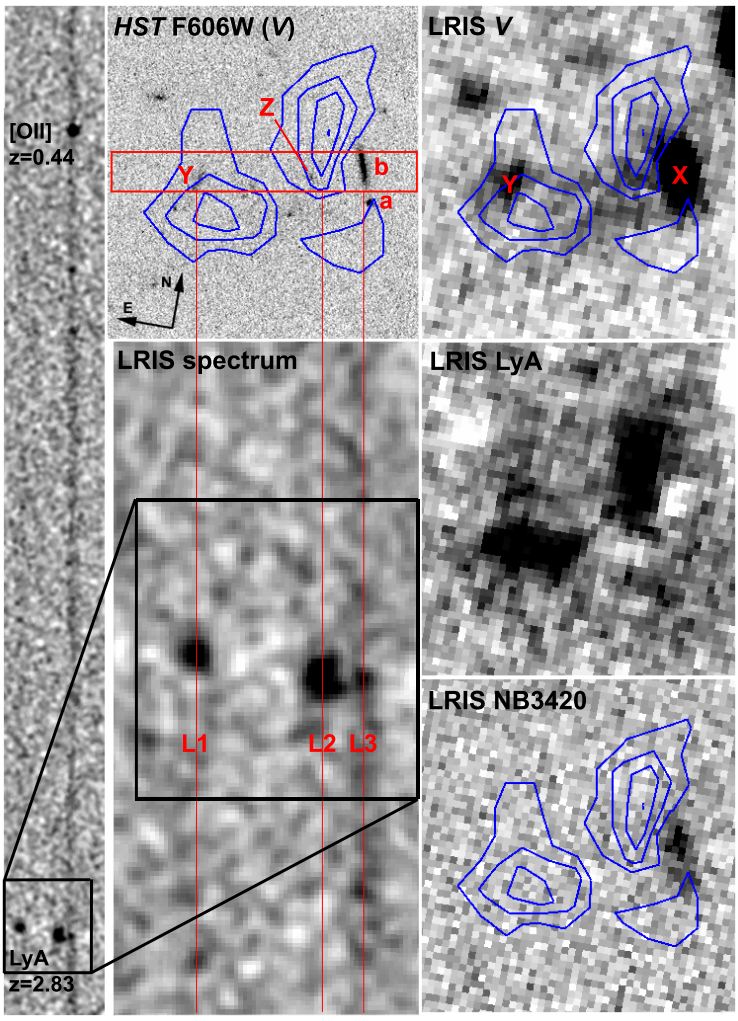

Figure 3.10 *HST* and LRIS Imaging for *lae2436* is displayed ($9\farcs5 \times 9\farcs5$), along with the LRIS spectrum probing the rest-frame UV at $z \sim 2.85$. Along the right-hand column of the figure, the morphology of the Lyα-blob in the vicinity of *lae2436* is shown in LRIS V (non-ionizing UV continuum), LRIS continuum-subtracted NB4670$-V$ (indicating Lyα emission), and LRIS NB3420 (LyC emission). To the left of the LRIS V image, the higher resolution *HST* V_{606} image is shown. Blue contours indicate the location of the Lyα emission based on the NB4670$-V$ image. The red rectangle in the *HST* V_{606} image shows the location of the $1\farcs2$ slit, and the LRIS 2D spectrum below is aligned to match in the orientation and spatial scale of the imaging. The zoomed-in portion of the 2D spectrum shows the Lyα emission (L1, L2, L3), and the full 2D spectrum is displayed on the left. In the original LRIS imaging, only two galaxies were visible near the Lyα-blob (X and Y). These galaxies were identified as LAEs based on their $V-$NB4670 colors and the Lyα emission in the LRIS spectrum. As discussed in Section 3.5.3.1, Galaxy Z was first identified in the *HST* imaging and is likely associated with the Lyα emission in the LRIS spectrum. Galaxy X, meanwhile, breaks into two segments in the *HST* image (a and b) that were both identified spectroscopically as foreground contaminants through reexamination of the available LRIS spectra. The [OII] ($z = 0.44$) emission from *lae2436b* is visible in the top of the full 2D spectrum. We conclude that there is no NB3420 emission associated with *lae2436*.

None of the SEDs for other galaxies in the vicinity of the L2 emission line demonstrate the typical features of $z \sim 2.85$ galaxies. As for object X, originally identified as *lae2436*, it breaks into two separate galaxies in the *HST* image (a and b), both of which are detected in NB3420. Subsequent reanalysis of the available spectra near the Lyα blob allowed us to confirm spectroscopic redshifts for both of these galaxies ($z = 2.04$ for *lae2436a*, $z = 0.44$ for *lae2436b*), and the SED fits to both objects are consistent with their spectroscopic redshifts. In particular, we draw attention to the spectrum of *lae2436b*, visible in Figure 3.10 on the right-hand side of the LRIS spectrum, coincident with L3. In the zoomed-out version of the spectrum, a spurious emission line is visible at 5375Å which we have identified as [OII] at $z = 0.44$. The Lyα emission line originally identified for this object (L3) must be due to extended Lyα emission from the Lyα-blob. In conclusion, as both *lae2436a* and *lae2436b* are at $z < 2.82$, the NB3420 filter does not probe LyC emission for these galaxies and thus the NB3420 detections associated with both galaxies are foreground contamination.

Finally, we found that one object in the spectroscopic LAE sample, *lae7890*, was misidentified as an LAE. This object was presented in the Appendix of M13 as a faint LAE with a borderline color excess ($V-$NB4670 = 0.70) and a possible LyC detection, and was not analyzed with the main LAE sample for which a NB4670 magnitude limit of $m_{4670} \leq 26$ was imposed. A marginal emission line had been identified for this object, placing it at the spike redshift of $z = 2.85$, but the SED (similar to that of the contaminant in Figure 3.6) indicates unequivocally that *lae7890* is at low redshift, in the range of $1 < z < 2$. We considered [OII] as a possible source of the emission line, but that would place *lae7890* at $z = 0.26$, which is also inconsistent with the observed SED. Thus we conclude that this faint emission line is either spurious, or is possibly consistent with [CIII] 1907Å / CIII] 1909Å emission from a galaxy at $z = 1.45$. In either case, the NB3420 emission is not LyC.

In summary, 11/16 candidate LyC emitters in our sample show obvious signs of foreground contamination at the position of the NB3420 detection. For 9 objects, there is a bona fide $z = 2.85$ galaxy at the position of the LAE, with an additional foreground galaxy offset from the LAE and associated with the NB3420 emission. For 2 objects, $z = 2.85$ was erroneously assigned to the candidate LAE, and, again, the NB3420 emission is actually

non-ionizing UV flux from a low-redshift contaminant. In all of these cases, the available evidence suggests that we are not observing LyC emission at $z = 2.85$.

3.5.3.2 Ambiguous Cases

For the four photometric LAE candidates with NB3420 detections, the SED shape was ambiguous and there were no spectroscopic redshifts available to confirm that the objects are indeed at $z \sim 2.85$. These two factors make it impossible to confidently claim a LyC detection for any of these objects. We discuss the photometry and SED fits for these objects in detail in the Appendix, and summarize the results here. One object, *lae4070*, has similar $J_{125} - H_{160}$ and $V_{606} - J_{125}$ colors to many $z \sim 2.85$ galaxies in our sample and is the most promising photometric LAE candidate for true LyC emission. The other three objects (*lae5200*, *lae6510*, and *lae7180*) display the ambiguous SED shape described in Section 3.5.1, which may describe galaxies at many redshifts. As we cannot unambiguously determine whether or not the four photometric LAE candidates discussed in this section are truly at $z \sim 2.85$, we adopt a conservative approach and do not count the NB3420 detections for these objects as secure signatures of leaking LyC radiation.

3.5.3.3 LyC Emission from MD5

The best candidate for true LyC emission is the LBG MD5, which has a spectroscopic redshift of $z = 3.14$ confirmed by spectra from both LRIS and the MOSFIRE near-IR multi-object spectrograph (see Figure 3.11). The LRIS spectrum was taken in May 2011 (M13) and shows Lyα emission ($z = 3.147$), along with several absorption features (CII, SiII, and OI; $z = 3.139$). The $K-$band MOSFIRE spectrum was acquired in June 2012, and contains detections of both [OIII] emission lines (4959Å, 5007Å; $z = 3.1426$). Unfortunately, we were unable to measure the $z = 3.14$ Hβ emission line in this spectrum because it falls on a sky line. In the *HST* imaging, MD5 breaks into two clumps separated by $0\farcs58$ along a direction 32 degrees East of North (MD5a and MD5b; see Figure 3.11); only MD5b is coincident with the NB3420 emission. The orientation of the LRIS and MOSFIRE observations (slit PAs of

111 and 274 degrees, respectively) were such that both clumps fell within the spectroscopic slits. Although it is not possible to distinguish between the clumps in the spectra due to seeing (0.″7-1.″0 for LRIS, 0.″6 for MOSFIRE) and slit orientation, neither spectrum shows evidence for spurious emission or absorption features that would indicate the presence of a low-redshift interloper.

Ideally, as in the case of *Ion1* in Vanzella et al. (2012), a candidate LyC-emitting galaxy would have a simple, compact morphology. In such a case, the probability of a foreground interloper is negligible. However, it has been shown that high-redshift galaxies typically exhibit clumpy morphologies (see, e.g., Law et al., 2007; Lotz et al., 2006). Of the 35 LBGs in our $z \geq 2.82$ sample with imaging in V_{606}, only 20% have simple, compact morphologies. Close inspection reveals clumpy morphologies in all other cases, and several LBGs are comprised of clumps with offsets significantly greater than the 0.″58 offset of the MD5 clumps. For example, LBGs M23, MD9, and C13 are comprised of clumps suggested by SED fits to be at the LBG redshift with offsets of 0.″91, 1.″00, and 1.″19, respectively. As the majority of LBGs consist of several associated clumps at the same redshift, the fact that MD5 displays multiple clumps does not necessarily indicate that MD5b (the clump associated with the NB3420 detection) is a foreground contaminant.

However, the presence of the second clump opens the possibility that one of these clumps is a low-redshift interloper, and thus we examine the SED fits to MD5a and MD5b for evidence of foreground contamination (see Figure 3.11). Both clumps are nearly identical in V_{606} magnitude, and are within 0.1-0.2 magnitudes in J_{125} and H_{160}. MD5a has the SED shape typical of most $z \sim 3$ galaxies in our sample and is almost certainly at the spectroscopic redshift $z = 3.14$. MD5b has the ambiguous SED shape described in Section 3.5.1. As the spectroscopic redshift of MD5 is higher than most galaxies in our sample, the H_{160} filter actually falls right at the location of the Balmer break, rather than redwards of the break. Thus, the H_{160} filter is partially contaminated by flux bluewards of the Balmer break, and $J_{125} - H_{160}$ no longer probes the full strength of the break. Therefore, the fact that MD5b has a smaller $J_{125} - H_{160}$ color than the lower-redshift LBGs in our sample does not necessarily indicate a young age or low-redshift contaminant.

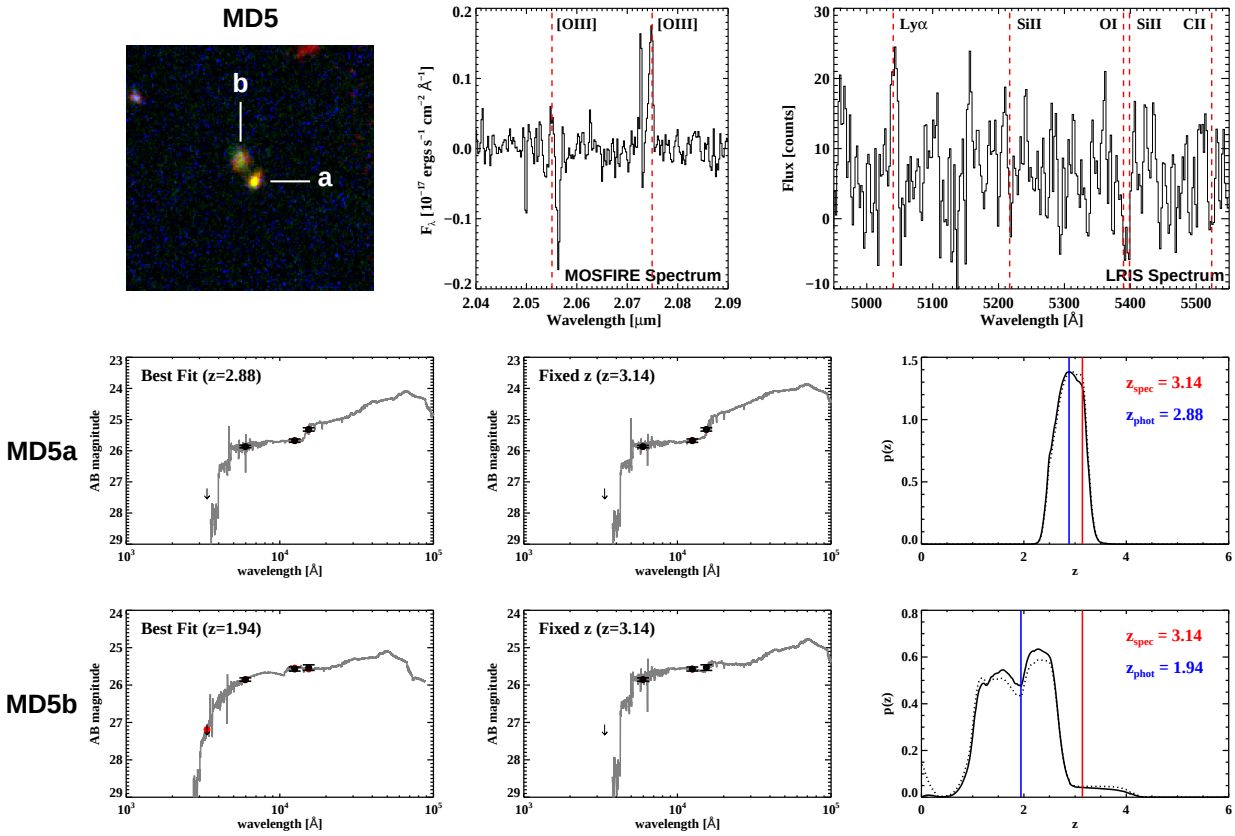

Figure 3.11 Imaging, spectra, photometry, and SED fits for MD5. The top left panel shows the $U_{336}V_{606}J_{125}$ color-composite *HST* image for MD5, indicating the two sub-arcsecond components (MD5a and MD5b). To the right of the image are displayed the MOSFIRE and LRIS spectra of MD5. We detect the [OIII] doublet (4959Å, 5007Å; $z = 3.1426$) in the MOSFIRE $K-$band spectrum, and Lyα emission ($z = 3.147$) along with several interstellar absorption lines (1303Å(OI + SiII), 1334Å(CII); $z = 3.139$) in the LRIS spectrum. The interstellar absorption lines are blueshifted relative to the Lyα and [OIII] emission, indicative of an outflow. Below the spectra and imaging are shown the EAZY output for MD5a and MD5b. In the left-most panel, the redshift is allowed to float during SED fitting, while in the middle panel the redshift is fixed to $z = 3.14$, the redshift indicated by the spectra. The right-most panel shows the redshift probability distribution. Colors and symbols are as in Figure 3.6. MD5a has the typical SED shape associated with $z \sim 3$ galaxies in our sample. MD5b, which is associated with the NB3420 detection, exhibits the ambiguous SED shape discussed in Section 3.5.1. As there is no evidence of foreground contamination in either the MOSFIRE or LRIS spectra, we propose that both of these clumps are at the spectroscopic redshift 3.14 and that the NB3420 emission associated with MD5b is true LyC emission.

Figure 3.8 shows MD5b plotted with respect to other galaxies in our sample in $V_{606}-J_{125}$ vs. $J_{125}-H_{160}$. If MD5b is truly at $z = 3.14$, it has a very small Balmer break ($J_{125}-H_{160} = 0.04\pm0.13$), a red UV slope ($V_{606}-J_{125} = 0.28\pm0.10$, equal to the mean of the LBG sample), and a U_{336} detection brighter than expected by standard stellar population synthesis models (unsurprising for a LyC emitter). If MD5b is a foreground interloper, EAZY estimates that the most likely redshifts for the interloper are $0 < z < 0.5$ or $2 < z < 2.5$ using PÉGASE models, and between $1 < z < 2.8$ using reddened BPASS models. In both cases, $z \sim 2.3-2.4$ is the most likely contaminant redshift.

The strongest evidence that MD5b is indeed at $z = 3.14$ is the lack of spurious emission or absorption lines in both the LRIS and MOSFIRE spectra. Because these spectra span different wavelength ranges (3100−7000 Å for LRIS and 1.95−2.4 μm for MOSFIRE), we can rule out strong emission lines for several redshift ranges. We can rule out Hα emission between $1.97 < z < 2.65$, Lyα emission at $z > 1.5$, [OII] emission at $z < 0.9$, and [OIII] emission at $z < 0.4$. We note that the lack of spurious emission lines in the $K-$band MOSFIRE spectrum rules out Hα emission right in the redshift range predicted by EAZY to be the most probable redshift of a contaminant ($2 < z < 2.6$). It might be possible to confirm the redshift of MD5b using MOSFIRE observations with the slit oriented along the axis connecting MD5a and MD5b. These observations would maximize the distance between the two clumps (separated by $0\farcs58$) and, if taken under conditions of good seeing, potentially distinguish emission from each clump individually.

3.6 Properties of the Lyman-Continuum Emitter MD5

One of the main goals of this work is to investigate the multiwavelength properties of galaxies with and without LyC emission, in order to better understand the mechanism of LyC photon escape from galaxies. We are also interested in investigating any systematic differences between galaxies with and without LyC emission, for such differences may facilitate the search for LyC-emitting galaxies both during and after the epoch of reionization. As our *HST* data has left us with only one robust candidate for LyC emission (MD5), we here discuss

the morphological properties and best-fit stellar population of this object with respect to the properties of typical LBGs.

3.6.1 Morphology of MD5

Figure 3.3 displays imaging of MD5 in all available bands. Morphologically, MD5 is composed of two clumps (MD5a, MD5b) separated by $0\farcs58$ (4.4 kpc at $z = 3.14$). The V_{606} magnitudes for each clump (representing the non-ionizing UV continuum) are $m_{606}^{MD5a} = 25.87 \pm 0.04$ and $m_{606}^{MD5b} = 25.85^{+0.05}_{-0.04}$. In Section 3.5.3.3 we present arguments for why both of these clumps are likely at the spectroscopic redshift of $z = 3.14$ and why foreground contamination is unlikely. The clumpy morphology of MD5 is similar to that of many other LBG systems, which commonly exhibit significant substructure. MD5b, which is more diffuse and lower in surface brightness than MD5a, is the clump associated with the NB3420 detection (i.e., the LyC emission).

Because of the particularly high redshift of MD5, we are able to directly map the LyC emission in the high-resolution *HST* U_{336} image. While most galaxies in our sample had redshifts of roughly $z \sim 2.85$ and the U_{336} filter was partially contaminated by non-ionizing flux redwards of the Lyman limit, MD5 is at high enough redshift ($z = 3.14$) that the U_{336} filter probes the LyC spectral region without any contamination. While MD5b is formally undetected in U_{336} at 3σ, emission at the location of MD5b is visible by eye in the U_{336} imaging. MD5b has a 2.25σ detection in U_{336} ($m_{336} = 27.37^{+0.64}_{-0.40}$), which is consistent within errors of the detection in NB3420 ($m_{NB3420} = 26.89^{+0.43}_{-0.31}$).[7]

In light of models in which LyC emission may escape anisotropically from galaxies (e.g., Gnedin et al., 2008; Zackrisson et al., 2013), we examined the offset between the centroid of the U_{336} and V_{606} emission for MD5b in order to determine if there was a significant offset between the ionizing and non-ionizing UV emission. We measured a value for this offset of $\Delta_{UV} = 0\farcs08$. As there are no additional $z \sim 3$ galaxies in our sample with U_{336} detections to compare to, we examined the distribution of $U_{336}-V_{606}$ offsets for the foreground

[7]We note that the U_{336} filter is wider than NB3420, and thus the fainter U_{336} magnitude may be due to increased IGM attenuation within the bluer half of the U_{336} filter.

contaminants in our sample. In this way, we measured Δ_{UV} for objects where U_{336} and V_{606} are both probing the non-ionizing continuum, and thus should not demonstrate significant offsets. For the contaminant sample, we found a roughly flat distribution of offsets between $0\farcs0$ and $0\farcs12$ with a mean offset of $0\farcs065$ and a standard deviation of $0\farcs031$. As MD5b has an offset consistent with the mean of the contaminant distribution, we conclude that its measured offset is not significant. This lack of significant offset implies either that LyC emission is escaping isotropically from MD5b, or that, if LyC emission escapes only from cleared holes in the ISM, MD5b must be oriented such that the opening is along our line of sight.

3.6.2 ISM Kinematics of MD5

The spectral features of MD5 shed light on the kinematics of its ISM. The [OIII] λ5007 nebular emission line observed in the MOSFIRE spectrum of MD5, which indicates the systemic redshift, places MD5 at $z = 3.1426$. This line has an intrinsic width of $\sigma_v = 37$ km s^{-1}, typical of LAEs, but half that of typical LBGs (Trainor et al., in prep; Pettini et al., 2001). The low-ionization interstellar absorption features observed in the LRIS spectrum of MD5 (OI + SiII λ1303, CII λ1334) are consistent with a redshift of $z = 3.139$, blueshifted relative to the [OIII] emission. The magnitude of this blueshift corresponds to a velocity offset of $\Delta v_{IS} \sim 280$ km s^{-1}, higher than the median Δv_{IS} for LBGs (150 km s^{-1}; Shapley et al., 2003), but fairly uncertain due to the low signal-to-noise of the LRIS spectrum. Additionally, the redshift derived from the centroid of the Lyα emission line ($z = 3.147$) corresponds to a velocity offset of $\Delta v_{Ly\alpha} \sim 300$ km s^{-1}, which is typical of LBGs ($\Delta v_{Ly\alpha}^{LBG} =$ 360 km s^{-1}; Shapley et al., 2003). Thus, in terms of its kinematics, MD5 does not stand out significantly with respect to the full population of LBGs, although the blueshift of its interstellar absorption lines is higher than average. We note that with the spatial resolution of our spectra, we cannot resolve the two components MD5a and MD5b separately and evaluate their individual kinematics. Finally, we note that our measured value of $\Delta v_{Ly\alpha}$ is inconsistent with predictions for LyC-leaking galaxies from Verhamme et al. (2014), who find small offsets between Lyα emission and the systemic redshift ($\Delta v_{Ly\alpha} \leq 150$ km s^{-1}) in

models of galaxies with leaking LyC radiation.

3.6.3 Stellar Populations of MD5

In addition to providing high-resolution imaging of MD5, the multiwavelength *HST* data also enabled us to fit the photometry for both sub-arcsecond components (MD5a and MD5b) with stellar population synthesis (SPS) models. For this purpose, we employed the stellar population fitting code FAST (Kriek et al., 2009). To model the photometry, we fixed the redshift to the spectroscopically measured value and used Bruzual & Charlot (2003) models ranging in age from 50 Myr to 2 Gyr with delayed-τ star-formation histories (SFR $\propto te^{-t/\tau}$) and a Chabrier (2003) initial mass function. The lower age limit of 50 Myr is adopted to reflect the LBG dynamical timescale, following Reddy et al. (2012). However, we note that this age limit is conservative, and may be larger than necessary given the small sizes of some galaxy subcomponents. For dust extinction, we employed the Calzetti et al. (2000) attenuation curve. We adopted solar metallicity for the models because, with only four photometric points, we did not have enough data to constrain metallicity. By performing tests with several values for fixed metallicity and with metallicity as a free parameter, we verified that metallicity does not have a significant effect on the final fit. We note that even when metallicity was allowed to float, the best-fit model for MD5b had solar metallicity.

We display the best fit models and photometry for MD5a and MD5b in Figure 3.12. We note that while the U_{336} data point for the LyC-emitter MD5b does not agree with the model prediction, this is to be expected from Bruzual & Charlot (2003) models, which do not have significant emission bluewards of 912Å. We also report the best-fit values and 68% confidence intervals for τ, stellar mass, star-formation rate (SFR), dust extinction, and age. For MD5a, the clump without leaking LyC emission, we found: $\log(\tau) = 8.6^{+1.4}_{-0.6}$, $\log(\text{Mass } [\text{M}_\odot]) = 9.70^{+0.25}_{-0.40}$, $\log(\text{SFR } [\text{M}_\odot \text{ yr}^{-1}]) = 0.51^{+0.43}_{-0.14}$, $E(B-V) = 0.02^{+0.10}_{-0.02}$, and $\log(\text{Age } [\text{yr}]) = 9.10^{+0.20}_{-0.67}$. In constrast, for MD5b, the clump with leaking LyC emission, we found: $\log(\tau) = 8.2^{+1.8}_{-0.2}$, $\log(\text{Mass } [\text{M}_\odot]) = 8.69^{+0.49}_{-0.10}$, $\log(\text{SFR } [\text{M}_\odot \text{ yr}^{-1}]) = 1.31^{+0.09}_{-0.47}$, $E(B-V) = 0.17^{+0.03}_{-0.09}$, and $\log(\text{Age } [\text{yr}]) = 7.70^{+1.058}_{-0}$.

[8]The confidence interval is bounded by $\log(\text{Age } [\text{yr}]) = 7.70$ (age = 50 Myr) because that is the minimum

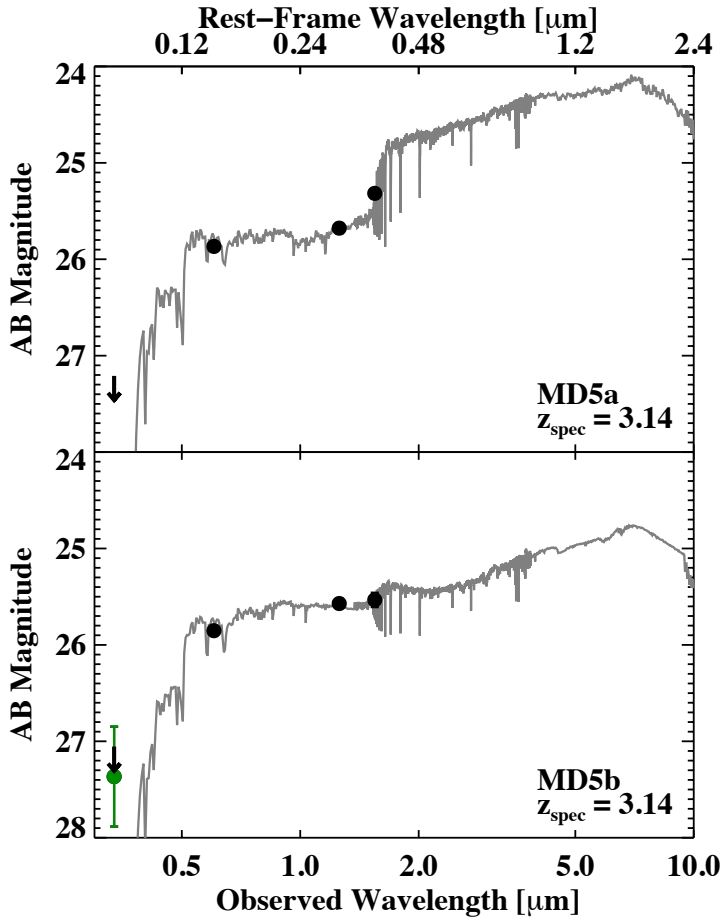

Figure 3.12 Best-fit Bruzual & Charlot (2003) stellar population synthesis models as computed by FAST (gray line) to *HST* $U_{336}V_{606}J_{125}H_{160}$ photometry for MD5a and MD5b (black circles), fit at the spectroscopic redshift of $z = 3.14$. One-sigma photometric uncertainties are smaller than the data points. For MD5b, the 2.25σ detection in U_{336} (probing the LyC spectral region at $z = 3.14$ with no contamination redwards of the Lyman limit) is plotted in green, with the formal 3σ limit indicated by the black arrow. We note that while the U_{336} data point for MD5b does not agree with the model prediction, this is to be expected from Bruzual & Charlot (2003) models, which do not have significant emission bluewards of 912Å. Parameters of the fits are listed in Table 3.4.

The fits to MD5a and MD5b describe two very different stellar populations. MD5a has an old stellar population with significant stellar mass, a low star-formation rate, and very little reddening. MD5b, however, is young and low-mass, with a much higher star-formation rate and a larger $E(B-V)$. While we have set a minimum LBG age limit of 50 Myr following Reddy et al. (2012), the best-fit model to MD5b without a minimum age requirement is even younger (10 Myr). Because of the differing stellar populations of MD5a and MD5b, it is possible that they are two distinct galaxies in the process of merging. It is also possible that they are simply two sub-regions of the same galaxy, one of which (MD5b) is undergoing a recent burst of star formation that has greatly increased its non-ionizing UV and LyC fluxes, making it more likely to detect LyC emission.

In addition to modeling the stellar populations of MD5a and MD5b individually, we used FAST to model the best-fit stellar population to the combined photometry of both components. While such modeling does not represent a physically meaningful stellar population[9], it facilitates a comparison to the results of ground-based LBG surveys, recreating the flux that would be measured by instruments lacking the high resolution of *HST*. For the combined photometry of MD5, we found: $\log(\tau) = 8.2^{+1.8}_{-0.2}$, $\log(\text{Mass } [\text{M}_\odot]) = 9.52^{+0.54}_{-0.53}$, $\log(\text{SFR } [\text{M}_\odot\ \text{yr}^{-1}]) = 1.13^{+0.58}_{-0.47}$, $E(B-V) = 0.1^{+0.11}_{-0.1}$, and $\log(\text{Age } [\text{yr}]) = 8.5 \pm 0.8$.

age we enforce upon the models.

[9]For example, the mass and SFR derived from the best-fit model to the combined photometry of MD5 are less than the summed individual masses and SFRs of MD5a and MD5b.

Table 3.4. Stellar Population Parameters

Sample	log(Stellar Mass) [$M_\odot$]	log(SFR) [$M_\odot$ yr^{-1}]	$E(B-V)$[a] [mag]	log(Age) [yr]
MD5a[b]	$9.70^{+0.25}_{-0.40}$	$0.51^{+0.43}_{-0.14}$	$0.02^{+0.10}_{-0.02}$	$9.10^{+0.20}_{-0.67}$
MD5b (LyC detected)[b]	$8.69^{+0.49}_{-0.10}$	$1.31^{+0.09}_{-0.47}$	$0.17^{+0.03}_{-0.09}$	$7.70^{+1.05}_{-0}$
MD5 combined photometry[b]	$9.52^{+0.54}_{-0.53}$	$1.13^{+0.58}_{-0.47}$	$0.10^{+0.11}_{-0.10}$	$8.50^{+0.80}_{-0.80}$
LBG sub-arcsecond components[c]	$9.26^{+0.72}_{-0.53}$	$0.75^{+0.76}_{-0.76}$	$0.10^{+0.20}_{-0.10}$	$8.80^{+0.20}_{-0.50}$
LBG combined photometry[c]	$9.77^{+0.58}_{-0.26}$	$1.05^{+0.59}_{-0.22}$	$0.10^{+0.12}_{-0.07}$	$8.80^{+0.40}_{-0.40}$
LBG combined photometry + contaminants[c]	$9.84^{+0.22}_{-0.19}$	$1.29^{+0.37}_{-0.41}$	$0.10^{+0.15}_{-0.05}$	$8.80^{+0.30}_{-0.40}$
$2.7 < z < 3.7$ LBGs from Reddy et al. (2012)[e]	$9.78^{+0.47}_{-0.39}$	$1.65^{+0.40}_{-0.49}$	$0.18^{+0.09}_{-0.10}$	$8.05^{+0.90}_{-0.35}$

[a]Derived from A_V, assuming $k(V) = k(5500) = 4.048$ from Calzetti et al. (2000).

[b]Best fit values from FAST assuming a delayed-τ star-formation history, a minimum age of 50 Myr, and Calzetti et al. (2000) attenuation. Uncertainties quoted are 68% confidence intervals.

[c]Median values for LBG samples are quoted, along with values bracketing the inner 68% of the distributions.

[e]Best-fit stellar population parameters for $2.7 < z < 3.7$ LBGs from Reddy et al. (2012), assuming a constant star-formation history, a minimum age of 50 Myr, and Calzetti et al. (2000) attenuation. Median values are quoted, along with values bracketing the inner 68% of the distributions.

In order to compare the derived properties of MD5a, MD5b, and the combined photometry with those of typical LBGs, we fit SPS models to the remainder of the LBGs in our sample and examined their stellar masses, star-formation rates, dust extinction, and ages. We performed this analysis both for individual sub-arcsecond components of LBGs, for the combined fluxes from all components of each LBG (simulating ground-based studies that are free of contamination), and for a combined-flux sample that also includes foreground contaminants in cases where the contaminant was indistinguishable from the LBG in the ground-based LRIS imaging (a fair simulation of ground-based studies). Figure 3.13 shows histograms of these three LBG samples, along with the best-fit values for MD5a, MD5b, and the combined photometry for MD5. MD5a and MD5b clearly have distinct stellar populations from each other, and MD5b, the LyC-emitting component, stands out as being among the youngest galaxies in the *HST* LBG sample.

For all the LBGs in our sample, we now compare the stellar population fits to individual clumps with fits to the combined photometry. As expected, we find that model fits to individual galaxy components generally yield smaller stellar masses and SFRs than fits to the combined photometry. Also, individual sub-arcsecond components exhibit a wider range of reddening values than do galaxies with combined photometry, although the median reddening value is the same for both samples. There is no significant difference in the median derived ages between the individual clumps and the combined photometry. Finally, we find that the addition of foreground contaminants does not significantly alter the sample-averaged LBG properties, as foreground contaminants close to LBGs are rare in the LBG sample without NB3420 detections. We conclude that occasional foreground contaminants superimposed upon LBGs do not greatly affect the stellar populations derived for galaxies in ground-based LBG surveys.

In order to compare the properties of MD5 with those of a much larger parent sample of LBGs, we consider the set of 570 LBGs at $2.7 < z < 3.7$ from the ground-based survey of Reddy et al. (2012). In Figure 3.14, we display parameters of the stellar population fit to MD5a, MD5b, and the combined photometry with respect to the LBGs from Reddy et al. (2012). The stellar population parameters we display for the Reddy et al. (2012) LBGs

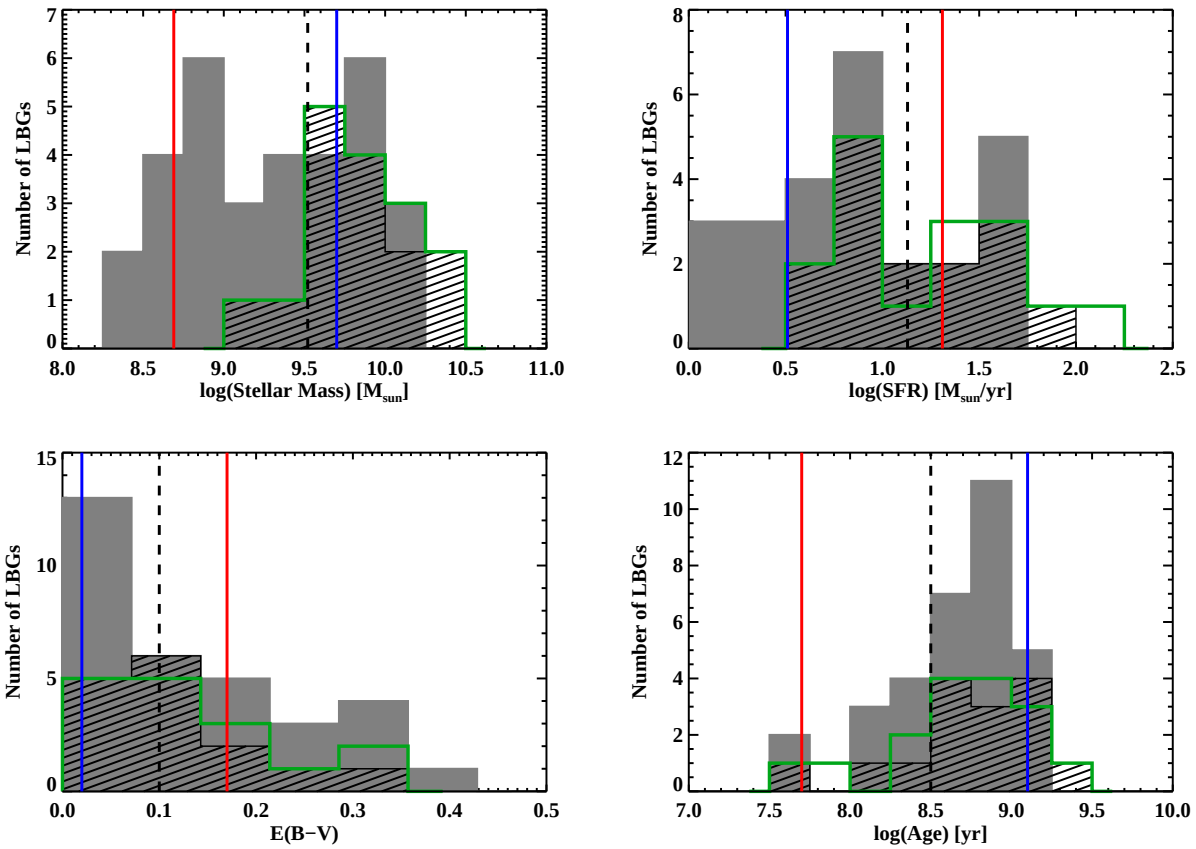

Figure 3.13 Histograms showing the stellar population parameters of MD5 calculated by FAST with respect to the distribution of parameters for all LBGs with $U_{336}V_{606}J_{125}H_{160}$ imaging. MD5b (the LyC-emitting component) is indicated by the red vertical line, MD5a is indicated by the blue vertical line, and the combined photometry for MD5a and MD5b is indicated by the black dashed vertical line. Gray filled histograms indicate parameters derived from fits to individual sub-arcsecond components of LBGs. Black hashed histograms indicate parameters derived from fits to combined photometry, mimicking ground-based studies. Green open histograms also indicate parameters derived from fits to combined photometry, but include known foreground contaminants in cases where the contaminant was indistinguishable from the LBG in the ground-based LRIS imaging. The similarities between the green and black histograms show that the inclusion of foreground contaminants does not significantly alter the sample-averaged LBG properties. MD5b stands out as having a young age with respect to the majority of the LBG sample.

have been derived from the latest solar metallicity models of S. Charlot & G. Bruzual, using constant star formation histories and a minimum age limit of 50 Myr. The median parameters of the Reddy et al. (2012) LBGs are consistent with those of our combined-photometry LBG sample, although the percentage of young galaxies (<100 Myr) in our *HST* sample is less than that of the Reddy et al. (2012) sample.[10]

To facilitate comparison with the Reddy et al. (2012) LBGs, we have re-fit the stellar populations of MD5a, MD5b, and the combined photometry of MD5 using the methods described in Reddy et al. (2012), employing CSF models, a minimum age of 50 Myr, and Calzetti et al. (2000) extinction. These fit results for MD5 (plotted in Figure 3.14) are qualitatively similar to those from our original delayed-τ fits. The data in Figure 3.14 show that the fit to the combined photometry of MD5 is unremarkable when compared to the ground-based photometry of the Reddy et al. (2012) LBG sample: it has a typical stellar mass and age, and slightly below-average values for SFR and $E(B-V)$. It is only when MD5a and MD5b are fit separately that the young stellar population of MD5b becomes apparent; an age of 50 Myr places it in the youngest third of the sample. Finally, we also fit the photometry for MD5b using SMC extinction. Reddy et al. (2012) found that ∼90% of LBGs with Calzetti-inferred ages of <100 Myr had older ages (>100 Myr) when fit using an SMC extinction curve. For MD5b, the best-fit model using SMC extinction had an age of 160 Myr, along with less reddening ($E(B-V) = 0.05$) than the best-fit Calzetti-attenuated model and qualitatively similar values for stellar mass and star-formation rate (log(Mass [$M_\odot$]) = 9.16, log(SFR [$M_\odot$ yr^{-1}]) = 0.95). Reddy et al. (2012) model their full LBG sample using a combination of extinction curves, employing Calzetti et al. (2000) attenuation for the majority of the sample, but using SMC extinction for galaxies with Calzetti-inferred ages younger than 100 Myr. Compared with the ages derived from these fits, the 160 Myr age estimated for MD5b is still in the youngest third of the sample. Table 3.4 summarizes the stellar population fits to MD5 with respect to those of the non-LyC-emitting galaxies in our

[10]The fact that we find few young galaxies (<100 Myr) among the *HST*-imaged LBGs and LAEs in the HS1549 field may be due to statistical variation inherent to our small sample size (40 galaxies with $U_{336}V_{606}J_{125}H_{160}$ imaging), a peculiarity of the HS1549 field, or possibly a property of all protoclusters (see, e.g., Steidel et al., 2005).

HST LBG sample and those of the LBGs from Reddy et al. (2012).

As the model fit to MD5b has a young age and low stellar mass, two properties typical of LAEs (e.g., Gawiser et al., 2007; Guaita et al., 2011), we also examined MD5b with respect to the LAEs in our sample, none of which exhibited LyC detections. We modeled LAE stellar populations with FAST using the same methods as for LBGs, but in order to account for the young ages and lower metallicities associated with LAEs we set the minimum age to 10 Myr and fixed metallicity at 20% solar. Figure 3.15 shows the distribution of stellar mass, star-formation rate, dust extinction, and age for LAEs, along with values for MD5a, MD5b, and the combined photometry of MD5. MD5b has a stellar mass more typical of the average LAE in our sample, but a higher than average SFR. Its age is still young compared to the LAE sample.

While the young age of MD5b is shared by several objects in our *HST* sample, none of these additional young objects exhibit LyC detections. In the LBG sample, two object subcomponents in addition to MD5b have ages less than 100 Myr, and five such components exist in the LAE sample. If the young stellar population of MD5b is responsible for its LyC emission, then we might also expect LyC detections from other LBG and LAE components with similarly young ages. Both of the young objects in the LBG sample (M16a and MD34f) have small stellar masses ($\log(\text{Mass } [\text{M}_\odot]) \sim 9$) and large SFRs ($\log(\text{SFR } [\text{M}_\odot \text{ yr}^{-1}]) > 1.6$) like MD5b, but both of these objects are redder ($E(B-V) \sim 0.4$). If LyC emission is being produced copiously by the hot stars in these two galaxies, the additional dust extinction might be the reason we do not detect the LyC photons. We note that MD34f is actually associated with a NB3420 detection (see Section 3.5.3.1), but its close proximity to a foreground contaminant makes it impossible to distinguish between emission from MD34f and the foreground contaminant in the seeing-limited NB3420 image. The LAE sample presents several additional young galaxy components that are undetected in the NB3420 image. These objects have reddening values similar to MD5b ($E(B-V) \sim 0.2$), lower than those of the young LBGs. One possible explanation for the lack of LyC detections in the LAE sample is that MD5b is located along a fortuitously clear IGM sightline, and these LAEs are not. Another possibility is that the LAEs are simply too faint to be detected in

our LyC imaging. The V_{606} magnitude of MD5b is $m_{606} = 25.9$, and its LyC detection is near the edge of our detection limit. The V_{606} magnitudes of the young LAEs in our sample (ages < 100 Myr) are much fainter on average, and range from $26.29 < m_{LyC} < 29.14$, with a median of 27.69. If these objects have the same ratio of ionizing to non-ionizing radiation as MD5b, the LyC magnitudes of these objects would range from $27.80 < m_{606} < 30.64$, with a median of 29.20. Such magnitudes are well below the detection limit of the NB3420 filter used for LyC imaging (27.3 mag), and thus these objects would not have been detected in the LyC.

3.6.4 No Evidence for AGN

Vanzella et al. (2015) discuss the possibility that some portion of the leaking ionizing radiation from the LyC-emitters *Ion1* and *Ion2* are due to contributions from low-luminosity AGNs within these galaxies. We considered this possibility in MD5b, but find no evidence for a low-luminosity AGN. There is no significant variability detected between the $V-$band magnitude of MD5 measured by LRIS in 2007 ($m_V = 24.96 \pm 0.11$) and the combined *HST* V_{606} magnitudes of MD5a and MD5b measured in 2013 ($m_{606} = 25.11 \pm 0.08$). Additionally, the available spectra of MD5 do not show any high ionization emission line features (e.g., NV λ1240 emission), although our spectrum does not cover CIV λ1550 or HeII λ1640, nor are we able to examine the OIII / Hβ ratio because Hβ falls on a sky line. We therefore find no evidence for AGN activity in MD5b with the information available.

3.7 Discussion

In this section, we consider the broader implications of our single robust detection of LyC emission in the HS1549 field. We discuss the actual rate of foreground contamination with respect to predictions from the contamination simulations of M13, and the LyC emission properties of MD5b, including its intrinsic ionizing to non-ionizing UV flux-density ratio and the implied LyC escape fraction. With the removal of all foreground contaminants from the M13 sample, we then obtain a revised estimate for the ionizing emissivity due to star-

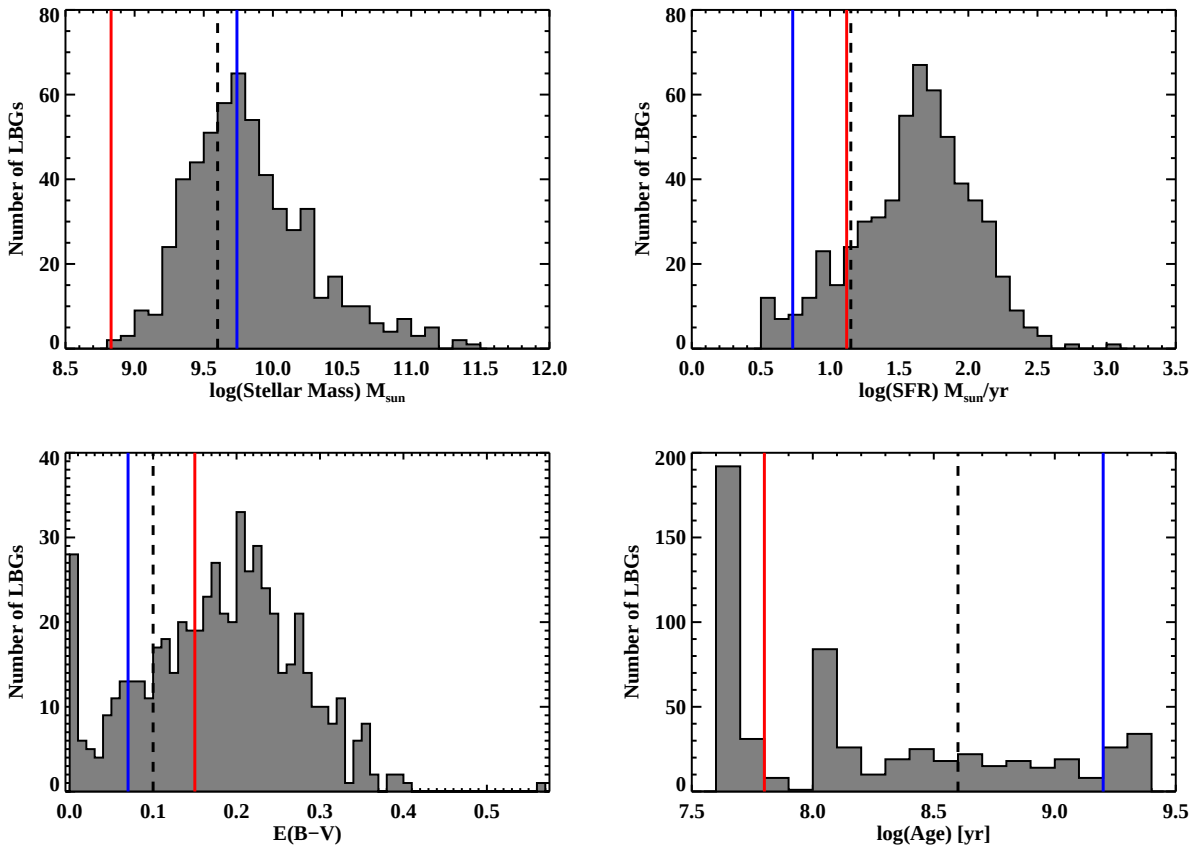

Figure 3.14 Histograms showing the stellar population parameters of MD5 calculated by FAST with respect to the distribution of parameters for the $2.7 < z < 3.7$ LBG sample of Reddy et al. (2012). MD5b (the LyC-emitting component) is indicated by the red vertical line, MD5a is indicated by the blue vertical line, and the combined photometry for MD5a and MD5b is indicated by the black dashed vertical line. All parameters plotted are derived using the stellar population fitting methods described in Reddy et al. (2012), with assumptions of constant star formation histories, a minimum age of 50 Myr, and Calzetti et al. (2000) dust attenuation. While the properties of the composite object MD5 (containing both MD5a and MD5b) do not stand out among other LBGs in the Reddy et al. (2012) sample, the LyC-emitting component MD5b stands out as being in the youngest third of the sample.

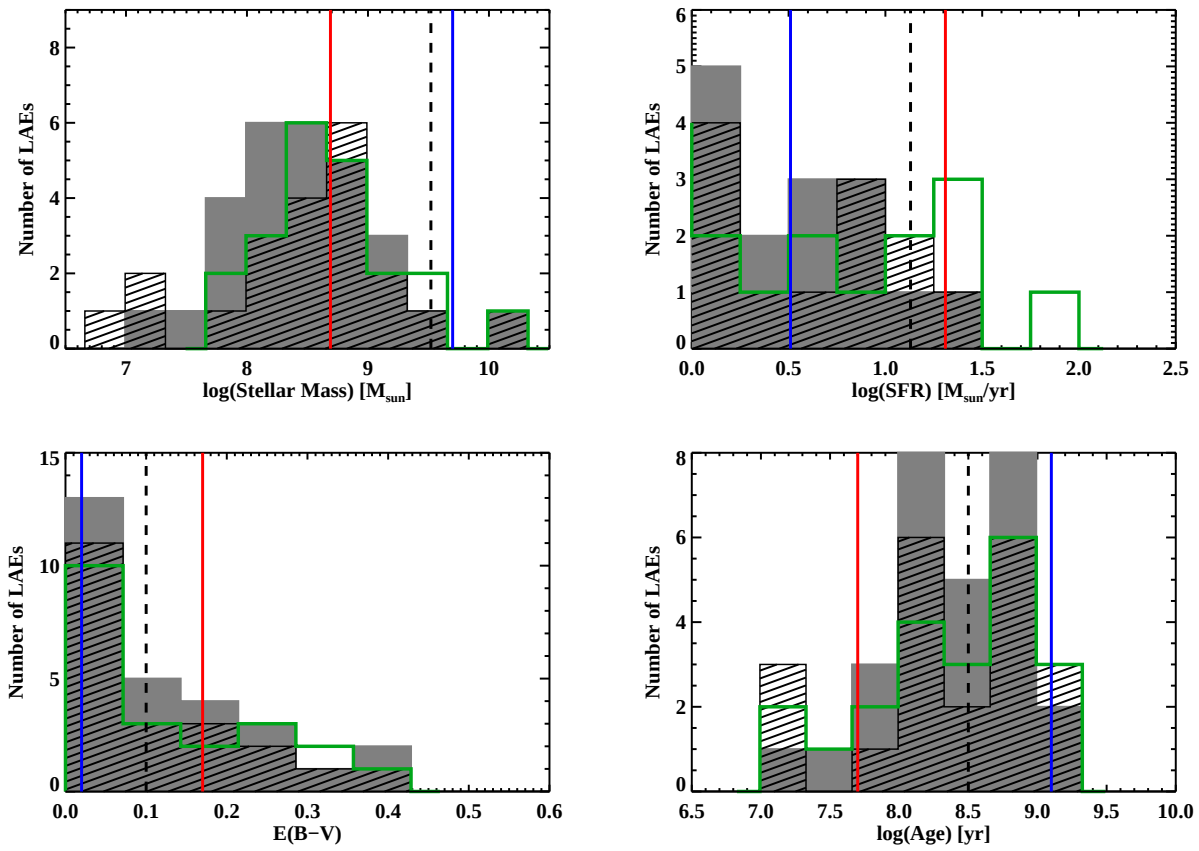

Figure 3.15 Histograms showing the stellar population parameters of MD5 calculated by FAST with respect to the distribution of parameters for all LAEs with $U_{336}V_{606}J_{125}H_{160}$ imaging. MD5b (the LyC-emitting component) is indicated by the red vertical line, MD5a is indicated by the blue vertical line, and the combined photometry for MD5a and MD5b is indicated by the black dashed vertical line. Histogram colors are as in Figure 3.13. The bottom-right plot shows several LAEs with log(age) < 8, similar to MD5, raising the question of whether or not these objects − which do not have NB3420 detections − may also emit LyC radiation. However, as discussed in Section 3.6.3, these LAEs are much fainter than MD5. If their observed ionizing to non-ionizing UV flux density ratios were equivalent to that of MD5, then they would be too faint to detect in the NB3420 image.

forming galaxies at $z = 2.85$. Finally, we discuss the prospects for future direct searches for LyC radiation in high-redshift galaxies.

3.7.1 Comparison to Previous Contamination Estimates

We wish to address the question of whether or not the simulations of foreground contamination from M13 accurately predicted the number of contaminants in the sample. The simulations (described in detail in M13; Nestor et al., 2013) employed the surface density of objects in the NB3420 image and the offset of each NB3420 detection to estimate the number of foreground contaminants and a contamination-corrected NB3420 magnitude. The simulations predicted that 1.5 ± 1.0 out of 4 LBGs and 4.3 ± 1.3 out of 7 LAEs in the main sample were real LyC-emitters. The prediction for the LBG sample has held out, as one LBG (MD5) remains a strong candidate for LyC emission. The prediction for the LAE sample, however, was too high. We were able to obtain $U_{336}V_{606}J_{125}H_{160}$ imaging for 6 out of 7 LAEs with LyC detections, yet none have proven to be true sources of LyC emission. We note that 2 of the 7 LAEs had misidentified redshifts (*lae2436* and *lae7180*), and should not have made it into this sample in the first place. Given the small number of galaxies with true LyC detections, contaminated NB3420 detections from even one or two objects with misidentified redshifts may introduce a non-negligible bias that is not taken into account in the contamination simulations of M13. Accordingly, we re-ran the same contamination simulations, but only considering the 4 spectroscopically-confirmed LAEs from the main sample of M13 for which we acquired $U_{336}V_{606}J_{125}H_{160}$ imaging. The revised simulations predict 2.1 ± 1.0 out of 4 galaxies to be real LyC-emitters. As none of the four NB3420 detections proved to be real, the prediction is still too high by $\sim 2\sigma$. With the small sample size of 4 objects, however, such variations may be expected. We conclude that the contamination simulations still serve as a useful, though blunt, tool for evaluating the likelihood of foreground contamination.

3.7.2 Ionizing to Non-ionizing UV Flux-density Ratios

One of the intriguing findings reported by all three ground-based LyC studies of galaxy protoclusters (Iwata et al., 2009; Nestor et al., 2011; M13) was the high apparent ratio of ionizing to non-ionizing radiation in many of the candidate LyC-emitters, which appeared to be in conflict with results from standard SPS models. Several models have been proposed to address this question. Iwata et al. (2009) proposed a top-heavy IMF. Nestor et al. (2013) investigated the intrinsic non-ionizing to ionizing UV flux-density ratios for two sets of stellar population models at varying ages and metallicites. These authors examined both Bruzual & Charlot (2003) models and BPASS models (Eldridge & Stanway, 2009), which include a more detailed treatment of stellar binaries and Wolf-Rayet stars and result in bluer galaxy spectra. In this work, we also consider SB99 models with improved treatment of stellar rotation (Leitherer et al., 2014), as rapidly rotating stars exhibit bluer spectra as well.

However, our current analysis, along with all previous follow-up work aimed at investigating contamination among candidate LyC-emitters (Vanzella et al., 2012; Siana et al., 2015), has ruled out all objects with high apparent ratios of ionizing to non-ionizing radiation as contaminants. In our sample of 16 galaxies with putative LyC emission, 12 had anomalous flux-density ratios of $(F_{UV}/F_{LyC})_{obs} < 3.0$. However, the results of our analysis show that MD5 remains the only robust candidate for LyC emission. The flux-density ratio of MD5, as calculated from the ground-based imaging of M13, is $F_{UV}/F_{LyC} = 5.9 \pm 2.0$. Using our follow-up *HST* U_{336} and V_{606} imaging to revise this flux-density ratio to only include MD5b, the component associated with the ionizing radiation, we obtain a value of $F_{UV}/F_{LyC} = 4.0 \pm 2.0$, still compatible with SPS models in the absence of significant IGM absorption. In similar work investigating contamination in candidate LyC-emitters, Siana et al. (2015) obtained spatially-resolved spectroscopy of the five LBG candidates for LyC emission presented in Nestor et al. (2011). While unable to confirm any candidates, their data showed that both galaxies in their sample with anomalously high apparent ratios of ionizing to non-ionizing radiation (MD32, aug96m16) are contaminated by lower-redshift objects. Additionally, neither of the LyC-emitters *Ion1* or *Ion2* (Vanzella et al., 2012, 2015)

exhibit anomalously high ratios of ionizing to non-ionizing radiation. While the two dozen LyC-emitter candidates in the literature with extensive follow-up data do not comprise the entire sample of high-redshift candidate LyC-emitters, the fact that all candidates with extreme $(F_{UV}/F_{LyC})_{obs}$ ratios have proven to be contaminants may indicate that the anomalously high ratios of ionizing to non-ionizing radiation originally inferred are simply a result of foreground contamination.

3.7.3 Escape Fraction for MD5

We can estimate the relative and absolute escape fractions of MD5b with the following equations:

$$f_{esc,\,rel}^{LyC} = \frac{(L_{UV}/L_{LyC})_{intr}}{(F_{UV}/F_{LyC})_{obs}} \tag{3.1}$$

$$f_{esc,abs}^{LyC} = \frac{(L_{UV}/L_{LyC})_{intr}}{(F_{UV}/F_{LyC})_{obs}} \left(f_{esc}^{UV}\right), \tag{3.2}$$

In these calculations, we assume an intrinsic flux-density ratio of $(L_{UV}/L_{LyC})_{intr} = 3$ based on the young age ($\sim$ 50 Myr) inferred for MD5b in the stellar population fitting, and the corresponding intrinsic ratio predicted by BPASS models of this age (for the range of possible values, see Table 7 of Nestor et al., 2013). We ignore IGM absorption, which is very uncertain for an individual sightline. Accordingly, our estimate of the escape fraction of MD5b is a lower limit. We use the value $f_{esc}^{UV} = 0.19$ to estimate the UV escape fraction at 1500Å. This value is calculated from the $E(B-V)$ value of the best-fit FAST model to MD5b, assuming the Calzetti et al. (2000) attenuation curve. From these equations, we obtain a relative escape fraction of $f_{esc,rel}^{MD5b} = 75\% \pm 38\%$ and an absolute escape fraction of $f_{esc,abs}^{MD5b} = 14\% \pm 7\%$. The errors in these escape fractions represent photometric uncertainties only, and are dominated by the uncertainty in the U_{336} flux.

Table 3.5. Revised Contributions to the Ionizing Background.

	LF[a]	F_{UV}/F_{LyC}[b]	Magnitude range[c]	ϵ_{LyC}[d]
		LyC Detections: MD5 only[e]		
(i)	LBG	140 ± 230	$M_{AB} \leq -19.7$	0.8 ± 1.3
(ii)	LAE	> 32	$-19.7 < M_{AB} \leq -17.7$	< 0.7
(iii)	LBG	> 32	$-19.7 < M_{AB} \leq -17.7$	< 3.2
(iv)	LBG	140 ± 230	$M_{AB} \leq -17.7$	1.5 ± 2.5
(v)	LAE	> 32	$M_{AB} \leq -17.7$	< 1.6
	Total (lum.-dep.)[f]	$\cdots$	$\boldsymbol{M_{AB} \leq -17.7}$	$\mathbf{2.4 \pm 1.6}$
	Total (LAE-dep.)[g]	$\cdots$	$\boldsymbol{M_{AB} \leq -17.7}$	$\mathbf{2.3 \pm 2.6}$
		LyC Detections: MD5, D24, *lae4680*[e]		
(i)	LBG	74 ± 65	$M_{AB} \leq -19.7$	1.5 ± 1.4
(ii)	LAE	71 ± 180	$-19.7 < M_{AB} \leq -17.7$	0.3 ± 0.8
(iii)	LBG	71 ± 180	$-19.7 < M_{AB} \leq -17.7$	1.4 ± 3.6
(iv)	LBG	74 ± 65	$M_{AB} \leq -17.7$	2.9 ± 2.5
(v)	LAE	71 ± 180	$M_{AB} \leq -17.7$	0.7 ± 1.8
	Total (lum.-dep.)[f]	$\cdots$	$\boldsymbol{M_{AB} \leq -17.7}$	$\mathbf{3.0 \pm 3.9}$
	Total (LAE-dep.)[g]	$\cdots$	$\boldsymbol{M_{AB} \leq -17.7}$	$\mathbf{3.6 \pm 3.1}$

[a]Luminosity function parameters are identical to those in M13.

[b]Sample average flux-density ratio corrected for IGM absorption, described in Section 3.7.4.

[c]Magnitude range over which the first moment of the luminosity function is determined. $M_{AB} = -19.7$ and -17.7 correspond to $0.34L_*$ and $0.06L_*$, respectively.

[d]Comoving specific emissivity of ionizing radiation in units of 10^{24} ergs s^{-1} Hz^{-1} Mpc^{-3}.

[e]As we do not have the full suite of $U_{336}V_{606}J_{125}H_{160}$ imaging for D24 and *lae4680*, we cannot determine whether their NB3420 detections are true LyC emission or foreground contamination. Therefore, we perform two calculations of the emissivity in order to determine the full range of its possible values. In the upper portion of this table we assume that both D24 and *lae4680* are foreground contaminants, and that MD5 is the only true LyC detection. In the bottom portion of the table, we assume that MD5, D24, and *lae4680* are all true LyC-emitters.

[f]Total for the luminosity-dependent model, determined by summing rows (i) and (iii). Limits are taken into account using the method described in Section 3.7.4.

[g]Total for the LAE-dependent model, determined by summing 0.77× row (iv) and row (v). Limits are taken into account using the method described in Section 3.7.4.

3.7.4 Revised LyC Emissivity for Star-forming Galaxies at $z = 2.85$

Here, we present a revised calculation of the emissivity of ionizing photons at $z = 2.85$ based on the analysis of the *HST* data in the HS1549 field. We estimate the comoving specific emissivity as

$$\epsilon_{LyC} = \left(\frac{F_{UV}}{F_{LyC}}\right)^{-1}_{corr} \int_{L_{min}}^{L_{max}} L\,\Phi\,dL \tag{3.3}$$

following the assumptions of M13 and Nestor et al. (2013). In this expression, L is the non-ionizing UV luminosity, Φ is the non-ionizing UV luminosity function, and $(F_{UV}/F_{LyC})_{corr}$ is the average flux-density ratio of non-ionizing to ionizing UV radiation for the entire galaxy sample, corrected for the mean IGM attenuation in the LyC spectral region. We perform this emissivity calculation separately for the main sample of spectroscopically confirmed LBGs and LAEs from M13 (using the UV luminosity functions from Reddy et al. (2008) for LBGs and Ouchi et al. (2008) for LAEs), and combine the LBG and LAE emissivities to obtain a total emissivity for star-forming galaxies. As in M13, we use the LRIS $V-$band to represent non-ionizing UV flux and NB3420 to represent LyC flux. The difference between our calculation and that of M13 lies in our estimation of the average flux-density ratio. Rather than estimating the average amount of foreground contamination from simulations, we instead know exactly which galaxies are contaminated based on the *HST* data. There were only two NB3420-detected galaxies in the M13 spectroscopic sample for which we were unable to acquire $U_{336}V_{606}J_{125}H_{160}$ imaging (D24 and *lae4680*), and for these objects we could not evaluate whether or not the NB3420 detections are due to foreground contamination. We thus calculate the emissivity twice in order to quote the full range of possible values: in one calculation we assume that MD5 is the only true LyC detection, and in the other calculation we assume that MD5, D24, and *lae4680* are all true LyC-emitters. In addition to using the *HST* data to remove the NB3420 flux of foreground contaminants, we also use these measurements to estimate the percentage of contaminated flux in the non-ionizing UV. All objects with foreground contaminants identified through the *HST* imaging are blended in the LRIS V imaging, and it is impossible to isolate the uncontaminated $z \sim 2.85$ flux in the

LRIS V image. Thus, for each contaminated object, we decrease its LRIS $V-$band flux to match the fraction of uncontaminated V_{606} flux in the HST imaging. For objects that do not have HST $U_{336}V_{606}J_{125}H_{160}$ imaging and are undetected in NB3420, we decrease their LRIS $V-$band flux to match the average fraction of uncontaminated V_{606} flux in the full sample of HST-imaged galaxies without NB3420 detections (99% for LBGs, 91% for LAEs). Finally, we use the same sample-averaged IGM correction to compute $(F_{UV}/F_{LyC})_{corr}$ as described in M13, employing statistics of HI absorbers from Rudie et al. (2013). We note that the clustering of Lyman limit systems is not taken into account in these absorber statistics, and thus the true mean IGM transmission may be slightly higher than the values presented in M13 (see, e.g., Prochaska et al., 2014).

In order to estimate the total contribution of star-forming galaxies to the ionizing emissivity at $z \sim 2.85$, we estimate the emissivity due to LBGs and LAEs separately and use two different models (described in detail in Nestor et al., 2013) to combine these values into a total emissivity of star-forming galaxies. In the first model, which we refer to as the luminosity-dependent model, the F_{UV}/F_{LyC} values for LAEs are assumed to represent those for star-forming galaxies with faint UV continuum magnitudes ($0.06L^* < L < 0.34L^*$, corresponding to $25.5 < V < 27.5$) while the F_{UV}/F_{LyC} values for LBGs represent those for brighter star-forming galaxies ($L > 0.34L^*$). The second model, referred to as the LAE-dependent model, considers the case that LAEs are not simply faint LBG-analogs, but that LBGs and LAEs are actually distinct populations of star-forming galaxies with systematically different F_{UV}/F_{LyC} values on average. In this model, LAEs are assumed to comprise 23% of the LBG population (Nestor et al., 2013), galaxies identified both as LBGs and LAEs are treated as LAEs, and the luminosity function is integrated over the full luminosity range ($0.06L^* < L < \infty$) for both LBGs and LAEs.

In Table 3.5, we summarize the contributions to ϵ_{LyC} as determined from galaxies in the HS1549 field. By considering MD5 as the only real LyC detection in the entire galaxy sample, we obtain values of the average UV flux-density ratio for LBGs and LAEs the HS1549 field to be $(F_{UV}/F_{LyC})_{corr}^{LBG} = 140 \pm 230$ and $(F_{UV}/F_{LyC})_{corr}^{LAE} > 32$. If we include the NB3420 detections for D24 and *lae4680* as well, these values become $(F_{UV}/F_{LyC})_{corr}^{LBG} = 74 \pm 65$

and $(F_{UV}/F_{LyC})^{LAE}_{corr} = 71 \pm 180$. The error bars on the flux-density ratios are large due to significant uncertainty in the average NB3420 flux due to our very few NB3420 detections. Based on these values for $(F_{UV}/F_{LyC})_{corr}$, we infer revised values of the comoving specific emissivity: considering NB3420 emission from MD5 only (or from MD5, D24, and *lae4680*) we obtain $\epsilon_{LyC} = 2.4 \pm 1.6$ $(3.0 \pm 3.9) \times 10^{24}$ ergs s^{-1} Hz^{-1} Mpc^{-3} for the luminosity-dependent model and $\epsilon_{LyC} = 2.3 \pm 2.6$ $(3.6 \pm 3.1) \times 10^{24}$ ergs s^{-1} Hz^{-1} Mpc^{-3} for the LAE-dependent model. The uncertainties in ϵ_{LyC} reflect only uncertainties in $(F_{UV}/F_{LyC})_{corr}$, which dominate over uncertainties in the luminosity function. For cases where the value of $(F_{UV}/F_{LyC})^{LAE}_{corr}$ is only a limit, we calculate the combined LBG and LAE emissivity by constructing a Monte Carlo simulation that treats the LBG emissivity as a normally-distributed random variable and the LAE emissivity as a uniform random variable below its limit. In the simulation, we randomly choose values from both distributions and add them together, creating a resulting distribution of total emissivities. We report the mean and standard deviation of the resulting distribution as the total emissivity and its uncertainty.

The revised values of ϵ_{LyC} are much lower than those computed in M13: $\epsilon_{LyC} = 15.0 \pm 6.7 \times 10^{24}$ ergs s^{-1} Hz^{-1} Mpc^{-3} for the luminosity-dependent model and $\epsilon_{LyC} = 8.8 \pm 3.5 \times 10^{24}$ ergs s^{-1} Hz^{-1} Mpc^{-3} for the LAE-dependent model. The lower emissivity value calculated in the current work is much more compatible with the total ionizing emissivity at $z = 2.85$, estimated in M13 from measurements of the Lyα-forest opacity (Bolton & Haehnelt, 2007; Faucher-Giguère et al., 2008) to be $\epsilon^{tot}_{LyC} \sim 5 - 10 \times 10^{24}$ ergs s^{-1} Hz^{-1} Mpc^{-3}. As measurements of the contribution of QSOs to the ionizing background at $z = 2.85$ range from $\epsilon^{QSO}_{LyC} \sim 1.5 \times 10^{24}$ ergs s^{-1} Hz^{-1} Mpc (Cowie et al., 2009) to $\epsilon^{QSO}_{LyC} \sim 5.5 \times 10^{24}$ ergs s^{-1} Hz^{-1} Mpc (Hopkins et al., 2007), our data indicate (with large uncertainties) that star-forming galaxies provide roughly the same contribution as QSOs to the ionizing background at this redshift.

3.7.5 The Future of LyC Surveys

The results from this work suggest that identifying true LyC-emitters at high redshift requires an extremely large parent sample of galaxies and/or significantly deeper LyC observations. With only one confirmed detection out of 49 LBGs, and zero confirmed detections among the 91 LAEs, the detection rate of LyC emitters at high redshift is very small. While several interesting methods of indirectly identifying LyC-emitting galaxies have been proposed − such as assessing the shape of the Lyα emission line (Verhamme et al., 2014), observing reduced flux in nebular emission lines (Zackrisson et al., 2013), and observing residual flux in the cores of saturated low-ionization absorption lines (Jones et al., 2013; Heckman et al., 2011) − it will not be possible to verify the validity these indirect methods without first obtaining a sample of galaxies with robust detections of LyC emission.

Given their low detection rate in the HS1549 field, it will likely be very difficult to amass a statistical sample of LyC emitters at $2 < z < 4$ without a dedicated survey. As the process of identifying and verifying LyC emission in this redshift range involves several steps, we outline here what we consider to be the most efficient method for doing so.

First, there is the question of efficient targeting. Because the average surface density of LBGs down to $R = 25.5$ is roughly $1 - 2$ galaxies per square arcminute (Steidel et al., 1999, 2004), the process of observing LBGs for LyC emission is greatly streamlined by observing galaxy protoclusters, which have an increased density of objects at a particular redshift. Several galaxy protoclusters have already been identified in the literature at $2 < z < 4$ (see, e.g., Venemans et al., 2007; Kodama et al., 2007; Hatch et al., 2011; Cucciati et al., 2014; Lemaux et al., 2014; Shimakawa et al., 2014; Diener et al., 2015). At the rate of one LyC detection per protocluster, observations of at least ~ 10 protoclusters would be necessary to obtain a sample large enough to investigate systematic differences between LyC-leakers and non-leakers. While the environment in the IGM surrounding protoclusters may not be typical of the universe as a whole, it is unlikely to affect the escape of ionizing photons through the ISM of LyC-emitting galaxies. The factor that is less well-constrained in protocluster environments is the estimate of the sample-averaged IGM transmission, which enters into

the calculation of the global ionizing emissivity. However, galaxies in protoclusters can still be very useful for studying the multiwavelength properties of LyC emitters. An additional potential problem with targeting protoclusters for LyC studies is that protoclusters may be composed of galaxies with older stellar populations on average (as we found in this work; also, see Steidel et al., 2005). If LyC emission is primarily emitted from galaxies with younger stellar populations (as suggested by the LyC detection for MD5b), then LyC emitters may be less common in protoclusters.

Next, there is the question of the required observations. Spectroscopic redshifts must be measured for a large sample of protocluster galaxies, as photometric redshifts are not sufficiently precise to determine whether or not apparent LyC emission originates below 912Å. Multiwavelength *HST* imaging should then be obtained to probe the SED shapes and LyC emission for all galaxy components near the high-redshift targets (as in this work). To allow for direct LyC imaging, the protocluster identified must be at a redshift where one of the currently available *HST* filters probes the LyC spectral region just bluewards of the Lyman limit (such as $F336W$ for $z > 3.06$, or $F275W$ for $z > 2.40$). To obtain useful limits on the amount of escaping ionizing radiation from the faintest galaxies, LyC magnitudes must be probed several times fainter than their non-ionizing UV magnitudes. The faintest galaxies in our sample, LAEs, have V_{606} magnitudes ranging from $26.08 < m_{606} < 29.14$ with a median of 27.62. In order to measure ionizing to non-ionizing flux-density ratios equivalent to that observed for MD5b ($F_{UV}/F_{LyC} \sim 4$) for the faintest LAE ($m_{606} = 29.14$), the required LyC observations must reach a depth of ~ 30.7 magnitudes. Assuming object sizes close to the PSF size, this requires imaging roughly 4 times more sensitive than the U_{336} observations in this current work. Larger objects, comparable in size to MD5b, would require imaging ~ 20 times deeper. In practice, the best way to measure the average F_{UV}/F_{LyC} ratio for the faintest galaxies may be with stacked LyC observations, or with the next-generation UV space telescope (e.g., ATLAST; Postman et al., 2009). Finally, if the morphology of the candidates for LyC emission are complex, the last step would be to obtain high-resolution spectroscopic follow-up of the LyC-emitting component of the galaxy.

This plan is streamlined relative to the process we have followed thus far because it skips

the time-intensive ground-based LyC imaging and analysis. The main benefit of the ground-based LyC imaging was that we were able to design a custom, narrowband filter for the exact redshift of the protocluster. Narrowband filters placed just bluewards of the Lyman limit are the least affected by IGM absorption, and probe LyC emission at wavelengths where the LyC photons are most likely to ionize hydrogen. Even so, these benefits do not outweigh the cost in time and resources if *HST* filters are already available at the correct wavelengths to probe LyC emission. For cluster redshifts where *HST* filters are not available for LyC imaging, but the Lyman limit falls above the atmospheric cut-off, it would be possible to obtain ground-based narrowband LyC imaging first at $z \sim 3$ with, e.g., Keck/LRIS. The roughly two dozen LyC-emitter candidates that would fall within a single Keck/LRIS pointing (most of which would be contaminants) could be followed up individually with an AO-assisted integral field spectrograph such as Keck/OSIRIS (Larkin et al., 2006). In all future LyC searches, it is imperative to obtain high-resolution imaging and redshift confirmation of each galaxy sub-arcsecond component associated with apparent LyC emission in order to rule out foreground contamination.

3.8 Summary

In M13, we identified 30 candidates for LyC emission via detection in the Keck/LRIS NB3420 filter: 5 LBGs and 7 LAEs spectroscopically confirmed at $z \geq 2.82$ (the main sample), 10 photometric LAE candidates, and 8 spectroscopically-confirmed LAEs not part of the main sample. In this current work, we have presented follow-up *HST* $U_{336}V_{606}J_{125}H_{160}$ observations of 16 of these objects: 4/5 LBGs and 6/7 LAEs in the main sample, 4/10 photometric LAE candidates, and 2/8 LAEs outside of the main sample.

In our high-resolution *HST* imaging, all of the candidates for LyC emission exhibit significant substructure. We have thus used the *HST* imaging to obtain photometric redshifts of each galaxy sub-arcsecond component in order to determine if the source of the NB3420 emission is truly at $z \geq 2.82$, or if it is from a lower-redshift contaminant. Of the sixteen galaxies with NB3420 detections imaged in $U_{336}V_{606}J_{125}H_{160}$, nine were located near foreground con-

taminants responsible for the NB3420 emission. Two objects had incorrect redshifts assigned to them, and thus the NB3420 emission was also from a low-redshift galaxy. Four objects, all LAEs without spectroscopic confirmation, exhibited ambiguous SED shapes consistent with both $z \sim 2.85$ galaxies and foreground contaminants. Lack of spectroscopic redshifts for these objects, combined with their ambiguous SED shapes, makes it impossible to verify their NB3420 detections as true LyC emission. In the end, only one robust candidate for LyC emission remained: the LBG, MD5.

MD5 has a spectroscopic redshift of $z = 3.14$, measured from LRIS and MOSFIRE spectra containing Lyα and [OIII] emission lines, along with multiple coincident interstellar absorption features, blueshifted with respect to the systematic redshift and indicative of an outflow ($\Delta v_{IS} \sim 280$ km s^{-1}). These spectra show no spurious emission or absorption features indicating a foreground contaminant. MD5 breaks into two clumps (MD5a and MD5b), which may either be two components of the same galaxy or two separate galaxies in the process of merging. MD5b is associated with the NB3420 detection. The best-fit stellar population synthesis model to MD5b indicates that while values for its stellar mass and reddening are typical of LBGs, it has a young stellar population ($\lesssim$50 Myr) and a high SFR (20 M$_\odot$ yr^{-1}) for such a low-mass object (5×10^8 M$_\odot$). This age places MD5b in the youngest 10% of the *HST* sample, and in the youngest third of typical LBGs. While MD5b is young compared to the full sample regardless of the fitting methods, we caution that the exact value for the best-fit age depends significantly on the dust attenuation curve and star-formation history assumed.

The LyC emission properties of MD5b are consistent with predictions of the intrinsic flux-density ratio for galaxies of 10−50 Myr from stellar population synthesis models (Nestor et al., 2013). Its observed flux-density ratio of $(F_{UV}/F_{LyC})_{obs} = 4.0 \pm 2.0$ is also compatible with some IGM absorption, depending on the details of the SPS model. With the assumption of no IGM absorption, the observed flux-density ratio results in lower limits to a relative escape fraction of $f_{esc,rel}^{MD5b} = 75\% \pm 38\%$ and an absolute escape fraction of $f_{esc,abs}^{MD5b} = 14\% \pm 7\%$. We also note that the emission in the U_{336} filter at the location of MD5b, which probes LyC emission at $z = 3.14$, shows no spatial offset from the V_{606} emission, supporting the

interpretation that the ionizing photons are escaping either isotropically, or through a hole in the ISM directly along our line of sight.

MD5b stands out as one of the youngest galaxies in our *HST*-imaged sample. The best-fit model to MD5b had the youngest age available (50 Myr), and the best-fit becomes even younger (10 Myr) without the minimum age requirement. While there are an additional two LBGs and five LAEs in our sample with ages <100 Myr, none of these galaxies exhibit NB3420 detections. The two young LBGs exhibit increased dust extinction ($E(B-V) \sim 0.4$), which may be the reason we do not detect the LyC photons. The young LAEs have less dust extinction ($E(B-V) \sim 0.2$), but have very faint UV continuum magnitudes (median $m_{606} = 27.7$). If the young LAEs have the same ratio of non-ionizing to ionizing radiation as MD5b, then their median LyC magnitude would be $m_{LyC} = 29.20$, well below the detection limit of the NB3420 filter used for LyC imaging (27.3 mag).

After eliminating foreground contaminants from our sample, we obtained a revised estimate for the comoving specific ionizing emissivity (ϵ_{LyC}) at $z = 2.85$. We calculated the emissivity associated with LBGs and LAEs separately, and combined these values using two different models, described in Section 3.7.4. If we consider MD5 as the only galaxy with a LyC detection, we obtain $\epsilon_{LyC} = (2.4 \pm 1.6) \times 10^{24}$ ergs s^{-1} Hz^{-1} Mpc^{-3} for the luminosity-dependent model and $\epsilon_{LyC} = (2.3 \pm 2.6) \times 10^{24}$ ergs s^{-1} Hz^{-1} Mpc^{-3} for the LAE-dependent model. If we also add in as true LyC detections the only two galaxies (D24 and *lae4680*) for which we were unable to obtain sufficient *HST* data to evaluate contamination, we obtain $\epsilon_{LyC} = (3.0 \pm 3.9) \times 10^{24}$ ergs s^{-1} Hz^{-1} Mpc^{-3} for the luminosity-dependent model and $\epsilon_{LyC} = (3.6 \pm 3.1) \times 10^{24}$ ergs s^{-1} Hz^{-1} Mpc^{-3} for the LAE-dependent model. These revised values of ϵ_{LyC} are much lower than those computed in M13, and much more compatible with the total ionizing emissivity at $z = 2.85$ ($\epsilon_{LyC} = (5.6 \pm 1.6) \times 10^{24}$ ergs s^{-1} Hz^{-1} Mpc^{-3}; M13). Within the large photometric uncertainties, and uncertainties due to the small dynamic range in which we can probe LyC emission, our data indicate that star-forming galaxies provide roughly the same contribution as QSOs to the ionizing background at this redshift.

Overall, the rate of foreground contamination for apparent LyC leakers in our $z \sim 2.85$

sample was very high. While the single detection in the LBG sample is consistent with contamination expectations from M13, the contamination rate in the LAE sample was higher than predicted by our simulations. With this work we have shown that ground-based LyC imaging studies are insufficient for obtaining a full understanding of LyC emission from star-forming galaxies because they are so heavily contaminated by foreground objects. In order to eliminate cases of foreground contamination, it is essential to obtain high-resolution observations of putative LyC-emitters to confirm the redshifts (either photometrically or spectroscopically) of all substructure associated with the galaxy. To date, all such observations have shown that candidate LyC-emitters from ground-based studies with anomalously high ratios of ionizing to non-ionizing radiation, both within our sample and in the literature, have proven to be from foreground contaminants.

Future progress in understanding the physical properties of LyC-emitters and the role of star-forming galaxies in reionization is contingent upon two factors. First, observations of sufficient depth to probe ionizing radiation in galaxies at the faint end of the luminosity function must be obtained efficiently for a large sample of galaxies. Second, these observations must be obtained at high spatial resolution, and with redshift information for each galaxy component. With such observations, it will be possible to distinguish between emission from foreground contaminants and genuine high-redshift LyC emitters, learn more about LyC photon escape by studying the multiwavelength properties of LyC emitters, and place more stringent constraints on the contribution of star-forming galaxies to the ionizing background.

We thank Anahita Alavi and Eros Vanzella for helpful discussions about the *HST* imaging reduction and photometry. Support for program GO-12959 was provided by NASA through a grant from the Space Telescope Science Institute (STScI), which is operated by the Association of Universities for Research in Astronomy, Inc., under NASA contract NAS 5-26555. A.E.S. acknowledges additional support from the David and Lucile Packard and Sloan Foundations, C.C.S. acknowledges support from the NSF grants AST-0908805 and AST-1313472, as well as STScI grants GO-11638.01 and GO-11694.02, and R.E.M. and A.E.S. acknowledge the generous support of Mr. Richard Kaplan. R.F.T. receives funding from the Miller Institute for Basic Research in Science at U.C. Berkeley. N.A.R. acknowledges support from

the Sloan Foundation. We wish to extend special thanks to those of Hawaiian ancestry on whose sacred mountain we are privileged to be guests. Without their generous hospitality, most of the observations presented herein would not have been possible.

3.9 APPENDIX A: Objects Without Full HST Coverage

Here we present postage stamp images of galaxies with NB3420 detections, but for which imaging was not available in all four HST filters (see Figure 3.16). While insufficient photometric data prevents us from fitting SEDs and determining photometric redshifts, we attempted to examine the morphologies of these objects in the V_{606} image, when available, to find objects with simple morphology where the possibility of contamination is low. However, none of the objects shown in Figure 3.16 have simple, compact morphologies in V_{606}. All objects either break into individual sub-arcsecond components or show extended diffuse emission. As both clumpy $z \sim 3$ galaxies and foreground contaminants may be responsible for these multi-component V_{606} morphologies, we are unable to draw any conclusions about the amount of contamination in this galaxy sample.

3.10 APPENDIX B: Objects with Ambiguous SEDs

Here we discuss the interpretation of four SEDs of photometric LAE candidates with NB3420 detections where the SED shape is ambiguous, and there are no spectroscopic redshifts available to confirm that the objects are indeed at $z \sim 2.85$. In total, we present three photometric LAEs from the Appendix of M13 (*lae4070*, *lae5200*, and *lae6510*) and one photometric LAE that was originally in the spectroscopic LAE sample, but for which the HST data showed that the wrong redshift had been assigned (*lae7180*). For *lae5200*, *lae6510*, and *lae7180*, Keck/LRIS spectroscopy with a total exposure time of 5400 seconds was attempted on clear nights with $0\farcs5-0\farcs6$ seeing, but no redshifts were measured. For *lae4070*, Keck/LRIS spectroscopy with a total exposure time of 17400 seconds was attempted under suboptimal conditions (intermittent clouds with seeing of $0\farcs7-1\farcs0$ during clear spells), but again, no

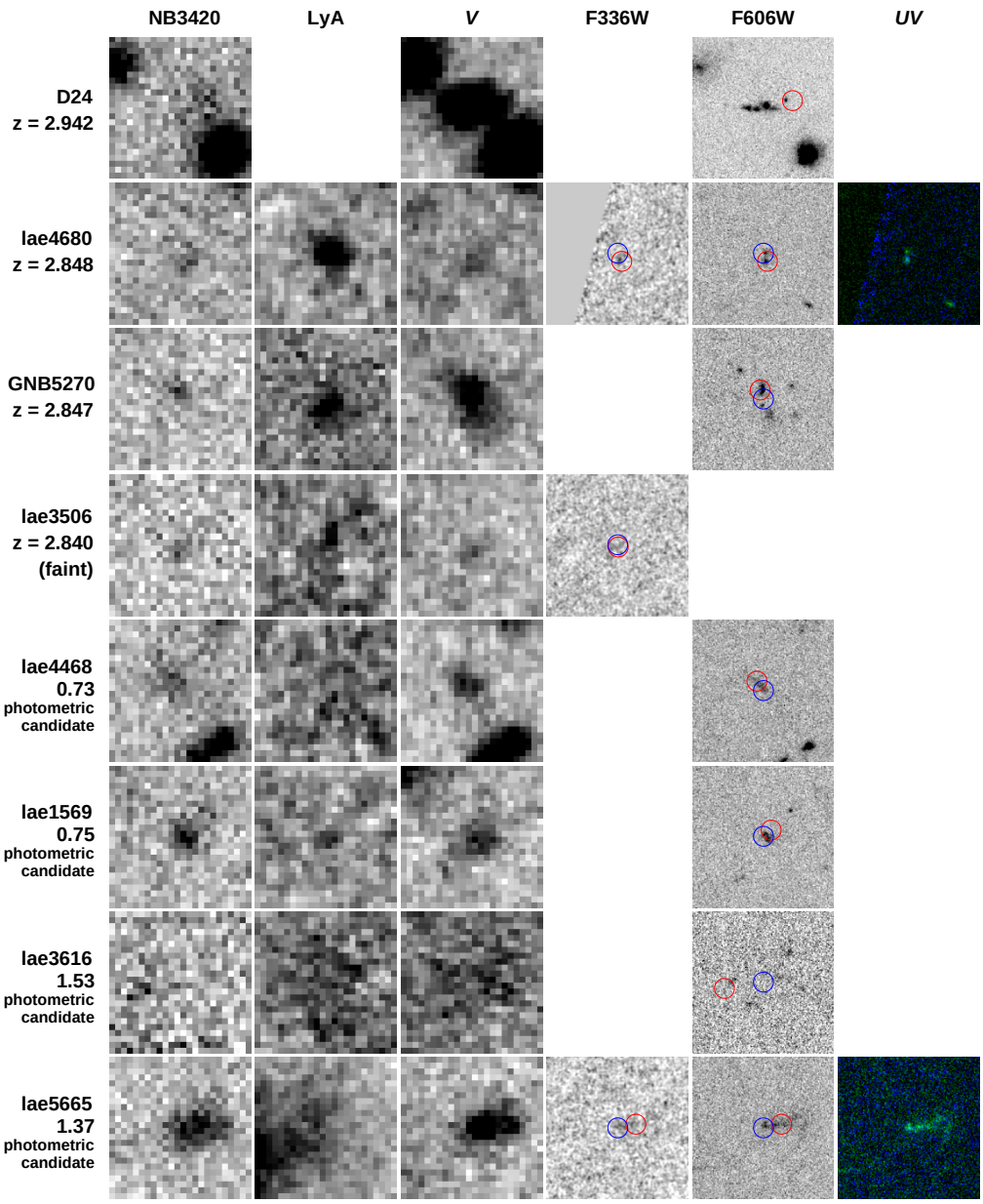

Figure 3.16 $5'' \times 5''$ postage stamp images of galaxies with NB3420 detections, but for which imaging was not available in all four *HST* filters. From left to right, objects are displayed in LRIS NB3420 (LyC emission), LRIS NB4670$-V$ (indicating Lyα emission), LRIS V (non-ionizing UV continuum), and (when available) *HST* U_{336} (a combination of $\sim 80\%$ LyC and $\sim 20\%$ non-ionizing UV) and *HST* V_{606} (non-ionizing UV continuum). For objects with imaging in both *HST* U_{336} and V_{606}, we show a color-composite image of these two bands. Red (blue) circles ($1\farcs0$ diameter) indicate the centroid of the NB3420 emission (Lyα emission). The redshift of each object is indicated below the object name, or, if the object is a photometric LAE candidate, the $V-$NB4670 color is indicated. Postage stamps follow the conventional orientation, with north up and east to the left. As there is insufficient photometric data to fit photometric redshifts for these objects and as none of these objects have simple, compact morphology that would lessen the chance of foreground contamination, we cannot draw conclusions about the contamination rate of this sample of objects.

redshift could be measured. The lack of spectroscopic redshifts for these LAE candidates makes it impossible to confidently claim a LyC detection for any of them. Furthermore, the shapes of their SEDs are ambiguous. Thus, while we can't unequivocally confirm any of these candidates as LyC-emitters, we also cannot rule them out as foreground contaminants.

The most promising LAE photometric candidate is *lae4070*. LAEs were selected by their $V-$NB4670 colors, as described in M13, and *lae4070* has a $V-$NB4670 color of 0.82, slightly below the median value of the LAE sample and 0.22 mag above the selection threshold of $V-$NB4670>0.6. While *lae4070* is fairly compact, it still breaks into two clumps separated by $0\farcs24$ (*lae4070a* and *lae4070b*, indicated in Figure 3.17) for which we analyzed separate SEDs. Both of these clumps are associated with NB3420 emission, and both clumps are detected individually in U_{336}. *Lae4070b* has the typical SED shape of a foreground contaminant. *Lae4070a*, however, has an SED shape that could not be well described by any of the stellar population models we used with EAZY. The feature that most strongly indicates a redshift of $z \sim 2.85$ for *lae4070a* is the large break between J_{125} and H_{160}, combined with a flat $V_{606} - J_{125}$ color. In Figure 3.8, *lae4070a* has colors that place it in the same region of color-color space as typical LAEs and LBGs at $z \sim 2.85$ ($J_{125} - H_{160} = 0.55$, $V_{606} - J_{125} = 0.18$). The emission in the U_{336} filter is anomalously high compared to any model that provides a good fit V_{606}, J_{125}, and H_{160}. While some of this emission may be contamination from nearby *lae4070b*, there is definitely emission in the U_{336} filter at the location of *lae4070a*, which was not the case for any of the LAEs or LBGs without NB3420 detections. If *lae4070a* is truly at $z \sim 2.85$, then it is a LyC emitter. However, in this case, measuring the ratio of ionizing to non-ionizing flux for *lae4070a* in our NB3420 image is impossible. The foreground galaxy *lae4070b* is located so close along the line of sight to *lae4070a* that there is no way to distinguish the NB3420 fluxes of these two objects with the $0\farcs7$ seeing in the LRIS NB3420 image. Finally, we note that the foreground contaminant *lae2436a* (which spectroscopy proved to be at $z = 2.04$) has an SED similar in shape to that of *lae4070a* in V_{606}, J_{125}, and H_{160}, and this object lies near *lae4070a* in Figure 3.8 ($J_{125} - H_{160} = 0.60$, $V_{606} - J_{125} = 0.06$). The fact that degeneracies still exist in this area of $J_{125} - H_{160}$ and $V_{606} - J_{125}$ color-color space where the majority of $z \sim 2.85$ LAEs and LBGs

lie demonstrates the need for spectroscopic redshifts to resolve cases with ambiguous SEDs.

We now consider the object *lae7180*, an LAE originally assigned a spectroscopic redshift of $z = 2.930$ based on a Keck/LRIS spectrum with a single high signal-to-noise emission line. The narrowband NB4670 filter used for LAE selection only probes redshifts of $2.80 < z < 2.88$, so the redshift of $z = 2.930$ was anomalously high for a NB4670-selected LAE candidate. However, we considered the possibility that a higher-redshift object with very large Lyα equivalent width scattered into the LAE sample, and therefore retained *lae7180* for analysis in M13. The *HST* imaging for this object, however, indicates that there is another faint galaxy in the vicinity of the $z = 2.930$ emission line, in addition to *lae7180*. Closer examination of the LRIS spectrum with respect to the *HST* images (see Figure 3.18) suggests that *lae7180* is offset by $1\farcs13$ from the location of the $z = 2.930$ emission. With the *HST* imaging we were able to identify the true galaxy associated with the emission line, an object so faint ($m_{606} = 28.85$) that it was undetected in the original LRIS imaging. The SED fit for this new object matches the redshift $z = 2.930$ identified in the spectrum, and we conclude that the emission line belongs to this faint, nearby object and not to *lae7180*. Now that the $z = 2.930$ redshift is no longer associated with *lae7180*, this object can be reevaluated as a photometric LAE candidate with a NB3420 detection.

Lae7180, *lae5200*, and *lae6510*, all exhibit ambiguous SED shapes. Rather than having SED shapes like that of *lae4070*, these objects have SED shapes similar to the one described in Section 3.5.1, which may represent either young, dusty, high-redshift galaxies or foreground contaminants. As shown in Figure 3.9 for a spectroscopically confirmed galaxy with an ambiguous SED shape, EAZY gives a wide range of possible values for the redshift using both the PÉGASE and SMC-reddened BPASS models. However, as Figure 3.9 also shows, the resulting redshift probability distributions may differ when using different sets of models. Thus, without spectroscopic redshifts, it remains unclear for these LAE photometric candidates with ambiguous SED shapes whether they are low-redshift foreground galaxies with an old stellar population, or high-redshift LAEs with young, dusty stellar populations and LyC detections. While we cannot absolutely confirm if they are LyC emitters without spectroscopic redshifts, the high-resolution *HST* imaging and SED fits can help narrow down

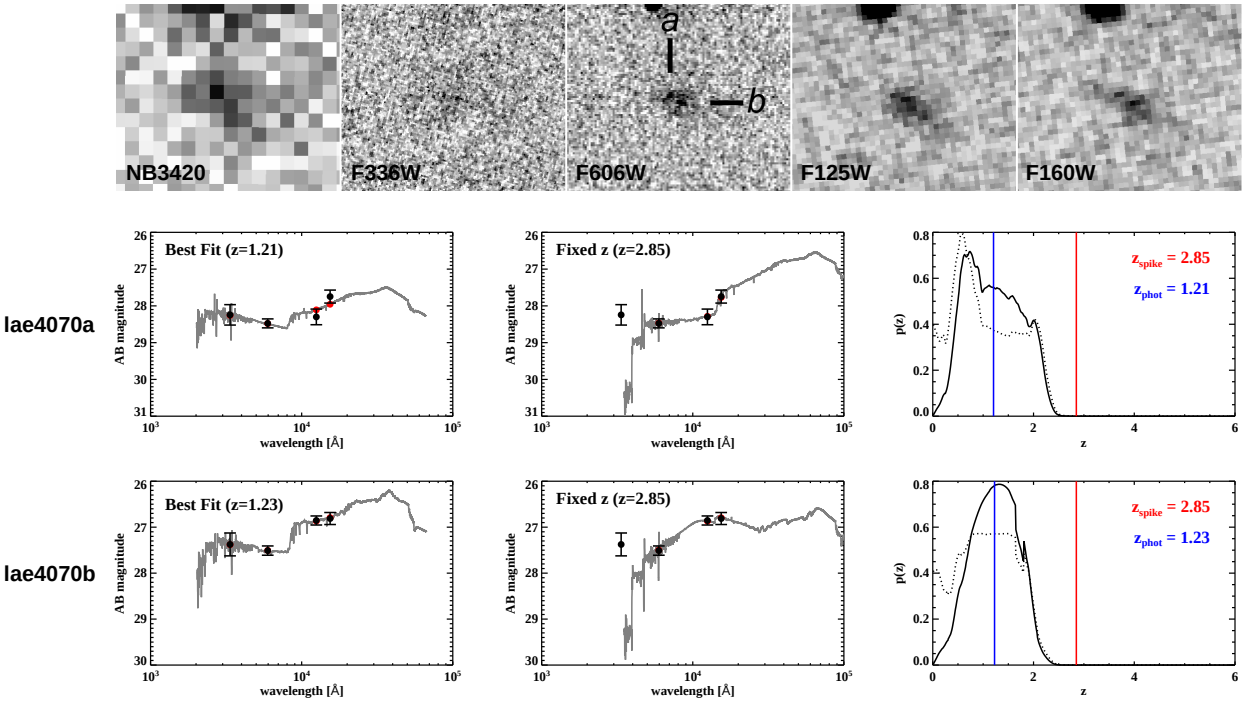

Figure 3.17 $3\farcs3 \times 2\farcs8$ postage stamp images of the photometric LAE candidate *lae4070*. From left to right, images displayed include LRIS NB3420 (LyC emission), *HST* U_{336} (a combination of LyC and non-ionizing UV), *HST* V_{606} (non-ionizing UV continuum), *HST* J_{125} (optical, bluewards of the Balmer break), and *HST* H_{160} (optical, redwards of the Balmer break). In the high resolution U_{336} and V_{606} images, *lae4070* breaks into two components (a and b, separated by $0\farcs24$; labeled on the V_{606} image). The photometry and EAZY SED fits for these two components are plotted below the images. In the left-most panel, the redshift is allowed to float during SED fitting, while in the middle panel the redshift is fixed to $z = 2.85$, the redshift corresponding to that of the redshift spike in the HS1549 field. The right-most panel shows the redshift probability distribution. Colors and symbols are as in Figure 3.6. The main qualitative difference between the SEDs of *lae4070a* and *lae4070b* is the magnitude in J_{125}. In the case of *lae4070b*, the resulting SED has the typical shape of a contaminant. However, in the case of *lae4070a*, the resulting SED cannot be well-fit by model spectra at any redshift. As discussed in Section 3.5.3.2, it is thus possible that this is a case of a LyC-emitting LAE (*lae4070a*) projected very close to a foreground contaminant (*lae4070b*).

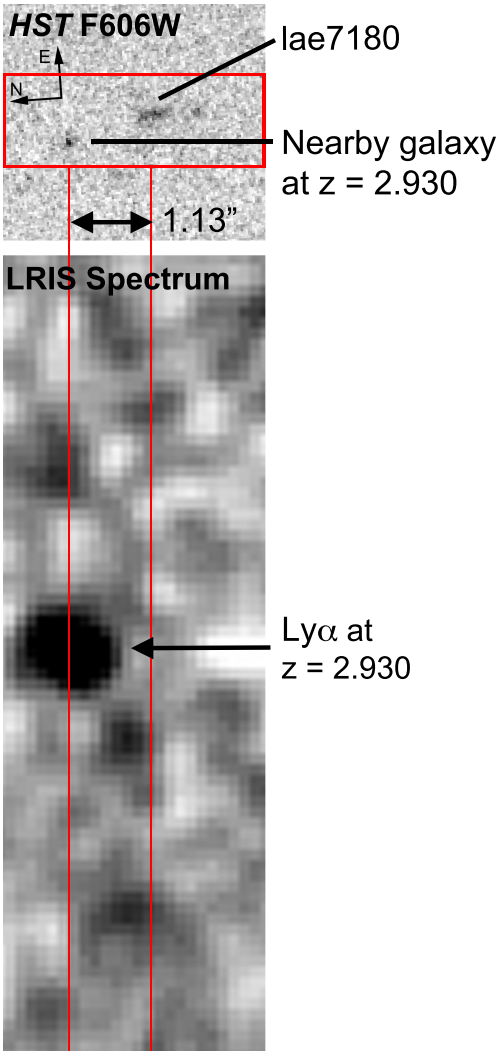

Figure 3.18 *HST* V_{606} imaging of *lae7180*, along with the corresponding Keck/LRIS spectrum. Thick red lines in the *HST* V_{606} image indicate the location of the 1.″2 slit, and the LRIS 2D spectrum is aligned to match in the orientation and spatial scale of the imaging. As explained in Section 3.5.3.2, the $z = 2.93$ galaxy near to *lae7180* was not visible in the lower resolution LRIS imaging, and thus the bright Lyα emission line in the spectrum was originally assigned to NB7180. However, analysis of the spatial distribution of the emission along the LRIS slit and how it corresponds to the *HST* imaging, along with the resulting SED fits of the sub-arcsecond components near *lae7180*, indicates that the neighboring galaxy is associated with the emission line and no emission line is visible at the location of *lae7180* (which is now only a photometric LAE candidate).

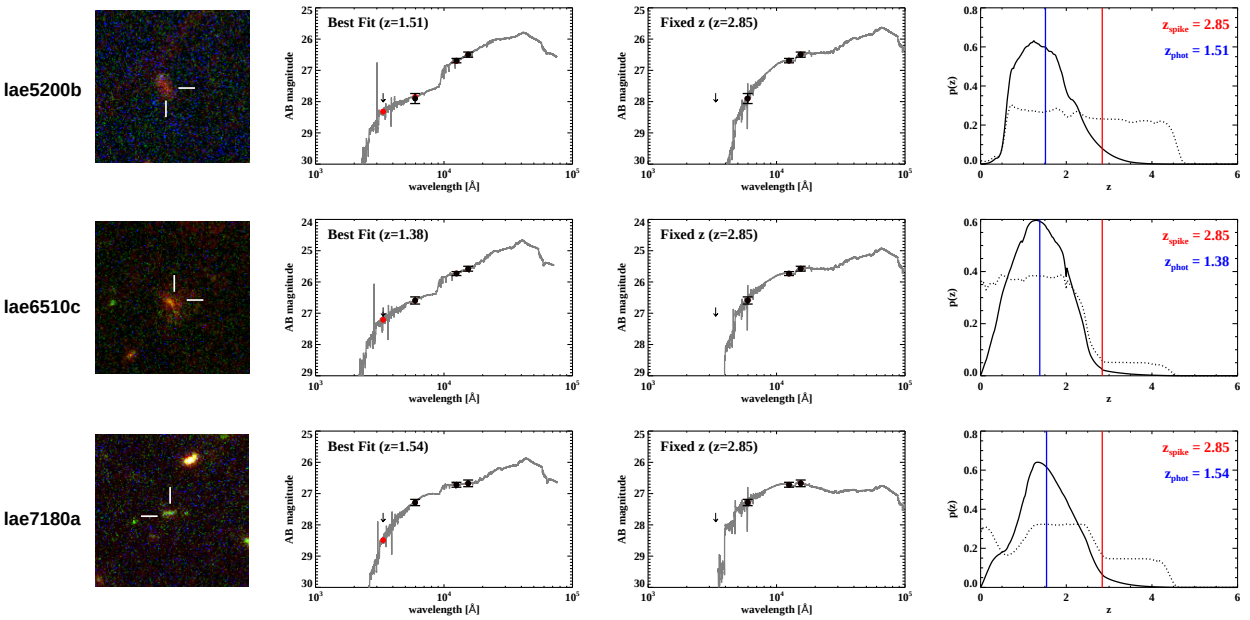

Figure 3.19 *HST* $U_{336}V_{606}J_{125}$ color-composite imaging ($5'' \times 5''$) and SED fits for the three photometric LAE candidates with the ambiguous SED shape described in Section 3.5.1. In all cases, the sub-arcsecond component shown is the main component associated with the LAE, and its position is indicated in the imaging. Results from EAZY are plotted in the three right hand panels. In the left-most panel, the redshift is allowed to float during SED fitting, while in the middle panel the redshift is fixed to $z = 2.85$, the redshift of the spike in the HS1549 field. The right-most panel shows the redshift probability distribution. Colors and symbols are as in Figure 3.6. Fits to these objects using the PÉGASE templates yield slightly different redshift probability distributions, but they are qualitatively similar in that they span a wide redshift range ($0 < z < 4.5$) for all objects.

the possible interpretations for these objects.

Figure 3.19 shows the *HST* imaging and photometry for the sub-arcsecond component of each LAE that is associated with the NB3420 emission, along with the EAZY redshift probability distributions for these components. For each component, EAZY predicts a wide range of possible redshifts ($0 < z_{phot} < 4.5$). Figure 3.19 shows BPASS SED fits to the photometry both at low and high redshift, and the fact that both redshifts can fit the data well demonstrates again the difficulties in distinguishing between low and high redshifts for galaxies with these SED shapes. In all of these cases, the detection of LyC emission depends on whether or not the LAE photometric candidate is truly at $z \sim 2.85$ - something that we cannot confirm for galaxies with ambiguous SED shapes and without spectroscopic redshifts.

Here we consider possible causes for the scenario in which all three of these photomet-

ric LAE candidates (*lae5200*, *lae6510*, and *lae7180*) were incorrectly identified as LAEs. *Lae6510* and *lae7180* have fairly marginal $V-$NB4670 colors (0.68 and 0.63, respectively) when compared to the LAE selection threshold of $V-$NB4670$>$0.6. These values are in the lowest 15% of the $V-$NB4670 colors for spectroscopically confirmed LAEs in M13, and indicate that these objects are among the weaker LAE candidates and may have scattered into the LAE sample through photometric errors. As for *lae5200*, its $V-$NB4670 color is 3.21, an anomalously high value that may be due to contaminating light from a nearby bright star. Finally, these photometric LAE candidates were chosen for follow-up because of their NB3420 emission. As our new dataset reveals, true LyC detections in $z \sim 3$ galaxies are rare. Therefore, while many of the LAE photometric candidates from M13 may be true LAEs, singling out objects from the photometric sample with NB3420 detections may result in a higher-than-average selection of foreground contaminants.

In summary, these four photometric LAE candidates with NB3420 detections all have ambiguous SED shapes that make it difficult to verify their redshifts photometrically and confirm their possible LyC detections. One object, *lae4070*, has similar $J_{125}-H_{160}$ and $V_{606}-J_{125}$ colors to many $z \sim 2.85$ galaxies in our sample and is the most promising photometric LAE candidate for true LyC emission. The other three objects (*lae5200*, *lae6510*, and *lae7180*) display the ambiguous SED shape described in Section 3.5.1, which may describe galaxies at many redshifts. As we cannot unambiguously determine whether or not the four photometric LAE candidates discussed in this section are truly at $z \sim 2.85$, we adopt a conservative approach and do not count the NB3420 detections for these objects as secure signatures of leaking LyC radiation.

CHAPTER 4

Concluding Thoughts

When I first started my thesis work in early 2010, the very first detections of directly-imaged LyC emission in high-redshift galaxies were being published (Iwata et al., 2009; Nestor et al., 2011). The large number of putative LyC detections in galaxies at $z \sim 3$, with their apparently extreme F_{UV}/F_{LyC} ratios, was quite intriguing − especially compared with the lack of confirmed LyC detections in galaxies at $z < 2$, at the time. Over the past 5 years, the number of low-redshift LyC detections has slowly crept up, and the number of high-redshift LyC detections has dramatically decreased, as new data have ruled out many candidate LyC-emitting galaxies because of foreground contamination. The most recent work in this field − including the work in this thesis, and that of Siana et al. (2015) and Vanzella et al. (2015) − also indicates that the apparently extreme F_{UV}/F_{LyC} ratios observed in the first high-redshift LyC imaging studies were due to foreground contaminants as well. What began as a fairly simple project to directly image LyC emission through a single narrowband filter, seemed to generate more new questions than it answered. As questions about the prevalence of foreground contaminants and complex galaxy morphologies began to demand more data, and the apparently extreme F_{UV}/F_{LyC} ratios required the consideration of new stellar population synthesis models, this project took new and unexpected turns, eventually growing into a full Ph.D. thesis.

It has been very exciting for me to undertake my thesis work in a field that is so young, and so full of opportunities for new discoveries and potential paradigm shifts. I hope that future work in this field can overcome the difficulties faced in current observations, and that this new data will lead to a more complete understanding of how LyC photons escape galaxies and uncover the true contribution of star-forming galaxies to the ionizing background.

Bibliography

Adelberger, K. L., Steidel, C. C., Pettini, M., Shapley, A. E., Reddy, N. A., & Erb, D. K. 2005, ApJ, 619, 697

Adelberger, K. L., Steidel, C. C., Shapley, A. E., Hunt, M. P., Erb, D. K., Reddy, N. A., & Pettini, M. 2004, ApJ, 607, 226

Atek, H., Kunth, D., Schaerer, D., Hayes, M., Deharveng, J. M., Östlin, G., & Mas-Hesse, J. M. 2009, A&A, 506, L1

Barnes, L. A., Haehnelt, M. G., Tescari, E., & Viel, M. 2011, MNRAS, 416, 1723

Bennett, C. L., Halpern, M., Hinshaw, G., Jarosik, N., Kogut, A., Limon, M., Meyer, S. S., Page, L., Spergel, D. N., Tucker, G. S., Wollack, E., Wright, E. L., Barnes, C., Greason, M. R., Hill, R. S., Komatsu, E., Nolta, M. R., Odegard, N., Peiris, H. V., Verde, L., & Weiland, J. L. 2003, ApJS, 148, 1

Bertin, E. & Arnouts, S. 1996, A&AS, 117, 393

Biretta, J. & Baggett, S. 2013, WFC3 Post-Flash Calibration, Tech. rep.

Blanc, G. A., Adams, J. J., Gebhardt, K., Hill, G. J., Drory, N., Hao, L., Bender, R., Ciardullo, R., Finkelstein, S. L., Fry, A. B., Gawiser, E., Gronwall, C., Hopp, U., Jeong, D., Kelzenberg, R., Komatsu, E., MacQueen, P., Murphy, J. D., Roth, M. M., Schneider, D. P., & Tufts, J. 2011, ApJ, 736, 31

Blanton, M. R. & Roweis, S. 2007, AJ, 133, 734

Bolton, J. S. & Haehnelt, M. G. 2007, MNRAS, 382, 325

Borthakur, S., Heckman, T. M., Leitherer, C., & Overzier, R. A. 2014, Science, 346, 216

Brammer, G. B., van Dokkum, P. G., & Coppi, P. 2008, ApJ, 686, 1503

Bridge, C. R., Teplitz, H. I., Siana, B., Scarlata, C., Conselice, C. J., Ferguson, H. C., Brown, T. M., Salvato, M., Rudie, G. C., de Mello, D. F., Colbert, J., Gardner, J. P., Giavalisco, M., & Armus, L. 2010, ApJ, 720, 465

Bruzual, G. & Charlot, S. 2003, MNRAS, 344, 1000

Calzetti, D., Armus, L., Bohlin, R. C., Kinney, A. L., Koornneef, J., & Storchi-Bergmann, T. 2000, ApJ, 533, 682

Chabrier, G. 2003, ApJL, 586, L133

Cooke, J., Ryan-Weber, E. V., Garel, T., & Díaz, C. G. 2014, MNRAS, 441, 837

Cowie, L. L., Barger, A. J., & Trouille, L. 2009, ApJ, 692, 1476

Cowie, L. L. & Hu, E. M. 1998, AJ, 115, 1319

Cucciati, O., Zamorani, G., Lemaux, B. C., Bardelli, S., Cimatti, A., Le Fèvre, O., Cassata, P., Garilli, B., Le Brun, V., Maccagni, D., Pentericci, L., Tasca, L. A. M., Thomas, R., Vanzella, E., Zucca, E., Amorin, R., Capak, P., Cassarà, L. P., Castellano, M., Cuby, J. G., de la Torre, S., Durkalec, A., Fontana, A., Giavalisco, M., Grazian, A., Hathi, N. P., Ilbert, O., Moreau, C., Paltani, S., Ribeiro, B., Salvato, M., Schaerer, D., Scodeggio, M., Sommariva, V., Talia, M., Taniguchi, Y., Tresse, L., Vergani, D., Wang, P. W., Charlot, S., Contini, T., Fotopoulou, S., López-Sanjuan, C., Mellier, Y., & Scoville, N. 2014, A&A, 570, A16

Dayal, P., Ferrara, A., Saro, A., Salvaterra, R., Borgani, S., & Tornatore, L. 2009, MNRAS, 400, 2000

Diener, C., Lilly, S. J., Ledoux, C., Zamorani, G., Bolzonella, M., Murphy, D. N. A., Capak, P., Ilbert, O., & McCracken, H. 2015, ApJ, 802, 31

Diolaiti, E., Bendinelli, O., Bonaccini, D., Close, L., Currie, D., & Parmeggiani, G. 2000, A&AS, 147, 335

Eldridge, J. J. & Stanway, E. R. 2009, MNRAS, 400, 1019

Fan, X., Carilli, C. L., & Keating, B. 2006a, ARAA, 44, 415

Fan, X., Strauss, M. A., Becker, R. H., White, R. L., Gunn, J. E., Knapp, G. R., Richards, G. T., Schneider, D. P., Brinkmann, J., & Fukugita, M. 2006b, AJ, 132, 117

Faucher-Giguère, C., Lidz, A., Hernquist, L., & Zaldarriaga, M. 2008, ApJ, 688, 85

Fioc, M. & Rocca-Volmerange, B. 1997, A&A, 326, 950

Fontanot, F., Cristiani, S., & Vanzella, E. 2012, MNRAS, 425, 1413

Förster Schreiber, N. M., Franx, M., Labbé, I., Rudnick, G., van Dokkum, P. G., Illingworth, G. D., Kuijken, K., Moorwood, A. F. M., Rix, H.-W., Röttgering, H., & van der Werf, P. 2006, AJ, 131, 1891

Förster Schreiber, N. M., Genzel, R., Bouché, N., Cresci, G., Davies, R., Buschkamp, P., Shapiro, K., Tacconi, L. J., Hicks, E. K. S., Genel, S., Shapley, A. E., Erb, D. K., Steidel, C. C., Lutz, D., Eisenhauer, F., Gillessen, S., Sternberg, A., Renzini, A., Cimatti, A., Daddi, E., Kurk, J., Lilly, S., Kong, X., Lehnert, M. D., Nesvadba, N., Verma, A., McCracken, H., Arimoto, N., Mignoli, M., & Onodera, M. 2009, ApJ, 706, 1364

Fruchter, A. S. e. 2010, in 2010 Space Telescope Science Institute Calibration Workshop, p. 382-387, 382–387

Fynbo, J. P. U., Jakobsson, P., Prochaska, J. X., Malesani, D., Ledoux, C., de Ugarte Postigo, A., Nardini, M., Vreeswijk, P. M., Wiersema, K., Hjorth, J., Sollerman, J., Chen, H.-W., Thöne, C. C., Björnsson, G., Bloom, J. S., Castro-Tirado, A. J., Christensen, L., De Cia, A., Fruchter, A. S., Gorosabel, J., Graham, J. F., Jaunsen, A. O., Jensen, B. L., Kann, D. A., Kouveliotou, C., Levan, A. J., Maund, J., Masetti, N., Milvang-Jensen, B., Palazzi, E., Perley, D. A., Pian, E., Rol, E., Schady, P., Starling, R. L. C., Tanvir, N. R., Watson, D. J., Xu, D., Augusteijn, T., Grundahl, F., Telting, J., & Quirion, P.-O. 2009, ApJS, 185, 526

Gawiser, E., Francke, H., Lai, K., Schawinski, K., Gronwall, C., Ciardullo, R., Quadri, R., Orsi, A., Barrientos, L. F., Blanc, G. A., Fazio, G., Feldmeier, J. J., Huang, J.-s., Infante,

L., Lira, P., Padilla, N., Taylor, E. N., Treister, E., Urry, C. M., van Dokkum, P. G., & Virani, S. N. 2007, ApJ, 671, 278

Glikman, E., Djorgovski, S. G., Stern, D., Dey, A., Jannuzi, B. T., & Lee, K.-S. 2011, ApJL, 728, L26

Gnedin, N. Y., Kravtsov, A. V., & Chen, H. 2008, ApJ, 672, 765

Gordon, K. D., Clayton, G. C., Misselt, K. A., Landolt, A. U., & Wolff, M. J. 2003, ApJ, 594, 279

Grimes, J. P., Heckman, T., Aloisi, A., Calzetti, D., Leitherer, C., Martin, C. L., Meurer, G., Sembach, K., & Strickland, D. 2009, ApJS, 181, 272

Grimes, J. P., Heckman, T., Strickland, D., Dixon, W. V., Sembach, K., Overzier, R., Hoopes, C., Aloisi, A., & Ptak, A. 2007, ApJ, 668, 891

Grogin, N. A., Kocevski, D. D., Faber, S. M., Ferguson, H. C., Koekemoer, A. M., Riess, A. G., Acquaviva, V., Alexander, D. M., Almaini, O., Ashby, M. L. N., Barden, M., Bell, E. F., Bournaud, F., Brown, T. M., Caputi, K. I., Casertano, S., Cassata, P., Castellano, M., Challis, P., Chary, R.-R., Cheung, E., Cirasuolo, M., Conselice, C. J., Roshan Cooray, A., Croton, D. J., Daddi, E., Dahlen, T., Davé, R., de Mello, D. F., Dekel, A., Dickinson, M., Dolch, T., Donley, J. L., Dunlop, J. S., Dutton, A. A., Elbaz, D., Fazio, G. G., Filippenko, A. V., Finkelstein, S. L., Fontana, A., Gardner, J. P., Garnavich, P. M., Gawiser, E., Giavalisco, M., Grazian, A., Guo, Y., Hathi, N. P., Häussler, B., Hopkins, P. F., Huang, J.-S., Huang, K.-H., Jha, S. W., Kartaltepe, J. S., Kirshner, R. P., Koo, D. C., Lai, K., Lee, K.-S., Li, W., Lotz, J. M., Lucas, R. A., Madau, P., McCarthy, P. J., McGrath, E. J., McIntosh, D. H., McLure, R. J., Mobasher, B., Moustakas, L. A., Mozena, M., Nandra, K., Newman, J. A., Niemi, S.-M., Noeske, K. G., Papovich, C. J., Pentericci, L., Pope, A., Primack, J. R., Rajan, A., Ravindranath, S., Reddy, N. A., Renzini, A., Rix, H.-W., Robaina, A. R., Rodney, S. A., Rosario, D. J., Rosati, P., Salimbeni, S., Scarlata, C., Siana, B., Simard, L., Smidt, J., Somerville, R. S., Spinrad, H., Straughn, A. N., Strolger, L.-G., Telford, O., Teplitz, H. I., Trump, J. R., van der Wel, A., Villforth, C.,

Wechsler, R. H., Weiner, B. J., Wiklind, T., Wild, V., Wilson, G., Wuyts, S., Yan, H.-J., & Yun, M. S. 2011, ApJS, 197, 35

Gronwall, C., Ciardullo, R., Hickey, T., Gawiser, E., Feldmeier, J. J., van Dokkum, P. G., Urry, C. M., Herrera, D., Lehmer, B. D., Infante, L., Orsi, A., Marchesini, D., Blanc, G. A., Francke, H., Lira, P., & Treister, E. 2007, ApJ, 667, 79

Guaita, L., Acquaviva, V., Padilla, N., Gawiser, E., Bond, N. A., Ciardullo, R., Treister, E., Kurczynski, P., Gronwall, C., Lira, P., & Schawinski, K. 2011, ApJ, 733, 114

Hatch, N. A., De Breuck, C., Galametz, A., Miley, G. K., Overzier, R. A., Röttgering, H. J. A., Doherty, M., Kodama, T., Kurk, J. D., Seymour, N., Venemans, B. P., Vernet, J., & Zirm, A. W. 2011, MNRAS, 410, 1537

Heckman, T. M., Borthakur, S., Overzier, R., Kauffmann, G., Basu-Zych, A., Leitherer, C., Sembach, K., Martin, D. C., Rich, R. M., Schiminovich, D., & Seibert, M. 2011, ApJ, 730, 5

Hogg, D. W., Cohen, J. G., Blandford, R., & Pahre, M. A. 1998, ApJ, 504, 622

Hopkins, P. F., Richards, G. T., & Hernquist, L. 2007, ApJ, 654, 731

Inoue, A. K., Iwata, I., Deharveng, J., Buat, V., & Burgarella, D. 2005, A&A, 435, 471

Inoue, A. K., Kousai, K., Iwata, I., Matsuda, Y., Nakamura, E., Horie, M., Hayashino, T., Tapken, C., Akiyama, M., Noll, S., Yamada, T., Burgarella, D., & Nakamura, Y. 2011, MNRAS, 411, 2336

Isobe, T. & Feigelson, E. D. 1990, in Bulletin of the American Astronomical Society, Vol. 22, Bulletin of the American Astronomical Society, 917–918

Iwata, I., Inoue, A. K., Matsuda, Y., Furusawa, H., Hayashino, T., Kousai, K., Akiyama, M., Yamada, T., Burgarella, D., & Deharveng, J. 2009, ApJ, 692, 1287

Jones, T. A., Ellis, R. S., Schenker, M. A., & Stark, D. P. 2013, ApJ, 779, 52

Kodama, T., Tanaka, I., Kajisawa, M., Kurk, J., Venemans, B., De Breuck, C., Vernet, J., & Lidman, C. 2007, MNRAS, 377, 1717

Koekemoer, A. M., Faber, S. M., Ferguson, H. C., Grogin, N. A., Kocevski, D. D., Koo, D. C., Lai, K., Lotz, J. M., Lucas, R. A., McGrath, E. J., Ogaz, S., Rajan, A., Riess, A. G., Rodney, S. A., Strolger, L., Casertano, S., Castellano, M., Dahlen, T., Dickinson, M., Dolch, T., Fontana, A., Giavalisco, M., Grazian, A., Guo, Y., Hathi, N. P., Huang, K.-H., van der Wel, A., Yan, H.-J., Acquaviva, V., Alexander, D. M., Almaini, O., Ashby, M. L. N., Barden, M., Bell, E. F., Bournaud, F., Brown, T. M., Caputi, K. I., Cassata, P., Challis, P. J., Chary, R.-R., Cheung, E., Cirasuolo, M., Conselice, C. J., Roshan Cooray, A., Croton, D. J., Daddi, E., Davé, R., de Mello, D. F., de Ravel, L., Dekel, A., Donley, J. L., Dunlop, J. S., Dutton, A. A., Elbaz, D., Fazio, G. G., Filippenko, A. V., Finkelstein, S. L., Frazer, C., Gardner, J. P., Garnavich, P. M., Gawiser, E., Gruetzbauch, R., Hartley, W. G., Häussler, B., Herrington, J., Hopkins, P. F., Huang, J.-S., Jha, S. W., Johnson, A., Kartaltepe, J. S., Khostovan, A. A., Kirshner, R. P., Lani, C., Lee, K.-S., Li, W., Madau, P., McCarthy, P. J., McIntosh, D. H., McLure, R. J., McPartland, C., Mobasher, B., Moreira, H., Mortlock, A., Moustakas, L. A., Mozena, M., Nandra, K., Newman, J. A., Nielsen, J. L., Niemi, S., Noeske, K. G., Papovich, C. J., Pentericci, L., Pope, A., Primack, J. R., Ravindranath, S., Reddy, N. A., Renzini, A., Rix, H.-W., Robaina, A. R., Rosario, D. J., Rosati, P., Salimbeni, S., Scarlata, C., Siana, B., Simard, L., Smidt, J., Snyder, D., Somerville, R. S., Spinrad, H., Straughn, A. N., Telford, O., Teplitz, H. I., Trump, J. R., Vargas, C., Villforth, C., Wagner, C. R., Wandro, P., Wechsler, R. H., Weiner, B. J., Wiklind, T., Wild, V., Wilson, G., Wuyts, S., & Yun, M. S. 2011, ApJS, 197, 36

Koekemoer, A. M., Fruchter, A. S., Hook, R. N., & Hack, W. 2003, in HST Calibration Workshop : Hubble after the Installation of the ACS and the NICMOS Cooling System, ed. S. Arribas, A. Koekemoer, & B. Whitmore, 337

Kornei, K. A., Shapley, A. E., Erb, D. K., Steidel, C. C., Reddy, N. A., Pettini, M., & Bogosavljević, M. 2010, ApJ, 711, 693

Kriek, M., van Dokkum, P. G., Labbé, I., Franx, M., Illingworth, G. D., Marchesini, D., & Quadri, R. F. 2009, ApJ, 700, 221

Larkin, J., Barczys, M., Krabbe, A., Adkins, S., Aliado, T., Amico, P., Brims, G., Campbell, R., Canfield, J., Gasaway, T., Honey, A., Iserlohe, C., Johnson, C., Kress, E., LaFreniere, D., Magnone, K., Magnone, N., McElwain, M., Moon, J., Quirrenbach, A., Skulason, G., Song, I., Spencer, M., Weiss, J., & Wright, S. 2006, New Astronomy Reviews, 50, 362

Lavalley, M. P., Isobe, T., & Feigelson, E. D. 1992, in Bulletin of the American Astronomical Society, Vol. 24, Bulletin of the American Astronomical Society, 839–840

Law, D. R., Shapley, A. E., Steidel, C. C., Reddy, N. A., Christensen, C. R., & Erb, D. K. 2012a, Nature, 487, 338

Law, D. R., Steidel, C. C., Erb, D. K., Pettini, M., Reddy, N. A., Shapley, A. E., Adelberger, K. L., & Simenc, D. J. 2007, ApJ, 656, 1

Law, D. R., Steidel, C. C., Shapley, A. E., Nagy, S. R., Reddy, N. A., & Erb, D. K. 2012b, ApJ, 759, 29

Leitet, E., Bergvall, N., Hayes, M., Linné, S., & Zackrisson, E. 2013, A&A, 553, A106

Leitet, E., Bergvall, N., Piskunov, N., & Andersson, B.-G. 2011, A&A, 532, A107

Leitherer, C., Ekström, S., Meynet, G., Schaerer, D., Agienko, K. B., & Levesque, E. M. 2014, ApJS, 212, 14

Leitherer, C., Ferguson, H. C., Heckman, T. M., & Lowenthal, J. D. 1995, ApJL, 454, L19

Lemaux, B. C., Cucciati, O., Tasca, L. A. M., Le Fèvre, O., Zamorani, G., Cassata, P., Garilli, B., Le Brun, V., Maccagni, D., Pentericci, L., Thomas, R., Vanzella, E., Zucca, E., Amorín, R., Bardelli, S., Capak, P., Cassarà, L. P., Castellano, M., Cimatti, A., Cuby, J. G., de la Torre, S., Durkalec, A., Fontana, A., Giavalisco, M., Grazian, A., Hathi, N. P., Ilbert, O., Moreau, C., Paltani, S., Ribeiro, B., Salvato, M., Schaerer, D., Scodeggio, M., Sommariva, V., Talia, M., Taniguchi, Y., Tresse, L., Vergani, D., Wang, P. W., Charlot,

S., Contini, T., Fotopoulou, S., Gal, R. R., Kocevski, D. D., López-Sanjuan, C., Lubin, L. M., Mellier, Y., Sadibekova, T., & Scoville, N. 2014, A&A, 572, A41

Loeb, A. & Barkana, R. 2001, ARAA, 39, 19

Lotz, J. M., Madau, P., Giavalisco, M., Primack, J., & Ferguson, H. C. 2006, ApJ, 636, 592

Malkan, M., Webb, W., & Konopacky, Q. 2003, ApJ, 598, 878

Massey, P., Strobel, K., Barnes, J. V., & Anderson, E. 1988, ApJ, 328, 315

Mostardi, R. E., Shapley, A. E., Nestor, D. B., Steidel, C. C., Reddy, N. A., & Trainor, R. F. 2013, ApJ, 779, 65

Nestor, D. B., Shapley, A. E., Kornei, K. A., Steidel, C. C., & Siana, B. 2013, ApJ, 765, 47

Nestor, D. B., Shapley, A. E., Steidel, C. C., & Siana, B. 2011, ApJ, 736, 18

Nilsson, K. K., Östlin, G., Møller, P., Möller-Nilsson, O., Tapken, C., Freudling, W., & Fynbo, J. P. U. 2010, ArXiv e-prints

O'Donnell, J. E. 1994, ApJ, 422, 158

Oesch, P. A., Bouwens, R. J., Illingworth, G. D., Carollo, C. M., Franx, M., Labbé, I., Magee, D., Stiavelli, M., Trenti, M., & van Dokkum, P. G. 2010, ApJL, 709, L16

Oke, J. B., Cohen, J. G., Carr, M., Cromer, J., Dingizian, A., Harris, F. H., Labrecque, S., Lucinio, R., Schaal, W., Epps, H., & Miller, J. 1995, PASP, 107, 375

Ouchi, M., Shimasaku, K., Akiyama, M., Simpson, C., Saito, T., Ueda, Y., Furusawa, H., Sekiguchi, K., Yamada, T., Kodama, T., Kashikawa, N., Okamura, S., Iye, M., Takata, T., Yoshida, M., & Yoshida, M. 2008, ApJS, 176, 301

Ouchi, M., Shimasaku, K., Okamura, S., Furusawa, H., Kashikawa, N., Ota, K., Doi, M., Hamabe, M., Kimura, M., Komiyama, Y., Miyazaki, M., Miyazaki, S., Nakata, F., Sekiguchi, M., Yagi, M., & Yasuda, N. 2004, ApJ, 611, 660

Pettini, M., Shapley, A. E., Steidel, C. C., Cuby, J.-G., Dickinson, M., Moorwood, A. F. M., Adelberger, K. L., & Giavalisco, M. 2001, ApJ, 554, 981

Postman, M., Argabright, V., Arnold, B., Aronstein, D., Atcheson, P., Blouke, M., Brown, T., Calzetti, D., Cash, W., Clampin, M., Content, D., Dailey, D., Danner, R., Doxsey, R., Ebbets, D., Eisenhardt, P., Feinberg, L., Fruchter, A., Giavalisco, M., Glassman, T., Gong, Q., Green, J., Grunsfeld, J., Gull, T., Hickey, G., Hopkins, R., Hraba, J., Hyde, T., Jordan, I., Kasdin, J., Kendrick, S., Kilston, S., Koekemoer, A., Korechoff, B., Krist, J., Mather, J., Lillie, C., Lo, A., Lyon, R., McCullough, P., Mosier, G., Mountain, M., Oegerle, B., Pasquale, B., Purves, L., Penera, C., Polidan, R., Redding, D., Sahu, K., Saif, B., Sembach, K., Shull, M., Smith, S., Sonneborn, G., Spergel, D., Stahl, P., Stapelfeldt, K., Thronson, H., Thronton, G., Townsend, J., Traub, W., Unwin, S., Valenti, J., Vanderbei, R., Werner, M., Wesenberg, R., Wiseman, J., & Woodgate, B. 2009, ArXiv e-prints

Prochaska, J. X., Madau, P., O'Meara, J. M., & Fumagalli, M. 2014, MNRAS, 438, 476

Reddy, N. A., Erb, D. K., Pettini, M., Steidel, C. C., & Shapley, A. E. 2010, ApJ, 712, 1070

Reddy, N. A., Pettini, M., Steidel, C. C., Shapley, A. E., Erb, D. K., & Law, D. R. 2012, ApJ, 754, 25

Reddy, N. A., Steidel, C. C., Erb, D. K., Shapley, A. E., & Pettini, M. 2006a, ApJ, 653, 1004

Reddy, N. A., Steidel, C. C., Fadda, D., Yan, L., Pettini, M., Shapley, A. E., Erb, D. K., & Adelberger, K. L. 2006b, ApJ, 644, 792

Reddy, N. A., Steidel, C. C., Pettini, M., Adelberger, K. L., Shapley, A. E., Erb, D. K., & Dickinson, M. 2008, ApJS, 175, 48

Rhoads, J. E., Malhotra, S., Dey, A., Stern, D., Spinrad, H., & Jannuzi, B. T. 2000, ApJL, 545, L85

Ricotti, M. 2002, MNRAS, 336, L33

Rudie, G. C., Steidel, C. C., Shapley, A. E., & Pettini, M. 2013, ApJ, 769, 146

Schaerer, D. 2002, A&A, 382, 28

Schlegel, D. J., Finkbeiner, D. P., & Davis, M. 1998, ApJ, 500, 525

Shapley, A. E., Steidel, C. C., Adelberger, K. L., Dickinson, M., Giavalisco, M., & Pettini, M. 2001, ApJ, 562, 95

Shapley, A. E., Steidel, C. C., Erb, D. K., Reddy, N. A., Adelberger, K. L., Pettini, M., Barmby, P., & Huang, J. 2005, ApJ, 626, 698

Shapley, A. E., Steidel, C. C., Pettini, M., & Adelberger, K. L. 2003, ApJ, 588, 65

Shapley, A. E., Steidel, C. C., Pettini, M., Adelberger, K. L., & Erb, D. K. 2006, ApJ, 651, 688

Shimakawa, R., Kodama, T., Tadaki, K.-i., Tanaka, I., Hayashi, M., & Koyama, Y. 2014, MNRAS, 441, L1

Siana, B., Polletta, M. d. C., Smith, H. E., Lonsdale, C. J., Gonzalez-Solares, E., Farrah, D., Babbedge, T. S. R., Rowan-Robinson, M., Surace, J., Shupe, D., Fang, F., Franceschini, A., & Oliver, S. 2008, ApJ, 675, 49

Siana, B., Shapley, A. E., Kulas, K. R., Nestor, D. B., Steidel, C. C., Teplitz, H. I., Alavi, A., Brown, T. M., Conselice, C. J., Ferguson, H. C., Dickinson, M., Giavalisco, M., Colbert, J. W., Bridge, C. R., Gardner GSFC), J. P., & de Mello (Catholic University), D. F. 2015, ArXiv e-prints

Siana, B., Smail, I., Swinbank, A. M., Richard, J., Teplitz, H. I., Coppin, K. E. K., Ellis, R. S., Stark, D. P., Kneib, J.-P., & Edge, A. C. 2009, ApJ, 698, 1273

Siana, B., Teplitz, H. I., Colbert, J., Ferguson, H. C., Dickinson, M., Brown, T. M., Conselice, C. J., de Mello, D. F., Gardner, J. P., Giavalisco, M., & Menanteau, F. 2007, ApJ, 668, 62

Siana, B., Teplitz, H. I., Ferguson, H. C., Brown, T. M., Giavalisco, M., Dickinson, M., Chary, R., de Mello, D. F., Conselice, C. J., Bridge, C. R., Gardner, J. P., Colbert, J. W., & Scarlata, C. 2010, ApJ, 723, 241

Songaila, A. & Cowie, L. L. 2010, ApJ, 721, 1448

Steidel, C. C., Adelberger, K. L., Giavalisco, M., Dickinson, M., & Pettini, M. 1999, ApJ, 519, 1

Steidel, C. C., Adelberger, K. L., Shapley, A. E., Erb, D. K., Reddy, N. A., & Pettini, M. 2005, ApJ, 626, 44

Steidel, C. C., Adelberger, K. L., Shapley, A. E., Pettini, M., Dickinson, M., & Giavalisco, M. 2000, ApJ, 532, 170

—. 2003, ApJ, 592, 728

Steidel, C. C., Bogosavljević, M., Shapley, A. E., Kollmeier, J. A., Reddy, N. A., Erb, D. K., & Pettini, M. 2011, ApJ, 736, 160

Steidel, C. C., Giavalisco, M., Pettini, M., Dickinson, M., & Adelberger, K. L. 1996, ApJL, 462, L17

Steidel, C. C., Pettini, M., & Adelberger, K. L. 2001, ApJ, 546, 665

Steidel, C. C., Rudie, G. C., Strom, A. L., Pettini, M., Reddy, N. A., Shapley, A. E., Trainor, R. F., Erb, D. K., Turner, M. L., Konidaris, N. P., Kulas, K. R., Mace, G., Matthews, K., & McLean, I. S. 2014, ApJ, 795, 165

Steidel, C. C., Shapley, A. E., Pettini, M., Adelberger, K. L., Erb, D. K., Reddy, N. A., & Hunt, M. P. 2004, ApJ, 604, 534

Stetson, P. B., Vandenberg, D. A., & Bolte, M. 1996, PASP, 108, 560

Trainor, R. F. & Steidel, C. C. 2012, ApJ, 752, 39

Vanzella, E., de Barros, S., Castellano, M., Grazian, A., Inoue, A. K., Schaerer, D., Guaita, L., Zamorani, G., Giavalisco, M., Siana, B., Pentericci, L., Giallongo, E., Fontana, A., & Vignali, C. 2015, ArXiv e-prints

Vanzella, E., Giavalisco, M., Inoue, A. K., Nonino, M., Fontanot, F., Cristiani, S., Grazian, A., Dickinson, M., Stern, D., Tozzi, P., Giallongo, E., Ferguson, H., Spinrad, H., Boutsia, K., Fontana, A., Rosati, P., & Pentericci, L. 2010a, ApJ, 725, 1011

Vanzella, E., Guo, Y., Giavalisco, M., Grazian, A., Castellano, M., Cristiani, S., Dickinson, M., Fontana, A., Nonino, M., Giallongo, E., Pentericci, L., Galametz, A., Faber, S. M., Ferguson, H. C., Grogin, N. A., Koekemoer, A. M., Newman, J., & Siana, B. D. 2012, ApJ, 751, 70

Vanzella, E., Siana, B., Cristiani, S., & Nonino, M. 2010b, MNRAS, 404, 1672

Venemans, B. P., Röttgering, H. J. A., Miley, G. K., van Breugel, W. J. M., de Breuck, C., Kurk, J. D., Pentericci, L., Stanford, S. A., Overzier, R. A., Croft, S., & Ford, H. 2007, A&A, 461, 823

Verhamme, A., Dubois, Y., Blaizot, J., Garel, T., Bacon, R., Devriendt, J., Guiderdoni, B., & Slyz, A. 2012, A&A, 546, A111

Verhamme, A., Orlitova, I., Schaerer, D., & Hayes, M. 2014, ArXiv e-prints

Yajima, H., Li, Y., Zhu, Q., Abel, T., Gronwall, C., & Ciardullo, R. 2012, ApJ, 754, 118

Zackrisson, E., Inoue, A. K., & Jensen, H. 2013, ApJ, 777, 39

Zastrow, J., Oey, M. S., & Pellegrini, E. W. 2013, ApJ, 769, 94